THE UNIVERSITY OF HULL

ELECTROCHEMICAL SENSOR FOR THE DETECTION OF SCALING IONS IN FORMATION WATER

being a Thesis submitted for the Degree of Doctor of Philosophy

in the University of Hull

by

Robert David Crapnell

MChem (University of Hull)

February 2018

Acknowledgements

I would first like to thank my supervisors Dr Jay Wadhawan, Dr Jason Eames and Dr Nathan Lawrence for their help, support and guidance throughout my PhD project. I am sincerely grateful for everything you have done for me and I feel privileged to have worked with you. Thanks also go to The University of Hull and Schlumberger Gould Research Ltd. for their financial support in sponsoring this project.

I would like to thank all the people at The University of Hull that have made my time here enjoyable; especially Ben, Jevan, Ana Maria, Anupam, Connor, Jamie, Khaled and Lee.

Finally, I would like to thank my family for being there for me throughout my time in education. I especially thank my father, John, for his constant encouragement, my mother, Caroline, for her patience throughout this journey, my sister, Lizzie, for all the support she has given me and Annie for always being there for me and making my time away from university so amazing. None of this could have been achieved without any of you.

Abstract

This thesis aims to develop appropriate sensing chemistry for the electrochemical detection of alkaline-earth metal ions in formation water. Accordingly, the first chapter outlines the relevance of this work and gives an overview of the methods currently used for the determination of alkaline-earth metals in aqueous conditions. The second chapter then details the electrochemical concepts that underpin the subsequent results and the third chapter outlines the experimental techniques used throughout this work.

The reliable measurement of peak potentials in non-aqueous conditions is challenging. IUPAC recommends the use of an internal standard, typically the ferrocene | ferricinium redox couple. Chapter 4 investigates the reliability of this system and finds that chloride ions present in the system interfere with the ferrocene. This chapter shows that the ferrocene | ferricinium redox couple can be used as an internal standard in non-aqueous environments alongside a quasi-reference electrode; however, the exact solution composition and conditions must be considered. Therefore, any result obtained must be thought of in terms of the system, where each component must be scrutinised.

Chapter 5 focusses on the interaction of chlorquinaldol and broquinaldol with alkaline-earth metals as a route for detection. Firstly, the voltammetric response of the two quinaldols is characterised in equimolar DMSO/H_2O with a DISP2 reaction process proposed for both due to the decrease in apparent diffusion coefficients with increasing concentrations. Both ligands produced an increase in the N_{eff} values in the presence of barium ions above 10 mM. It is also demonstrated that chlorquinaldol is more sensitive to barium ions over strontium and calcium ions.

The use of compounds soluble in aqueous conditions allows for the use of a reliable commercial Ag | AgCl reference electrode. Ferrocenemethanol is a water-soluble derivative of ferrocene that interacts with thiols. Chapter 6 explores the EC' electrode mechanism that is present for ferrocenemethanol and tiopronin. It shows how the turnover number can be manipulated by changing the solution pH in order to increase

the reactivity of the tiopronin. The introduction of barium ions to the system (above 10 mM) is shown to reduce the turnover number; this allows for their determination but not to levels low enough for the desired application of this work.

The first two sensing methodologies explored utilised amperometric changes to determine the presence of alkaline-earth metal cations. Chapter 7 utilises an entirely novel approach to ion sensing by using changes in both the peak potential and current to successfully determine the concentration of alkaline-earth metal ions. It looks at the voltammetric response of disodium rhodizonate which is a water soluble compound that can bind with barium to produce a solid precipitate. This complexation is shown to produce an oxidative shift in the reductive peak potentials and a decrease in the peak current. The system exhibits the ability to detect alkaline-earth metal cations in this way at pH 8.5 (sea water), pH 7 (formation water) and at 35 % salinity (sea water). A 3-Dimensional model is produced that allowed for the prediction of barium ion concentrationn in samples containing strontium ions as an interfering substance. This model produced good results with every test sample producing a peak potential within 5 mV of the true value.

Table of Contents

List of Abbreviations

AC	alternating current
AES	atomic emission spectroscopy
BAPTA	(1,2-bis(*o*-aminophenoxy)ethane-N.N,N',N'-tetraacetic acid
BQ	broquinaldol
CE	counter electrode
Cp	cyclopentadiene
CQ	chlorquinaldol
CV	cyclic voltammetry
DC	direct current
DISP1	disproportionation reaction where the first step is the slow step
DISP2	disproportionation reaction where the second step is the slow step
DMSO	dimethyl sulfoxide
DNA	deoxyribonucleic acid
EDTA	ethylenediamine tetraacetic acid
EGTA	ethyleneglycol-bis-N,N,N',N'-tetraacetic acid
EMF	electromotive force
ET	electronic tongue
FAAS	flame atomic absorption spectroscopy
Fc	ferrocene
FcMeOH	ferrocenemethanol
FT	Fourier transform
GBHA	glycoxal-bis(2-hydroxyanil)
GC	glassy carbon
GO-ODA	graphene oxide octadecylamine
HCL	hollow cathode lamp
HOMO	highest occupied molecular orbital
ICP	inductively coupled plasma
IHP	inner Helmholtz plane
ISE	ion selective electrode
IUPAC	International Union of Pure and Applied Chemistry
L	ligand
LOD	limit of detection

LSV	linear sweep voltammetry
LUMO	lowest unoccupied molecular orbital
M	metal
MRI	magnetic resonance imaging
MSA	2-mercaptosuccinic acid
NaRZ	sodium rhodizonate
NMM	N-methyl mesoporphyrin
NMR	nuclear magnetic resonance
NP	nanoparticle
OHP	outer Helmholtz plane
PET	photo induced electron transfer
PVC	polyvinyl chloride
RDE	rotating disc electrode
RDV	rotating disc voltammetry
RE	reference electrode
R-S	Randles-Ševčík
SHE	standard hydrogen electrode
SWV	square wave voltammetry
TBAP	tetrabutylammonium perchlorate
TGA	thioglycolic acid
THBQ	tetrahydroxybenzoquinone
Tio	tiopronin
TMS	tetramethylsilane
TOF	turnover frequency
TON	turnover number
UV	ultraviolet
Vis	visible
WE	working electrode

List of Symbols

A	area
C	capacitance / concentration
D	diffusion coefficient
E	electromotive force
E_a	activation energy
E^0	standard electrode potential
E_{cell}^0	measured electrode potential
E_f^0	formal potential
E_{mid}	$½(E_p^{ox}+E_p^{red})$
E_p	peak potential
F	force
G	Gibbs energy
h	hydration number
I	current / ionic strength
I_p	peak current
i_{lim}	limiting current
j	flux
k	rate constant
K_{sp}	solubility product
k_{xy}	selectivity coefficient
M	molecular weight
m_T	mass transfer coefficient
N_{app}	measured limiting current normalised by the blank limiting current
N_{eff}	N_{app} multiplied by the normalised solution viscosity
n	number of moles / number of electrons
P	pressure
Q	charge
R	molar gas constant / resistance
R_e	Reynolds number
r	radius
T	temperature

t	time
V	voltage
Z	charge
α	activity
α/β	Tafel transfer coefficients
γ	activity coefficient / excess factor
ΔE	peak-to-peak separation
ΔH_L^0	lattice enthalpy
λ	kinetic parameter
μ	chemical potential
ν	scan rate / kinematic viscosity
ϕ	potential
φ	volta potential
ω	rotation velocity
[]	concentration

1 Introduction

This thesis is aimed toward the development of a low cost, down hole, electrochemical sensor capable of detecting scaling ions in formation water. Scaling ions such as calcium, strontium and barium can form sparingly soluble inorganic salts in oilfield operations. The accumulation of these compounds on oilfield equipment can cause major flow assurance problems and possibly halt oilfield operations.[1] Currently, scale inhibitors can be used in bulk to deter the accumulation of these compounds.[2] The ability to predict the location and volume of scale formation in oilfield operations would increase efficiency, have environmental benefits from the reduced use of inhibitors, and greatly reduce costs.

1.1 Scale

Scale is a deposit of insoluble, or slightly soluble, compounds formed upon the surface of another material; e.g. metal or rock. The most widely known example of this is the formation of limescale, figure 1.1, on the inside of pipes and containers charged with the heating of water.

Figure 1.1 - An image showing the build-up of limescale on the inside of a kettle.

There are two common classifications of scale that occurs in oilfield operations; inorganic scale and organic scale.[3,4] In the oil industry, some of the most frequently encountered organic scales are paraffin wax, asphaltenes and gas hydrates. This thesis will focus on the other primary form of scale; inorganic scale.

Inorganic scale is a crystalline deposit, typically consisting of one or more compounds, that results from the precipitation of minerals from water. There are numerous varieties of inorganic scale, table 1.1, which can form depending on the ions present in the system. Deep subsurface water that is present in an oilfield operation will typically become enriched in ions depending on its surrounding environment; e.g. sandstone reservoirs will become saturated with calcium (Ca^{2+}) and magnesium (Mg^{2+}) cations.[1]

Table 1.1 - A table presenting the chemical name, mineral name and formula of some common inorganic scale found in oilfield operations.

Chemical Name	Mineral Name	Formula
Calcium carbonate	Calcite	$CaCO_3$
Calcium carbonate	Aragonite	$CaCO_3$
Calcium carbonate	Vaterite	$CaCO_3$
Calcium sulfate	Anhydrite	$CaSO_4$
Calcium sulfate dihydrate	Gypsum	$CaSO_4.2H_2O$
Strontium sulfate	Celestite	$SrSO_4$
Barium sulfate	Barite	$BaSO_4$
Iron sulfide	Pyrite	FeS_2
Sodium chloride	Halite	NaCl
Calcium fluoride	Fluorite	CaF_2
Lead (II) sulfide	Galena	PbS

Inorganic scale formation is apparent in three main ways; supersaturation of conditions arising from a change in the pressure or temperature, the mixing of two incompatible fluids or through a microbial induced method.[5,6] Not all scales form for the same reason or in the same location within an oilfield operation. Carbonate based scale will form predominantly in the wellbore and production facilities following a change in the temperature or pressure.[7] Calcium carbonate is the most common carbonate scale that is formed.

$$Ca^{2+}_{(aq)} + 2HCO^{-}_{3(aq)} = CaCO_{3(s)} + CO_{2(aq)} + H_2O_{(l)} \qquad 1.1$$

In addition to this, it is naturally abundant in deep sea water; where it undergoes the same chemical changes due to alterations in the temperature and pressure.[8]

The mixing of incompatible fluids is the primary way of inducing sulfate scale formation. A common example of this is the introduction of sea water (typically a high sulfate concentration) to bottom hole formation water (typically rich in Ca^{2+}, Sr^{2+} and Ba^{2+}).

$$Ba^{2+}_{(aq)} + SO^{2-}_{4(aq)} = BaSO_{4(s)} \qquad 1.2$$

This form of scale will commonly occur inside the wellbore, near the wellbore area or in the production facilities.

The formation of these scales present a massive problem to the extraction of oil from wells. The build-up of these sparingly soluble compounds on the pipelines will dramatically reduce the interior area of the pipes, figure 1.2.

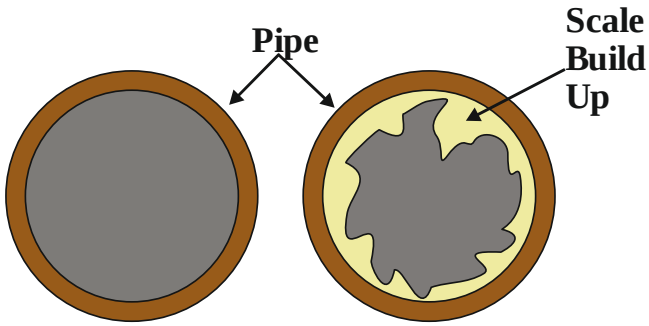

Figure 1.2 - An image showing the formation of scale on the interior of a pipe and the resulting reduced area.

Consequently, this reduction in area, A, means a much greater force, F, is required to achieve the same recovery or pressure, P.

$$P = \frac{F}{A} \qquad 1.3$$

In fact, the accumulation of scale can be devastating to oil recovery; where a North Sea well observed a reduction in production from 30,000 barrels per day to zero in the space of 24 hours.[9]

Scale formation is clearly a key aspect to consider when looking at the efficiency of oil recovery capable from an oil well. Both of the two main mechanisms of scale formation involve aqueous solutions, be it the supersaturation of water or the mixing of incompatible ones. Consequently, understanding the composition of different waters is key.

1.2 Formation, produced and sea water

Formation water is water that has been isolated with oil and natural gas between layers impermeable rock for millions of years.[10] In a petroleum reservoir, below the target layer of hydrocarbons sits a layer of water known as formation water, figure 1.3.

Figure 1.3 - A schematic showing the typical structure of an oil reservoir.

The properties of formation water vary depending on the specific reservoir. It is typically slightly acidic, with a pH just less than[10] 7.0 and its viscosity increases with pressure, salinity and decreasing temperature.[11] As mentioned earlier, these waters will typically become enriched with different ions depending on its surroundings. This formation water is described as produced water once it has been combined with injected water, figure 1.4.

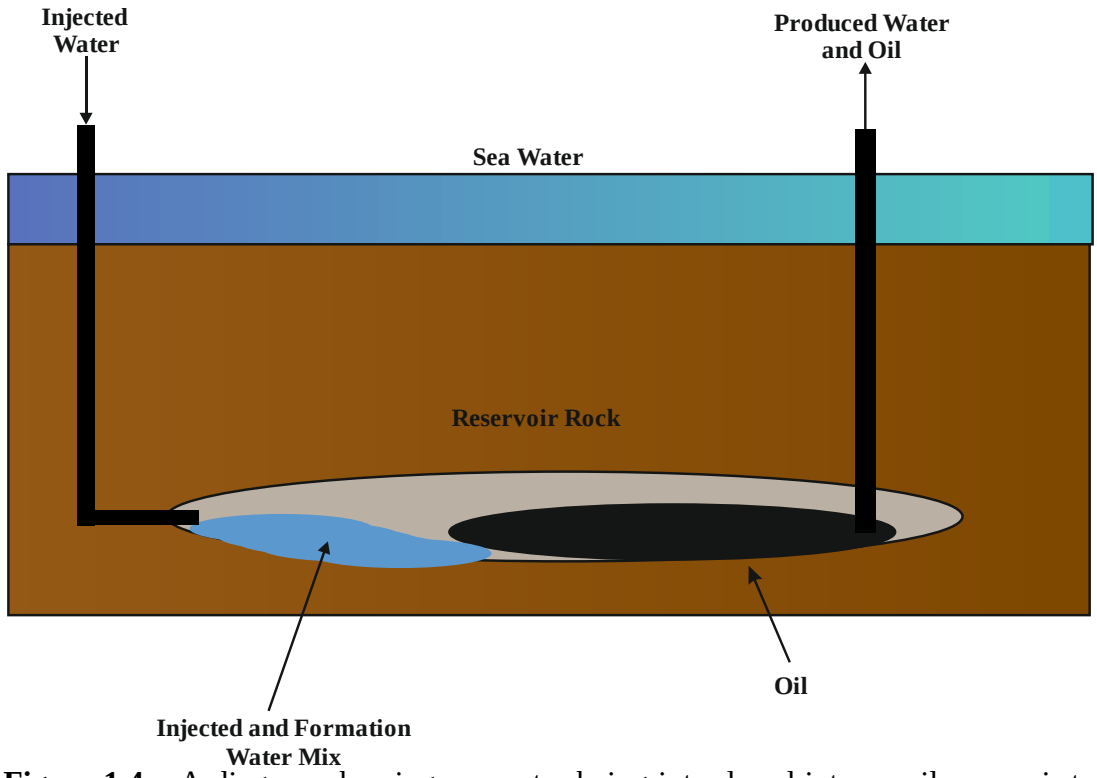

Figure 1.4 – A diagram showing sea water being introduced into an oil reservoir to aid in secondary oil recovery. The sea water mixes with the formation water naturally present in the reservoir to form produced water.

This produced water is generated during the production of oil and gas from wells as water is commonly injected into the system during secondary recovery.[12] Produced water is a complex concoction of different chemicals, organic and inorganic. An overview of the mean concentrations of some ions that are present in produced water and a comparison to their typical concentrations in 35 % salinity seawater is given in table 1.2. It can be observed from table 1.2 that the concentrations of significant cations is much larger in produced water than sea water. This means that, as produced water is a mixture of formation water and injected water; formation water must have a much larger concentration of these ions in. Consequently, when water is injected into the system (commonly this is sea water) compounds that are abundant, such as sulfates and carbonates, will react with these ions to form scale. Sea water typically has a salinity, or total dissolved solids, of 35 g kg^{-1} and a pH in the range of 8.08-8.33.[14] As this is commonly used in second phase oil recovery, the typical composition of sea water for these compounds that can lead to the formation of scale are given in table 1.2 and 1.3.

Table 1.2 - A table showing mean concentrations of significant ions in produced water and sea water. Data is taken from Collins (1975)[10] and Neff (2002).[13]

Chemical (Formula)	Sea Water Concentration (mg L^{-1})	Produced Water Concentration (mg L^{-1})
Sodium	10,560	65 - 97,000
Potassium	380	3 - 6,500
Magnesium	1,270	4 - 11,700
Calcium	400	13 - 118,800
Strontium	13	7 - 3,200
Barium	0.003 - 0.034	≤0.001 - 2,000

Table 1.3 - A table showing the typical sea water composition for significant compounds. Data obtained from Lyman and Fleming (1940).[15]

Chemical	Sea Water Concentration (mg L^{-1})
Sulfate	2,649
Bicarbonate	140
Flouride	1

Tables 1.2 and 1.3 show that sea water contains a large concentration of sulfate ions and a very low concentration of barium ions. When mixed with formation water however, there is a large concentration of both ions present; hence the formation of barite scale.

It can be seen through table 1.1 that a vast majority of scale that forms in oilfield operations involves the alkaline-earth metals. The alkaline-earth metals refer to calcium, strontium, barium and radium. For the sake of this thesis, radium will not be discussed; however, magnesium will be included in part. Therefore, the next section will look to understand what these metals are and why it is they are prone to this sort of chemistry.

1.3 Alkaline-earth metal ions

This thesis is primarily concerned with magnesium, calcium, strontium and barium. Magnesium and calcium are two of the most abundant elements in the Earth's crust; eight and fifth respectively. They are also the third and seventh most abundant elements present in sea water.[16] Barium and strontium occur far less commonly, being the fourteenth and fifteenth most abundant elements on Earth.[17] Due to its high abundance, magnesium is commercially extracted from sea water; where 1 g of Mg ions can be obtained from 1 L of sea water. This process functions due to the solubility of mononegative salts in water increases as you descend the group. Therefore, adding calcium hydroxide (or oxide) to sea water forces the precipitation of magnesium hydroxide; which is then converted to a chloride *via* treatment with hydrochloric acid.[16]

$$CaO_{(s)} + H_2O_{(l)} \rightarrow C(OH)_{2(aq)} \rightleftharpoons Ca^{2+}_{(aq)} + 2OH^-_{(aq)} \quad 1.4$$

$$Mg^{2+}_{(aq)} + 2OH^-_{(aq)} \rightarrow Mg(OH)_{2(s)} \quad 1.5$$

$$Mg(OH)_{2(s)} + 2HCl_{(aq)} \rightarrow MgCl_{2(aq)} + 2H_2O_{(l)} \quad 1.6$$

The other three elements are typically extracted from their molten chlorides through electrolysis; whilst barium and strontium can be obtained through their reduction *via* aluminium.[16]

$$6SrO_{(s)} + 2Al_{(l)} \rightarrow 3Sr_{(s)} + Sr_3Al_2O_{6(s)} \quad 1.7$$

The alkaline-earth metals are defined by their silvery metal appearance, ionic model bonding and their ns^2 valence electron configuration. They exhibit similar trends to other groups in the periodic table; for example their ionic radii increasing and first ionization energy decreasing as you descend the group. Some of the key properties of these elements are presented in table 1.4.

Table 1.4 - Some selected properties of the alkaline-earth metal ions including magnesium. Data obtained from Shriver and Atkins.[16]

	Magnesium (Mg)	**Calcium (Ca)**	**Strontium (Sr)**	**Barium (Ba)**
Metallic radius (pm)	150	197	215	217
Ionic radius (pm)	72	100	126	142
Coordination number	6	6	8	8
First ionization energy (kJ mol^{-1})	900	736	590	502
$E^{\ominus}$ (M^{2+}, M) (V)	-2.38	-2.87	-2.89	-2.90
Density (g cm^{-3})	1.74	1.54	2.62	3.51
Melting point (°C)	650	850	768	714
$\Delta_{hyd}H^{\ominus}$ (kJ mol^{-1})	-1920	-1650	-1480	-1360

It can be seen from table 1.4 that the metallic radius increases down the group; this is indicative of the electron being further away from the nucleus, at a higher potential energy and, consequently, less tightly bound to the nucleus. Even so, only a very small increase in metallic radii is seen between calcium, strontium and barium due to the lanthanide contraction. This phenomena is due to the poor shielding provided by f electrons, which results in a higher than expected nuclear charge. The ionic radii of the alkaline-earth metals follows a more uniform increase in size. This refers to the size of the M^{2+} ion. It follows that the coordination number, or typical number of atoms or ions that immediately surround the central M^{2+} in a complex or crystal, increases as the ionic radii increases. Descending the group makes the formation of M^{2+} ions easier,

in turn this results in increased electro positivity and increased reactivity down the group. This is reflected in the standard potentials, $E^{\ominus}$, for the M^{2+} | M becoming increasingly negative as you descend the group. The increase in reactivity is observed through their reaction with water; whereby calcium, strontium and barium will react with cold water, whereas, magnesium will only react with hot water.

$$M_{(s)} + 2H_2O_{(l)} \rightarrow M(OH)_{2(aq)} + H_{2(g)} \qquad 1.8$$

This can also be observed in terms of the lattice enthalpies, $\Delta H_L^{\ominus}$, of the different systems. It is defined as the standard molar enthalpy change accompanying the formation of a gas of ions from the solid.[16] The lattice enthalpies play a key role when investigating solubility as it involves the breaking of the solid lattice. In general, as the difference in size of the ions involved becomes larger, the more soluble the compound is in water. When observing the alkaline-earth metal hydroxides, scheme 1.8; the solubility increases as you trend down the group from magnesium to barium. This shows that for a small anion, OH^-, a large cation, Ba^{2+}, increases the solubility.

Table 1.1 showed that the alkaline-earth metals form two types of compounds of particular interest to this work; carbonates and sulfates. Calcium carbonate is the most common of these in nature; appearing as limestone, chalk, marble and coral to name a few. It can appear in three different polymorphs, calcite (most common, hexagonal), aragonite (orthorhombic) and vaterite (least common, hexagonal). Calcium carbonate, along with the other alkaline-earth metal carbonates, is sparingly soluble in water. The solubility of the carbonates in water can be measured by their solubility products, K_{sp}. This is known as the equilibrium constant for a chemical reaction where a solid ionic compound is dissolved to yield its ions in solution.

$$K_{sp} = [M^+][X^-] \qquad 1.9$$

This can be compared to the K_{sp} for the other alkaline-earth metal carbonates, table 1.5.

Table 1.5 - A table showing the solubility products, K_{sp}, for the alkaline-earth metal carbonates and sulfates at 25 °C. Data obtained from Lide.[18]

Element	Carbonate K_{sp}	Sulfate K_{sp}
Mg	6.82×10^{-6}	-
Ca	3.36×10^{-9}	4.93×10^{-5}
Sr	5.6×10^{-10}	3.44×10^{-7}
Ba	2.58×10^{-9}	1.08×10^{-10}

It can be seen that all of the carbonates are sparingly soluble in water, with magnesium being much more soluble than the others. The trend mentioned earlier, whereby mismatched ion size increases solubility, is observed in the K_{sp} values for the alkaline-earth metal sulfates. The sulfate anion is large and therefore, the large Ba^{2+} cation is not a good match for solubility purposes. The K_{sp} values quoted above, alongside equation 1.9, can be used to calculate the concentration of something that can be dissolved in a medium. This 'carrying capacity' can also be thought of as a saturation level. Water saturation levels were discussed in terms of water balance by Langelier.[19] He developed the Langelier Saturation Index, which measured this water balance. A perfect score on 0.0 describes a system whereby the dissolved solids are saturated and balanced. The negative part of the scale indicates that the water can be corrosive; whereas, the positive scale indicates that the water will begin to form scale as it is over-saturated.

The sulfates have a wide range of uses; from calcium sulfate dihydrate ($CaSO_4.2H_2O$, gypsum) being used as plaster of Paris upon heating,[20] to barium sulfate being used in X-ray imaging as a 'barium meal' due to its chemical stability and X-ray absorbing properties.[21] In addition to this, as mentioned previously, barium sulfate is also one from of scale that greatly hinders oilfield operations. Present methods of stopping this include the use of chemical inhibitors to stop the formation of the sulfate. Knowing exactly how much of this compound to add is a problem as it is very difficult to know the exact concentrations of the alkaline-earth metal ions present due to the very stable compounds that they form.

One common property of alkaline-earth metals that has been manipulated for sensing purposes is their ability to form complexes.[22–25] Some of the most widely seen complexes that the alkaline-earth metal cations form are with crown ethers and cryptand ligands, figure 1.5.

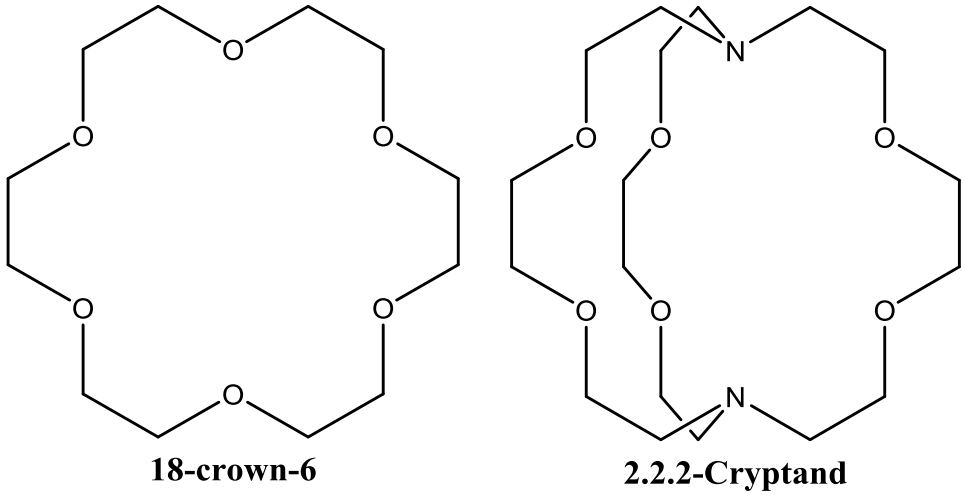

Figure 1.5 - A structural example for a crown ether (left) and cryptand (right).

The ability to form these complexes has been manipulated to create sensors for the alkaline - earth metal ions. A sensor is made out of two main components; the sensing chemistry and a transducer to relay this signal.

The following sections will investigate the different areas of research into the sensing chemistry for the detection of alkaline-earth metal ions. It will seek to explain the basic concepts and chemistry that allow these techniques to work; as well as evaluating their efficiency for the desired application of this thesis. In turn, this will help explain why an electrochemical dipstick probe is a proficient method of sensing for this application.

1.4 Titrations

One of the longest standing methods of alkaline-earth metal determination is the use of complexometric titrations. Typically, a standard solution is added, *via* a burette, to a solution of interest as in figure 1.6. In this scenario a metal : ligand complex would be formed in the conical flask and the end point found.

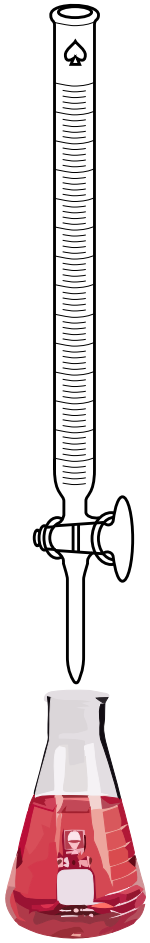

Figure 1.6 - A schematic diagram of a classic titration set up including a burette containing the standard solution (titrant) and conical flask containing the analyte.

In the beaker, once the ligand has been added from the burette, a complex can form between the metal ion and ligand. EDTA (ethylenediaminetetraacetic acid), figure 1.7, given as H_2X, is a classic example of this.

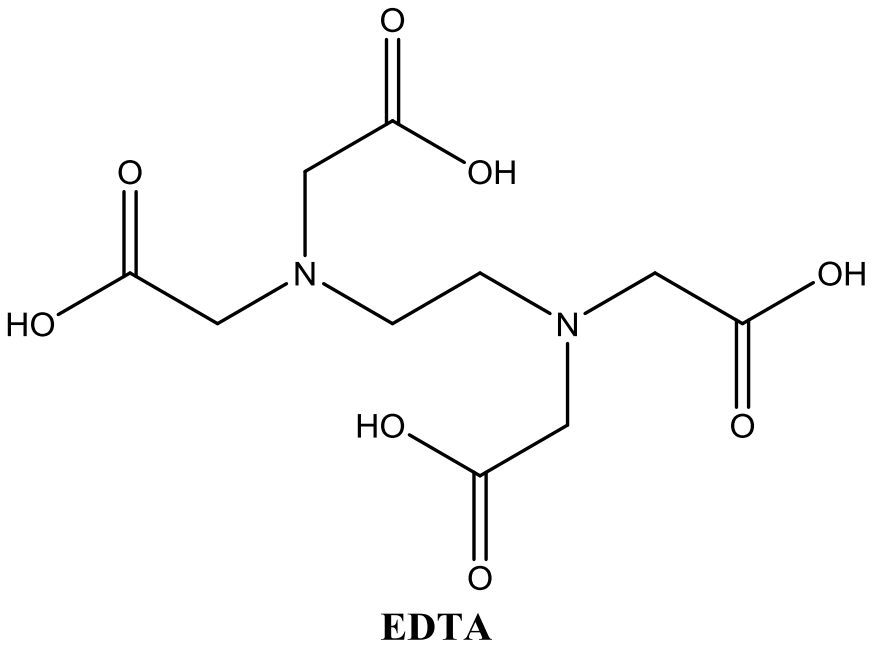

Figure 1.7 – The skeletal structure of ethylenediaminetetraacetic acid (EDTA).

It can complex to metal ions with various charges.

$$M^{2+}_{(aq)} + H_2X^{2-}_{(aq)} \rightarrow MX^{2-}_{(aq)} + 2H^{+}_{(aq)} \quad 1.10$$

$$M^{3+}_{(aq)} + H_2X^{2-}_{(aq)} \rightarrow MX^{-}_{(aq)} + 2H^{+}_{(aq)} \quad 1.11$$

$$M^{4+}_{(aq)} + H_2X^{2-}_{(aq)} \rightarrow MX_{(aq)} + 2H^{+}_{(aq)} \quad 1.12$$

The end point is typically identified by a physical change in the solution. This can be detected through multiple avenues; a natural colour change, an indicator colour change or precipitation.

The detection of calcium has been achieved through complexometric titration for years. Ethylene glycol-bis-N,N,N’,N’-tetraacetic acid (EGTA), figure 1.8, developed by Schwarzenbach *et al.*, has been utilised in this vein for many years due to its high stability constant for calcium; up to five orders of magnitude larger than for the common interferent magnesium.[26]

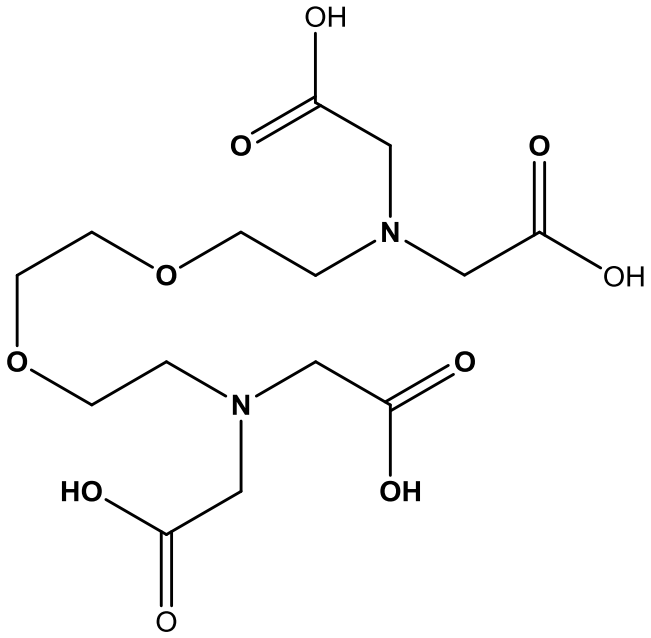

EGTA

Figure 1.8 – Skeletal structure of ethylene glycol-bis-N,N,N',N'tetraacetic acid (EGTA), originally reported by Schwarzenbach *et al* (1957)[26] and utilised by Tsunogai *et al* (1968).[27]

This was turned into a simple and effective test for calcium by Tsunogai *et al.* in 1968 using the metal indicator glycoxal-bis(2-hydroxyanil) (GBHA).[27] Whereby, the red calcium chelate complex formed with GBHA at pH 11.7 is replaced by the colourless free indicator after titration with EGTA. This test has been extensively studied and common interferents, magnesium and strontium, are accounted for by correction factors.

These titration methods are still used today due to their high precisions (~ 0.10 %),[27] however the sample volume required and detection time remained larger than ideal. More recently, Xiaowan *et al* reported the use of an automatic potentiometric titrator to increase the efficiency of the same process.[28] This set-up reduced the required sample size down from > 20 mL down to ~ 1 mL, alongside a determination time of 5 minutes; with this increase in efficiency being at the cost of a small amount of precision (~ 0.25 %).

Early methods, utilising the same procedures, for the detection of barium and strontium were based around another common ligand, analogous to EGTA, ethylenediaminetetraacetic acid (EDTA), figure 1.7.

Some of the first examples used back titrations; for example the determination of barium sulfate, whereby it was dissolved in an excess of EDTA and titration against an excess of magnesium ions.[29] The problem with early methods was, unlike the relationship between EGTA and Ca^{2+} ions, the affinity of EDTA was not for a single cation; hence the separation of individual elements was required. EDTA can be used in analytical chemistry to measure a vast array of elements in the periodic table via direct titration or indirect methods. Regarding the alkaline-earth metals, EDTA will complex with all of them with very similar formation constants. Typically indirect methods have been used for strontium and barium determination, especially utilising their precipitation as sulphates.[30]

Simultaneous detections of species in mixtures is extremely important and the use of ion-selective electrodes have aided in the determination of titration end points in this regard. Recently, del Valle and Calvo proposed the use of electronic tongues (ETs), arrays of non-specific sensors, for the simultaneous detection of Mg^{2+}, Ca^{2+} and Sr^{2+} in mixtures.[31] When applied to external samples acceptable correlation was observed for calcium; however, magnesium had a very poor correlation with respect to the reference method, atomic spectroscopy.

The inability to perform on-site measurements in the presence of multiple interferents is a key factor in this methodology being unsuitable for the desired application. There is no feasible way to miniaturise and control this method suitably for a down-hole application. One method that is excellent at dealing with interferents is atomic spectroscopy.

1.5 Atomic spectroscopy

Atomic spectroscopy is a commonly used analytical technique that utilises the energetic transitions experienced by atoms. These transitions are primarily the result of either the absorption or emission of a photon.

Atomic emission spectroscopy (AES) utilises thermal or electrical energy to excite an electron from its ground state atomic orbital to a higher energy one. The relaxation of this electron back to its ground state is normally accompanied by the emission of a photon. An instrument can measure the intensity of this emitted photon as a function of the wavelength. The key to the use of this technique for identifying elemental compositions is the discrete nature of atomic orbitals. These well-defined energies allow for the concentration of elements elements in various sample compositions to be determined.

A flame atomic spectrophotometer is the most commonly used piece of equipment for AES. This typically consists of four main parts; a light source, a burner/flame, a monochromator and a detector, figure 1.9.

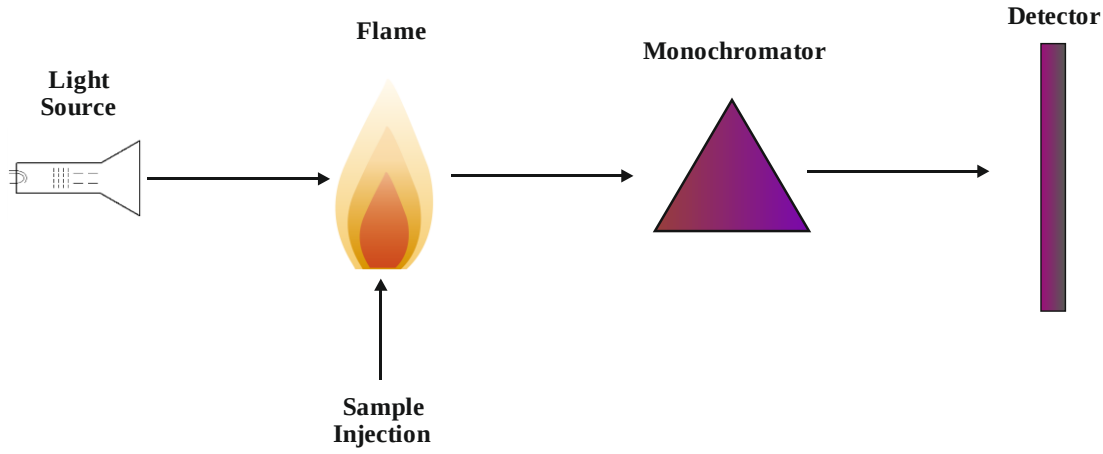

Figure 1.9 - A schematic showing the basic set up of a flame atomic spectrophotometer.

Initially this methodology employed flames, DC and AC arc lamps as the atom cells; however, modern instruments have transitioned to inductively coupled plasmas (ICP). This produces extremely good detection limits due to the ultra high temperatures they

function at; this reduces the chemical interferences. Samples ready to be tested are introduced into a nebulizer; in this, they are mixed with a fuel and an oxidant, and then passed into the burner in the form of an aerosol. This process produces a high temperature flame that removes any excess solvent and breaks the sample down into its constituent free atoms in addition to stimulating their atomic emission.[32]

In atomic absorption spectroscopy an electron is excited, through the absorption of a photon, from a lower energy state to a higher energy one. An instrument will then measure the absorbance at a wavelength specific to the element of interest. A light source is directed through the sample, utilising the fact that neutral gaseous species will absorb some of the light, reducing its intensity. This reduction, or absorbance, is proportional to the concentration of atoms in the cell in accordance with the Beer-Lambert Law. Hollow cathode lamps (HCLs) are typically used in this form of spectroscopy due to the single emission of atomic lines. This method has excellent selectivity but significantly reduces the abiity for multi-component analysis.[32]

The influence of physical properties of analytes has been problematic in the use of flame atomic absorption spectroscopy (FAAS). The introduction of flow injection allowed for more efficient performance and large scale analysis. It allowed for the reduction in sample volume, reduced analysis time, improved precision and a higher tolerance for dissolved solids; without any loss in sensitivity.[33]

Calcium is one of the most frequently analysed elements using atomic absorption spectroscopy. Initial work was focussed on the calcium present in urine, soil or serum samples.[34,35] Determination of calcium is fairly straight forward with minimal interferences when using a nitrous oxide/ acetylene flame. However, using an air/ acetylene flame produces lots of interferences from a variety of sources.[36] Due to the common nature of calcium, the higher sensitivity gained from the use of a graphite furnace is rarely required. Early examples of atomic absorption spectroscopy compared favourably to other techniques, such as EDTA titration, used at the time. The obvious advantages were the massive reduction in required sample size, removal of interferents problems and no problematic end-point to find. The major problem with the technique for the detection of calcium in water was the pH dependence of the perceived calcium concentration. The concentration remained constant at between pH

1.8 – 3, increased when moving from pH 7.0 towards pH 3.8 and decreased after pH 1.8.[37] One such case where it is beneficial to use a graphite furnace is when the matrix is brine, due to the extremely high concentrations of NaCl present. This interferes both chemically and physically with the analyte. To overcome this a graphite furnace method alongside a L'vov platform, a small pyrolytic graphite plate, can be used to minimize the interference.[38]

Strontium can be detected using either the air/ acetylene or nitrous oxide/ acetylene flames, with the cooler flame producing the larger number of interferences. Due to this, much research has been done on the optimisation of detection by utilising mixtures of the two flames.[39] Atomic absorption spectroscopy has typically been used regularly for the determination of strontium concentration in collected geological water samples.[40]

Barium, like calcium, exhibits large amounts of interference when analysed in an air/ acetylene flame. Again these are diminished or completely removed in the presence of a nitrous oxide/ acetylene flame.[41] Due to the high atomization temperatures, alongside the typical low concentrations of barium present in samples, graphite furnace methods and electrothermal atomic absorption methods have been popular.[42] Krug *et al* produced a detection limit of 10 - 20 pg using the electrothermal method, however interference from large concentrations of calcium remained an issue.[43]

Although atomic spectroscopy can produce low limits of detection with precision and is still regularly used in research for ion concentrations for environmental analysis; it is not a suitable method for the applications focussed on in this work. The requirement for sample collection, treatment and analysis away from the site makes the process unnecessarily inconvenient. Miniaturisation of the technique is possible, but the precise arrangement of the light source, injection and detector mean that it is very difficult. This technique is also a destructive one; a non-destructive technique to consider is nuclear magnetic resonance spectroscopy.

1.6 Nuclear Magnetic Resonance spectroscopy

Nuclear Magnetic Resonance (NMR) spectroscopy is one of the most dominant methods of analysis for the determination of chemical structures due to the large amount of information gathered by a single set of analytical tests. It utilises the same principles as Magnetic Resonance Imaging (MRI) which is an extremely common method used in medical imaging. NMR is concerned with the atomic property of nuclear spin and the most common methods of NMR, ^{1}H, ^{13}C, ^{19}F and ^{31}P, all have a nuclear spin equal to ½. When placed in a magnetic field, a nucleus with a spin of this value will either align itself with the field or against the field. Nuclei aligning itself with the field, in a lower energy state, can flip to the position of higher energy when radio waves are applied to the system. Fourier transform (FT) is used to excite all the nuclei in a system; following this, the absorption of energy or release of energy can be analysed by a computer.

A key component of this method is that the effective magnetic field experienced by a nucleus is a product of the nearby environment, including nuclei and electrons, as well as the applied field. This variation in environment for the various nuclei is the reason that different nuclei absorb at slightly different frequencies. These different 'chemical shifts' in the obtained spectrum are produced relative to the standard zero point; this is the standard reference resonant frequency, typically tetramethylsilane (TMS), figure 1.10.

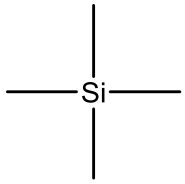

tetramethylsilane

Figure 1.10 - The skeletal structure of tetramethylsilane (TMS).

Kula *et al.* first reported this method for the detection of alkaline-earth metal cations by utilising their ability to complex with ethylenediamineetraacetic acid (EDTA).[44] This was used mainly to detect the fact that complexation was occurring, not the

detection of the metal ion specifically. Since then, work has been done to progress the ability for the detection of specific ions. ^{1}H-NMR has been proposed as a simple determination method for diamagnetic metal ions in aqueous environments.[45] This utilises the ^{1}H chemical shifts of the known chelator EDTA, figure 1.6, and how this shift differs depending on the coordinating metal in question. This removes the use of an indicator and subjectivity of a colour change.

Although NMR is a non-destructive and often rapid method of detection. The requirement for laboratory based equipment, high cost and difficulty to process complex mixtures of substances, often involving long pre-treatment steps are serious problems. These alongside the difficulty in miniaturising such a set up makes this technique highly unsuitable for down-hole applications. One technique that can be miniaturised fairly easily is fluorescence spectroscopy.

1.7 Fluorescence

The use of fluorescence based systems for the detection of metal ions, including alkaline-earth metal cations, has been researched extensively with many reviews produced.[46–48] When the absorption of a photon promotes a molecule from its ground electronic state to an excited electronic state, several events can occur. These are commonly presented in the form of a Jablonski diagram, figure 1.11.

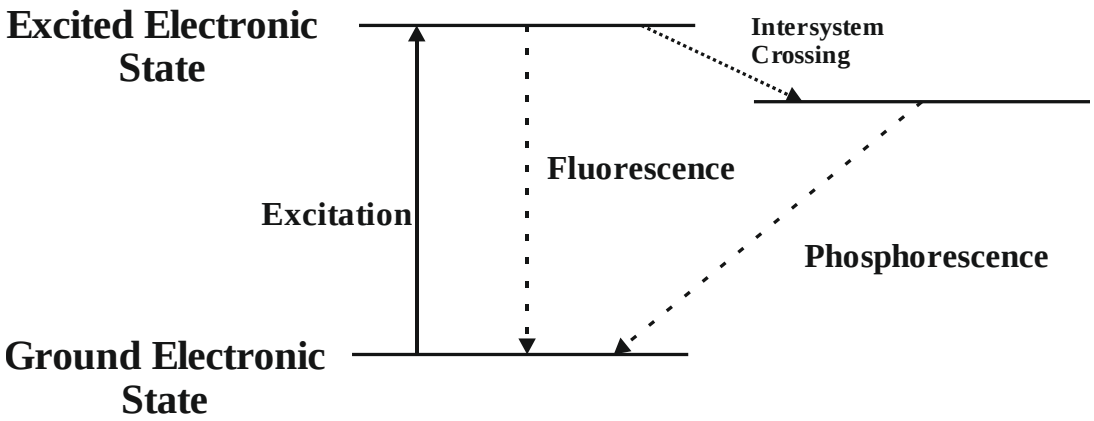

Figure 1.11 - A simplistic drawing of a Jablonski diagram showing the excitation followed by either fluorescence or phosphorescence.

Fluorescence, a radiational transition, is the process in which the molecule relaxes from this excited state directly by re-emitting a photon. This transition produces a higher energy than similar processes, such as phosphorescence, and hence occurs at a shorter wavelength with a lifetime of approximately 10^{-8} – 10^{-4} s. Fluorescence detection typically incorporates two moieties, a fluorophore and receptor, which can be separated by a linker/spacer or incorporated into a single system. The receptor is responsible for binding to the desired analyte. The binding of an analyte is transmitted as either an enhancement or quenching of fluorescence. Typically, this approach has high sensitivity and is used regularly in the detection of metal ions. The following sections will focus on recent advancements made in the area of alkaline-earth metal ions.

One of the most extensively researched receptors for Ca^{2+} cations over the past three decades is BAPTA, figure 1.12, (1,2 – bis(*o*-aminophenoxy)ethane-,N,N,N',N'-tetracetic acid).[49–55]

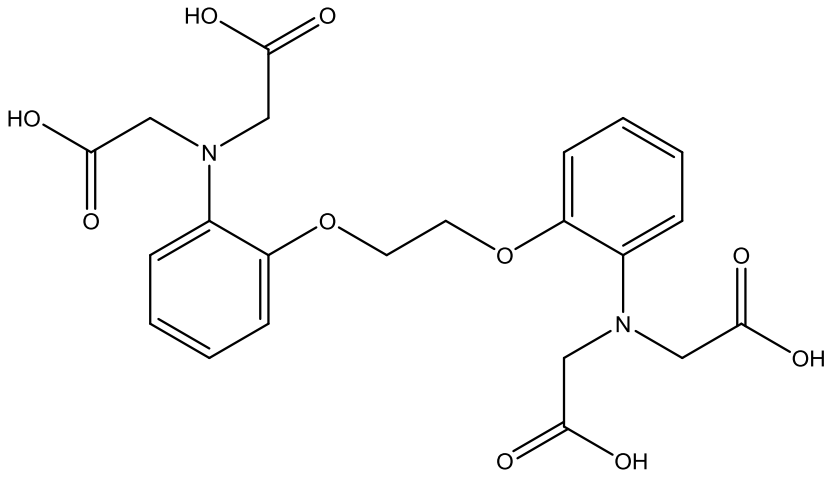

BAPTA

Figure 1.12 - A skeletal structure of the BAPTA ligand. Initially reported by Tsien.[56]

It was initially reported in the 1980's by Tsien[56] and was found to be particularly adept for intracellular (~100 nM) calcium detection due to its extremely strong binding properties.[57–59] To produce a system suitable for extracellular levels of calcium (~1 mM) the BAPTA molecule needed to be modified to reduce its binding affinity. Methods investigated included the addition of nitro groups or halogens to the ring system; this successfully reduced the binding affinity, however, introduced alternate problems in fluorescence quenching among others.[60] Alongside this, problems with

decomposition in aqueous environments was overcome with the immobilisation of the fluorophores onto an amino functionalised cellulose polymer matrix.[61]

Recently, Sui *et al.* have produced a highly water soluble sensor for the detection of extracellular calcium.[62] This system uses the BODIPY fluorophore and a calcium ion recognition group, based on bis(hydroxyethyl)aniline, figure 1.13, that forms a 1:1 metal: ligand complex and has a dissociation constant of 0.92 mM; which is within the desired extracellular range.

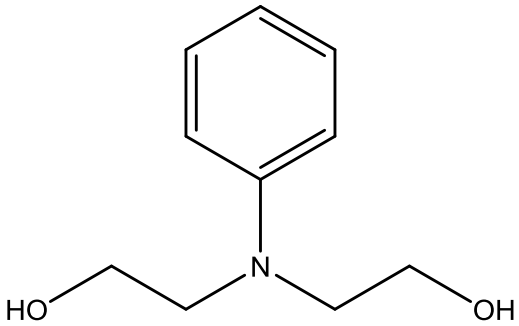

bis(hydroxyethyl)aniline

Figure 1.13 – The skeletal structure of bis(hydroxyethyl)aniline. The common backbone from which Sui *et al.* developed the derivative for their Ca^{2+} sensor.[62]

In the absence of the target analyte, the non-bonding electron pair on the nitrogen can transfer a single electron to the fluorophore to quench the produced fluorescence via PET (photo induced electron transfer). This is the most commonly investigated fundamental process of fluorescence enhancement.[63–68] In the presence of Ca^{2+} cations there is a reduction in the PET process and therefore an inherent enhancement in the observed fluorescence. This system experiences interference from Zn^{2+}, which is common among Ca^{2+} sensors, but this can be overcome by the addition of TPEN. In addition to this, the system will only function above pH 6.8. Although appropriate for the detection of extracellular levels of calcium, it is not appropriate for water levels.

Typically, sea water levels of calcium are an order of magnitude higher than the standard extracellular levels (~10 mM). Liu *et al.*[69] followed on work by He *et al.*[61], using a 4-amino-1,8-naphthalimide based fluorophore with phenylimino-diethoxyacetic acid as a calcium receptor, figure 1.14, to produce a suitable system for a fresh and sea water environment.

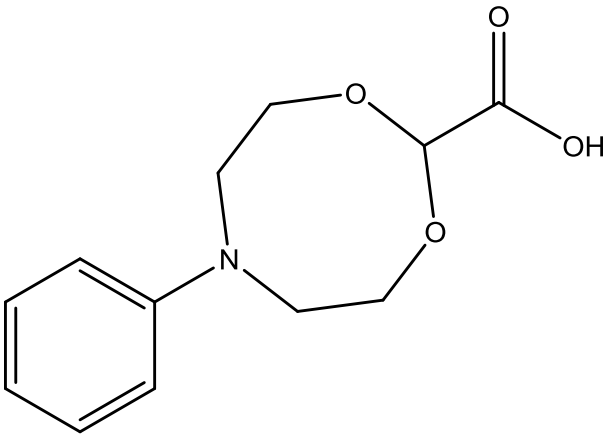

phenyliminodiethoxyacetic acid

Figure 1.14 – The skeletal structure of phenyliminodiethoxyacetic acid. Used as the Ca^{2+} receptor for Liu *et al.*.[69]

The original work used a calcium receptor that was appropriate for extracellular levels of calcium; for the application to water samples, the binding affinity needed to be reduced. This was achieved by the removal of ethoxy groups from the receptor, in turn reducing the amount of binding sites available for the calcium. The system worked in a similar way to that above; in which, there is a nitrogen free to act and an electron donor to the fluorophore through a PET process. This produced a method suitable for long term analysis in freshwater and saltwater with no interferences from strontium and only a small, correctable, interference from magnesium. The main source of interference was found to be alterations in pH; hence, the incorporation of a pH sensor into the overall system would be required for the corrections necessary.

Research into fluorescence sensing systems for the detection of Sr^{2+} has lagged behind that of Ca^{2+}; somewhat due to the reduction in biological importance. Kaur *et al.* have recently produced a polyamine based fluorescence sensor for the detection of Sr^{2+} in aqueous media.[70] Inorganic nanoparticles have been available for a while; however, they are non-degradable and toxic, making them unsuitable for use in biological systems.[71–74] Their organic counterparts have been developed and used due to their superior water solubility, optical properties, low toxicity and biodegradability.[75,76]

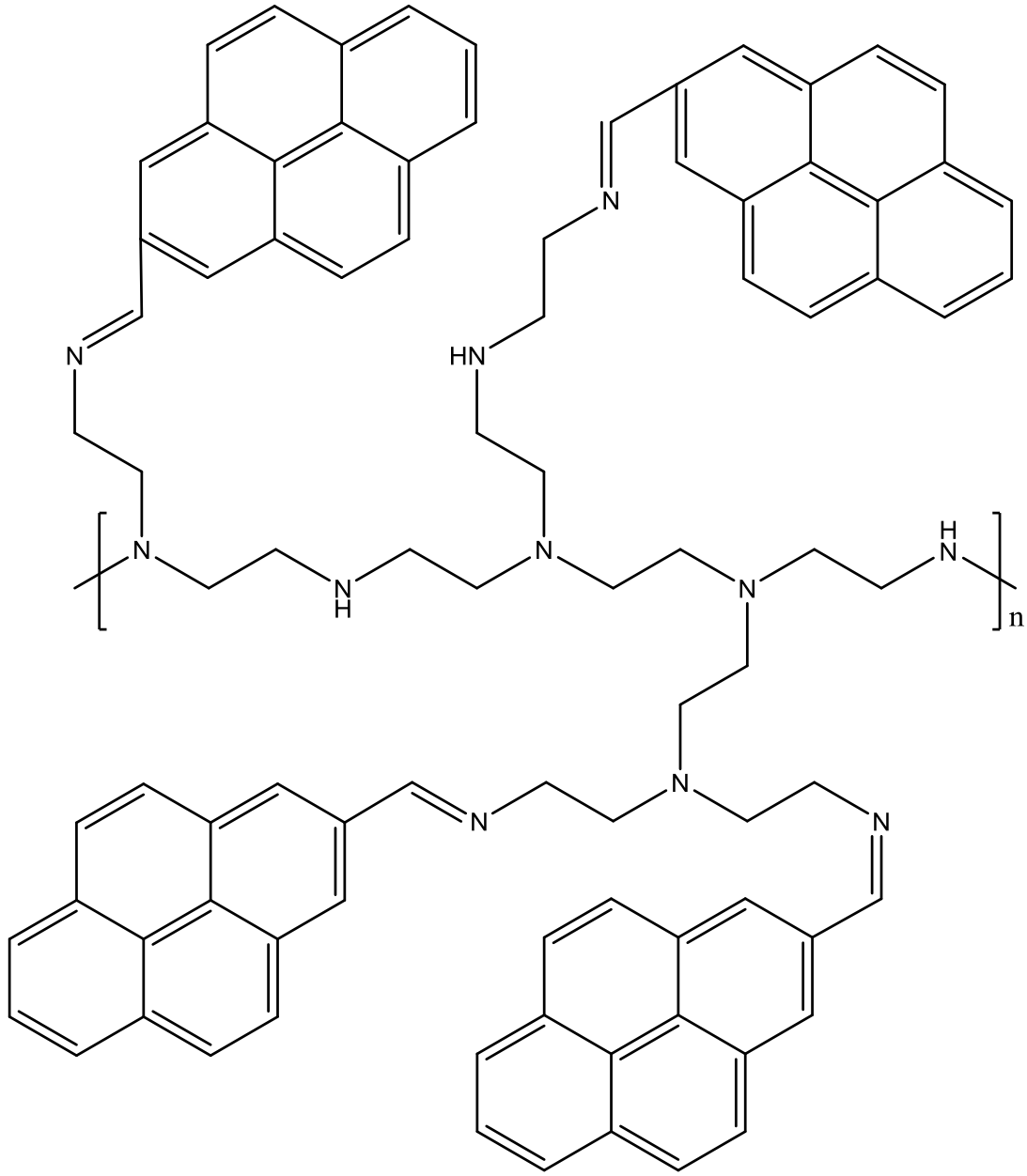

Figure 1.15 – A skeletal diagram of the molecules synthesised by Kaur *et al.* for their Sr^{2+} fluorescence based sensor.[70]

The work by Kaur, figure 1.15, utilises the long singlet lifetime of the pyrene moiety and is produced by a one-step condensation reaction between pyrene-1-carboxaldehyde and polyamine. This organic nanoparticle system utilises excimer excitation of the π - π stacking between pyrene moieties. Upon strontium binding, a conformational change is observed resulting in an extension of the pyrene-pyrene spacing; which, in turn quenches the fluorescence. This system can detect strontium up to 9 nM, is invariable to changes in pH or other metal ions and has been successfully

deployed in tap and river water with the lowest detection limit found in literature for the detection of strontium.

As with strontium, there has been considerably less development of sensing methods for barium in comparison to the more biologically relevant calcium ions. One of the most challenging aspects to tackle in barium detection through fluorescence is the common interference of Pb^{2+}. One method, reported by Wang *et al.*, is the use of imine based compounds. These are attractive due to their ease of preparation, high selectivities and the attractive electronic and photo-physical properties they possess. Compounds, such as imines, that include a C=N are dominated by fluorescence quenching and PET processes. The work by Wang *et al.* reports N-salicylidene-3-aminopyridine, figure 1.16, which demonstrates good selectivity for Ba^{2+} and, in turn, exhibits fluorescence enhancement upon coordination.[77]

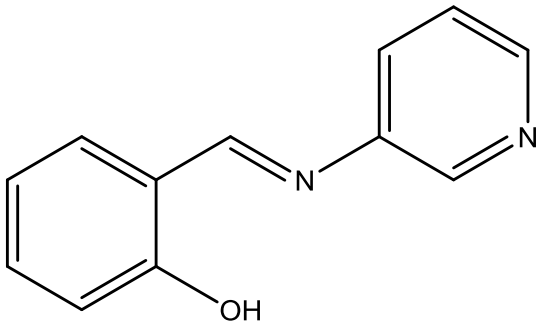

N-salicylidene-3-aminopyridine

Figure 1.16 – The skeletal structure of N-salicylidene-3-aminopyridine. Utilised by Wang *et al.* due to its selectivity for Ba^{2+}.

The compound itself is not soluble in 100% aqueous media, so is dissolved in acetonitrile first to create a 1: 9 MeCN: H_2O mixture. The coordination and selectivity for barium, in a 1: 2 ligand to metal ratio, is promising over other commonly competing cations, however strontium is not tested in this study. It is proposed that the selectivity for barium is due to the size of the coordination platform provided by the imine group and pyridine nitrogen being in the meta position; this conformation is not optimal for small sized cation encapsulation. Upon coordination with barium, the fluorescence emission is saturated at 10 µM; with a detection limit of 0.7 µM. This platform was tested in pH adjusted drinking, tap and river water with promising

results. However, it is not in the desirable concentration range for use in formation water, which lies up to an order of magnitude higher.

Selectivity between Ba^{2+} and Pb^{2+} is a common problem in this area of research. Xu *et al.* reported a G-quadraplex fluorescence detection system for Ba^{2+}.[78] G-quadraplexes are a four-stranded structure that is generated from four guanine bases in a planar arrangement through hydrogen bonds.[79] Previously, the formation of these structures has been shown to be promoted by monovalent cations, K^+ and Na^+;[80] however the divalent cations Pb^{2+} and Ba^{2+} show stronger stabilisation effects due to their ionic radius and larger charge density.[81,82] This strong stabilisation provided an effective assay method for the detection of Ba^{2+} although interference from other metal ions, K^+ and Pb^{2+} has provided issues.[83–85]

The work by Xu *et al.* used G-quadraplex AGRO100 alongside fluorescence component N-methyl mesoporphyrin IX (NMM), figure 1.17, to produce a Ba^{2+}-induced "turn-on" fluorescence sensor. NMM exhibits weak fluorescence in the presence of AGRO100 in its standard 'random coil' structure. The addition of Ba^{2+} produces a conformation change in the AGRO100 from the random coil to G-quadraplex structures. This folding into a G-quadraplex is reflected in a significant increase in fluorescence from NMM, which occurs up to 1 μM concentrations of Ba^{2+}. It was reported that when altered to pH 8.5 the common interference experienced from Pb^{2+} was greatly suppressed, which is suggested to be from the low solubility product of $Pb(OH)_2$ at this pH range. This system had a limit of detection 4 nM and gave a linear response between 0 – 600 nM. The ability for the AGRO100-NMM probe to detect Ba^{2+} was tested in artificially contaminated water samples. It achieved a recovery value of between 105 - 110 %, indicative of a system with promise but in need of further optimisation and testing.

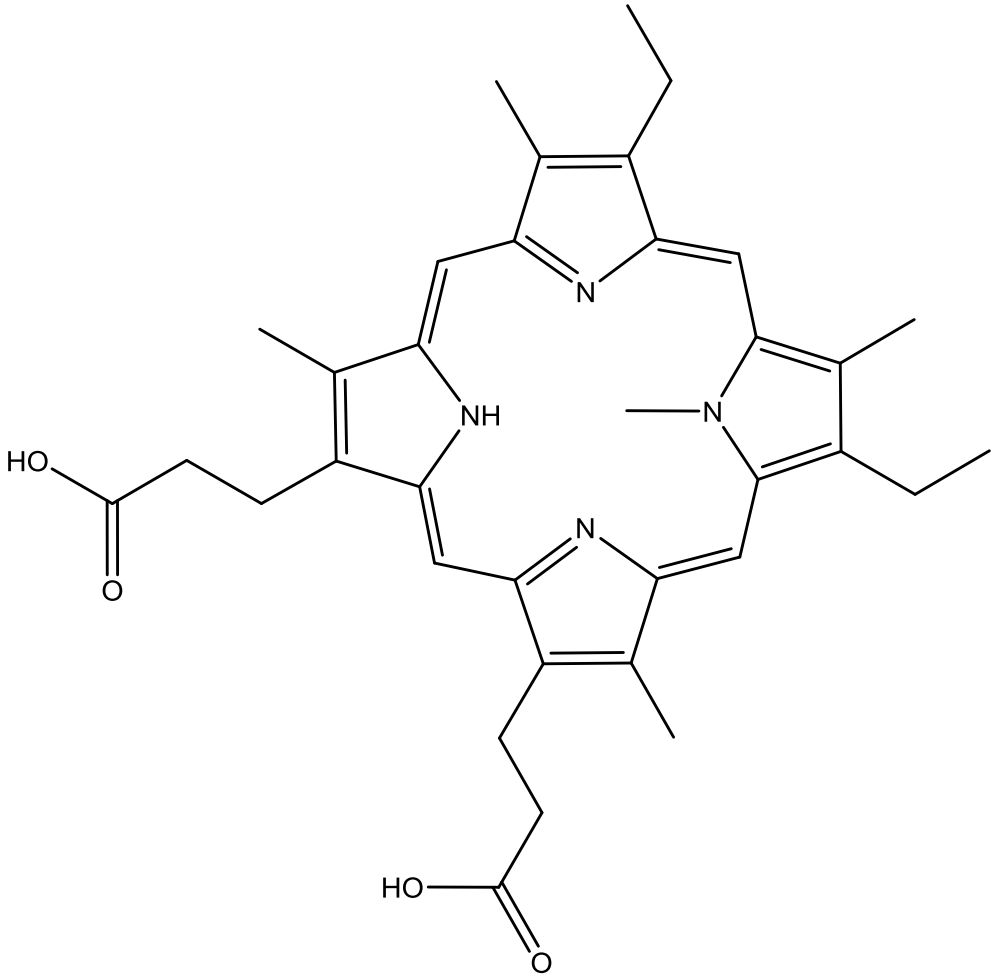

N-methyl mesoporphyrin IX

Figure 1.17 – The structure of N- methyl mesoporphyrin IX. Used alongside a G-quadraplex by Xu *et al.* for a Ba^{2+} fluorescence sensor.[78]

The detection of ions using fluorescence can produce very accurate results; however, the need for sample collection, treatment and analysis in hand or lab is again problematic. Some systems have been developed with the naked-eye detection as an option that do not require these pre-treatment steps. Typically these involve the use of functionalised nanoparticles (NPs). The most commonly used variants of these are gold (AuNPs) and silver (AgNPs).

1.8 Colorimetric

Gold or silver nanoparticle (AuNPs and AgNPs) based colorimetric sensors have received more attention recently due to the naked-eye detection possibilities that they present. This method of sensing utilises the specific optical and electronic properties

possessed by these metal nanoparticles. They have produced comparable sensitivity to conventional fluorescence probes due to the high extinction coefficients that these AuNPs and AgNPs possess. The addition of target analytes to solutions containing these NPs will produce a characteristic colour change; yellow to red for AgNPs and pink to blue for AuNPs. This occurs due to aggregation of the NPs. This aggregation forces the overlap of the plasmon fields that cause a red shift in their LSPR (localised surface plasmon resonance). In turn, this increases the intensity of the LSPR and produces the easily observable colour shift. Research into AuNPs was pioneered by the work of Mirkin *et al.*, who utilised them to detect target DNA molecules.[86] Since this, many gold and silver nanoparticles have been produced for the detection of metal ions.[87,88]

Relatively few attempts have been made at utilising these functionalised nanoparticles for the detection of alkaline-earth metal cations. One of the first Ca^{2+} sensing platforms in this field utilised lactose-functionalised AuNPs that underwent Ca^{2+} mediated self-aggregation.[89] Following this, Yang *et al.* produced AuNPs that show excellent selectivity for Ca^{2+}, Sr^{2+} and Ba^{2+}.[90] The AuNPs are functionalised with 2-mercaptosuccinic acid, figure 1.18, to produce MSA-AuNPs.

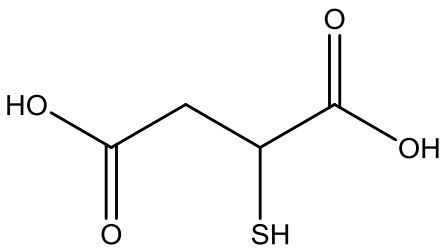

2-mercaptosuccinic acid

Figure 1.18 – The skeletal structure of 2-mercaptosuccinic acid. Utilised by Yang *et al.* to functionalise AuNPs for the detection of alkaline – earth metal ions.[90]

Upon the addition of the three alkaline-earth metal ions, a red to blue colour change was observed. This colour change was attributed to the cation mediated particle aggregation, confirmed by the fact bridging interactions are removed by the addition of EDTA to solutions. The limits of detection and dynamic ranges of the system indicate an enhanced selectivity for the larger Ba^{2+} ion. Even so, the platform was used for the detection of calcium in water samples from various sources, exhibiting a

dynamic range between 10 - 80 μM. This method shows obvious interference from Sr^{2+} and Ba^{2+} however, due to the minute concentrations of these ions in surface waters they are ignored for the study. This is obviously impossible for the application in formation water.

Strontium has proved to be very difficult to produce a selective sensor in this field. The majority of platforms exhibit detection for all of the alkaline-earth metal ions. For example the work by Wu *et al.*, who have developed TGA (thioglycolic acid), figure 1.19, functionalised AgNPs, that undergo a colour change from yellow to orange/red when exposed to all of the alkaline-earth metal cations.[91]

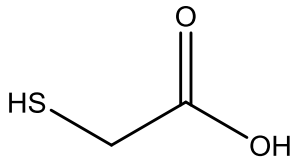

thioglycolic acid

Figure 1.19 – The skeletal structure of thioglycolic acid (TGA). Utilised by Wu *et al.* to functionalise AgNPs for the detection of alkaline – earth metal cations.[91]

It is proposed that the alkaline-earth metal ions coordinate with the free carboxy group on the TGA. This causes aggregation of the NPs and, in turn, the colour change. The rate of colour change showed an enhanced effect from the larger coordinating ions. This is reflected in the affinity for the larger ions and the LOD decreasing as you descend the group; with a LOD of 1.25 μM for Sr^{2+} and 0.833 μM for Ba^{2+}. This platform was used for the quantification of hardness in water samples. The system exhibited decent agreement with ICP methods; however, the lack of selectivity for a particular ion is an issue.

Shrivas *et al.* have produced AuNPs for the detection of Ba^{2+}, and Ni^{2+}, in aqueous environments by capping them with malonate groups, figure 1.20.[92]

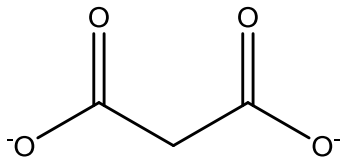

malonate

Figure 1.20 – The skeletal structure of malonate. Utilised by Shrivas *et al.* to functionalise AuNPs for the detection of Ba^{2+}.[92]

In the absence of barium or nickel the AuNPs are dispersed in the aqueous system. Upon the addition of the metal ions, there is inherent coordination between the metal and the carbonyl group of the malonate group causing aggregation of the NPs. This reduction in inter-particle size causes a strong enhancement in the localized electric field which, in turn, produces a distinctive red shift in the LSPR spectrum. This shift is accompanied by a clear shift in colour from pink to blue that is visible *via* the naked-eye. The AuNP system exhibited a linear detection range for the addition of Ba^{2+} from 15 - 500 ng mL^{-1}, with a LOD of 5 ng mL^{-1} and no significant interference from any ions other than Ni^{2+}. The platform showed good results when tested in water samples, however, the detection range is not suitable for use in a formation water sample.

Although these systems present some encouraging signs for the detection of ions in water samples, they appear to be more suitable for the application to surface waters; mainly due to location and concentration ranges that are detectable *via* these systems. The application of down-hole detection, especially of barium, requires lower detection limits. Ion selective electrodes have been known to produce very low detection limits.

1.9 Ion Selective Electrodes

The main sensing component of an ion selective electrode (ISE) is the membrane that separates the sample and the internal half-cell, figure 1.21, for example a reference electrode or solid contact system.

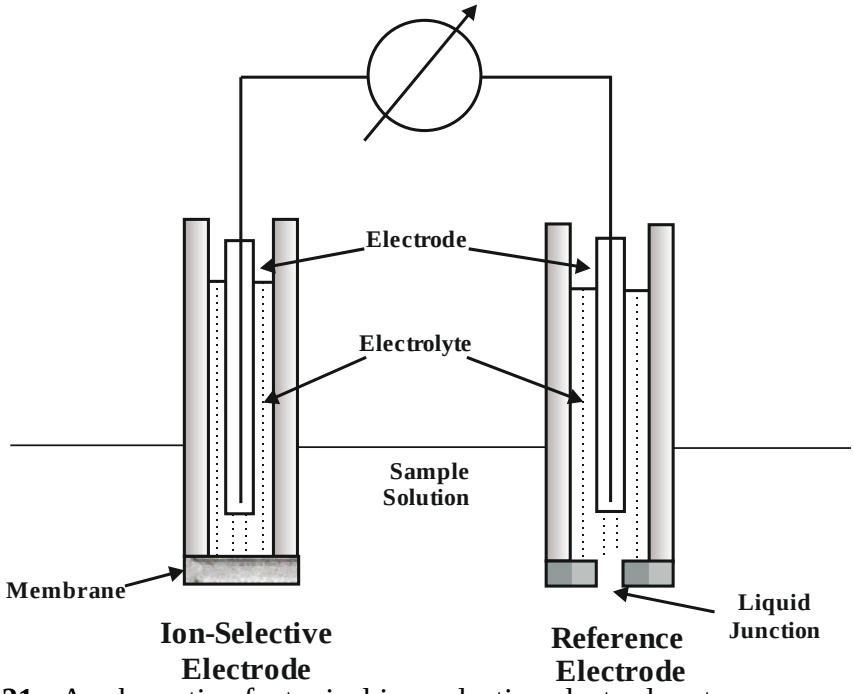

Figure 1.21 - A schematic of a typical ion-selective electrode set up.

The internal reference electrode, like a Ag/AgCl electrode, provides a stable potential and is connected to the sample through a salt bridge. The electromotive force (EMF) change in the ISE is then measured and, depending on the sample composition, will vary while ideally obeying the Nernst equation. Much of the research over the decades has been spent primarily on increasing the lifetime, selectivity and stability of the ISE.

An example of how an ISE works is a calcium ISE. The ISE will have a membrane impregnated with a molecule that selectively allows the positive Ca^{2+} ions to cross the membrane. Upon the immersion of this electrode in a solution of Ca^{2+} ions there is no EMF across the membrane as on both sides of it the solutions are balanced based on the electrical charges. Then, after initial immersion, the Ca^{2+} ions will begin to diffuse across the membrane from the solution of high calcium concentration to low. This influx of positive charge on the inside of the membrane and corresponding remaining

negative charge outside the membrane is what causes the potential difference. Once the system reaches equilibrium, the potential is measured and known as the membrane potential.

A membrane does not exist that is purely selective for one single ion. There is always some form of interference from a non – target ion. The interference produced by this secondary ion is governed by the Nikolski-Eisenman equation, which utilises the charges (z) and activities (α) of the primary (x) and secondary ions (y), the selectivity coefficient (k_{xy}) and the standard electrode potential, E^0.

$$E = E^0 + \frac{RT}{z_x F} \ln \left[\alpha_x + \sum_y \left(k_{xy} \alpha_y^{\frac{z_x}{z_y}} \right) \right] \quad 1.13$$

Where E is the emf, R is the molar gas constant, T is the temperature and F is Faraday's constant.

An ISE membrane commonly contains an ionophore with good selectivity, a lipophilic salt as an ion exchanger and a polymeric membrane as a matrix (commonly plasticized PVC).[93] Common issues that occur are that the mobile membrane components, in particular the ionophore, would leach out of the membrane and in turn influence the selectivity, sensitivity and lifetime of the electrode. In attempts to remedy these problems, investigations into covalently immobilising the ionophore onto the polymer backbones was completed.[94–98] This in turn had issues with adjusting the ionophore and polymer contents, with highly functional polymers dramatically affecting the selectivity. Gyurcsanyi *et al.* attempted to overcome this by attaching the ionophores onto gold nanoparticles (AuNPs).[99] This method struggled with the attachment of a necessary thiol group to the ionophore, which reduced the purity and in turn increased the cost. Therefore, there is a need to develop a simple, efficient, low-cost method for ionophore immobilisation to prevent leaching.

Recently, all-solid-state polymeric membranes have gained increasing interest over the traditional liquid contact ISEs due to the ability to miniaturise them easily and requiring low maintenance.[100] However, there are problems with the long term potential stability due to their poorly defined interface between the conductor and membrane.[101,102] To improve this aspect, investigations have been completed into

using conducting polymers,[103] carbon-based nanomaterials,[104–107] and noble metal based nanomaterials.[108,109]

Ion selective electrodes for the purpose of sensing Ca^{2+} cations were some of the first commercially accessible in the world.[110,111] Yin *et al.* recently reports an all-solid-state Ca^{2+} selective membrane based on graphene oxide functionalised with octadecylamine, figure 1.22, to produce a GO-ODA system.[112]

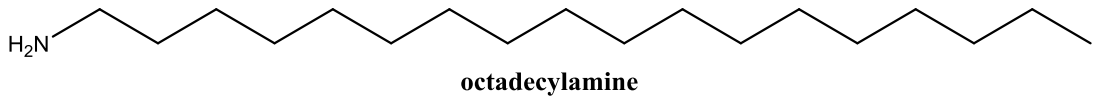

octadecylamine

Figure 1.22 – The skeletal structure of octadecylamine. Utilised by Yin *et al.* as the backbone for graphene oxide for an all-solid-state Ca^{2+} selective membrane.[112]

The alkyl chains present help immobilise calcium ionophore IV, as well as acting as a transduction element to aid the potentials stability of the system. The electrodes, after overnight conditioning, produced a linear 24.7 ± 0.3 mV/decade Nernstian response between 0.3 μM - 1 mM Ca^{2+} concentrations with a detection limit of 0.16 ± 0.2 μM. The interference on the system increased proportionally with an increase in the amount of GO-ODA composite present. This interference was proposed to be down to the graphene oxide influencing the formation of complexes between the calcium ionophore and the calcium in a 3:1 ratio. The response of the system was found to be virtually constant over a pH range of 6 - 9, indicating suitability for application to water samples. The produced GO-ODA electrodes showed an improved stability over other ISEs for Ca^{2+} sensing and exhibited no water layer between the membrane and electrode surface. This platform was applied to the detection of Ca^{2+} in artificial sea water samples producing a recovery rate between 90 - 105 %.

Typically, ISEs utilise potentiometric analysis; however, the incorporation of stripping voltammetry alongside an ISE allows for an increase in sensitivity. This works through the analyte ion being potentiostatically transferred from the aqueous solution phase into the membrane of the ISE. The resulting confined ions are then stripped from the surface resulting in an enhanced voltammetric current. The detection levels obtainable are dependant largely on the size of the membrane used, with thinner membranes producing detection limits 1 to 2 orders of magnitude better.[113,114] Amemiya *et al.* reported a system utilising this theory for the detection of sub-nano molar concentrations of calcium in aqueous systems.[115] The Ca^{2+} selective ETH129, figure 1.23, that forms a 1:3 metal:ligand complex, was utilised as the ionophore in a PVC membrane.

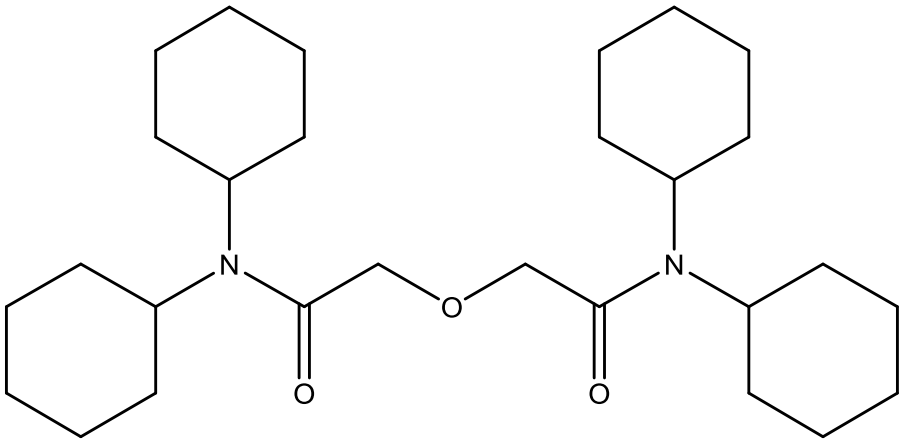

ETH129

Figure 1.23 – The skeletal structure of ETH129 (calcium ionophore II). Utilised as the Ca^{2+} selective component by Amemiya *et al.* for their ISE.[115]

The stripping voltammetric responses were measurable after 30 mins of pre-treatment producing a linear response in peak current from 0.1 - 1 nM. The system was applied to the detection of Ca^{2+} contamination in commercial ultrapure waters producing good results that exhibited the calcium present in these samples were present and within their stated limits.

As with other areas of detections, strontium ISEs (Sr-ISEs) have received less attention than the more biologically relevant calcium ions; although some Sr-ISEs have been reported.[116–120] All the mentioned systems produce an appropriate potentiometric response to the presence of Sr^{2+} cations, but suffer from a variety of

limitations such as selectivity over competing ions to limited pH ranges and response times. Due to the smaller breadth of ionophores specialised for strontium, Chandra *et al.* have produced an ISE platform that utilised acetophenone semicarbazone as the ionophore, figure 1.24.[121] This sensing platform produced a linear 29.4 mV/decade Nernstian response for Sr^{2+} between 0.1 μM - 10 mM with a detection limit of 27 nM; this is an ideal concentration range for typical formation water. One problem for the system was that the more ionophore present, the worse the Nernstian response was.

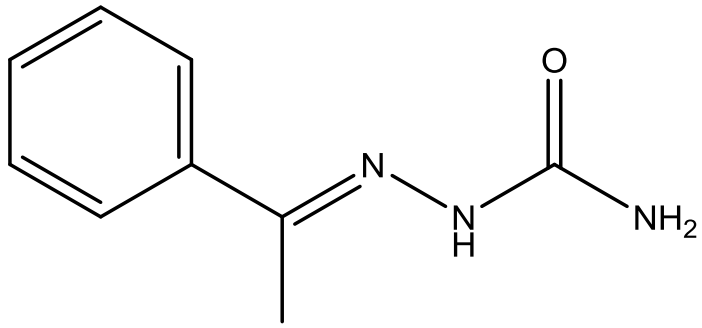

acetophenone semicarbazone

Figure 1.24 – The skeletal structure of acetophenone semicarbazone. Utilised as an ionophore for Sr^{2+} by Chandra *et al.*[121]

The electrode worked well over a large pH range of 2.5 - 10, suitable for all water samples. Outside of this pH range, the hydronium ions affect the membrane and hydrolysis of the Sr^{2+} causes problems. The ionophore responds individually to many metal ions, but shows good selectivity for strontium over any others, in addition to production a reliable reading over eight months. The system was applied to the detection of Sr^{2+} ions in river water samples, giving results in good agreement with AS methods. It was concluded this platform was adequate for the estimation of Sr^{2+} concentrations in natural water sources.

In a similar vein to strontium, barium has received far less attention than calcium in the realms of ISEs. Some of the first reported Ba^{2+}-ISEs were produced by Levins,[122] Thomas *et al.*,[123] and Simon *et al.*.[124] These initial systems all suffered from similar limitations of poor lifetime, predominantly due to the lipophilicity of the ionophore. Improvements to the lipophilicity were made by Simon *et al.* when they introduced

barium ionophore I, figure 1.25, (N,N,N',N'-tetracyclohexy-oxybis(*o*-phenyleneoxy)-diacetamide).[125]

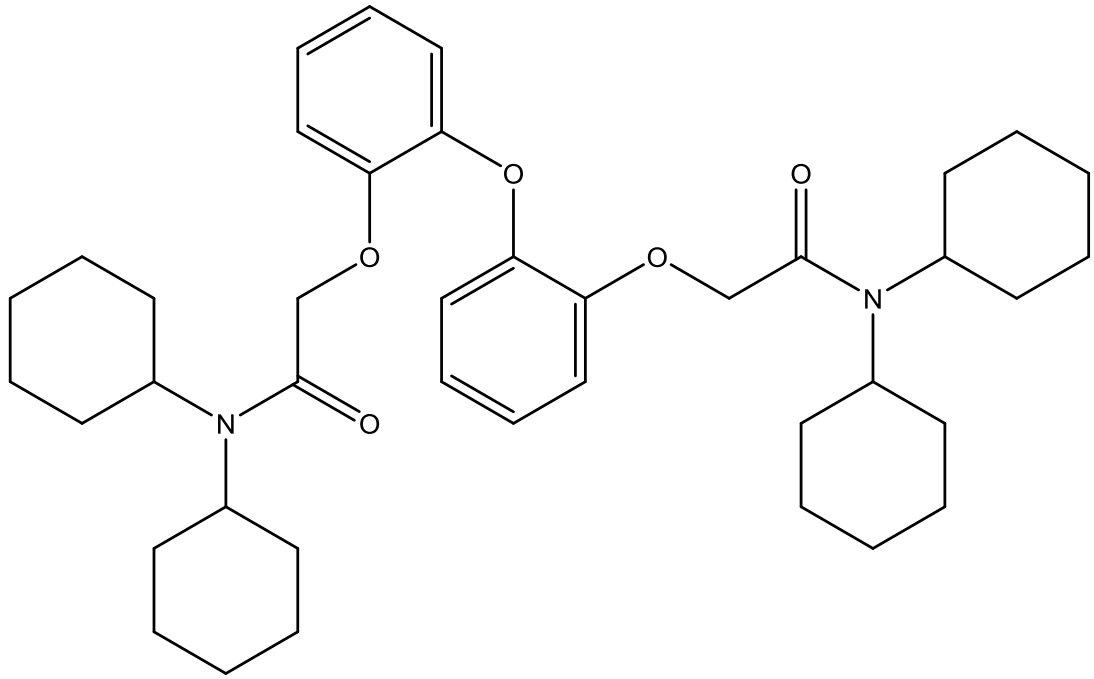

barium ionophore I

Figure 1.25 – The skeletal structure of barium ionophore I (N,N,N',N'-tetracyclohexy-oxybis(*o*-phenyleneoxy)-diacetamide). Produced by Simon *et al.* to improve the lipophilicity of barium ionophores.[124]

This was a stalwart for many Ba^{2+}-ISEs onwards, despite its high interference from Ca^{2+} cations and poor stability of a range of pH.

In aqueous media barium forms a coloured, insoluble, 1:1 complex ion associate when mixed with rose bengal. El-Shahawi *et al.* reported the incorporation of the well-known barium - rose bengal complex, figure 1.26, into an ISE.[126] Rose bengal on its own is not suitable as an ionophore in a PVC membrane; however, the complex ion associate with barium is. It was found as the amount present in the membrane increases the performance of the overall ISE increased up to a peak of 10 mg. The produced ISE exhibited a linear, 28.5 ± 0.5 mV/decade Nernstian response between 10 μM - 0.1 M with a detection limit of 2.5 μM. The performance was good in the pH range of 4.5 - 10. Below this range, the complex ion pair was destabilised. Above this range and the hydrolysis of Ba^{2+} is problematic.

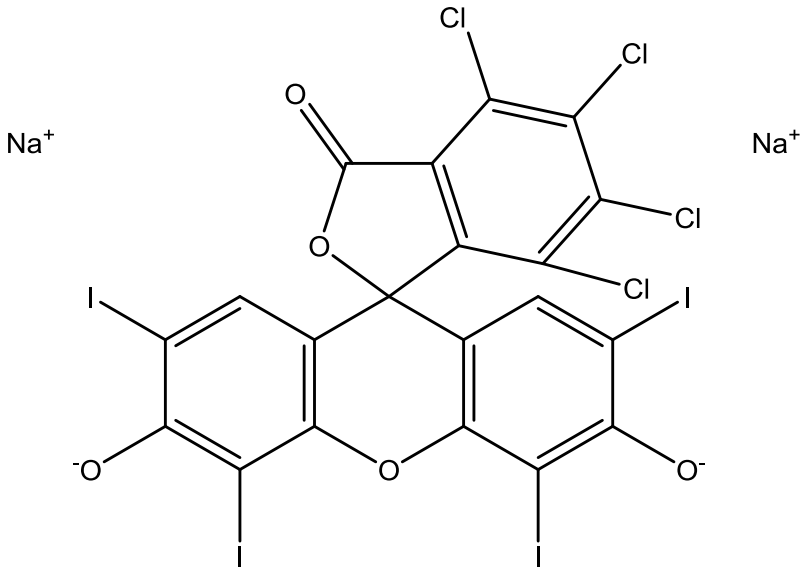

rose bengal

Figure 1.26 – The skeletal structure of Rose Bengal. Utilised by El-Shahawi *et al.* for a Ba^{2+} selective ISE.[126]

Significant interference was observed from K^+ and Sr^{2+} during interference studies. Even so, the system was tested for its ability to detect Ba^{2+} in wastewater samples. The platform exhibited a high recovery rate and had excellent agreement with the AAS results obtained. These results were promising; however, the only interferents in the samples were Cu, Cr and Ni, not the known interferents. The large interference from these two commonly found ions explains why this system is inappropriate for the application of oilfield analysis.

There is a lack of appropriate ISE systems for the application proposed in this thesis; through either the lack of desired concentration range or high amount of interferents. This, coupled with the often tedious preparation of ISEs is off putting in regards to using this method.

1.10 Aims and objectives

This thesis seeks to develop a low-cost, downhole, electrochemical sensor, capable of detection scaling ions present in formation water. A sensor will always consist of two main parts; the sensing chemistry and the transducer. Potentiometric sensors for scaling ions do exist; however, they are expensive to produce, have relatively poor sensitivity and poor selectivity. Therefore, a new variant on the sensing chemistry is required. Scaling ions themselves are electrochemically inactive, therefore the routes we will explore in this thesis involve utilising their reactions with other molecules.

The first sensing route this thesis looks to investigate is in a non-aqueous environment. Achieving this is dependent on accurate and reliable readings of potential in non-aqueous environments. This is notoriously tricky as many commercial reference electrodes are designed to perform in aqueous environments. In this scenario it is common place to utilise a quasi-reference electrode; in this work a silver wire is used. Alongside quasi-references IUPAC recommends the use of an internal standard, for example the ferrocene | ferricinium redox couple.[127,128] Chapter 4 seeks to investigate the reliability of this redox couple and assess its suitability to the desired application of this work.

Chapter 5 then seeks to explore the detection of alkaline-earth metal cations through a change in the voltammetric response of a one-electron electroactive ligand, L, upon chelation to a metal ion, M.

$$M^{2+} + 2L \rightleftharpoons L_2M^{2+} \quad 1.14$$

$$L - e^- \rightleftharpoons L^{\cdot +} \quad 1.15$$

The second chemical sensing route explored is the voltammetric detection of scaling ions based on a reduction in the current. This seeks to use binding preference as a way to reduce the current. If two molecules, coordinated together, produced a distinct peak current. Then a molecule is introduced, a scaling ion, that one molecule will preferentially bind to, this will reduce the current.

$$M^{2+} + A \rightleftharpoons MA \quad 1.16$$

$$A + P \longrightarrow Q + B \quad 1.17$$

$$Q \pm e^{-} \rightleftharpoons P \quad 1.18$$

This route depends greatly on the reaction time between the metal ion and species A. The time required for equation 1.16 to reach equilibrium is the minimum time that the sensor could take for reliable detection. This method is explored in chapter 6.

The third method, investigated in chapter 7, is the voltammetric detection of scaling ions based on a change in both the potential and current. The change in potential is caused through the complexation of the metal ion and ligand in solution. Whereas, the change in the peak current is due to the complex precipitating out of solution due to the poor solubility of the formed complex.

$$M^{2+}_{(aq)} + A^{2-}_{(aq)} \rightleftharpoons MA_{(s)} \quad 1.19$$

$$A^{2-}_{(aq)} \pm e^{-} \rightleftharpoons B_{(aq)} = E^{o}_{1} \quad 1.20$$

$$MA_{(aq)} \pm e^{-} \rightleftharpoons MB_{(aq)} = E^{o}_{2} \quad 1.21$$

The following chapter seeks to outline the experimental procedures used throughout this thesis. It details the chemicals used alongside their supplier and purity; as well as and purification or alteration to these chemicals before use in experiments. Alongside this it details any instrumentation used and specific experimental set ups.

1.11 References

1 M. Crabtree, D. Eslinger, P. Fletcher, M. Miller, A. Johnson and G. King, *Oilf. Rev.*, 1999, 30–45.

2 A. A. Olajire, *J. Pet. Sci. Eng.*, 2015, **135**, 723–737.

3 M. A. Kelland, *Production chemicals for the oil and gas industry*, CRC Press, Boca Raton, 2nd edn., 2014.

4 W. W. Frenier and M. Ziauddin, *Formation, Removal, and Inhibition of Inorganic Scale in the Oilfield Environment*, Society of Petroleum Engineers, 2008.

5 M. Rogerson, H. M. Pedley, J. D. Wadhawan and R. Middleton, *Geochim. Cosmochim. Acta*, 2008, **72**, 4976–4987.

6 M. Rogerson, H. M. Pedley, A. Kelham and J. D. Wadhawan, *Earth Surf. Dyn.*, 2014, **2**, 197–216.

7 T. Ogino, T. Suzuki and K. Sawada, *Geochim. Cosmochim. Acta*, 1987, **51**, 2757–2767.

8 J. W. Morse, R. S. Arvidson and A. Lüttge, *Chem. Rev.*, 2007, **107**, 342–381.

9 M. Brown, *BP Technol. Mag.*, 1998, 30–32.

10 A. G. Collins, *geochemistry of oilfield waters*, Elsevier Pub. Co, New York, 1975.

11 J. W. Amyx, C. M. J. Bass and R. L. Whiting, *Petroleum Reservoir Engineering*, McGraw-Hill, New York City, 1960.

12 J. Neff, K. Lee and E. M. DeBlois, in *Produced Water*, Springer New York, New York, 2011, pp. 3–54.

13 J. M. Neff, *Bioaccumulation in Marine Organisms*, Elsevier Ltd., Oxford, 2002.

14 G. M. Marion, F. J. Millero, M. F. Camões, P. Spitzer, R. Feistel and C.-T. A. Chen, *Mar. Chem.*, 2011, **126**, 89–96.

15 J. Lyman and R. H. Fleming, *J. Mar. Res.*, 1940, **3**, 134–146.

16 P. Atkins, T. Overton, J. Rourke, M. Weller and F. Armstrong, *Inorganic Chemistry*, Oxford University Press, Oxford, Fifth., 2010.

17 K. K. Turekian and K. H. Wedepohl, *GSA Bull.*, 1961, **72**, 175–192.

18 D. R. Lide, *Hanbook of Chemistry and Physics*, CRC Press, 84th edn., 2004.

19 W. F. Langelier, *Am. Water Work. Assoc.*, 1936, **28**, 1500–1521.

20 H. C. Fett, *Am. J. Surg.*, 1937, **36**, 288–289.

21 G. D. Schott, *Med. Hist.*, 1974, **18**, 9–21.

22 J. M. Lehn and J. P. Sauvage, *J. Am. Chem. Soc*, 1975, **97**, 6700–6707.

23 E. T. Clarke and A. E. Martell, *Inorganica Chim. Acta*, 1991, **190**, 27–36.

24 P. G. Daniele, C. Foti, A. Gianguzza, E. Prenesti and S. Sammartano, *Coord. Chem. Rev.*, 2008, **252**, 1093–1107.

25 T. Kirichenko, V. Vetrogon, S. Scherbakov and N. Lukyanenko, *Anal. Chim. Acta*, 2004, **505**, 277–282.

26 G. Schwarzenbach, H. Senn and G. Anderegg, *Helv. Chim. Acta*, 1957, **40**, 1886–1900.

27 S. Tsunogai, *Talanta*, 1968, **15**, 385–390.

28 X. Tao, Y. Ni, X. Pu, A. Hu and C. Yang, in *2009 3rd International Conference on Bioinformatics and Biomedical Engineering*, IEEE, 2009, pp. 1–4.

29 R. Belcher, D. Gibbons and T. S. West, *Chem. Ind.*, 1954, 127.

30 B. C. Sinha and S. K. Roy, *Analyst*, 1973, **98**, 289.

31 D. Calvo and M. del Valle, *Microchem. J.*, 2007, **87**, 27–34.

32 D. J. Butcher, *Appl. Spectrosc. Rev.*, 2013, **48**, 261–328.

33 Z. Arslan and J. F. Tyson, *Talanta*, 1999, **50**, 929–937.

34 J. B. Willis, *Spectrochim. Acta*, 1960, **16**, 259-E5.

35 J. B. Willis, *Anal. Chem.*, 1961, **4**, 556–559.

36 T. Ramakrishna, J. Robinson and P. West, *Anal. Chim. Acta*, 1966, **36**, 57–64.

37 E. M. Bentley and G. F. Lee, *Environ. Sci. Technol.*, 1967, **1**, 721–724.

38 L. A. Powell and R. L. Tease, *Anal. Chem.*, 1982, **54**, 2154–2158.

39 A. Fulton and L. R. P. Butler, *Spectrosc. Lett.*, 1968, **1**, 317–325.

40 A. M. Stueber, P. Pushkar and E. A. Hetherington, *Appl. Geochemistry*, 1987, **2**, 477–494.

41 B. Welz, *Atomic Absorption Spectrometry*, VCH Verlagsgesellschaft mbH, Weinheim, 2nd edn., 1985.

42 M. I. C. Monteiro, A. J. Curtius, E. A. Norman, L. K. Polzik and M. Mojica, *J. Anal. At. Spectrom.*, 1995, **10**, 329.

43 M. M. Silva, R. B. Silva, F. J. Krug, J. A. Nobrega, H. Berndt, H. Berndt and P. Püschel, *J. Anal. At. Spectrom.*, 1994, **9**, 861.

44 R. J. Kula, D. T. Sawyer, S. I. Chan and C. M. Finley, *J. Am. Chem. Soc.*, 1963, **85**, 2930–2936.

45 S. Han and Y. Ba, *J. Solution Chem.*, 2004, **33**.

46 S. Sahana and P. K. Bharadwaj, *Inorg. Chim. Acta*, 2014, **417**, 109–141.

47 K. P. Carter, A. M. Young and A. E. Palmer, *Chem. Rev.*, 2014, **114**, 4564–4601.

48 J. L. Sessler, M. H. Lee and J. S. Kim, *Chem. Soc. Rev.*, 2015, **44**, 4185–4191.

49 G. Grynkiewicz, M. Poenie and R. Y. Tsien, *J. Biol. Chem.*, 1985, **260**, 3440–50.

50 A. Minta, J. P. Kao and R. Y. Tsien, *J. Biol. Chem.*, 1989, **264**, 8171–8.

51 H. M. Kim, B. R. Kim, M. J. An, J. H. Hong, K. J. Lee and B. R. Cho, *Chem. - A Eur. J.*, 2008, **14**, 2075–2083.

52 H. M. Kim, B. R. Kim, J. H. Hong, J.-S. Park, K. J. Lee and B. R. Cho, *Angew. Chemie Int. Ed.*, 2007, **46**, 7445–7448.

53 X. Dong, Y. Yang, J. Sun, Z. Liu and B.-F. Liu, *Chem. Commun.*, 2009,

0, 3883.

54 A. Matsui, K. Umezawa, Y. Shindo, T. Fujii, D. Citterio, K. Oka and K. Suzuki, *Chem. Commun.*, 2011, **47**, 10407.

55 T. Egawa, K. Hanaoka, Y. Koide, S. Ujita, N. Takahashi, Y. Ikegaya, N. Matsuki, T. Terai, T. Ueno, T. Komatsu and T. Nagano, *J. Am. Chem. Soc.*, 2011, **133**, 14157–14159.

56 R. Y. Tsien, *Biochemistry*, 1980, **19**, 2396–2404.

57 G. Csordás and G. Hajnóczky, *J. Biol. Chem.*, 2003, **278**, 42273–82.

58 M. F. Leite, E. C. Thrower, W. Echevarria, P. Koulen, K. Hirata, A. M. Bennett, B. E. Ehrlich and M. H. Nathanson, *Proc. Natl. Acad. Sci. U. S. A.*, 2003, **100**, 2975–80.

59 D. A. Rusakov and A. Fine, *Neuron*, 2003, **37**, 287–297.

60 K. Takesako, K. Sasamoto, Y. Ohkura, K. Hirose and M. Iino, *Anal. Commun.*, 1997, **34**, 391–392.

61 H. He, K. Jenkins and C. Lin, *Anal. Chim. Acta*, 2008, **611**, 197–204.

62 B. Sui, X. Liu, M. Wang and K. D. Belfield, *Chem. Eur. J.*, 2016, **22**, 10351–10354.

63 D. C. Magri, J. F. Callan, A. P. de Silva, D. B. Fox, N. D. McClenaghan and K. R. A. S. Sandanayake, *J. Fluoresc.*, 2005, **15**, 769–775.

64 J. An, Z. Yang, M. Yan and T. Li, *J. Lumin.*, 2013, **139**, 79–83.

65 Y. Li and C. M. Yang, *J. Am. Chem. Soc.*, 2005, **127**, 3527-3530.

66 Y.-W. Wang, Y.-T. Shi, Y. Peng, A.-J. Zhang, T.-H. Ma, W. Dou and J.-R. Zheng, *Spectrochim. Acta Part A Mol. Biomol. Spectrosc.*, 2009, **72**, 322–326.

67 H. J. Kim and J. S. Kim, *Tetrahedron Lett.*, 2006, **47**, 7051–7055.

68 R. Velu, V. T. Ramakrishnan and P. Ramamurthy, *Tetrahedron Lett.*, 2010, **51**, 4331–4335.

69 D. Liu, J. Qi, Z. Yu, X. Liu, R. Yang, H. Yang, H. Chang, H. He and G. Yang, *Anal. Methods*, 2014, **6**, 3555.

70 A. Kaur, G. Kaur, A. Singh, N. Singh and N. Kaur, *ACS Sustain. Chem. Eng.*, 2016, **4**, 94–101.

71 I. Díez and R. H. A. Ras, *Nanoscale*, 2011, **3**, 1963.

72 R. Jin, *Nanoscale*, 2010, **2**, 343–362.

73 X. Zhang, S. Wang, L. Xu, L. Feng, Y. Ji, L. Tao, S. Li and Y. Wei, *Nanoscale*, 2012, **4**, 5581.

74 X. Wang, S. Xu and W. Xu, *Nanoscale*, 2011, **3**, 4670.

75 J. Allouche, in *Nanomaterials: A Danger or a Promise?*, Springer London, London, 2013, pp. 27–74.

76 H. Soo Choi, W. Liu, P. Misra, E. Tanaka, J. P. Zimmer, B. Itty Ipe, M. G. Bawendi and J. V Frangioni, *Nat. Biotechnol.*, 2007, **25**, 1165–1170.

77 L. Zhao, D. Sui and Y. Wang, *J. Lumin.*, 2015, **162**, 81–86.

78 L. Xu, Y. Chen, R. Zhang, T. Gao, Y. Zhang, X. Shen and R. Pei, *J. Fluoresc.*, 2016, 1–6.

79 M. L. Bochman, K. Paeschke and V. A. Zakian, *Nat. Rev. Genet.*, 2012, **13**, 770–780.

80 J. R. Williamson, M. K. Raghuraman and T. R. Cech, *Cell*, 1989, **59**, 871–880.

81 F. W. Kotch, J. C. Fettinger and J. T. Davis, *Org. Lett.*, 2000, **2**, 3277–3280.

82 W. Guschlbauer, J.-F. Chantot and D. Thiele, *J. Biomol. Struct. Dyn.*, 1990, **8**, 491–511.

83 J. S. Lee, *Nucleic Acids Res.*, 1990, **18**, 6057–6060.

84 M. Vairamani and M. L. Gross, *J. Am. Chem. Soc*, 2003, **125**, 42–43.

85 D. Zhang, T. Huang, P. S. Lukeman and P. J. Paukstelis, *Nucleic Acids Res.*, 2014, **42**, 13422–13429.

86 R. Elghanian, J. J. Storhoff, R. C. Mucic, R. L. Letsinger and C. A. Mirkin, *Science*, 1997, **277**.

87 D. Xu, H. W. Zhao, C. Z. Huang, L. P. Wu, W. D. Pu, J. J. Zheng and Y. Zuo, *J. Nanosci. Nanotechnol.*, 2012, **12**, 3006–3010.

88 X. Wu, Y. Xu, Y. Dong, X. Jiang and N. Zhu, *Anal. Methods*, 2013, **5**, 560–565.

89 A. J. Reynolds, A. H. Haines and D. A. Russell, *Langmuir*, 2006, **22**, 1156–1163.

90 J. Zhang, Y. Wang, X. Xu and X. Yang, *Analyst*, 2011, **136**, 3865.

91 X. Wu, W. Tang, C. Hou, C. Zhang and N. Zhu, 2014.

92 K. Shrivas, P. Maji and K. Dewangan, *Spectrochim. Acta Part A Mol. Biomol. Spectrosc.*, 2017, **173**, 630–636.

93 E. Bakker, P. Buehlmann and E. Pretsch, *Chem. Rev.*, 1997, **97**, 3083–3132.

94 T. L. Blair, S. Daunert and L. G. Bachas, *Anal. Chim. Acta*, 1989, **222**, 253–261.

95 Y. Tsujimura, T. Sunagawa, M. Yokoyama and K. Kimura, *Analyst*, 1996, **121**, 1705.

96 M. Püntener, T. Vigassy, E. Baier, A. Ceresa and E. Pretsch, *Anal. Chim. Acta*, 2004, **503**, 187–194.

97 M. Püntener, M. Fibbioli, E. Bakker and E. Pretsch, *Electroanalysis*, 2002, **14**, 1329–1338.

98 L. Y. Heng and E. A. H. Hall, *Electroanalysis*, 2000, **12**, 178–186.

99 G. Jágerszki, A. Grün, I. Bitter, K. Tóth and R. E. Gyurcsányi, *Chem. Commun.*, 2010, **46**, 607–609.

100 J. Bobacka, A. Ivaska and A. Lewenstam, *Chem. Rev.*, 2008, **108**, 329–351.

101 J. Sutter and E. Pretsch, *Electroanalysis*, 2006, **18**, 19–25.

102 R. De Marco, J.-P. Veder, G. Clarke, A. Nelson, K. Prince, E. Pretsch and E. Bakker, *Phys. Chem. Chem. Phys.*, 2008, **10**, 73–76.

103 J. Bobacka, *Electroanalysis*, 2006, **18**, 7–18.

104 F. Li, J. Ye, M. Zhou, S. Gan, Q. Zhang, D. Han and L. Niu, *Analyst*, 2012, **137**, 618–623.

105 B. Paczosa-Bator, *Talanta*, 2012, **93**, 424–427.

106 J. Ping, Y. Wang, Y. Ying and J. Wu, *Anal. Chem.*, 2012, **84**, 3473–3479.

107 M. Fouskaki and N. Chaniotakis, *Analyst*, 2008, **133**, 1072.

108 M. Zhou, S. Gan, B. Cai, F. Li, W. Ma, D. Han and L. Niu, *Anal. Chem.*, 2012, **84**, 3480–3483.

109 B. Paczosa-Bator, L. Cabaj, R. Piech and K. Skupień, *Anal. Chem.*, 2013, **85**, 10255–10261.

110 M. S. Frant, *J. Chem. Educ.*, 1997, **74**, 159.

111 D. Ammann, E. Pretsch and W. Simon, *Anal. Lett.*, 1972, **5**, 843–850.

112 T. Yin, J. Li and W. Qin, *Electroanalysis*, 2016.

113 M. Senda, H. Katano and Y. Kubota, *Collect. Czechoslov. Chem. Commun.*, 2001, **66**, 445–455.

114 H. Katano and M. Senda, *Anal. Sci.*, 1998, **14**, 63–65.

115 B. Kabagambe, M. B. Garada, R. Ishimatsu and S. Amemiya, *Anal. Chem.*, 2014, **86**, 7939–7946.

116 G. Qian, M. Bin Wu, G. Wu, S. Huang, Y. Yan and B. Tian, *Talanta*, 1998, **47**, 1149–1155.

117 V. K. Gupta, A. K. Jain, U. Khurana and L. P. Singh, *Sens. Act. B Chem.*, 1999, **55**, 201–211.

118 V. K. Gupta, R. Ludwig and S. Agarwal, *Anal. Sci.*, 2005, **21**, 293–296.

119 M. Shamsipur, S. Rouhani, H. Sharghi, M. R. Ganjali and H. Eshghi, *Anal. Chem.*, 1999, **71**, 4938–4943.

120 M. A. Zanjanchi, M. Arvand, N. O. Mahmoodi and A. Islamnezhad, *Electroanalysis*, 2009, **21**, 1816–1821.

121 S. Chandra, K. Sharma and A. kumar, *J. Saudi Chem. Soc.*, 2014, **18**, 555–560.

122 R. J. Levins, *Anal. Chem.*, 1971, **43**, 1045–1047.

123 A. M. Y. Jaber, G. J. Moody and J. D. R. Thomas, *Analyst*, 1976, **101**, 179.

124 M. Güggi, E. Pretsch and W. Simon, *Anal. Chim. Acta*, 1977, **91**, 107–112.

125 M. W. Laeubli, O. Dinten, E. Pretsch, W. Simon, F. Voegtle, F. Bongardt and T. Kleiner, *Anal. Chem.*, 1985, **57**, 2756–2758.

126 A. M. Othman, M. S. El-Shahawi and M. Abdel-Azeem, *Anal. Chim. Acta*, 2006, **555**, 322–328.

127 G. Gritzner and J. Kuta, *Pure Appl. Chem.*, 1982, **54**, 1527–1532.

128 G. Gritzner and J. Kuta, *Pure Appl. Chem.*, 1984, **56**, 461–466.

2 Electrochemical Theory

This chapter seeks to outline the fundamental theory underpinning the electrochemical systems examined in the subsequent chapters. It covers topics including electrode potentials, electrode processes and a variety of dynamic electroanalytical techniques.

2.1 Equilibrium Electrochemistry

2.1.1 *Equilibrium*

Equilibrium predicts the direction of any spontaneous chemical change that may occur within a chemical system; it can be understood through thermodynamics. Any chemical reaction may be considered through the net heat change in the system that may occur and the capacity of the system to do work. These two effects combine through the Gibbs energy, which is system-centric. This is advantageous as only the system needs to be considered; changes in the surroundings may be neglected in this framework. In this way, equilibrium occurs when the Gibbs energy is minimised, *i.e.* zero change in the Gibbs energy, ΔG.

$$\Delta G = 0 \tag{2.1}$$

When considering a reaction such as

$$aA + bB \rightleftharpoons xX + yY \tag{2.2}$$

the Gibbs energy change, ΔG, associated with the change in moles, Δn, of the reaction from left to right, where v is the stoichiometric factor.

$$\Delta G = \sum_{i=Products} v_i G_i - \sum_{j=Reactants} v_j G_j \tag{2.3}$$

$$\Delta G = (xG_X + yG_Y) - (aG_A + bG_B) \tag{2.4}$$

The change in the Gibbs energy of a pure species, i, is related to its chemical potential, μ_i, in equation 2.5. The chemical potential of a pure species, i, is defined as the Gibbs energy per mole of i,

$$\mu_i = \left(\frac{\partial G}{\partial n_i}\right)_{T,\, P, n_j \neq n_i} \tag{2.5}$$

where T is the absolute temperature and P is the pressure. Therefore, for the previously stated equilibrium, it follows that,

$$a\mu_A + b\mu_B = x\mu_X + y\mu_Y \quad 2.6$$

which shows that under constant conditions the sum of the chemical potentials of the reactants and products in a system at equilibrium are equal.

In the case of a perfect gas,

$$\mu_X = \mu_X^o + RT \ln\left(\frac{P_X}{P^o}\right) \quad 2.7$$

where $\mu_X{}^o$ is the standard chemical potential of species X, R is the universal gas constant (8.314 J K^{-1} mol^{-1}), P_X is the pressure of gas X and P^o is the standard pressure (10^5 N m^{-2}). It follows that for the above equilibrium,

$$x\mu_X^o + y\mu_Y^o - a\mu_A^o - b\mu_B^o = \quad 2.8$$
$$-xRT \ln\left(\frac{P_X}{P^o}\right) - yRT \ln\left(\frac{P_Y}{P^o}\right) + aRT \ln\left(\frac{P_A}{P^o}\right) + bRT \ln\left(\frac{P_B}{P^o}\right)$$

so that the left hand side corresponds to the Gibbs energy change accompanying the reaction

$$\Delta G^0 = -RT\ ln(K) \quad 2.9$$

and the right hand side is constant at a given temperature,

$$K_P = \frac{\left(\frac{P_X}{P^o}\right)^x \left(\frac{P_Y}{P^o}\right)^y}{\left(\frac{P_A}{P^o}\right)^a \left(\frac{P_B}{P^o}\right)^b} \quad 2.10$$

due to an ideal gas only being dependant on the standard chemical potential. When gases are not ideal, this parameter also becomes pressure dependant.

The chemical potential, μ_j, of a species, j, in solution when ideal is given,

$$\mu_j = \mu_j^0 + RT \ln\frac{[j]}{C^0} \quad 2.11$$

in which C^0 is the standard concentration and is by definition one molar. This gives a general equilibrium constant.

$$K_c = \frac{\left(\frac{[X]}{[C]^0}\right)^x \left(\frac{[Y]}{[C]^0}\right)^y}{\left(\frac{[A]}{[C]^0}\right)^a \left(\frac{[B]}{[C]^0}\right)^b} \quad 2.12$$

When species in a reaction are pure solids or pure liquids, their chemical potentials approximate to their standard chemical potentials.

$$\mu_j \cong \mu_j^0 \qquad 2.13$$

The standard chemical potential is independent of the amount of material present. Consequently, terms for these do not appear in expressions for the equilibrium constant.

2.1.2 *The Nernst Equation*

We have seen that chemical potentials control the position of chemical equilibria; in electrochemistry, it is electrochemical equilibria that we are primarily concerned with. The position of the equilibria in this framework is governed by a balance between the chemical energies and electrical energies present. In order to represent both forms of energy fully, we introduce the term of electrochemical potential of a species X.

$$\overline{\mu_X} = \mu_X + Z_X F\phi \qquad 2.14$$

This sums the contribution from the chemical potential, μ_X, and the electrical energy; with Z_X being the formal charge on species X, F representing Faraday's constant (96486.4 C) and ϕ being the potential of the specific phase, be that electrode or solution, where species X resides. The equation above allows for the analysis of electrochemical equilibria, recognising that the electrochemical potentials of products and reactants will balance, as shown before with chemical potentials. Returning to our previous reaction,

$$Fe^{3+} + e^- \rightleftharpoons Fe^{2+} \qquad 2.15$$

would mean the conditions of the equation are

$$\overline{\mu_{Fe^{3+}}} + \overline{\mu_{e^-}} = \overline{\mu_{Fe^{2+}}} \qquad 2.16$$

therefore, applying the definition of electrochemical potential described above,

$$(\mu_{Fe^{3+}} + 3F\phi_S) + (\mu_{e^-} - F\phi_M) = (\mu_{Fe^{2+}} + 2F\phi_S) \qquad 2.17$$

where ϕ_S and ϕ_M refer to the potentials of the solution and metal electrode respectively. This is rearranged.

$$F(\phi_M - \phi_S) = \mu_{Fe^{3+}} + \mu_{e^-} - \mu_{Fe^{2+}} \qquad 2.18$$

Knowing that,

$$\mu_{Fe^{3+}} = \mu^o_{Fe^{3+}} + RT \ln\left(\frac{[Fe^{3+}]}{C^o}\right), \text{and} \qquad 2.19$$

$$\mu_{Fe^{2+}} = \mu^{o}_{Fe^{2+}} + RT \ln\left(\frac{[Fe^{2+}]}{C^{o}}\right) \quad 2.20$$

we find the Nernst equation for a single electrode/solution interface,

$$\phi_M - \phi_S = \frac{\Delta\mu^0}{F} + \frac{RT}{F} \ln\left(\frac{[Fe^{3+}]}{[Fe^{2+}]}\right) \quad 2.21$$

where,

$$\Delta\mu^{o} = \mu^{o}_{Fe^{3+}} + \mu^{o}_{e^-} - \mu^{o}_{Fe^{2+}} \quad 2.22$$

which remains constant at a stated pressure and temperature.[1]

2.1.3 *Standard and Formal Potentials*

For the Nernst equation at a single electrode/solution interface we used the relationship between chemical potential and concentration.

$$\mu_j = \mu^{o}_{j} + RT \ln\left(\frac{[j]}{C^{o}}\right) \quad 2.23$$

This is true for an ideal system. In practice however, solutions of electrolytes do not behave ideally. Consequently, it is appropriate to discuss the effective concentrations, otherwise known as the activity.

$$\alpha_j = \gamma_j [j] \quad 2.24$$

Where α_j is the activity of species j and γ_j the activity coefficient for the species. When this coefficient is below unity, the electrolyte solution is stabilized compared to a scenario where the ions have no charge. Likewise, when the activity coefficient is above unity the solution is destabilized compared to a scenario where the ions have no charge. It is possible to calculate the activity coefficient in aqueous solutions at 298 K, devised by Debye and Hückel in 1923.[2,3]

$$log_{10}\gamma_j = -0.509\, Z_j^2 \sqrt{I} \quad 2.25$$

$$log_{10}\gamma_{\pm} = -0.509\, |Z_+ Z_-| \sqrt{I} \quad 2.26$$

Where γ_j is the activity coefficient for an individual ion, j, $\gamma_{\pm}$ is the mean ionic activity coefficient for an electrolyte solution, Z is the charge on the ion in question and I is the ionic strength.

$$I = \frac{1}{2} \sum C_i Z_i^2 \quad 2.27$$

In which, C is the concentration of species i and Z is the charge on species i. The Debye - Hückel law predicts the activity coefficient accurately for $I \leq 10^{-2}$ M; above which it deviates dramatically due to solvation effects. This activity coefficient is therefore incorporated into the first equation of this section.

$$\mu_j = \mu_j^o + RT \ln(\frac{\gamma_j[j]}{C^o}) \quad 2.28$$

When however, the chemical potentials of a redox couple are equal, the coefficient is equal to unity and hence removed from the equation.

The effects of ion solvation in this context were explored by Bjerrum,[4] followed by Stokes and Robinson;[5,6] whereby, they utilised the Debye – Hückel equation to calculate the mean rational activity coefficient, $f_{\pm}$, in order to calculate the mean molal activity coefficient, $\gamma_{\pm}$,

$$log\ \gamma_{\pm} = log\ f_{\pm} - \frac{h}{v}\ log\ \alpha_w - log\ [1 - 0.018(h - v)m] \quad 2.29$$

Where h is the hydration number, v is the stoichiometric ion number of the electrolyte, α_w is the activity of water and m is the molality of the solution.

There are extensive tables[7–9] of standard electrode potentials in literature that are all measured against the standard hydrogen electrode as mentioned previously.[10] This means for a measured electrode potential, E_{cell}^0, of a general formal cell reaction,

$$aA + bB \rightleftharpoons xX + yY \quad 2.30$$

$$E_{cell}^0 = E^0(A, B \rightarrow X, Y) + \frac{RT}{F} \ln\left(\frac{\gamma_A^a \gamma_B^b [A]^a [B]^b}{\gamma_X^x \gamma_Y^y [X]^x [Y]^y}\right) \quad 2.31$$

where E^0(A, B→X, Y) is the standard electrode potential of the A,B/X,Y couple. It is extremely difficult to create the scenario where the activity coefficients are equal to unity. Consequently, the term of formal potential, E_f^0, is introduced which is a good approximation of the standard potentials.

$$E = E_f^0(A, B \rightarrow X, Y) + \frac{RT}{F} \ln\left(\frac{[A]^a [B]^b}{[X]^x [Y]^y}\right) \quad 2.32$$

The formal potential is a combination of the standard electrode potential and the activity coefficient term in equation 2.31.

$$E_f^0 = E^0 + \frac{RT}{F} \ln\left(\frac{\Pi_{\text{React}} \gamma_i}{\Pi_{\text{Prod}} \gamma_j}\right) \quad 2.33$$

Formal potentials, as with standard potentials, are dependant of temperature and pressure, due to the definition of 'standard' being at 10^5 N m^{-2} pressure for the standard hydrogen electrode. They also depend on the electrolyte concentration in the entire solution. This variable loses the thermodynamic generality of the standard potential but allows for experimental work to proceed.

2.1.4 *Electrode Potentials*

Electrochemistry is the study of interfacial charge transfer. Typically, this is across a metal/liquid interface. Therefore, in the case where a redox reaction is studied, when no current flows, for example

$$Fe^{3+} + e^- \rightleftharpoons Fe^{2+} \qquad 2.34$$

an electrochemical equilibrium is created in the presence of an electrode. This equilibrium is established at the surface of the electrode and involves the compounds in solution, along with the electrons present in the metal. The rates of heterogeneous charge transfer in the forward and reverse direction are identical under equilibrium conditions; with no significant changes in the concentration of the two charged species occurring once an equilibrium is established. In this framework, ion Fe^{2+} may be oxidised at the surface of the electrode to yield Fe^{3+} and electrons in the metallic electrode, likewise, Fe^{3+} may be reduced by taking an electron from the electrode to form Fe^{2+}. Since the reactions both occur at the same rate, there is no net build-up of charge in the electrode.[1]

When an equilibrium has been established a charge separation will exist between the electrode and solution. Consequently, a potential exists on the electrode relative to the solution. At an electrode | solution interface the overall potential difference that exists consists of two types of potential; the Volta (outer) potential and the Galvani (inner) potential. The Volta potential, φ, corresponds to across the metal | electrolyte interface and is defined as the work required to move a point charge from infinite distance to just outside (0.1 – 10 μm) the phase surface.[11] The Galvani potential, ϕ, is the electrostatic potential experienced by a charged particle while it is inside a phase and is defined as the work required to bring a point charge from infinite distance to inside

the phase.[12] This means the drop in potential at the interface between the electrode and solution, $\Delta\phi_{M/S}$,

$$\Delta\phi_{M/S} = \phi_M - \phi_S \qquad 2.35$$

where ϕ_M and ϕ_S are defined as the potentials of the metal electrode and solution respectively. The potential drop, E or $\phi_M - \phi_S$, is not directly measurable at a single electrode/solution interface as there would be two of these interfaces present; therefore, a reference electrode is utilised. A reference electrode (R.E) maintains a constant potential value against which the potential drop, E, at the working electrode (W.E) can be measured.

$$E = (\phi_M - \phi_S)_{W.E} - (\phi_M - \phi_S)_{R.E} \qquad 2.36$$

The standard hydrogen electrode, E° = 0.00 V, is the reference that all electrochemical datum are conveniently reported against. The electrode is only considered to be standard when it is has a set value for the pressure at 10^5 N m^{-2} and hydrogen ion concentration of unity. In reality however, this is not fully realised as the solution itself is not ideal, therefore, the proton concentration must be slightly higher at 1.18 mol dm^{-3}. This reference is not always used experimentally however; other references, such as a calomel electrode, are used as well. To continue to report data against the correct reference is achieved by adding a correlating term to the measured potential. For example, a calomel reference electrode gives a value of + 0.242 V when measured against a standard hydrogen electrode. Consequently, potentials measured with a calomel reference should have this number added to correlate with the standard hydrogen electrode data.

The concept of electrode potentials can be re-evaluated by looking at the energy levels associated with the potential determining equilibrium, considering the same process as before,

$$Fe^{3+} + e^- \rightleftharpoons Fe^{2+} \qquad 2.37$$

taking place at an interface between a metal electrode and solution. In metals, the electronic structure consists of conduction bands and valence bands. In conductors the valence band and conduction band overlap. This overlap allows for the free movement of electrons through the structure of the solid. The energy levels in these bands fill up to a maximum level, known as the Fermi level. In solution the energy levels differ; they are discrete and relate to an unfilled conduction band in the Fe^{3+} ion which joins

with an electron to form Fe^{2+}. It is important to realise that the energy value of the electron in the two different complexes will vary due to changes in the solvation around the ion as it goes from Fe^{3+} to Fe^{2+}.

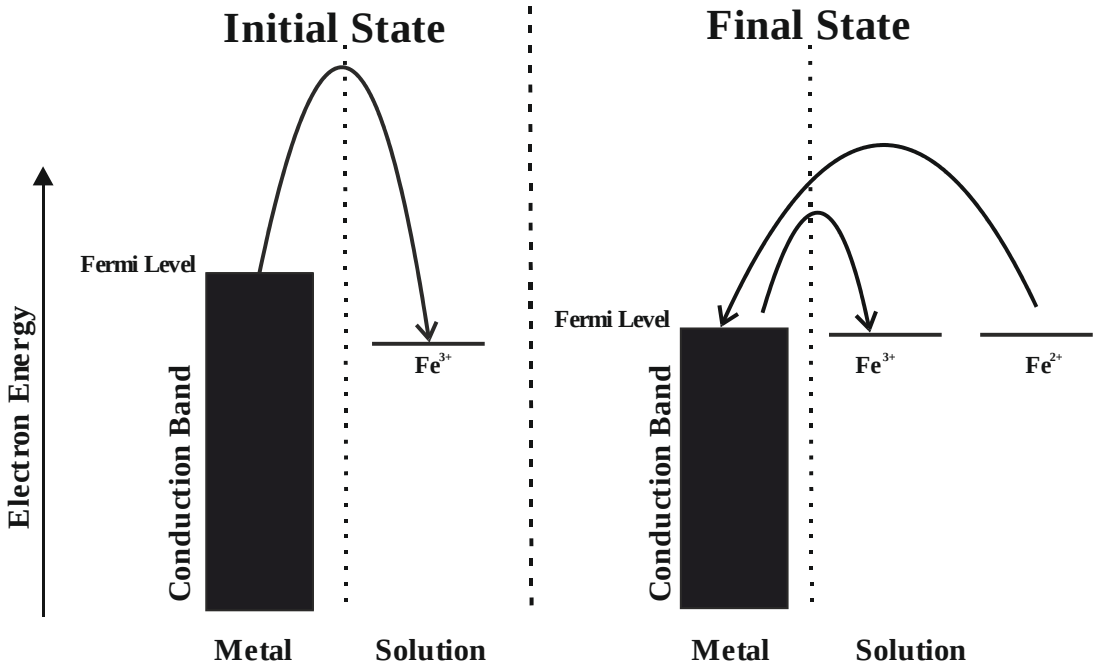

Figure 2.1 – A diagram indicating the relative levels of electron energy in the electrochemical system, before and after electron transfer occurs.

Prior to electron transfer in this electrochemical reaction, the Fermi level of the metal electrode in the system is of a higher energy than the vacant orbital in Fe^{3+}, shown in the initial state in figure 2.1. This indicates that it is energetically favourable for the electrons in the Fermi level to exit the metal and join the vacant orbital, in turn converting Fe^{3+} into Fe^{2+}. Logically, the metal electrode will now have a net positive charge after the departure of the negatively charged electron; whereas the solution will have a net negative charge from the influx of these electrons. The implication of this is a reduction in the Fermi level energy of the metal, as the energy refers directly to electron energy, and an increase in the solution energy. This continues until an equilibrium is reached, whereby the energy levels of the three species are equal, shown in the final state of figure 1. Once this situation is attained, there is no further net charge alteration, there is, however, the presence of a charge separation between the electrode and solution.[1]

2.1.5 *The Electric Double Layer*

When an electrode is under potentiostatic control, there will be an influence on the species in solution from the charge held at the electrode. The resulting strong interactions between an electrode and species in solution give rise to the electric double layer, initially presented by Helmholtz in 1853.s[13] He suggested that there would be a charge density on the electrode, either negative due to an excess of electrons or positive due to a deficiency of electrons. This in turn would force the rearrangement of ions in solution close to the electrode surface to neutralize the interface.

The result is two layers of charge separated by a certain distance, as shown in figure 2.2, and hence known as the double layer which is analogous to an electrical capacitor.

Figure 2.2 – A graphical representation of the first double layer proposed by Helmholtz.

The distance between the two sets of charges is limited by the radius of the ion and its solvation sphere. Many alterations were made to the initial model, by Gouy[14] and Chapman[15], Stern[16], Grahame[17] and finally Bockris, Devanthan and Müller.[18] The model used presently, figure 2.3, shows the several layers that the interfacial regions is separated into.

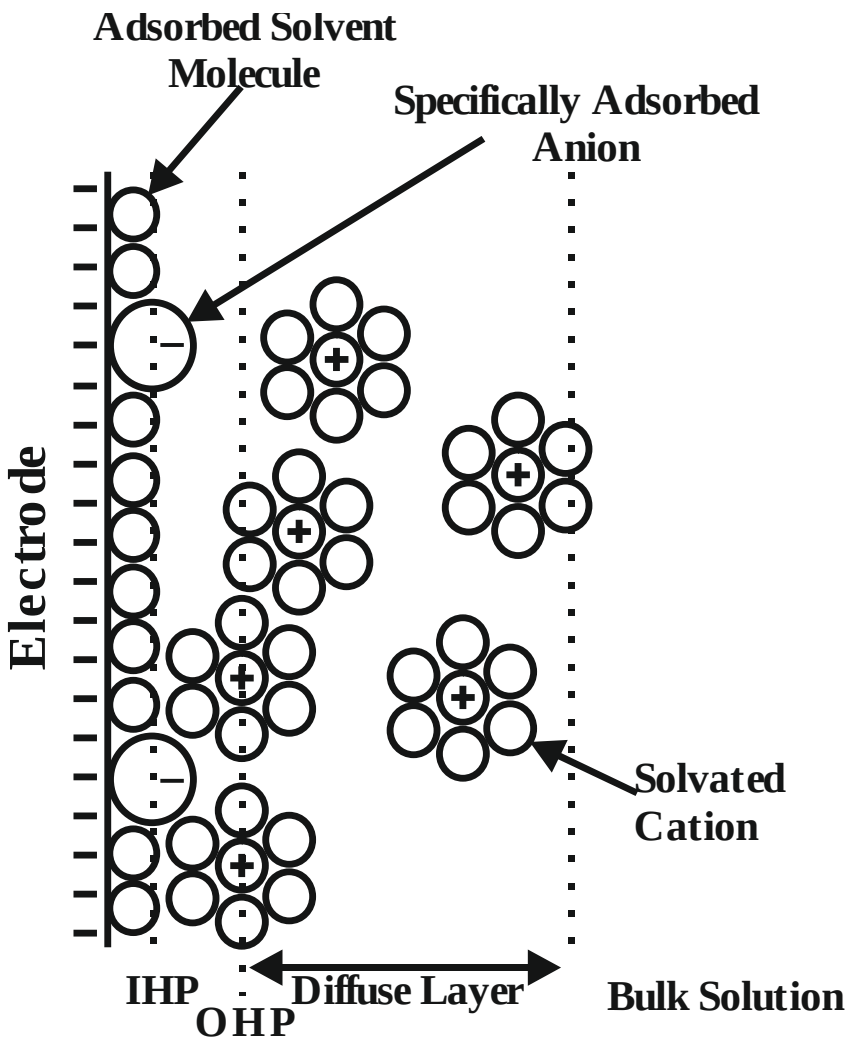

Figure 2.3 – A graphical representation of the current model of the interfacial region.

The closest layer to the electrode surface, defined as the *loci* of the centres of the specifically adsorbed ions, is known as the Inner Helmholtz Plane (IHP). It consists of mainly solvent molecules as well as specifically adsorbed species on the electrode surface. This layer is defined by the centre of the largest specifically adsorbed species. The second layer, defined as the *loci* of the centres of the solvated ions of opposite charge to the specifically adsorbed ions, is known as the Outer Helmholtz Plane (OHP). The volume from the OHP to the bulk solution is known as the diffuse layer, this consists of a three-dimensional arrangement of non-specifically adsorbed molecules.

2.1.6 *Faradaic and Non-Faradaic Processes*

At the electrode itself there are two types of current flow that can occur; these are categorised as Faradaic and non-Faradaic processes. A Faradaic process refers to the current passed when an electroactive species has a change in oxidation state, through interfacial electron transfer, and can provide crucial information as to the rate of a redox reaction. Due to the nature of these reactions, *via* the transfer of electrons, they are ruled over by Faraday's Laws of electrolysis, which are described below.

Faraday's first law states that the amount of any substance that is altered at an electrode, through the process of electrolysis, is directly proportional to the amount of charge passed at the electrode. Whereas, his second law explains that for any given amount of charge, the amount of each particular substance that is altered is governed by the stoichiometry of the electrode reaction. The charge, Q, therefore can be calculated,

$$Q = nNF \qquad 2.38$$

where N corresponds to the number of moles of reactant and F is Faraday's constant (96484.6 C mol^{-1}), this represents the charge on one mole of electrons.

Non-Faradaic processes refer to any charge within the system that arises from anything except a chemical reaction or electron transfer. This can be attributed to various sources at the electrode/electrolyte interface, such as the movement of electrolyte ions, the reorientation of solvent molecules containing a dipole or adsorption and desorption effects. These are basically the forms of background electrical current found during voltammetric experiments; for example the charging of the electric double layer prior to any electron transfer process. This charging process limits the electrochemical systems as the application of a voltage, which is temporarily dependant, cannot be faster than the time constant for this capacitor charging. In addition to this, the non-Faradaic current in the system is inherently coupled to the Faradaic process *via* the Ohmic loss. This is where the solution resistance is a major cause behind the voltage drop that occurs. The solution resistance is related to the nature of the supporting electrolyte in the system, as well as the cell geometry.[19] This variance becomes a problem when subtracting baseline currents from obtained voltammograms. In reality

the total current, i_T, observed in an electrochemical system is governed by both the Faradaic, i_f, and non-Faradic, i_{nf}, processes.

$$i_T = i_f + i_{nf} \quad 2.39$$

2.2 Electrode Kinetics

This section primarily aims to outline the fundamental process that occurs at an electrode surface for reactions involving electron transfer.

2.2.1 *Currents and Reaction Flux*

In an electroreduction reaction such as,

$$Fe^{3+} + e^- \rightleftharpoons Fe^{2+} \quad 2.40$$

the electrode transfer process between the electrode and the Fe^{3+} ion occurs *via* a process known as quantum mechanical tunnelling. This is a phenomenon where a particle can overcome a barrier that it could not classically. The electric double layer consists of many adsorbed species and solvent molecules that can hinder the electroactive species obtaining direct contact with the electrode surface. Consequently, the Fe^{3+} ion must be within 1 – 2 nm of the electrode surface for the required overlap of wavefunctions describing the electron locations in the donor (electrode) and acceptor (Fe^{3+} ion). The transfer of an electron results in the passage of electrical current, I (A). This parameter can be related to the flux, j, of a species when undergoing electrolysis involving one electron,

$$I = FAj \quad 2.41$$

where A is the electrode area and F is Faraday's constant. This flux is known as the rate of heterogeneous electrochemical reaction taking place. It can therefore also be described in terms of a rate law,

$$j = k(n)[Fe^{3+}]_0^n \quad 2.42$$

with n being the order (usually n = 1), k(n) indicating the order of the rate constant and the subscript 0 defining the concentration of Fe^{3+} as that at the surface of the electrode. Electrochemical rate constants are similar to heterogeneous and homogenous ones in that they are temperature and pressure dependant; in addition to

this though, they are highly dependent on the potential. An exponential increase is seen; when altering (ϕ_m - ϕ_s) by 1 V the value of k can change by a factor of 10^9.

2.2.2 *The Potentiostat*

To study the electrode kinetics quantitatively a potentiostat, figure 2.4, in conjunction with three electrodes is required; a working electrode (W.E), reference electrode (R.E) and counter electrode (C.E). The aim of an electrochemical experiment is to observe the current at the working electrode/solution interface as a function of an applied potential.

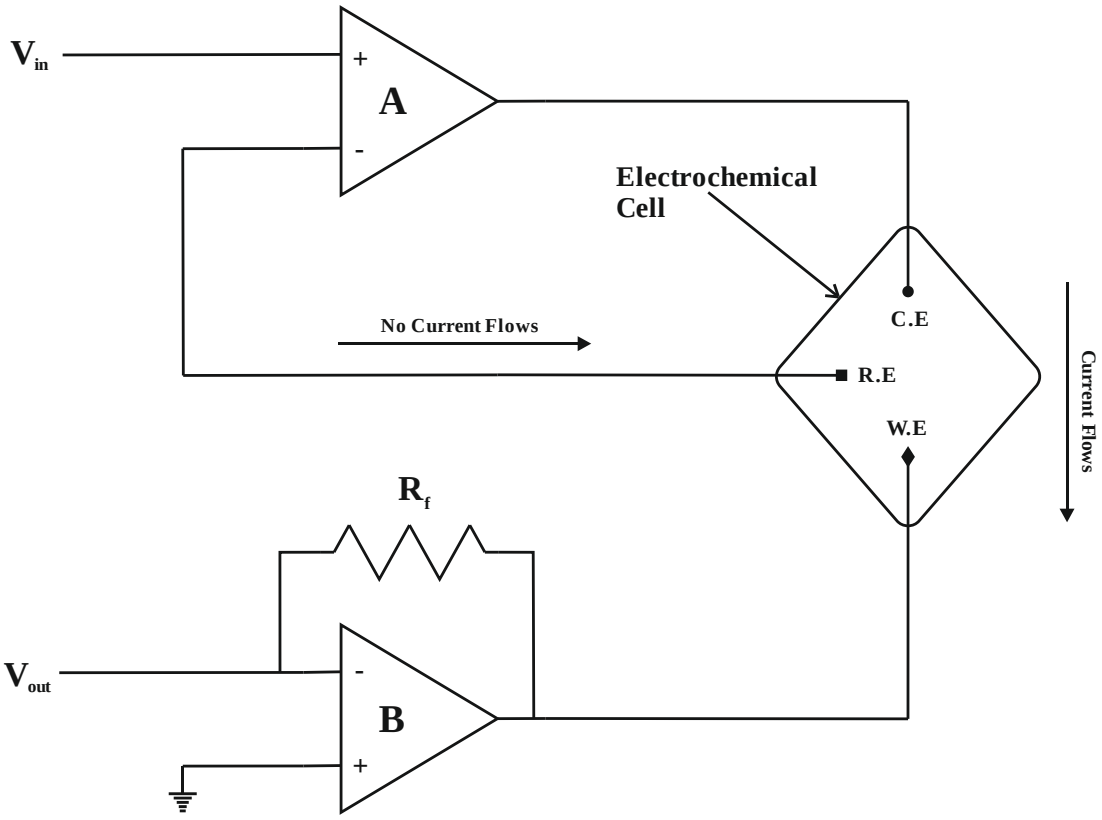

Figure 2.4 – A basic schematic of a potentiostat design.

The potentiostat imposes a fixed potential between the working and reference electrode as no current will be drawn through the reference due to operational amplifier A. This is because operational amplifiers, denoted by triangles A and B in figure 2.4, do not allow current to travel across them.

$$E = (\phi_M - \phi_S)_{W.E} - (\phi_M - \phi_S)_{R.E} \qquad 2.43$$

The purpose of the reference electrode is to provide a stable potential; consequently, any variance in the measured value of E will be directly as a result of changes at the working electrode. The imposition of the potential drop on the working electrode interfacial region will cause current to flow. In turn, this current is converted to voltage by operational amplifier B. This is the role of the counter electrode; to pass this same induced current that is present at the working electrode. Hence, the potentiostat drives the counter electrode, through the feedback circuit R_f, to the required potential to pass this current. Without the counter electrode in the system, the previous expression would be useless as either current would pass through the reference electrode consequently disturbing the system and inducing a chemical change which, in turn alters the steady potential, or, there would be electrical resistance in the bulk solution between the reference and working electrodes leading to a scenario where,

$$E = (\phi_M - \phi_S)_{W.E} + IR - (\phi_M - \phi_S)_{R.E} \qquad 2.44$$

and changes in E would cause unknown changes in IR, leading to a system where $(\phi_m - \phi_s)_{W.E}$ cannot be controlled. One exception to this is when using a microelectrode at steady state; when the system is not at steady state a microelectrode trends towards the characteristics of a macro electrode.

For a macro electrode the Ohmic loss is directly proportional to the radius of the electrode.

$$\pi r_0^2 . \frac{1}{r_0} \propto r_0 \qquad 2.45$$

However, for a microelectrode at steady state the Ohmic loss is proportional to unity.

$$r_0 . \frac{1}{r_0} \propto 1 \qquad 2.46$$

2.2.3 *Butler-Volmer Kinetics*

This model underpins the most commonly used interpretations of electrode kinetics. It revolves around looking at an electrochemical reaction in the form of,

$$Fe^{3+} + e^- \rightleftharpoons Fe^{2+} \qquad 2.47$$

where the forward rate constant is denoted by k_c and the reverse rate constant by k_a, representing the cathodic and anodic processes respectively. These are both highly potential dependant; whereby we expect cathodic reduction at a negative potential and

anodic oxidation at a positive potential. From previously, we can write a rate law for the entire process.

$$j = k_c[Fe^{2+}]_0 - k_a[Fe^{3+}]_0 \quad 2.48$$

In the reaction considered, all of the species are charged. Consequently the reaction profile is as a function of both ϕ_M and ϕ_S. This means by making ϕ_M more negative and keeping ϕ_S constant we raise the energy of the reactants, as this contains the electrons that are present in the metal phase. Counter to this, making ϕ_S more negative and maintaining ϕ_M we raise the energy of both reactants and products, as both Fe^{3+} and Fe^{2+} reside in the solution phase but the energy of Fe^{2+} is raised by a larger amount because of the differences in charge on the ions.

This means the reaction profiles, figure 2.5, can be altered by varying the potential of the metal and solution phases to either favour the reduction or oxidation process. The reduction is favoured for ϕ_M moving more negatively (or ϕ_S positively), whereas oxidation is favoured for ϕ_M moving more positively (or ϕ_S more negatively).

This means for a reaction profile we can write,

$$k_c = A_c \exp\left(\frac{-\Delta G_c^{(\dagger)}}{RT}\right) \quad 2.49$$

$$k_a = A_a \exp\left(\frac{-\Delta G_a^{(\dagger)}}{RT}\right) \quad 2.50$$

where the Arrhenius equation relates the Gibbs energies of activation to the rate constants, with A_c and A_a being pre exponential factors,

$$\Delta G_c^0(\dagger) = G_\dagger^0 - G^0(R) \quad 2.51$$

$$\Delta G_a^0(\dagger) = G_\dagger^0 - G^0(P) \quad 2.52$$

where † represents the transition state, R the reactants and P the products.

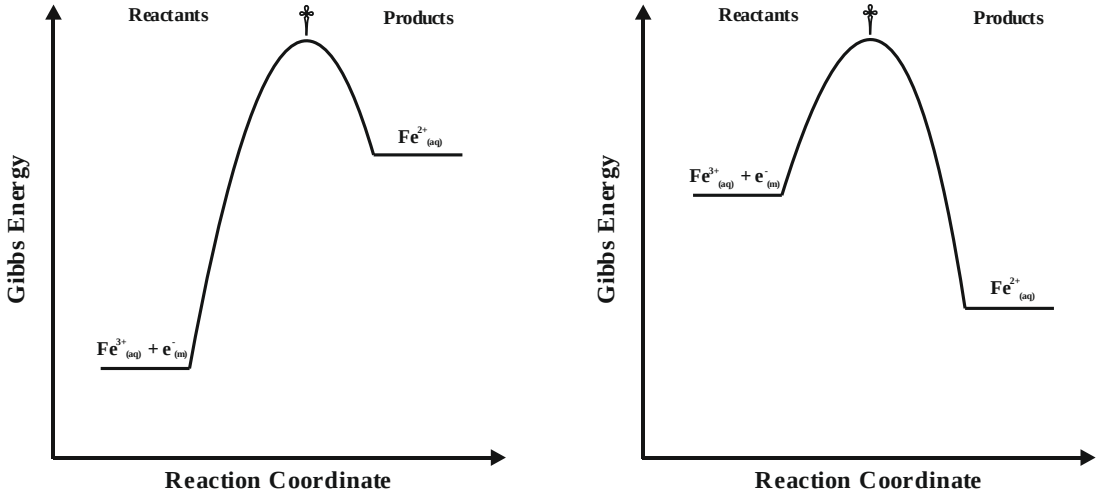

Figure 2.5 – Reaction profiles of an electrochemical process for an electrode held at differing potentials.

From section 2.1.2,

$$G^0(R) = c - 4F\phi_S - F(\phi_M - \phi_S) \quad 2.53$$

$$G^0(P) = c' - 4F\phi_S \quad 2.54$$

where c and c' are constants. combining equations 2.53 and 2.54, along with the assumption that the transition state will have a Gibbs energy between that of the reactants and products,

$$\Delta G^0(\dagger) = c'' - 4F\phi_S - \beta F(\phi_M - \phi_S) \quad 2.55$$

where β represents the transfer coefficient ($0 < \beta < 1$) and c″ is a further constant. From the transfer coefficient we can see that the transition state is more 'product like' when it is close to zero and more 'reactant like' when it is nearing unity. This can in turn be used to evaluate the electrochemical rate constants,

$$k_c \propto k_c^0 \exp\left[\frac{-\alpha F\left(E - E_f^0\right)}{RT}\right] \quad 2.56$$

$$k_a \propto k_a^0 \exp\left[\frac{\beta F\left(E - E_f^0\right)}{RT}\right] \quad 2.57$$

where $(E - E_f^0)$ measures the potential applied to the working electrode relative to the formal potential of the system. If we consider the reaction process to be in equilibrium, whereby the reduction and oxidation currents are equal and hence the flux is zero. Also knowing that the transfer coefficients α and β must equal unity,

$$E = E_f^0 + \frac{RT}{F}\ln\left(\frac{[Fe^{2+}]}{[Fe^{3+}]}\right) + \frac{RT}{F}\ln\left(\frac{k_a^0}{k_c^0}\right) \quad 2.58$$

but in the scenario where no net current is flowing,

$$k_a^0 = k_c^0 = k^0 \quad (2.59)$$

where k^0 is the standard electrochemical rate constant, we produce the most convenient form of the the Butler – Volmer model:

$$k_c = k^0 \exp\left[\frac{-\alpha F(E - E_f^0)}{RT}\right] \quad (2.60)$$

$$k_a = k^0 \exp\left[\frac{\beta F(E - E_f^0)}{RT}\right] \quad (2.61)$$

2.2.4 *Supporting Electrolyte*

We have observed how much alterations in (ϕ_m - ϕ_s) can disturb the values of electrochemical rate constants. We understand from section 2.2.1 that the potential drop must be within 1 – 2 nm of the electrode surface, due to quantum mechanical tunnelling, as this is where electron transfer occurs. Consequently, in experimental voltammetry, excess electrolyte is added to a solution to compress the potential drop distance, making sure it is in the required range. In turn, increasing the concentration of electrolyte will lower the Debye length, which is a measure of its effect on the surrounding solution. If this was not enforced, the described derived rate constants would be inaccurate. Typically, large concentrations (~ 0.1 M) of electrolyte, which is chemically inert at the potentials to be investigated, is used.

2.2.5 *The Tafel Law*

We have explored the relationship between the net flux in an electrochemical system at equilibrium and the associated rate constants.

$$j = k_c[Fe^{3+}]_0 - k_a[Fe^{2+}]_0 \quad (2.62)$$

$$j = k_c^0 \exp\left[\frac{-\alpha F(E - E_f^0)}{RT}\right][Fe^{3+}]_0 - k_a^0 \exp\left[\frac{\beta F(E - E_f^0)}{RT}\right][Fe^{2+}]_0 \quad (2.63)$$

It describes how when a potential, E, is imposed on an electrode, the resulting net flux is a balance between the reduction currents and oxidation currents. When extreme potentials are considered two scenarios arise; $E >> E_f^0$ or $E << E_f^0$, in either case one term from the above equation can be neglected as the process occurring become essentially irreversible. In terms of a reduction process,

$$Fe^{3+} + e^{-} \rightarrow Fe^{2+} \quad 2.64$$

$$j = k^0 \exp\left[\frac{-\alpha F(E - E_f^0)}{RT}\right][Fe^{3+}]_0 \quad 2.65$$

or an oxidation.

$$Fe^{2+} - e^{-} \rightarrow Fe^{3+} \quad 2.66$$

$$j = k^0 \exp\left[\frac{\beta F(E - E_f^0)}{RT}\right][Fe^{2+}]_0 \quad 2.67$$

Consequently, this implies as long as the values for $[Fe^{3+}]_0$ and $[Fe^{2+}]_0$ do not vary greatly from their values in bulk solution,

$$\ln|I_{Red}| = \frac{-\alpha FE}{RT} + constant \quad 2.68$$

$$\ln|I_{Ox}| = \frac{\beta FE}{RT} + constant \quad 2.69$$

where I_{Red} and I_{Ox} refer to the measured currents for the reduction and oxidation processes respectively. The magnitude of the transfer coefficients can be elucidated by Tafel plots, figure 2.6, of ln I versus E when the concentration of a species is constant over the potential investigated.

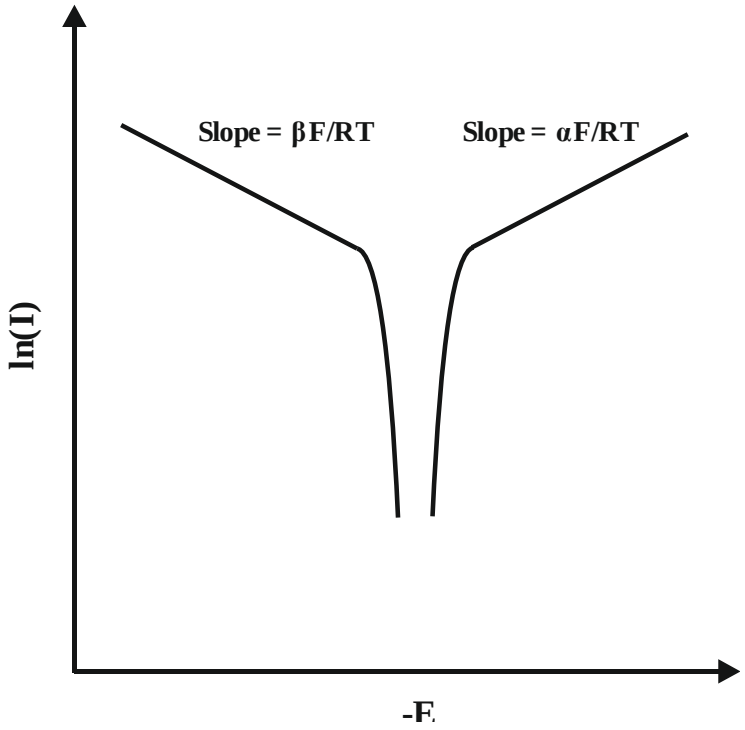

Figure 2.6 – Tafel plot representations for a reduction and oxidation process respectively.

Hence for a reduction process,

$$\alpha = \frac{-RT}{F}\frac{\Delta \ln|I_{Red}|}{\Delta E} \tag{2.70}$$

and an oxidation,

$$\beta = \frac{RT}{F}\frac{\Delta \ln|I_{Ox}|}{\Delta E} \tag{2.71}$$

remembering that the sum of transfer coefficients is always equal to unity for a single electron transfer process.

$$\alpha + \beta = 1 \tag{2.72}$$

2.2.6 *Multistep Electron Transfer*

So far we have considered a single electron transfer process at an electrode surface. In reality, there are many processes that involve two or more steps in the reaction. To put this into context we will consider the evolution of hydrogen gas from an acidic solution.

$$H^+_{(aq)} + e^- \rightarrow \frac{1}{2}H_{2(g)} \tag{2.73}$$

This process occurs through the adsorption of hydrogen ions onto a metal surface, M.

$$H^+_{(aq)} + e^- + M_{(s)} \rightleftharpoons HM_{(aq)} \tag{2.74}$$

$$H^+_{(aq)} + HM_{(aq)} + e^- \rightleftharpoons H_{2(g)} + 2M_{(s)} \tag{2.75}$$

If we assume the rate laws derived earlier hold true, we can determine the fluxes for each step.

$$j_{H^+} = -k^0_{\frac{H^+}{HM}} \exp\left[\frac{-\alpha_1 F}{RT}\left(E - E^0_{f,\frac{H^+}{HM}}\right)\right][H^+]_0 + k^0_{\frac{H^+}{HM}} \exp\left[\frac{\beta_1 F}{RT}\left(E - E^0_{f,\frac{H^+}{HM}}\right)\right][HM]_0 \tag{2.76}$$

$$j_{HM} = k^0_{\frac{H^+}{HM}} \exp\left[\frac{-\alpha_1 F}{RT}\left(E - E^0_{f,\frac{H^+}{HM}}\right)\right][H^+]_0 - k^0_{\frac{H^+}{HM}} \exp\left[\frac{\beta_1 F}{RT}\left(E - E^0_{f,\frac{H^+}{HM}}\right)\right][HM]_0 + k^0_{\frac{HM}{H_2}} \exp\left[\frac{\beta_2 F}{RT}\left(E - E^0_{f,\frac{HM}{H_2}}\right)\right][C]_0 - k^0_{\frac{HM}{H_2}} \exp\left[\frac{-\alpha_2 F}{RT}\left(E - E^0_{f,\frac{HM}{H_2}}\right)\right][HM]_0 \quad 2.77$$

$$j_{H_2} = k^0_{\frac{HM}{H_2}} \exp\left[\frac{-\alpha_2 F}{RT}\left(E - E^0_{f,\frac{HM}{H_2}}\right)\right][HM]_0 - k^0_{\frac{HM}{H_2}} \exp\left[\frac{\beta_2 F}{RT}\left(E - E^0_{f,\frac{HM}{H_2}}\right)\right][H_2]_0 \quad 2.78$$

Noting that,

$$j_{H^+} + j_{HM} + j_{H_2} = 0 \quad 2.79$$

as matter must be conserved.

We know that in the multistep reaction above, one of the steps must be the rate determining or the 'slow' step. There are two primary possibilities for this example; step 1 or step 2. First, let's consider the scenario where step 1 is rate determining.

$$H^+_{(aq)} + e^- + M_{(s)} \xrightarrow{Slow} HM_{(aq)} \quad 2.80$$

$$H^+_{(aq)} + HM_{(aq)} + e^- \xrightarrow{Fast} H_{2(g)} + 2M_{(s)} \quad 2.81$$

In this framework, the concentration of HM present in the system will be negligible and subsequently removed from the rate law.

$$j_{H^+} = k^0_{\frac{H^+}{HM}} \exp\left[\frac{-\alpha_1 F}{RT}\left(E - E^0_{f,\frac{H^+}{HM}}\right)\right][H^+]_0 \quad 2.82$$

Therefore, Tafel analysis can be completed.

$$\ln|I_{Red}| = \frac{-\alpha_1 FE}{RT} + constant \quad 2.83$$

If Tafel analysis produces a slope of ~ 0.5 then it is highly likely for the first step to be the rate determining one. This scenario is typical for metals that possess lower enthalpies of adsorption for hydrogen, such as gold, silver, nickel, copper, iron and zinc.

Considering the alternative scenario, where the second step is rate determining.

$$H^+_{(aq)} + e^- + M_{(s)} \xrightarrow{Fast} HM_{(aq)} \quad 2.84$$

$$H^+_{(aq)} + HM_{(aq)} + e^- \xrightarrow{Slow} H_{2(g)} + 2M_{(s)} \quad 2.85$$

In this framework, the first step can be observed as a 'pre-equilibrium'. Therefore, in this scenario, where the electrode area is represented by A and Faraday's constant by F.

$$I_{Red} = FA(j_{H^+} + j_{HM}) = -FAj_{H_2} \quad 2.86$$

Consequently, with Tafel analysis, where the oxidation of H_2 can be ignored.

$$j_{H_2} = -k^0_{\frac{HM}{H_2}} \exp\left[\frac{-\alpha_2 F}{RT}\left(E - E^0_{f,\frac{HM}{H_2}}\right)\right][HM]_0 \quad 2.87$$

However, because of the previously stated pre-equilibrium,

$$\frac{[HM]_0}{[H^+]_0} = \exp\left[\frac{-F}{RT}\left(E - E^0_{f,\frac{H^+}{HM}}\right)\right] \quad 2.88$$

which therefore means that j_{H_2} will actually be,

$$j_{H_2} = -k^0_{\frac{HM}{H_2}} \exp\left[\frac{-\alpha_2 F}{RT}\left(E - E^0_{f,\frac{HM}{H_2}}\right)\right] \exp\left[\frac{-F}{RT}\left(E - E^0_{f,\frac{H^+}{HM}}\right)\right][H^+]_0 \quad 2.89$$

therefore, as long as $[H^+]_0$ remains similar to its value in bulk solution.

$$\ln|I_{Ox}| = \frac{-(1+\alpha_2)FE}{RT} + constant \quad 2.90$$

In this scenario Tafel analysis will give a slope value of ~1.5, indicating that the second step is rate determining. As the removal of hydrogen from the metal surface is rate determining, it follows that this scenario is typical of metals that possess a larger enthalpy of adsorption for hydrogen; such as platinum, tungsten and molybdenum. Which scenario a metal falls into is governed by the strength of the M-H bond it forms *versus* the standard electrochemical rate constant, k^0. This was first proposed by Parsons[20] and can be presented in the form of a 'volcano plot', figure 2.7.

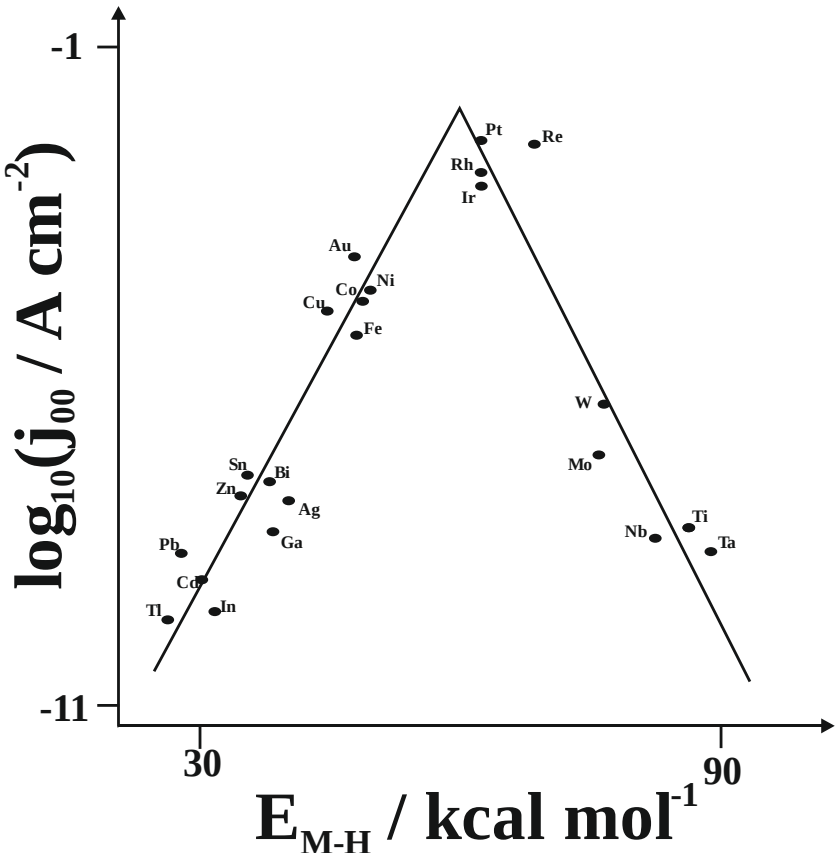

Figure 2.7 - A volcano plot of current density *versus* the energy of hydride formation, adapted from Quaino *et al.*[21] using data from Trasatti.[22]

The two discussed scenarios can also be represented in the form of reaction profiles, figure 2.8.

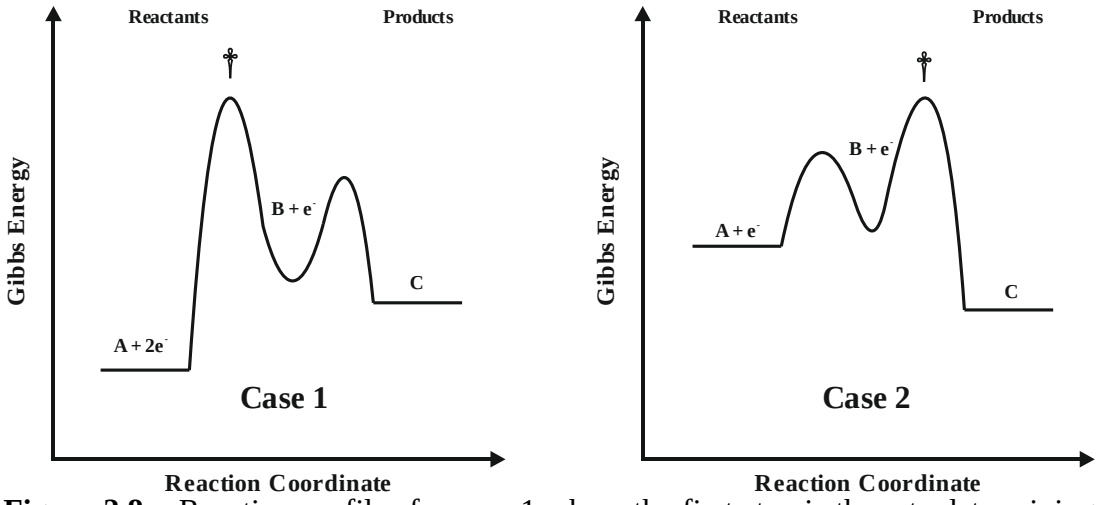

Figure 2.8 – Reaction profiles for case 1 where the first step is the rate determining step and case 2 where the second step is rate determining for the evolution of hydrogen gas.

There is a third scenario that occurs in this situation from the use of a palladium electrode. Tafel analysis of this scenario produces a slope of ~ 2. It arises from a second order electrochemical process in which the second step is the rate determining reaction as follows.

$$H^+_{(aq)} + e^- + M_{(s)} \xrightarrow{Fast} HM^{\cdot} \quad 2.91$$

$$2HM^{\cdot} \xrightarrow{Slow} H_2 + 2M \quad 2.92$$

In which, HM· is the surface coverage of hydrogen on the electrode surface.

$$rate \propto [HM^{\cdot}]^2 \quad 2.93$$

The pre-equilibrium step in this scenario means that the electrode potential, E, is in control of the coverage; this is seen using the Nernst equation.

$$E = E^0_{f\left(\frac{H^+}{HM^{\cdot}}\right)} + \frac{RT}{F}\ln\left(\frac{[H^+]}{[HM^{\cdot}]}\right) \quad 2.94$$

This allows for the concentration of adsorbed species to be found.

$$[HM^{\cdot}] = [H^+]\exp\left[-\frac{F}{RT}\left(E - E^0_{f\left(\frac{H^+}{HM^{\cdot}}\right)}\right)\right] \quad 2.95$$

$$rate \propto [HM^{\cdot}]^2 \propto [H^+]^2\exp\left[-\frac{2F}{RT}\left(E - E^0_{f\left(\frac{H^+}{HM^{\cdot}}\right)}\right)\right] \quad 2.96$$

This results in a transfer coefficient equal to 2.

2.2.7 *Marcus Theory*

Marcus theory was developed by Marcus[23,24] and Hush[25] following work by Franck and Libby[26] and concerns itself with the underlying principles in the process of electron transfer. If we consider the potential energy against reaction coordinate profiles, figure 2.9, for the reactants and products in the following reaction.

$$Fe^{2+} \rightarrow Fe^{3+} + e^- \quad 2.97$$

The Frank-Condon principle tells us that the transfer of an electron occurs over a much shorter timescale than that of a molecular vibration. This means in the profile, an electron ‘jump’ would occur as a vertical transition in regards to reaction coordinate. All of this says that the reaction itself must proceed *via* thermal activation of the reactant so that it may reach the minimum energy requirement of the crossing point in

the profile. This thermal activation occurs *via* bond lengths and angles in the molecule undergoing stretching, compression and distortion. Once the reactant has obtained the required energy, during vibrations of the excited ion the electron tunnelling process may take place to form a vibration induced excited product ion with an identical energy. Following this, rapid thermal deactivation of the molecule takes place *via* collisions with solvent molecules until a ground state is reached.

As a general rule, if the oxidised and reduced species are similar in molecular geometries then the value of k^0 will be large as a small activation barrier will be present. Conversely, if the oxidised and reduced species are significantly structurally different then k^0 will be small as the activation barrier is large.

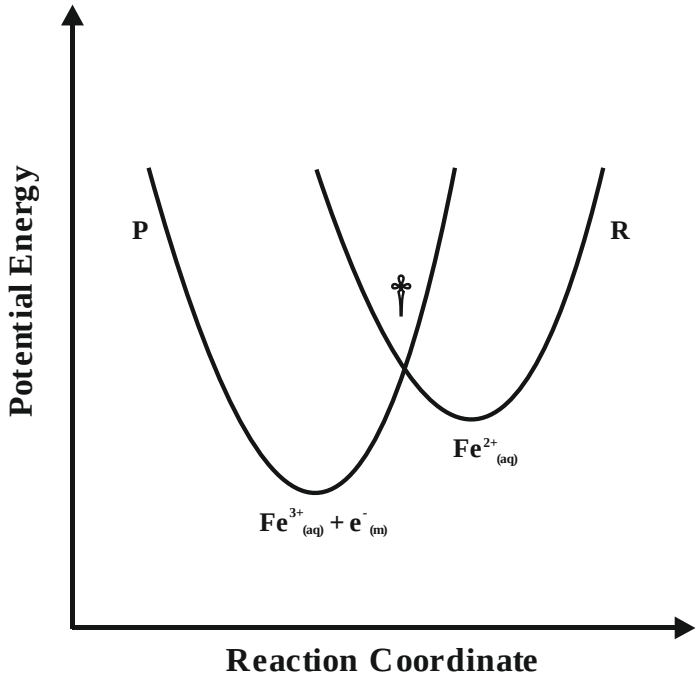

Figure 2.9 – Plot of potential energy versus reaction coordinate for the oxidation of Fe^{2+} to Fe^{3+}.

Electron transfer events can occur in two main ways, inner and outer sphere processes. This concept is familiar for homogenous chemistry, where electron transfer occurs either *via* weak interactions between reactive species or, via a common shared ligand; in regards to heterogeneous chemistry it refers to the interfacial region mentioned previously.

Outer sphere processes (A), figure 2.10, happen when the reactant centre is in the Outer Helmholtz Plane. Inner sphere processes (B), figure 2.10, involve specifically adsorbed species and hence depend greatly on the nature of the electrode surface.

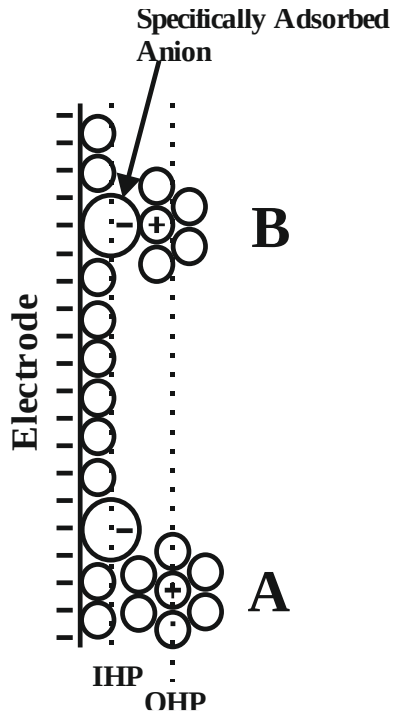

Figure 2.10 – A diagram showing the interfacial region where outer (A) and inner sphere processes (B) occur.

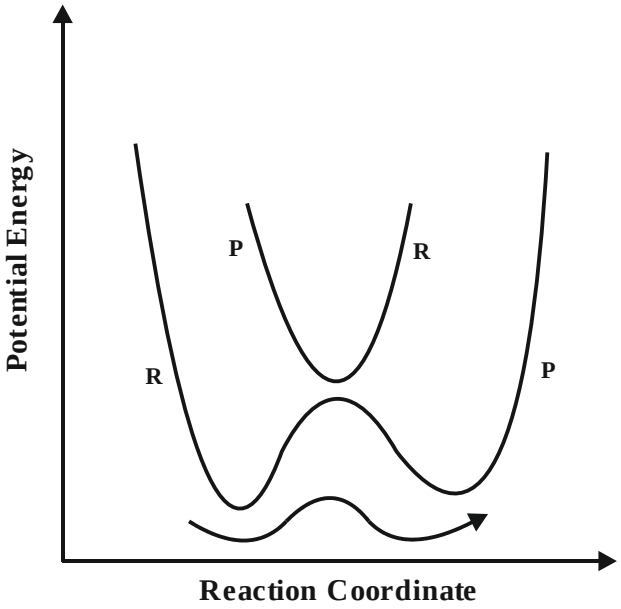

Figure 2.11 – Plot showing an adiabatic process in Marcus theory.

Exploring Marcus theory further produces two scenarios, adiabatic and non-adiabatic. In the potential energy plot, figure 2.11, where the two curves would meet there is instead potential mechanical splitting producing an energy gap known as resonance energy.

If this splitting is significant, the reaction will proceed *via* the lower pathway, denoted by the arrow, with the probability of occurring close to unity; this is known as the adiabatic limit. Conversely, if the perturbation in potential energy is small, resulting in a small gap, a non-adiabatic process takes place whereby the probability of electron transfer greatly shifts away from unity trending towards zero. In most cases the energy gap is a few kilojoules per mole meaning that most reactions are adiabatic. This means that the electrochemical rate constant can be defined as,

$$k = \kappa Z e^{\frac{-\Delta G(\dagger)}{RT}} \tag{2.98}$$

where κ is the transition probability (~ 1 for adiabatic processes) and Z is a pre-exponential factor. Therefore, this means the Gibbs energy of activation can be calculated from the potential energy curves and transition state location can be approximated.

These plots can be treated as parabola, hence formulas for the Gibbs energy derived.

$$G_R = G_R(X = X_R) + \frac{1}{2}k(X - X_R)^2 \tag{2.99}$$

$$G_P = G_P(X = X_P) + \frac{1}{2}k(X - X_P)^2 \tag{2.100}$$

This in turn, at the transition state, implies these equations are equal, hence solving in terms of X† gives,

$$X_\dagger = \frac{1}{2}(X_R + X_P) - \frac{G_P(X = X_P) - G_R(X = X_R)}{k(X_R - X_P)} \tag{2.101}$$

which can produce a simplified equation for the Gibbs energy of activation.

$$\Delta G(\dagger) = \frac{(\lambda + \Delta G)^2}{4\lambda} \tag{2.102}$$

where,

$$\lambda = \frac{1}{2}k(X_R - X_P)^2 \; and \; \Delta G = G_P(X = X_P) - G_R(X = X_R) \tag{2.103}$$

This equation relates the size of k^0 to changes between the geometries of reactants and products; whereby a larger λ value gives a larger Gibbs energy of activation. The term λ has two contributing factors,

$$\lambda = \lambda_i + \lambda_o \qquad 2.104$$

where λ_i refers to bending and stretching in a molecule.

$$\lambda_i = \sum_j \frac{k_j^R k_j^P}{k_j^R + k_j^P} (X_R^j - X_P^j)^2 \qquad 2.105$$

In which k_j^R and k_j^P are normal mode force constants in the reactants and products respectively and $(X_R^j - X_P^j)$ represents changes in bond lengths and angles between the reactants and products.

The variable λ_o refers to solvent reorganisation, where these changes arise from random fluctuations of solvent molecules around a species,

$$\lambda_o = \frac{e^2}{8\pi\varepsilon_0}\left(\frac{1}{r} - \frac{1}{2d}\right)\left(\frac{1}{\varepsilon_{op}} - \frac{1}{\varepsilon_s}\right) \qquad 2.106$$

where d is the distance from the reactant to the electrode surface, ε_{op} is the optical dielectric constant and ε_s is the static dielectric constant.

2.3 Mass Transport

This section specifically deals with the processes that define the movement of species in solution and how this affects the electrochemical process taking place. Mass transport can be separated into three main forms; convection, migration and diffusion. We will consider these cases and look at how they can be used to gain vital information about the systems.

2.3.1 *Convection*

Convection is mechanical bulk fluid movement within a solution, outside of the diffusion layer, around an electrode surface; this allows it to be utilised for hydrodynamic electrodes. The phenomenon can be present in two separate forms, natural and forced convection. Natural convection is present in all solutions and can arise from three main sources. Thermal gradients can be created by electrode processes

being exothermic or endothermic in nature, density gradients arise from bulk solution reactant densities varying from that of the bulk solution and finally Marangoni effects, or surface tension gradients, are produced by local perturbations that increase the area of solution adjacent to the surface of the electrode. Natural convection effects are undesirable as they are extremely difficult to predict or model; however, they can be assumed irrelevant when measurements are short lived, under 10-20 seconds. Secondly, forced convection is mechanical fluid movement given to the system through agitation methods such as rotation (rotating disc voltammetry) and hydrodynamic flow (channel flow voltammetry). This convection overwhelms the natural form and can be controlled or altered; this changes the reaction timescale, allowing for information about the kinetics or mechanisms to be obtained.

2.3.2 *Migration*

Generally, in electroanalytical experiments, migration of the electroactive species can be neglected due to the high excess of inert electrolyte present in solution. Migration itself refers to the transport of ions under an electrical potential. It is the electrolyte that transports the majority of charge via ion transport between electrodes; this leaves the electroactive species unaffected.

2.3.3 *Diffusion*

Diffusion is an entropically driven process; it occurs with solute species moving down a concentration gradient where a species will move from an area of high concentration to an area of low concentration. At any point, x, along this concentration gradient, there will be a corresponding diffusive flux, j, which is quantified by Fick's first law.

$$j = -D\frac{\partial c}{\partial x} \qquad 2.107$$

Where D is the diffusion coefficient, c is the concentration and the negative sign implies that the movement of species, due to diffusion, is down the concentration gradient. The flux can be looked at as the number of moles of something passing through a unit area in a unit of time. Logically, in general, this means that larger molecules tend to have smaller diffusion coefficients; however, this is not always the

case. Voltammetry should be thermostatically controlled due to the highly dependent nature of the diffusion coefficient on temperature,

$$D = D_{\infty} \exp\left[\frac{-E_a}{RT}\right] \quad 2.108$$

with D_{∞} representing the diffusion coefficient at an infinite temperature, E_a the activation energy, R the molar gas constant and T the absolute temperature. In addition to temperature control, excess supporting electrolyte should be added to solutions to eliminate the impact of electric fields on the solution. If this was not the case and the species present in solution were of a charged nature, an electric field would make a significant difference in the diffusive properties.

Fick's first law told us the flux of a species at a particular point; his second law concerns itself with how the concentration, c, at a point, x, varies with time, t.

$$\frac{\partial c}{\partial t} = D\frac{\partial^2 c}{\partial x^2} \quad 2.109$$

This corresponds to a one dimensional scenario. In three dimensions, all axis must be accounted for, x, y and z.

$$\frac{\partial c}{\partial t} = D\left(\frac{\partial^2 c}{\partial x^2} + \frac{\partial^2 c}{\partial y^2} + \frac{\partial^2 c}{\partial z^2}\right) \quad 2.110$$

2.3.4 *The Cottrell Equation*

In experiments, the current, I, at an electrode is given as,

$$I = nFAj \quad 2.111$$

where n is the number of electrons passed in the reaction, F is Faraday's constant, A is the electrode area and j is the flux. This flux is given by Fick's first law,

$$j = D\frac{\partial c}{\partial x} = \frac{D}{2\sqrt{Dt}}\frac{\partial c}{\partial \Gamma} \quad 2.112$$

where D is the diffusion coefficient, t is the time, Γ is defined by,

$$\Gamma = \frac{x}{2\sqrt{Dt}} \quad 2.113$$

and is utilised to solve Fick's second law when considering the scenario of a potential step. This is when at a time, t = 0, a potential is applied to an electrode so that the system goes from a state of no reaction to one where all electroactive species at the

electrode will react. It follows that the current resulting from when a potential step decays to zero has an inversely proportional dependency on the square root of time. This relationship is described in the Cottrell equation.[27]

$$I = \frac{nFA\sqrt{D}C^*}{\sqrt{\pi t}} \qquad 2.114$$

In which C^* is the bulk concentration and n is the number of electrons transferred. We are also able to calculate the charge, Q, passed as a function of time.

$$Q = 2nFA\frac{\sqrt{Dt}}{\sqrt{\pi}}C^* \qquad 2.115$$

This is especially useful to quantify the extent of electrolysis in a system by giving the number of moles of a reactant, N, that has been consumed.

$$N = \frac{Q}{nF} \qquad 2.116$$

2.3.5 *The Nernst Diffusion Layer*

In reality, the current in an experiment will not drop to zero as predicted by the Cottrell equation; but rather it will fall to a steady state value, which is in agreement with the Nernst Diffusion Layer Model, figure 2.12.

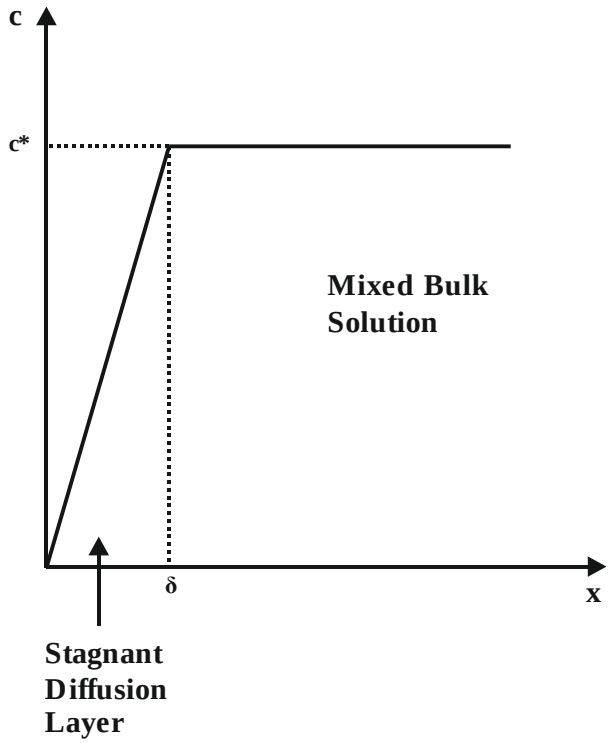

Figure 2.12 – A pictorial representation of the Nernst Diffusion Layer Model.

This model describes the solution past a certain distance, δ, away from the electrode surface as 'well mixed'; therefore maintaining a constant concentration of electroactive species. The mixing that occurs in solution can be through natural convection, which in turn can be driven by poor thermostatic control. Close to the electrode surface however, natural convection is no longer a factor for consideration due to the frictional forces present in conjunction with the rigidity of the electrode itself. This zone between the electrode surface and δ is known as the diffusion layer. The concentration of species only changes in this layer where diffusional transport is operational; consequently, the steady state diffusional flux can be calculated by utilising Fick's first law,

$$j = D\frac{\partial c}{\partial x} = \frac{DC^*}{\delta} \qquad 2.117$$

with the corresponding steady state current, I_{ss}, given by:

$$I_{ss} = nFAm_T C^* \qquad 2.118$$

where m_T is the mass transfer coefficient.

$$m_T = \frac{D}{\delta} \qquad 2.119$$

Realistically, the stagnant diffusion zone and mixing zones presented in figure 2.12 merge into one another with a typical diffusion distance between 10 – 100 microns.

2.3.6 *Mass Transfer Versus Electrode Kinetics*

To observe the effect of both variables previously discussed, electrode kinetics and mass transport, we will consider the following reaction.

$$A + e^- \rightleftharpoons B \qquad 2.120$$

To do this correctly, certain assumptions must be made; firstly, that the concentrations in the bulk solution are $[A]_{Bulk}$ and $[B]_{Bulk}$ and the electrode will have a diffusion layer with a mass transport coefficient.

$$m_T = \frac{D}{\delta} \qquad 2.121$$

Whereby, the diffusion coefficient for both species A and B are equal. Secondly, assuming that potentiostatic three electrode control is implemented the electrochemical rate constants can be written as discussed previously.

$$k_c = k^0 \exp\left[\frac{-\alpha F}{RT}\left(E - E^0_{f,\left(\frac{A}{B}\right)}\right)\right] \quad 2.122$$

$$k_a = k^0 \exp\left[\frac{\beta F}{RT}\left(E - E^0_{f,\left(\frac{A}{B}\right)}\right)\right] \quad 2.123$$

This scenario is one dimensional if the electrode surface is uniformly accessible, therefore the corresponding fluxes are given.

$$j_A = m_T[A]_0 - [A]_{Bulk} = -j_B \quad 2.124$$

$$j_B = m_T[B]_0 - [B]_{Bulk} \quad 2.125$$

$$-j_A = k_c[A]_0 - k_a[B]_0 \quad 2.126$$

These equations can be solved by introducing transport limited currents, in turn eliminating the unknown variable of surface concentrations.

$$j_{A,lim} = -m_T[A]_{Bulk} \quad 2.127$$

$$j_{B,lim} = -m_T[B]_{Bulk} \quad 2.128$$

This results in the flux being represented by,

$$j = -j_A = j_B \quad 2.129$$

$$j = \frac{k_c j_{A,lim} - k_a j_{B,lim}}{m_T + k_c + k_a} \quad 2.130$$

which results in three possible scenarios.

1) $k_c >> k_a, m_T$

In this framework, the flux will trend to $j_{A, lim}$.

$$j \to j_{A,lim} \quad 2.131$$

The flux is controlled by the maximum rate of diffusion as the current seen is independent of the potential applied. This corresponds to a scenario where the electrode surface concentration of A is reduced to zero.

$$j_{A,lim} = \frac{-D[A]_{Bulk}}{\delta} \quad 2.132$$

This can be achieved experimentally by applying a large negative potential to an electrode. This encourages a rapid rate of forward reaction and negligible reverse reaction.

$$A + e^- \to B \quad 2.133$$

2) $k_a >> k_c, m_T$

In this framework, the flux trends to $-j_{B, lim}$.

$$j \rightarrow -j_{B,lim} \quad 2.134$$

This scenario also produces a transport controlled environment, hence, potential independent flux is again observed.

$$j_{B,lim} = \frac{D[B]_{Bulk}}{\delta} \quad 2.135$$

Experimentally this is achieved by applying very large positive potentials to an electrode. This makes the reverse process extremely quick.

$$B \rightarrow A + e^{-} \quad 2.136$$

3) $m_T >> k_c, k_a$.

In this framework, the system is under control of the electrode kinetics rather than the mass transport. This means that the current flowing in the system is sensitive to the electrode potential. The flux is therefore calculated as follows.

$$j = \frac{k_c j_{A,lim} - k_a j_{B,lim}}{m_T} \quad 2.137$$

$$j = -k_c[A]_{Bulk} + k_a[B]_{Bulk} \quad 2.138$$

This framework produces three types of dependence on the potential, known commonly as voltammograms, figure 2.13, where $\theta = F[E-E_f^0]/RT$ and j is the flux.

A. $k^0 >> m_T$ (A – full line)

A single voltammetric peak is observed that centres around the tabulated formal potential for the given redox couple

B. $k^0 \sim m_T$ (B – dashed line)

This is the intermediate case where the voltammogram is centred around the formal potential but spread much wider than the case above.

C. $k^0 << m_T$ (C – dotted line)

Two distinct peaks are seen; these refer to the two individual sides of the redox couple. There is negligible current flowing at the value of the formal potential and hence overpotentials have to be utilized to drive the reactions.

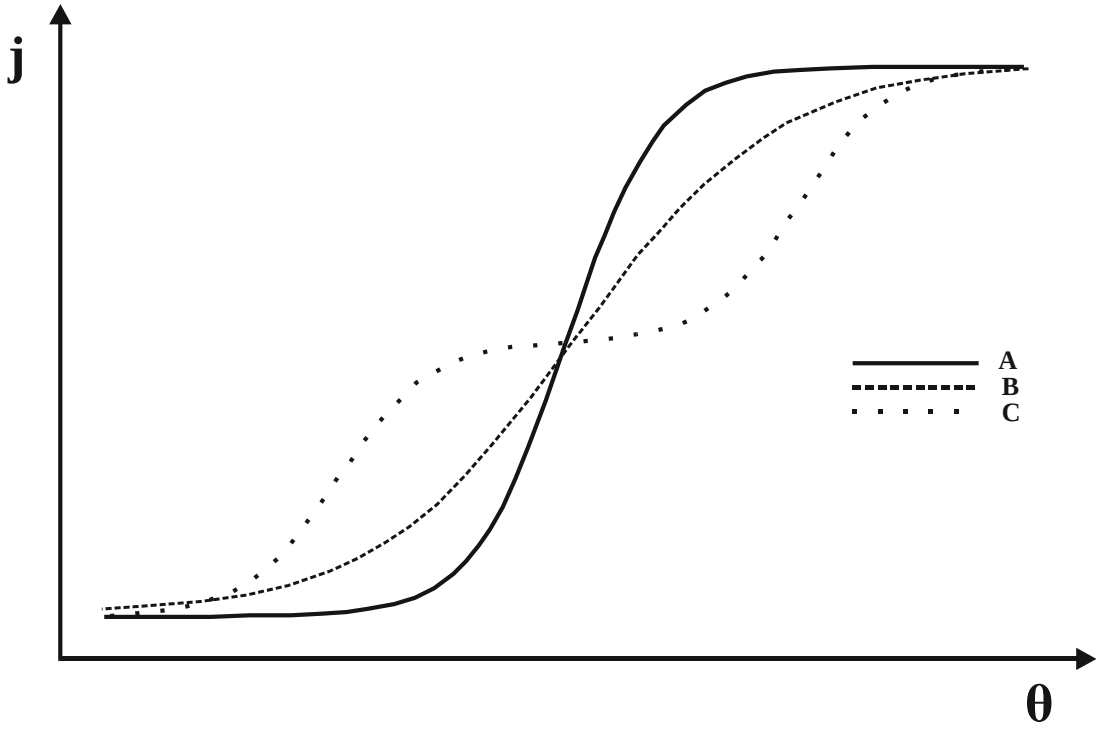

Figure 2.13 – Voltammograms showing the three scenarios arising when the voltammetry is under the control of the electrode kinetics; (A) the rate constant is much greater than the mass transport coefficient, (B) the rate constant and mass transport coefficient are similar and (C) the rate constant is much smaller than the mass transport coefficient. Where j is the flux and $\theta = F[E-E_f^0]/RT$.

2.4 Electroanalytical Techniques

2.4.1 *Cyclic Voltammetry*

Cyclic voltammetry is a vital and extensively employed electroanalytical technique. It revolves around the application of a potential, $E_{initial}$, to the working electrode and 'sweeping' it linearly to another defined potential, E_{final}; at this point the scan is reversed, typically but not always, back to E_1. The classical waveform that is applied is shown in figure 2.14.

Experimentally the current flowing through the working electrode is recorded as a function of the applied potential. This is represented in a plot of this current, I, versus potential, E, more commonly referred to as a voltammogram.

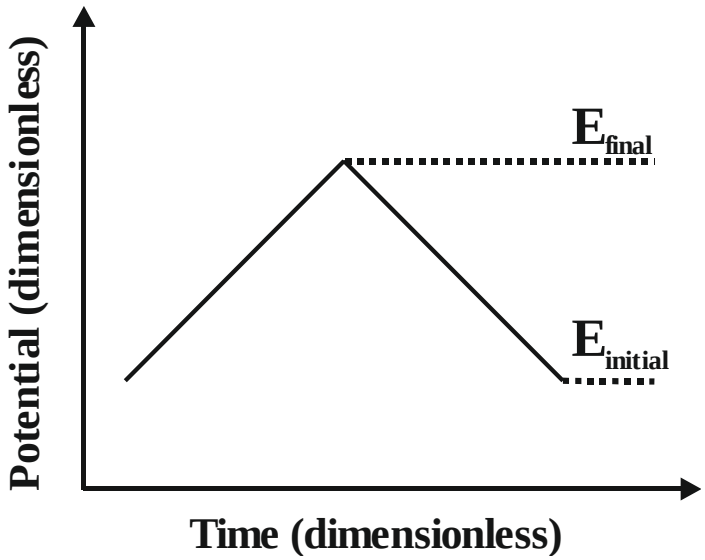

Figure 2.14 – A triangular waveform used for cyclic voltammetry.

2.4.2 *Reversibility*

Previously we have observed how larger or smaller electrochemical rate constants, k^0, can be produced by the presence of fast or slow electron transfer; the terms 'large' and 'small' are relative to the rate of mass transport. This change in electrochemical rate constant can provide very differing voltammograms.

Matsuda and Ayabe[28] suggested that slow electrode kinetics are indicative of an irreversible system (typically $k^0 < 10^{-5}$ cm s^{-1}); whereas, fast electrode kinetics represent a reversible one (typically $k^0 > 10^{-1}$ cm s^{-1}). In between these two limits is known as a quasi-reversible system (typically $10^{-1} > k^0 > 10^{-5}$ cm s^{-1}).

Noticeably, these voltammograms do not reach a steady state as seen in previous sections. This is due to the diffusion layer; in steady state systems it has a fixed size, whereas here it does not. The diffusion layer is constantly expanding as the scan progresses, hence, once the concentration of electroactive species at the electrode surface approaches zero, the current in turn will drop, creating a peak current maximum, seen in figures 2.15, 2.16 and 2.17.

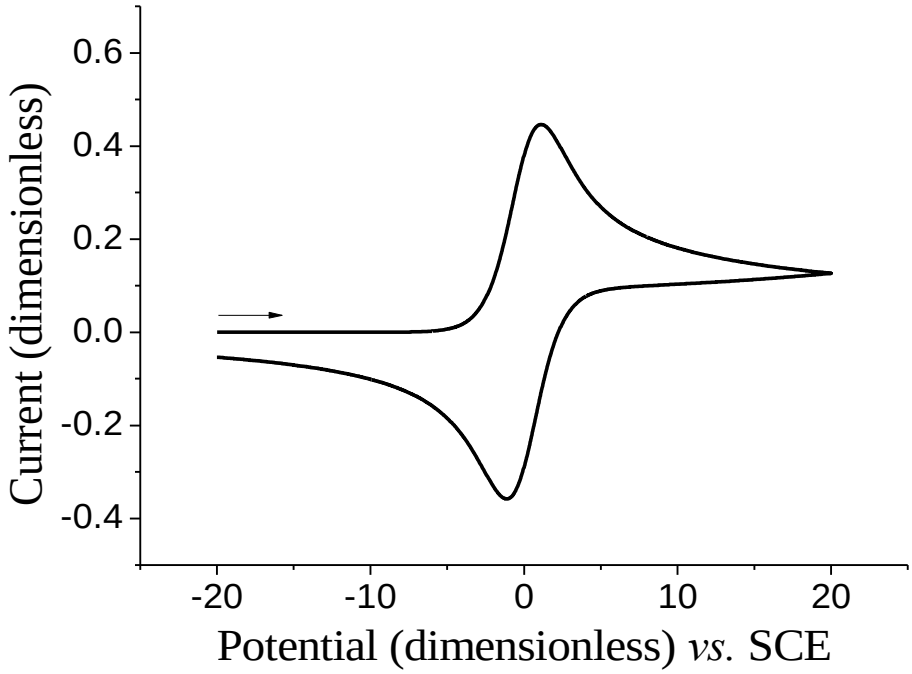

Figure 2.15 – An example of a voltammogram collected for an electrochemically reversible electrode process performed *versus* a standard calomel reference electrode. Reproduced with permission from J D Wadhawan.

In a reversible system, figure 2.15, the anodic peak, $E_{p,a}$, and cathodic peak, $E_{p,c}$, are based around the formal potential, E_f^0, of the A/B redox couple.

$$E_f^0 = \frac{E_{p,a} + E_{p,c}}{2} \qquad 2.139$$

This peak separation, E_{ps}, is independent of the scan rate and can be used to elucidate the amount of electrons, n, transferred in a redox process.

$$E_{ps} = E_{p,a} - E_{p,c} = \frac{0.059}{n} \qquad 2.140$$

This tells us that a reversible one electron redox process should have a peak separation equal to ~59 mV.

The rate at which you apply the potential sweep, or scan rate, ν, will lead to changes in the flux. Consequently, for a reversible system, a relationship between the peak current, I_p, and the scan rate is seen, known as the Randle-Sevcik equation.

$$I_p = 2.69x10^5\, AD^{\frac{1}{2}}C\nu^{\frac{1}{2}} \quad (298\ K) \qquad 2.141$$

Where A is the electrode area, D is the diffusion coefficient, C is the bulk concentration and ν represents the scan rate. We can see that the peak current is proportional to the concentration of species and the square root of the scan rate.

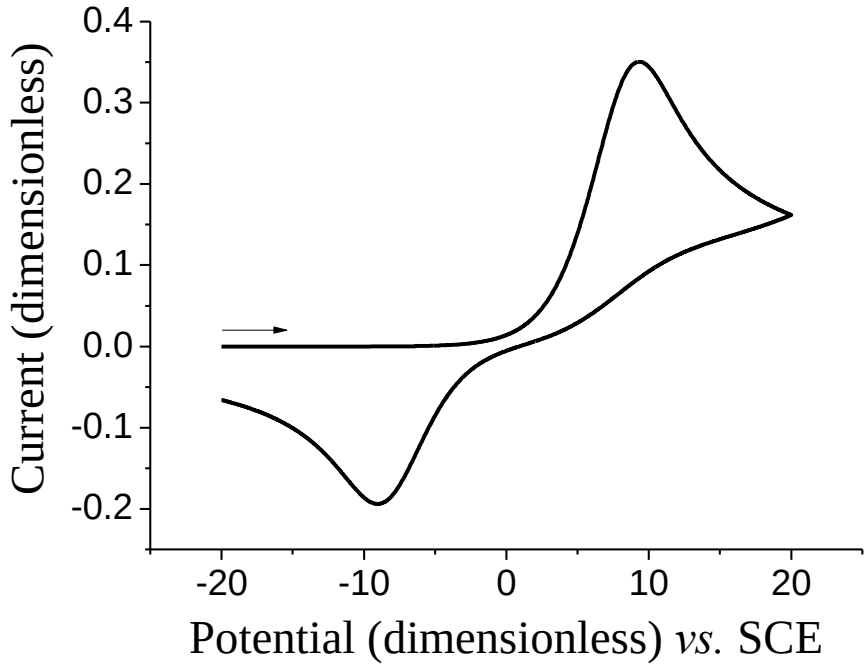

Figure 2.16 – An example of a voltammogram collected for an electrochemically irreversible electrode process performed *versus* a standard calomel reference electrode. Reproduced with permission from J D Wadhawan.

In comparison to reversible systems, irreversible systems, shown in figure 2.16, exhibit slow electron transfer. This produces characteristic peaks of reduced magnitude and increased separation away from the formal potential of the redox couple. An irreversible system will have no net flow of current at the accepted formal potential, instead it will require a large overpotential in either direction to afford an oxidation or reduction. The peak current, I_p, of an irreversible electrode process is given by a modified Randles – Sevcik equation,

$$I_p = 2.99x10^5 \alpha^{\frac{1}{2}} D^{\frac{1}{2}} C A v^{\frac{1}{2}} \quad (298\ K) \qquad 2.142$$

in which α represents the transfer coefficient. The peak current can still be observed to be proportional to the square root of the scan rate as the process is still diffusion controlled. In the case of irreversible electrode processes, the peak separation varies with the change in scan rate, known to be approximately 30 mV per decade.

$$E_{ps} = \frac{59.4}{\alpha} + constant \qquad 2.143$$

A quasi reversible system, figure 2.17, will lie in between the two discussed limits of reversibility. The recorded current in the system is controlled by both charge transfer and mass transport, allowing the waveshapes to be altered significantly by changes in the scan rate. Quick scan rates will shift the waveshape to exhibit behaviour characteristically in line with an irreversible system; whereas, slow scan rates make the process appear much more reversible.

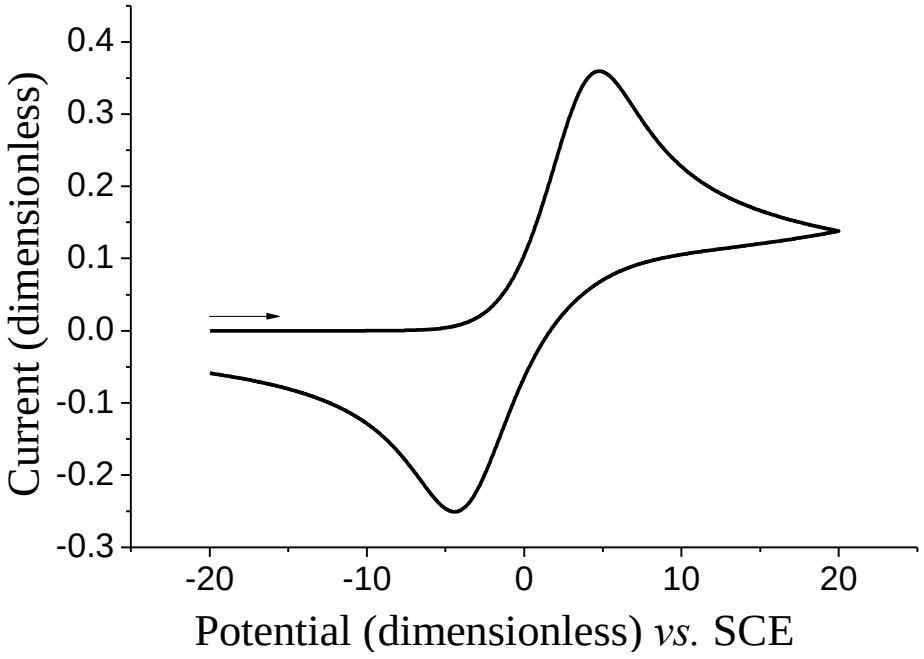

Figure 2.17 – An example of a voltammogram collected for an electrochemically quasi-reversible electrode process performed *versus* a standard calomel reference electrode. Reproduced with permission from J D Wadhawan.

2.4.3 Electrode mechanisms

When a reaction occurs at an electrode surface, there are many different types of reaction mechanisms that can occur. To describe these different processes, traditionally the Test and Reinmuth[29] notation is used; in which, an 'E' represents a heterogeneous electron transfer step and a 'C' represents a homogeneous (or chemical reaction) step.

2.4.3.1 The E electrode mechanism

The E electrode mechanism is the most simple and refers to a single heterogeneous one-electron oxidation or reduction to form a stable radical cation or anion. A classic example of this electrode reaction is for the ferrocene|ferricinium redox couple.

$$FeCp_2 - e^- \rightleftharpoons FeCp_2^+ \quad (E) \tag{2.144}$$

2.4.3.2 The EC electrode mechanism

In many cases an electron transfer will yield an unstable product, often a homogeneous chemical reaction will follow. In an EC-type reaction mechanism, the homogeneous chemical step will yield an electrochemically inactive product.

$$A - e^- \rightleftharpoons B \quad (E) \tag{2.145}$$

$$B \rightarrow C \quad (C) \tag{2.146}$$

2.4.3.3 The ECE electrode mechanism

The ECE type reaction follows a similar pattern to the EC reaction mechanism; whereby, a chemical step follows the first electron transfer step. In this scenario the product of the chemical transfer step is electrochemically active.

$$A - e^- \rightleftharpoons B \quad (E) \tag{2.147}$$

$$B \overset{k_1}{\rightarrow} C \quad (C) \tag{2.148}$$

$$C - e^- \rightleftharpoons Z \quad (E) \tag{2.149}$$

This mechanism can produce very different voltammetric responses depending on the rate constant, k_1, the scan rate employed and the thermodynamics of the two redox couples.

2.4.3.4 The DISP electrode mechanism

The DISP mechanism is extremely similar to the ECE reaction mechanism. In fact, it is often extremely difficult to differentiate between the two experimentally. The key difference between the DISP and ECE type reaction mechanisms are in the second electron transfer step. In an ECE mechanism this occurs heterogeneously at the

electrode surface; whereas, in a DISP process this occurs homogeneously in the bulk solution through a disproportionation reaction.

$$A - e^- \rightleftharpoons B \quad 2.150$$

$$B \overset{k_1}{\rightarrow} C \quad 2.151$$

$$B + C \rightleftharpoons A + Z \quad 2.152$$

There are two types of DISP reaction mechanisms, DISP1 and DISP2. The DISP1 process has equation 2.151 as the rate determining step and DISP2 process has equation 2.152 as the rate determining step.

2.4.3.5 The EC' electrode mechanism

The EC' mechanism is one of the most extensively studied electron transfer pathways.[30–32] Chapter 6 will concentrate on this electrode mechanism and therefore this section will go into much more detail than previously. It operates through and electron transfer step, equation 2.153, followed by a chemical reaction, equation 2.154, where the chemical step is a catalytic process. It differentiates from an EC type mechanism through the product of the electron transfer step, B, reacting with a species, X, to regenerate the original species, A. In this way it acts as a feedback loop for the initial electron transfer step.

$$A - e^- \rightleftharpoons B \quad (E) \quad 2.153$$

$$B + X \overset{k_{EC'}}{\longrightarrow} A + Y \quad (C') \quad 2.154$$

In this scheme, the redox couple acts as the mediator and does not undergo any reaction with the analyte; it is only oxidised and reduced by it. This is best represented by comparing cyclic voltammograms obtained from an electrochemically reversible electrochemical reaction that follows and E mechanism and an electrochemical reaction coupled with a homogeneous chemical reaction, figure 2.18.

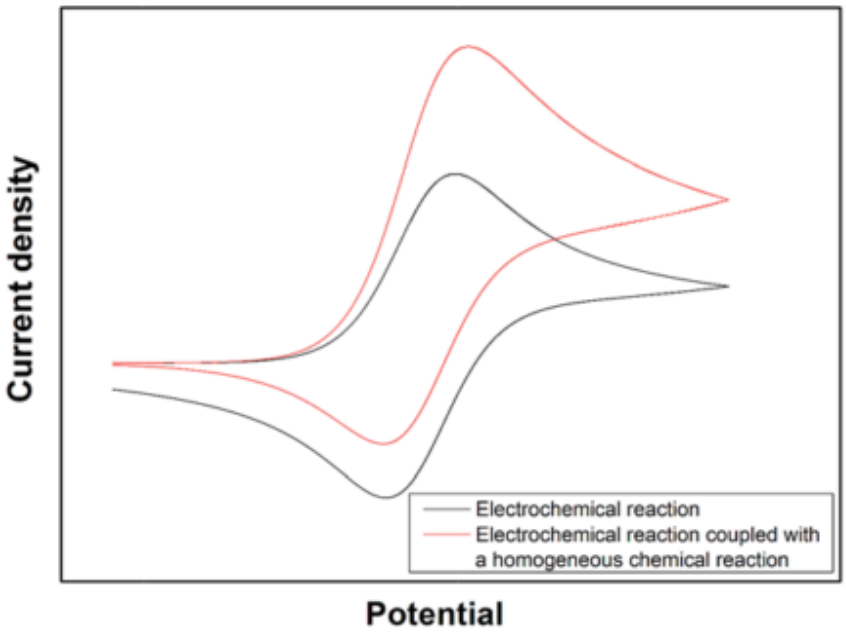

Figure 2.18 - Theoretical cyclic voltammograms obtained for an E and EC' type reaction. Reproduced from Ref. 30 with permission from The Royal Society of Chemistry.[30]

The E type reaction (figure 2.18, black line), where there is no species X present, exhibits a single, electrochemically reversible oxidative peak and the corresponding reductive peak with no chemical reaction taking place. In the EC' type reaction (figure 2.18, red line), where species X is present, the electron transfer step occurs first, hence the single oxidative peak corresponding to the conversion of A to B. Once B is formed in this system the chemical reaction step begins, where X acts as a catalyst and B is chemically converted back to A. This results in the reduced reductive current seen in figure 2.18. In this way the catalytic current that is measured is dependent on the concentration of species X in solution in addition to the rate constant, $k_{EC'}$.

The catalyst in this type of electron transfer mechanism can be looked at in terms of its essential reactivity parameters; turnover number (TON) and turnover frequency (TOF). The TON refers to the number of moles of substrate that a mole of catalyst can convert; whereas, the TOF refers to the number of turnovers per unit of time. In a system free from perturbation through side-phenomena the peak current, I_p^0, of the catalyst in the absence of substrate can be used to calibrate the catalytic response and therefore, variations in the TON, I_p/I_p^0, can be observed.[33]

The cyclic voltammetric response of an EC' type process is dependent on two parameters; the kinetic parameter, λ, and the excess factor, γ.

$$\lambda = \left(\frac{RT}{F}\right)\left(\frac{k_e C_X^0}{\nu}\right) \qquad 2.155$$

$$\gamma = \frac{C_A^0}{C_X^0} \qquad 2.156$$

In which, k_e is the rate constant of outer sphere electron transfer, $C_X{}^0$ is the bulk concentration of the catalyst, $C_A{}^0$ is the concentration of the substrate, R is the molar gas constant, T is the temperature, F is Faraday's constant and ν is the scan rate.

The cyclic voltammograms produced by an electrochemically reversible process where the electron transfer process at the electrode surface is fast and the diffusion coefficient is constant can be identified through a kinetic zone diagram, figure 2.19.[34,35]

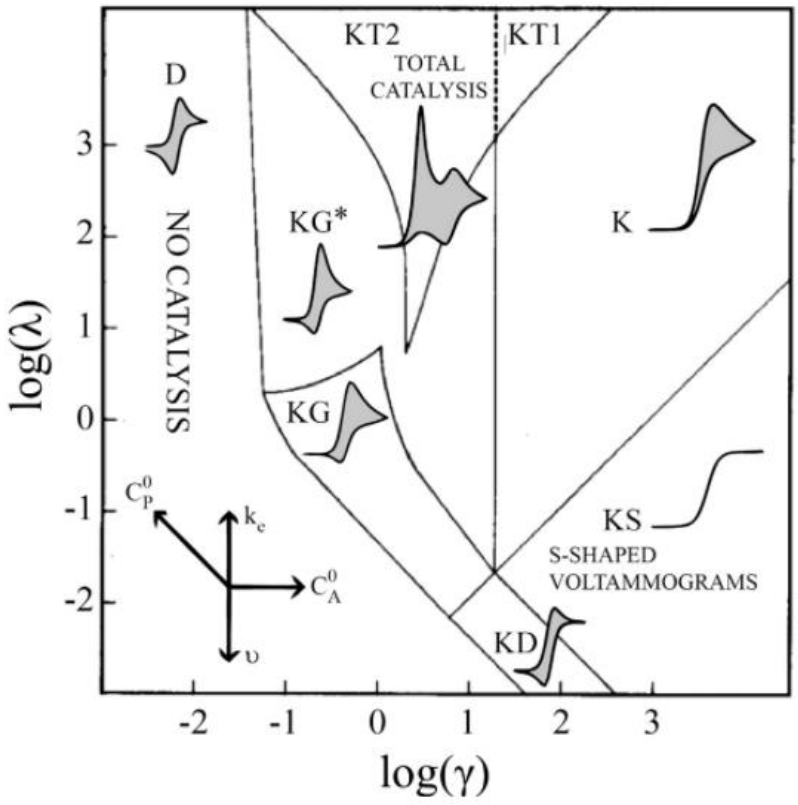

Figure 2.19 - A kinetic zone diagram and simulated waveforms for the EC' mechanism. The compass shows how catalysis moves between the different zones; where C_P^0 is the initial concentration of the catalyst, C_A^0 is the initial concentration of substrate, ν is the scan rate and k_c is the rate constant for the electron transfer between the catalyst and substrate. Reprinted with permission from reference 34. Copyright (2014) American Chemical Society.

In this scheme there are seven scenarios that can occur in an EC' mechanism. The most simple is if the D zone where no catalysis occurs. In this region the cyclic voltammetry of the electrochemically reversible redox couple is observed.

The KS zone is where there are pure kinetic conditions, no substrate is consumed and the waveshape tends to sigmoidal behaviour. In this situation the substrate concentration present at the electrode surface is equal to that of the bulk solution and the forward and reverse scans trace each other.

Zone K, is characterised by a peak shaped forward scan, the reverse scan not tracing the forward and no reverse redox wave being observed. This is caused by competition between the consumption of the substrate *via* the rate determining step and the diffusion of the substrate to the electrode surface. There is no reverse redox process observed due to the catalytic turnover despite substrate depletion.

The zone marked KT2 is characteristic of total catalysis. This is where the catalyst immediately consumes all of the substrate accessible during the timescale imposed. This happens so quickly that two peaks are observed; the first corresponding to the substrate diffusion and the second corresponding to catalyst seen in zone D. The system can move from KT2 to KT1 if there is an increase in the excess factor. This will cause the electrochemically reversible redox wave to become buried beneath the catalytic current wave.[34]

Zone KD refers to the case where there is no substrate consumption. It is similar to that of zone KS, but does not form the perfect sigmoidal shaped wave. This is due to a reduction in the kinetic parameter, λ. Catalysts will move to this zone from KS if the catalytic rate constants are slower; or the scan rate is increased.

Finally, zone KG and KG* are similar to KT2, whereby, they are limited by the diffusion of the catalyst to the electrode surface. Catalysts can move from KT2 to these zones by increasing the scan rate or by having slower catalytic rate constants.

The first thing to do is to observe the ferrocenemethanol | ferriciummethanol redox couple, the D zone, in aqueous conditions using cyclic voltammetry. Following this we will add tiopronin to the system to observe any changes in the cyclic voltammetric response.

2.4.4 *Microelectrodes*

Microelectrodes, as the name suggests, have characteristic dimensions on the micrometre scale (< 25 μm). They vary greatly from macro electrodes, which favour their use for the study of fast electrochemical processes. Due to these fast processes it

is possible to undertake experimental work in highly resistive organic solvents such as benzene and hexane.[1] In addition to this, they have a reduced capacitance, C, and consequently a faster time constant than macro electrodes. This in turn, has an influence on the scan rates,ν, that are viable to use in experimental procedures as the charging current, I_{cc}, can obscure the faradaic process under investigation.

$$I_{cc} = C\nu \tag{2.157}$$

There is also a reduction in ohmic loss (iR) for microelectrodes at steady state,

$$r_0 . \frac{1}{r_0} \propto 1 \tag{2.158}$$

where r_0 is the electrode radius. This is advantageous as it allows for systems to only use two electrodes instead of the three always required by a macro electrode set up as the combined potential of the counter and reference electrodes is on the nanoampere scale, making it highly unlikely to cause a significant difference. Microelectrodes also possess a greater signal, i_c, to noise, i_{cap}, ratio compared to macro electrodes.

$$\frac{i_c}{i_{cap}} \propto \frac{r_0}{\pi r_0^2} \tag{2.159}$$

Therefore, a reduced electrode area results in a larger ratio. Microelectrodes facilitate the investigation of fast electrode kinetics due to their non-planar diffusion. This can be observed in terms of spherical/ hemispherical or microdisc frameworks.

At a microdisc electrode, the scenario is challenging as the electrode is not uniformly accessible. We look at Fick's second law with regards to a cylinder.

$$\frac{\partial c}{\partial t} = D\frac{\partial^2 c}{\partial r^2} + \frac{D}{r}\frac{\partial c}{\partial r} + D\frac{\partial^2 c}{\partial z^2} \tag{2.160}$$

In which, D is the diffusion coefficient, r is the radius from the centre of the disc electrode and z is the perpendicular distance from the electrode surface. This was solved, with approximations, by Shoup and Szabo for the following boundary conditions.[36]

$$t < 0, all\ r, z, C = C^* \tag{2.161}$$

$$t \geq 0, z = 0, r < r_e, C = 0$$

$$t \geq 0, z \to \infty, all\ r, C = C^*$$

$$t \geq 0, r \to \infty, all\ z, C = C^*$$

The diffusion layer thickness expands, increasing its surface area. This introduces more electroactive species to maintain the concentration gradient and therefore feeds the electrode with more reagent. This framework produces convergent diffusion which is approximate to a hemisphere, figure 2.20. A transient response is observed at long time limits which produces a steady state current response, I,

$$I = 4nFC^{*}Dr_{e} \qquad 2.162$$

where n is the number of electrons associated, F is Faraday's constant and r_e is the electrode radius. With a corresponding flux,

$$j = \frac{2}{\pi}\frac{C^{*}D}{\sqrt{r_e^2 - r^2}} \qquad 2.163$$

this implies an infinite flux at the disc edges, in reality this is limited by the kinetics. The steady state current however is dominated by that flowing at the edge of the disc. At shorter timescales, the diffusion is not convergent but effectively planar with a thin diffusion layer atop the electrode surface, figure 2.20. The timescale upon which case happens is a balance between a Cotrellian term and a steady state term, resulting in a scenario where there smaller the electrode area, the shorter the experimental times required to reach a steady state. This steady state framework means that current does not decay to zero as predicted by the Cottrell equation but rather reaches a maximum and maintains it.

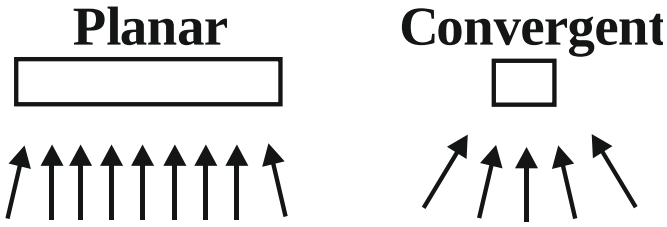

Figure 2.20 – Pictorial representation of the difference in diffusion to an electrode depending on its size. Macro electrodes are dominated by planar diffusion whereas, microelectrodes trend towards convergent diffusion.

If we consider cyclic voltammetry corresponding to a simple oxidation.

$$A - e^{-} \rightleftharpoons B \qquad 2.164$$

Two diffusion equations must be solved,

$$\frac{\partial[A]}{\partial t} = D_A\left(\frac{\partial^2[A]}{\partial r^2} + \frac{1}{r}\frac{\partial[A]}{\partial r} + \frac{\partial^2[A]}{\partial z^2}\right) \quad 2.165$$

$$\frac{\partial[B]}{\partial t} = D_B\left(\frac{\partial^2[B]}{\partial r^2} + \frac{1}{r}\frac{\partial[B]}{\partial r} + \frac{\partial^2[B]}{\partial z^2}\right) \quad 2.166$$

in alignment with the following boundary conditions,

$$0 < t < t_{switch}, E = E_1 + \nu t \quad 2.167$$
$$t_{switch} < t, E = E_1 + \nu t_{switch} - \nu(t - t_{switch})$$
$$t_{switch} < t, = E_1 + 2\nu t_{switch} - \nu t$$

which describe the triangular potential sweep that is applied to the working electrode in the system.

$$all\ t, z = 0, 0 < r < r_e, D_A\frac{\partial[A]}{\partial t} = -D_B\frac{\partial[B]}{\partial t} \quad 2.168$$
$$= k_a[A]_0 - k_c[B]_0$$

That describe the rate of interfacial reaction, governed by Butler-Volmer kinetics, alongside the loss of A and generation of B at the electrode surface.

$$t \leq 0, all\ r, all\ z, [A] = [A]_{bullk}, [B] = 0 \quad 2.169$$
$$all\ t, r, z \to \infty, [A] = [A]_{bullk}, [B] = 0$$

Which describe the initial concentrations of species.

It is observed in cyclic voltammetry that large microelectrodes can produce similar wave shapes to planar macro electrodes. Smaller microelectrodes tend towards a sigmoidal plot, figure 2.21.

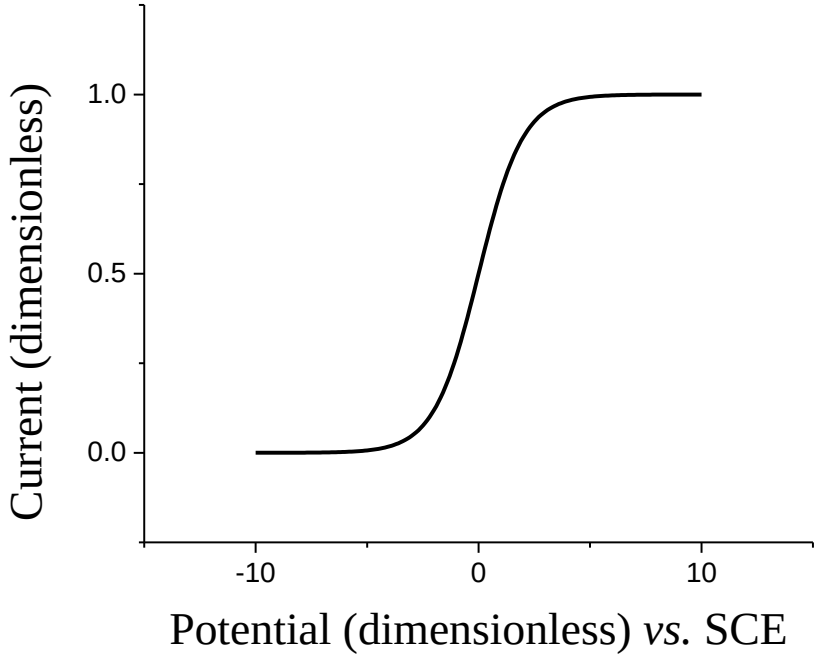

Figure 2.21 – An example of the sigmoidal shape expected in a voltammogram when a smaller microelectrode is used for voltammetry.

If the time required to reach steady state is small in comparison to the time taken for the acquisition of the voltammogram this steady state behaviour will be seen.

$$\frac{r_e^2}{D} \ll \frac{RT}{F\nu} \tag{2.170}$$

Hence, if we introduce a new parameter, P, we can predict the voltammogram behaviour.

$$P = \sqrt{\frac{Fr_e^2\nu}{RTD}} \tag{2.171}$$

When this parameter is below unity, steady state behaviour is expected above unity is referred to as the limit of cyclic voltammetry. In this framework the peak current is,

$$I_P = 4Fr_e[A]_{bulk}\left[0.34e^{-0.66P} + 0.66 - 0.13e^{-\frac{11}{P}} + 0.351P\right] \tag{2.172}$$

With limits for steady state and the cyclic voltammetry limit respectively.

$$P \to 0 = I_P \to 4Fr_e[A]_{bulk} \tag{2.173}$$
$$P \to \infty = I_P = 1.4Fr_e[A]_{bulk}P$$

If we run an experiment at a sufficiently low scan rate, we can analyse steady state behaviour. This can be used to elucidate information about the kinetics and requires the mass transport coefficient to be large in comparison with the standard electrochemical rate constant.

$$m_T \sim \frac{D}{r_e} \gg k^0 \qquad 2.174$$

Oldham and Zoski[37] produced work, which was built on by Aoki[38] to summarize the shape of voltammograms when the species diffusion coefficients are of an equal value.

$$\frac{I}{I_{lim}}(1 + \exp(\pm\varsigma) = \frac{\lambda}{\left(\lambda + \left(\frac{2\lambda + 12}{\lambda + 3\pi}\right)\right)} \qquad 2.175$$

in which,

$$\varsigma = \frac{F}{RT}(E - E_f^0) \qquad 2.176$$

$$\lambda = \frac{k^0 r_e}{D}\left(e^{-\alpha\xi} + e^{\beta\xi}\right) \qquad 2.177$$

In addition to this, Mirkin and Bard[39] produced a method of extracting kinetic data from quasi-reversible voltammograms, such as k^0, α and E_f^0 from the easily accessible experimental parameters of $\Delta E_{1/4}$ and $\Delta E_{3/4}$.

2.4.5 *Square wave voltammetry*

Square wave voltammetry initially originated from the Kalousek commutator and Barker's square wave polarography, followed by important innovations by Barker and Jenkins in 1952.[40] The waveform is comprised of a square wave superimposed of time, t_s, on a staircase wave of the same time, t_s, and height, ΔE_s, figure 2.22. This produces a combined staircase and square wave with amplitude, ΔE_p. In this system the currents present at the end (typically the last 280 μs) of the forward, I_F, and reverse, I_B, waves are measured. These two readings are compiled, ΔI, as a function of this staircase potential to produce the overall square wave voltammograms as the primary result, figure 2.23.

$$\Delta I = I_F - I_B \qquad 2.178$$

This minimized the influence of capacitative currents to the system and allowed for the discrimination between current and faradaic current.

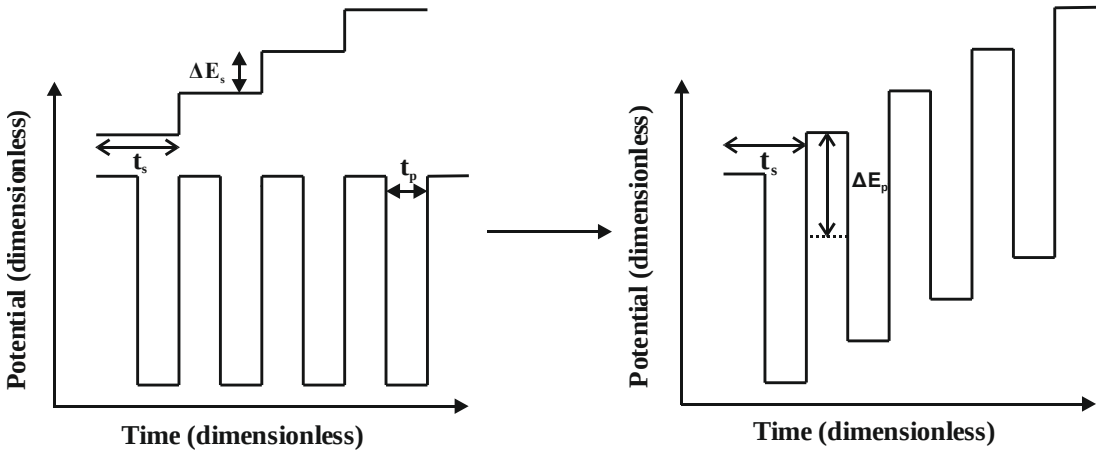

Figure 2.22 – A pictorial representation of the square wave and staircase that superimpose to make the waveform used in square wave voltammetry.

This technique is often chosen for analytical studies because of the high sensitivity of the system.[1] The detection limit can be as low as 10^{-8} M, which is at least an order of magnitude better than similar pulse techniques, with short pulses and high scan rates; this gives a short experimental time. Additionally, only small amounts of electro-active species are actually consumed in each scan, this leads to a much smaller probability of electrode blocking compared to other similar techniques.

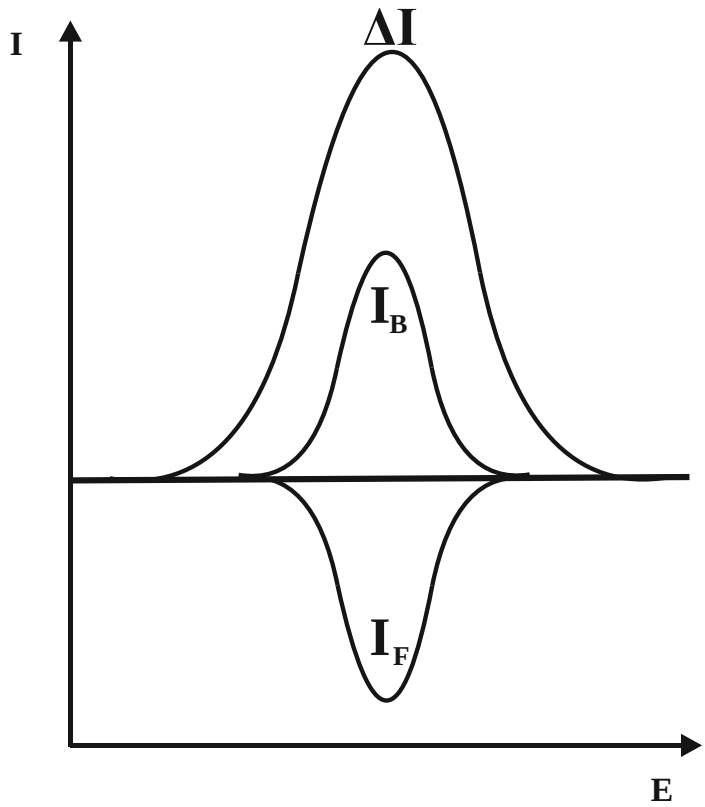

Figure 2.23 – A representation of the three voltammograms obtained during a square wave experiment. The forward scan, I_F, backward scan, I_B, and the overall primary result, ΔI.

2.4.6 *Rotating disc voltammetry*

A rotating disc electrode is a type of hydrodynamic electrode. These work by increasing the transport of electroactive species to the electrode via forced convection; this creates a thin layer of solution next to the electrode where all concentration gradients occur and only diffusion occurs. Using hydrodynamic electrodes and forced convection leads to higher currents, as well as greater sensitivity and reproducibility. Typically, a rotating disc electrode is produced from an insulating sheath surrounding typical working electrode materials; for example platinum, gold and glassy carbon. When the electrode is rotated, typically with rotation speed 0 – 50 Hz, a regular laminar flow pattern is established in the vicinity. The electrode pulls solution vertically towards itself and then removes it, as shown in figure 2.24.

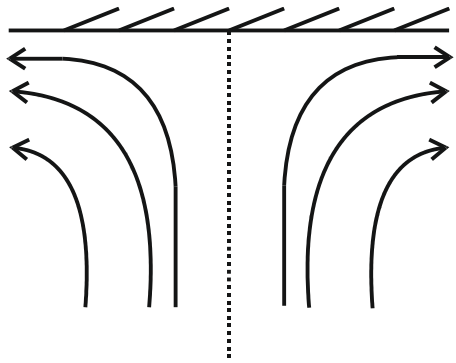

Figure 2.24 - A schematic of the flow caused by the rotation of a disc working electrode.

This laminar flow is maintained, for a rotating disc electrode, only if the Reynolds number, R_e, does not exceed its critical value, ~ 2 x 10^3,

$$R_e = \frac{\omega r^2}{\nu} \qquad 2.179$$

where ω is the rotation velocity (Hz), r is the rotating disc radius (m) and ν is the kinematic viscosity ($m^2\ s^{-1}$). Exceeding this value of Reynolds number can lead to the laminar flow changing to transitional or turbulent flow, as shown in figure 2.25.

Figure 2.25 - Schematics showing the variations between laminar, transitional and turbulent flow in hydrodynamic systems.

The most integral parameter of the rotating disc electrode is the limiting current, I_L, the equation for which differs between hydrodynamic electrodes, is given by the equation,

$$I_L = 1.554\pi r^2 nFc_\infty D^{2/3}\nu^{-1/6}\omega^{1/2} \qquad 2.180$$

where ω corresponds to the rotation velocity (Hz), ν is the kinematic viscosity ($m^2\ s^{-1}$), r is the electrode radius (m), c is the bulk concentration and D is the diffusion coefficient. The current in the system is directly proportional to the electrode area corresponding to a uniformly accessible area. In experimental practice the rotation

velocity of the electrode is varied and the limiting current recorded for each speed individually. From this data, the diffusion coefficient of the forced convection system can be calculated by utilising a Levich plot. This is a plot of the limiting current (A) versus the rotation speed (Hz).

Using the research and electrochemical theory covered in the first two chapters of this work, we will aim to design and produce an online, low-cost, downhole electrochemical sensor for the determination of alkaline-earth metals in formation water.

2.5 References

1 R. G. Compton and C. E. Banks, *Understanding Voltammetry*, Imperial College Press, London, 2nd edn., 2011.

2 P. Debye and E. Huckel, *Phys. Z*, 1923, **24**, 185.

3 P. Debye and E. Huckel, *Phys. Z*, 1923, **24**, 305.

4 N. Bjerrum, *Kgl. Danske Vidensk. Selsk. Mat-Fys. Medd.*

5 R. H. Stokes and R. A. Robinson, *J. Am. Chem. Soc.*, 1948, **70**, 1870.

6 R. A. Robinson and R. H. Stokes, *Electrolyte solutions*, Butterworths, London, 2nd edn., 1965.

7 G. Milazzo, S. Caroli and V. K. Sharma, *Tables of Standard Electrode Potentials*, Wiley, Chichester, 1978.

8 A. J. Bard, R. Parsons and J. Jordan, *Standard Potentials in Aqueous Solutions*, Marcel Dekker, New York, 1985.

9 S. G. Bratsch, *J. Phys. Chem. Ref. Data*, 1989, **18**, 1–21.

10 A. J. Bard and L. R. Faulkner, *Electrochemical methods : fundamentals and applications*, Wiley, 2001.

11 S. Trasatti and R. Parsons, *Pure Appl. Chem.*, 1983, **55**, 1251–1268.

12 I. Mills, T. Cvitas, K. Homann, N. Kallay and K. Kuchitsu, *Quantities, Units and Symbols in Physical Chemistry*, Blackwell Science Ltd., Oxford, 2nd edn., 1993.

13 H. Helmholtz, *Ann. der Phys. und Chemie*, 1853, **165**, 353–377.

14 M. Gouy, *J. Phys. Théorique Appliquée*, 1910, **9**, 457–468.

15 D. L. Chapman, *Philos. Mag. Ser. 6*, 1913, **25**, 475–481.

16 O. Stern, *Zeitschrift für Elektrochemie und Angew. Phys. Chemie*, 1924, **30**, 508–516.

17 D. C. Grahame, *Chem. Rev.*, 1947, **41**, 441–501.

18 J. O. Bockris, M. A. V. Devanathan and K. Muller, *Proc. R. Soc. A Math. Phys. Eng. Sci.*, 1963, **274**, 55–79.

19 J. E. Halls, A. Hawthornthwaite, R. J. Hepworth, N. A. Roberts, K. J. Wright, Y. Zhou, S. J. Haswell, S. K. Haywood, S. M. Kelly, N. S. Lawrence and J. D. Wadhawan, *Energy Environ. Sci.*, 2013, **6**, 1026.

20 R. Parsons, *Trans. Faraday Soc.*, 1958, **54**, 1053.

21 P. Quaino, F. Juarez, E. Santos and W. Schmickler, *Beilstein J. Nanotechnol.*, 2014, **5**, 846–54.

22 S. Trasatti, *J. Electroanal. Chem.*, 1972, **39**, 163.

23 R. A. Marcus, *J. Chem. Phys.*, 1956, **24**, 966.

24 R. A. Marcus, *J. Chem. Phys.*, 1965, **43**, 679.

25 N. S. Hush, *J. Chem. Phys.*, 1958, **28**, 962–972.

26 W. F. Libby, *J. Phys. Chem.*, 1952, **56**, 863–868.

27 C. M. A. Brett and A. M. O. Brett, *Electrochemistry: Principles, Methods, and Applications*, Oxford University Press, 1993.

28 H. Matsuda and Y. Ayabe, *Elektrochem*, 1955, **59**, 494–503.

29 A. C. Testa and W. H. Reinmuth, *Anal. Chem.*, 1961, **33**, 1320–1324.

30 P. Song, A. C. Fisher, J. D. Wadhawan, J. J. Cooper, H. J. Ward and N. S. Lawrence, *RSC Adv.*, 2016, **6**, 70237–70242.

31 K. R. Ward, N. S. Lawrence, R. S. Hartshorne and R. G. Compton, *J. Phys. Chem. C*, 2011, **115**, 11204–11215.

32 K. Harriman, D. J. Gavaghan, P. Houston and E. Süli, *Electrochem. Commun.*, 2000, **2**, 163–170.

33 C. Costentin, S. Drouet, M. Robert and J.-M. Savéant, *J. Am. Chem. Soc.*, 2012, **134**, 11235–11242.

34 J.-M. Saveant and K. B. Su, *J. Electroanal. Chem.*, 1984, **171**, 341–349.

35 E. S. Rountree, B. D. McCarthy, T. T. Eisenhart and J. L. Dempsey, *Inorg. Chem.*, 2014, **53**, 9983–10002.

36 D. Shoup and A. Szabo, *J. Electroanal. Chem.*, 1982, **140**, 237–245.

37 K. B. Oldham and C. G. Zoski, *J. Electroanal. Chem. Interfacial Electrochem.*, 1991, **313**, 17–28.

38 K. Aoki, *Electroanalysis*, 1993, **5**, 627–639.

39 M. V. Mirkin and A. J. Bard, *Anal. Chem.*, 1992, **64**, 2293–2302.

40 G. C. Barker and I. L. Jenkins, *Analyst*, 1952, **77**, 685.

3 Experimental Procedures

This chapter outlines the key experimental methods utilised in this thesis; including details of the equipment required to carry out the experiments. In addition to this it notes all of the chemicals used throughout the work, detailing their purity and company of production.

3.1 Electrochemical set up

3.1.1 Potentiostat

Electrochemical measurements throughout were performed on a Metrohm Autolab B.V. μ-Autolab type-III potentiostat, Netherlands. This was controlled by General Purpose Electrochemical System (GPES, Metrohm) software installed on a Viglen Genie desktop PC installed with Windows Vista™.

3.1.2 Electrodes

Electrochemical experiments were all performed using a standard three-electrode set up, unless otherwise stated, consisting of a working electrode, reference electrode and auxiliary (counter) electrode. These were connected to the potentiostat and placed in the solution under investigation inside a custom glass cell, figure 3.1.

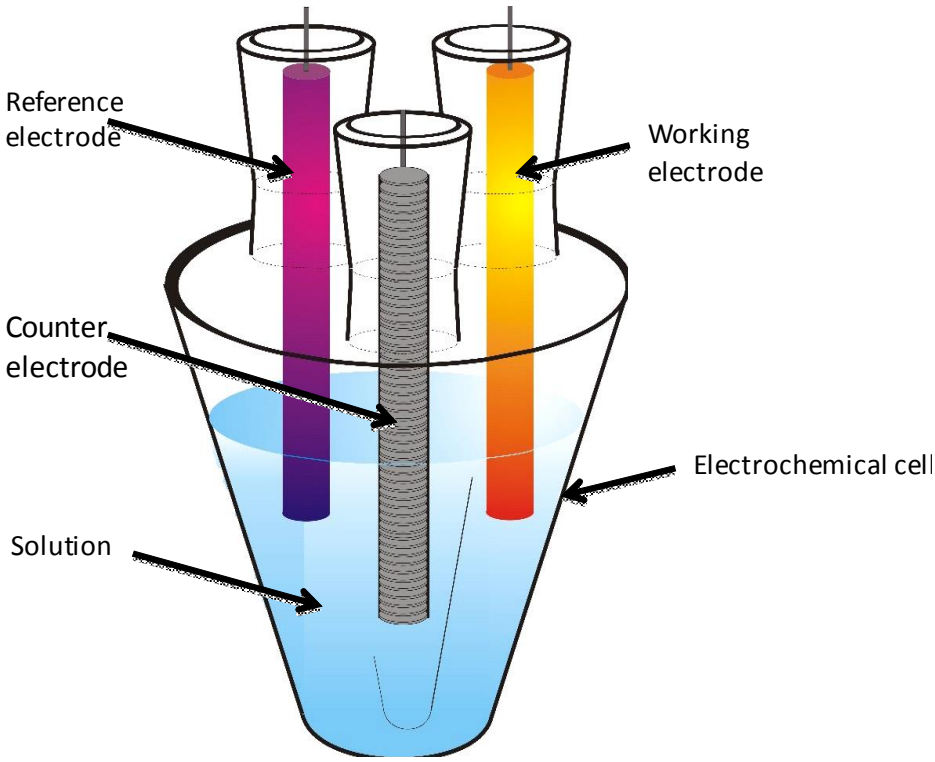

Figure 3.1 - A pictorial representation of a typical three-electrode electrochemical system in a three-necked glass cell. Reproduced with permission from J D Wadhawan.

3.1.2.1 Working Electrodes

Multiple working electrodes were used in this thesis composing of two materials; glassy carbon and gold. Two glassy carbon working electrodes were used, a macro (3 mm, BAS) and a micro (11 μm, BAS). Five gold working electrodes were used, one macro (3 mm, BAS) and four micro (12.5 μm, 25 μm, 33μm and 50 μm).

Before electrochemical experiments, working electrodes were polished using various grades of carburundum paper (P400, P1200, P2400, P4000, Presi, France) and then finished with alumina slurry (0.3 μm, Presi, France) on a wetted polishing cloth. The microelectrode was dipped in 10 % nitric acid solution before being polished using the alumina slurry and polishing cloth.

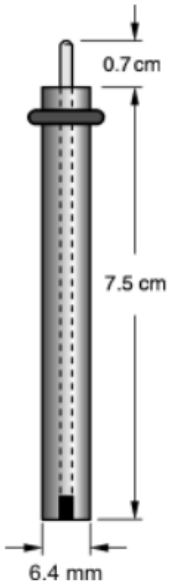

Figure 3.2 – A schematic illustration of a glassy carbon or gold working electrode.[1]

3.1.2.2 Reference Electrodes

One standard silver | silver chloride (BAS) reference electrode was utilised for electrochemical measurements in aqueous media. Where this reference was not appropriate, a silver wire quasi reference was used.

3.1.2.3 Auxiliary (counter) Electrodes

A graphite auxiliary electrode was used throughout this work.

3.1.3 Solution preparation

Solutions were prepared at 298.15 ± 1 K (unless otherwise stated) and purged of oxygen prior to use with an inert gas; nitrogen or argon (BOC Gases, UK). Solutions under electrochemical investigation were placed inside a Faraday cage to reduce interference from the surroundings.

3.2 Chemicals

3.2.1 Chemical Compounds

Table 3.1 – A table of the chemical compounds used in this thesis; alongside their purities (if known) and the supplier from which they were obtained.

Name (Formula)	Purity / %	Supplier
Chlorquinaldol ($C_{10}H_7Cl_2NO$)	98	Sigma Aldrich
Broquinaldol ($C_{10}H_7Br_2NO$)	-	Schlumberger
Tetrabutylammonium perchlorate ($C_{16}H_{36}ClNO_4$)	≥ 99.0	Sigma Aldrich
	≥ 97.0	Sigma Aldrich
Tetrabutylammonium chloride ($C_{16}H_{36}ClN$)	98	Sigma Aldrich
Tetrabutylammonium nitrate ($C_{16}H_{36}N_2O_3$)	97	Avocado Research
Ferrocene ($C_{10}H_{10}Fe$)	> 95	TCI
Hydroxymethyl ferrocene ($C_{11}H_{12}FeO$)	> 96.0	TCI
Tiopronin ($C_5H_9NO_3S$)	100.04	Fisher Scientific
Boric acid (H_3BO_3)	99.89	Fisher Scientific
Ammonium chloride (NH_4Cl)	99.5	Fisher Scientific
Potassium chloride (KCl)	86.8	Fisher Scientific
Potassium hydroxide (KOH)	> 90.0	TCI
Disodium rhodizonate ($C_6Na_2O_6$)	≥ 99.5	Fisher Scientific
Sodium chloride (NaCl)	98.0 - 102.0	Sigma Aldrich
Magnesium nitrate hexahydrate ($Mg(NO_3)_2.6H_2O$)		
Calcium nitrate tetrahydrate ($Ca(NO_3)_2.4H_2O$)	99 - 103	Sigma Aldrich
Strontium nitrate ($Sr(NO_3)_2$)	≥ 99.0	Sigma Aldrich
Barium nitrate ($Ba(NO_3)_2$)	≥ 99.0	Fluka
Lanthanum nitrate ($La(NO_3)_3$)	≥ 99	Hopkin & Williams
Silver nitrate ($AgNO_3$)	99.9	Fisher Scientific
Potassium nitrate (KNO_3)	99.5	BDH - AnalaR
Magnesium chloride hexahydrate ($MgCl_2.6H_2O$)	99 - 102	Prime Chemicals
Calcium chloride ($CaCl_2$)	-	BDH - AnalaR
Strontium chloride ($SrCl_2$)	99	Fluka
Barium chloride dihydrate ($BaCl_2.2H_2O$)	> 99	

3.2.2 Solvents

Table 3.2 – A table containing the solvents used throughout this thesis; alongside their purities (if known) and the supplier from which they were purchased.

Name (Formula)	Purity / %	Supplier
Acetonitrile (C_2H_3N)	> 99	Fischer Scientific UK
Dimethyl sulfoxide (C_2H_6OS)	99 +	Alfa Aesar
Water (H_2O)	-	ElgaStat
Nitric Acid (HNO_3)	70	Fischer Scientific UK
Hydrochloric Acid (HCl)	-	Fischer Scientific UK

3.3 Ferrocene sublimation

Electrochemical investigation of ferrocene occasionally produced a split peak due to impurities in the ferrocene used. To overcome this, the ferrocene was purified via sublimation on a hotplate (Stuart heat-stir CB162) at 100 °C in a crystallising dish, figure 3.2. The purified ferrocene crystals were collected from the lid of the dish and used accordingly.

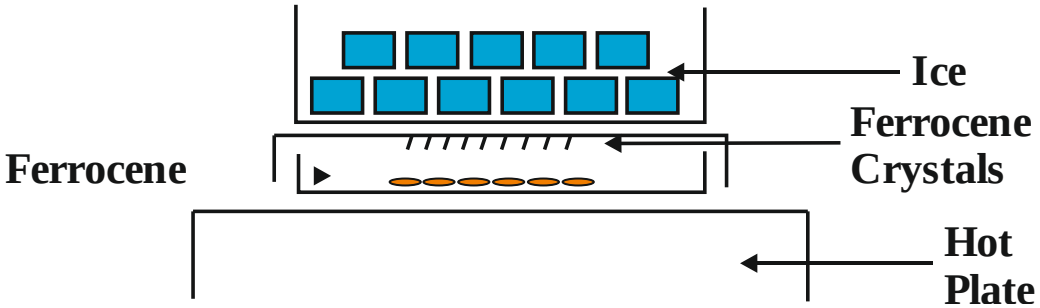

Figure 3.2 - Experimental set up for the purification of ferrocene *via* sublimation.

3.4 Solution pH alteration

The pH of solutions was determined using Hydrus 300 pH meter (Fisher, UK) connected to a pH probe (Jenway). Solutions were placed in a beaker on a magnetic stirrer plate (stuart heat-stir CB162). They were adjusted to the desired pH using either hydrochloric acid (Fisher, UK) or potassium hydroxide (Fisher, UK).

3.5 Rotating Disc Electrode

A glassy carbon electrode (3 mm, BAS) was utilised in conjunction with an external motor (Metrohm). Linear sweep voltammetry ($\nu = 5$ mV s^{-1}) was then performed with this working electrode rotating at various frequencies (500 – 3000 rpm). The obtained limiting currents were used to produce a Levich plot to elucidate the diffusion coefficient of the system under investigation.

3.6 Temperature Control

A water bath and circulator (Grant – Type RI) was connected to a custom four-necked, two compartment, electrochemical cell. The water was heated to a specific temperature (± 0.1 K) and then circulated through the outer compartment to maintain the solution under investigation at the desired temperature.

3.7 Interference Testing of Sodium Rhodizonate

Sodium rhodizonate (4 mM) solutions were prepared with boric acid (0.1 M) and a specific concentration of either strontium nitrate (1 – 8 mM), calcium nitrate (20 – 200 mM) or magnesium nitrate (4 – 80 mM). The solutions were then adjusted to pH 7. Sequential additions of barium nitrate stock solutions (10 mM and 100 mM) were then added and square wave voltammetry performed using a gold working electrode (3 mm, BAS), silver | silver chloride reference electrode (BAS) and graphite counter electrode.

3.8 UV – Vis

UV-Vis spectra were obtained using a Perkin Elmer Lambda Bio-10 UV-Vis spectrometer controlled by UV Winlab v.6.0.4 software. The solutions of known concentration were prepared and analysed spectrophotometrically over the wavelength range of 250 - 700 nm. This was performed using a quartz cuvette with a 1 cm path length and 1 cm^3 volume.

3.9 Ostwald Viscometer

An Ostwald viscometer or U – tube viscometer, figure 3.3, is used to measure the viscosity of a liquid. It achieves this through measuring the time taken for a liquid to flow between the upper mark and the lower mark. The viscosities can then be calculated in regards to a reference liquid with a known viscosity at a specific temperature *i.e.* water at 298 K.

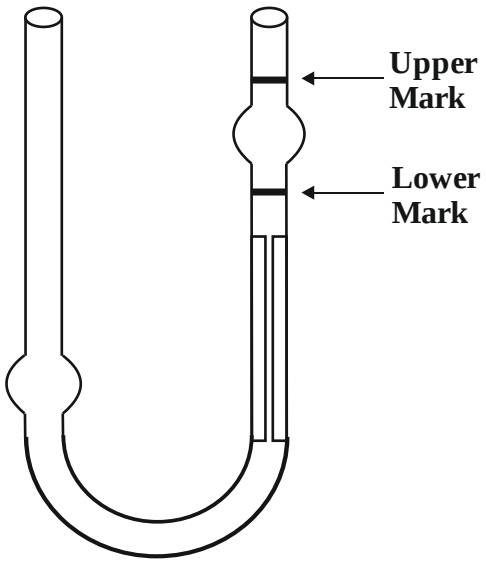

Figure 3.3 - A pictorial representation of an Ostwald viscometer showing the two marks in which the solution movement is timed.

3.10 References

1 BASi Working Electrode, *https://www.basinc.com/products/MF-2070*. (accessed 09/01/2018)

4 The unsuitability of ferrocene as an internal standard

The desired application of this thesis is to produce a sensor capable of detecting alkaline-earth metal ions in down-hole aqueous environments. To achieve this, the primary focus will be on the sensing chemistry involved. Chapter 1 outlined some of the methods used to achieve the detection of alkaline-earth metals in other conditions. These processes primarily used the complexation of a ligand and the target ion as a means of detection. This thesis will seek to measure the complexation that occurs in a system through changes in the measured voltammetric peak potentials or currents. Chlorquinaldol will be the first molecule focussed on for the application of sensing chemistry. It is not soluble in aqueous conditions; consequently, either a non-aqueous solvent or a mixture of solvents is required. It is paramount that a reliable way to record redox potentials in non-aqueous environments is used. In solvents such as this an internal reference is commonly applied, in line with IUPAC reccomendations.[1,2] This chapter seeks to test the reliability of the recommended internal redox couple ferrocene | ferricinium for the measurement of potential shifts.

4.1 Introduction

A variety of reference electrodes are commercially available for use in aqueous solvents; such as the calomel, silver | silver chloride and standard hydrogen electrodes. These systems are not suitable for use in a non-aqueous environment.[3] The search for a reliable way to study the electrochemical response of compounds in non-aqueous environments produced the internal standard, or reference redox system. The aim of internal standards was to produce a reversible stable, chemically and electrochemically, reliable and reproducible redox couple; against which to measure the electroactive redox couple of interest. One of the first proposed redox couples was based around rubidium; namely the Rb^+ | Rb and Rb^+ | Rb(Hg) couples.[4] This was based on the assumption of the large ionic radius would negate any solvation effects, which was not the case. Later, a comprehensive collection of requirements that organometallic redox reference systems should adhere to was produced.[5]

The ferrocene | ferricinium redox couple, figure 4.1, is the archetypal internal standard for electrochemical systems and is IUPAC recommended alongside the bis(biphenyl)chromium(0) | bis(biphenyl)chromium(I) couple.[1,2]

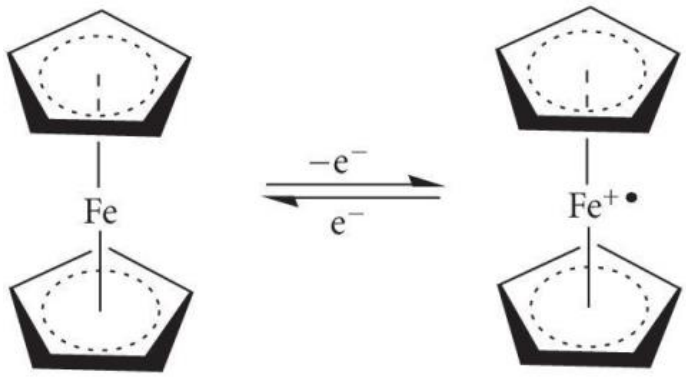

Figure 4.1 - The ferrocene | ferricinium redox couple.

Ferrocene and its derivatives have been utilised in systems for the detection of anions and cations.[6–8] They have been shown to detect the presence of Cu^{2+}, Zn^{2+}, Ca^{2+} and Mg^{2+} among others using a shift in the measured electrochemical peak potentials.[9–17] Much of the work using ferrocene concentrates solely on the peak potentials, ignoring variations in the measured peak current that occur; especially in the case of chloride ions.[18–22] In addition, inconsistencies in the recorded potentials have been reported for the ferrocene redox couple when used to determine molecular orbital levels.[23] This has been reported as a common problem in general electrochemical practice, especially in acetonitrile; whereby, the recorded potential values are subject to environmental factors.[24]

This chapter looks to characterise the use of the ferrocene | ferricinium redox couple as an internal standard in an equimolar mixture of dimethyl sulfoxide and water. This will be accomplished by mixing various amounts of alkali and alkaline-earth metal chlorides to the solutions of ferrocene and observing any changes in the cyclic voltammetric response at macro and microelectrodes.

4.2 Results and discussion

The cyclic voltammetric response of ferrocene (1 mM) with tetrabutylammonium perchlorate (TBAP, 0.1 M) in a dimethyl sulfoxide and water mix (80: 20) was probed using cyclic voltammetry at a glassy carbon electrode (3 mm) with a graphite auxiliary electrode and silver wire quasi-reference electrode. The ferrocene was sublimed prior to any experiments to purify it. The solutions in these experiments were not degassed prior to electrochemical measurements being taken. The cyclic voltammograms obtained at various scan rates (ν, 0.02 – 0.5 V s^{-1}) are presented in figure 4.2.

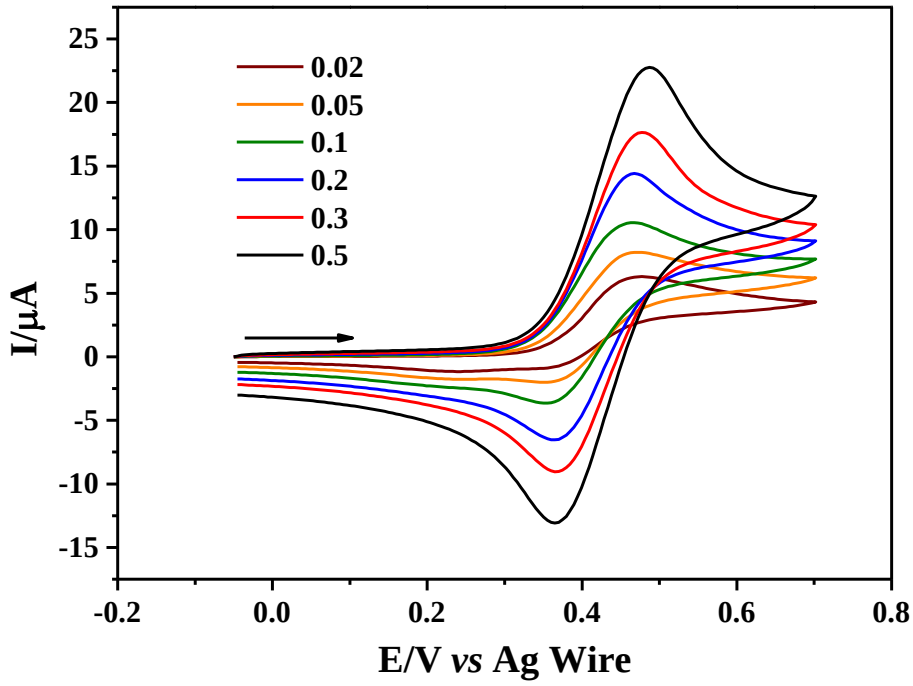

Figure 4.2 - Cyclic voltammograms obtained for ferrocene (1 mM) with TBAP (0.1 M) in DMSO/H_2O (80:20) at various scan rates (0.02 – 0.5 V s^{-1}). Performed at a glassy carbon working electrode (3 mm, BASi), with a graphite counter electrode and silver wire quasi reference electrode at 293.15 ± 1 K.

After the reduction peak in the voltammograms a small peak is observed. This is proposed to be due to the solution not being degassed prior to the experiment. It is expected to be the oxygen reacting with the formed ferricinium cation.[25,26]

$$Fc^+ + O_2 \rightarrow Fc + O_2^{-\cdot} \qquad 4.1$$

A single oxidation and reduction peak were observed for the ferrocene | ferricinium redox couple with an E_{mid} = 0.419 ± 0.004 V *versus* a Ag wire quasi reference electrode. The plot of peak potential against the log of the scan rate, figure 4.3 (left), shows stable oxidation and reduction peak potentials at low scan rates (< 100 mV/s). This has a peak-to-peak separation of ΔE = 103 mV trending up to ΔE = 122 mV at 500 mV/s indicating the electron transfer process is quasi - reversible in nature. The plot of peak current against the square of the scan rate, figure 4.3 (right), does not pass through the origin and is slightly curved indicating it is not a solely E process.

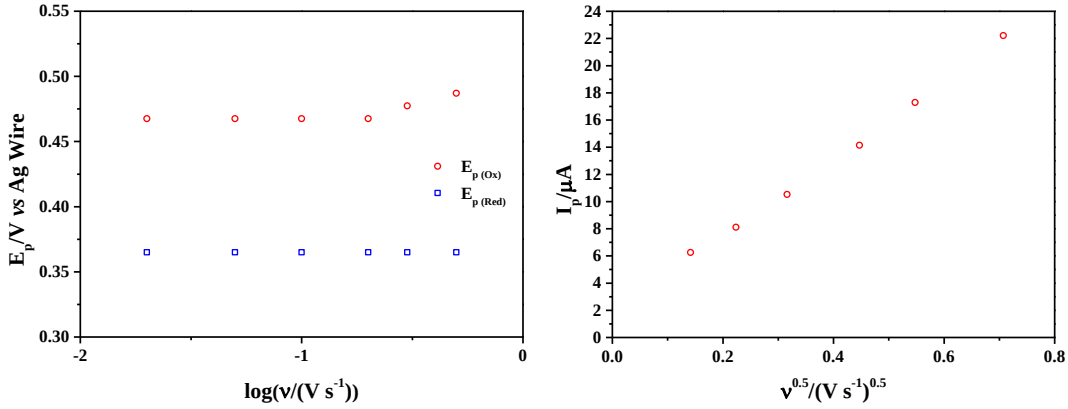

Figure 4.3 - Plot of peak potential, E_p, versus the log of the scan rate (left) and peak current, I_p, versus the square root of the scan rate (right) for ferrocene (1 mM) with TBAP (0.1 M) in DMSO/H_2O (80:20). Performed at a glassy carbon working electrode (3 mm, BASi), with a graphite counter electrode and silver wire quasi reference electrode at 293.15 ± 1 K.

The Randles-Ševčík plot, figure 4.3 (right), allowed for the elucidation of the experimental diffusion coefficient, D_{exp}, for ferrocene in this medium. Using the generated gradient through the origin a calculated D_{exp} of 2.3 ± 0.3 × 10^{-10} m^2 s^{-1} was obtained; which is consistent with literature values.[27]

The overall aim of this research is to produce a novel sensing method for alkaline-earth metal cations found in formation water. In light of this, alkaline-earth metal chlorides were introduced into the system to observe the reliability of the reference redox system in the presence of these compounds. As ferrocene should not interact with these molecules, it was expected that no change in the voltammetric behaviour would be observed.

Sequential, exponential concentrations (1 µM – 10 mM) of alkaline-earth metal chlorides ($MgCl_2$, $CaCl_2$, $SrCl_2$ and $BaCl_2$) were added to solutions of ferrocene (1 mM) with TBAP (0.1 M) in DMSO/H_2O (80:20). Cyclic voltammograms ($\nu = 0.1$ V s^{-1}) obtained for each of these additions are presented in figure 4.4. A peak following the reduction peak on the reverse scan is still present due to the solutions not being degassed prior to electrochemical measurements.

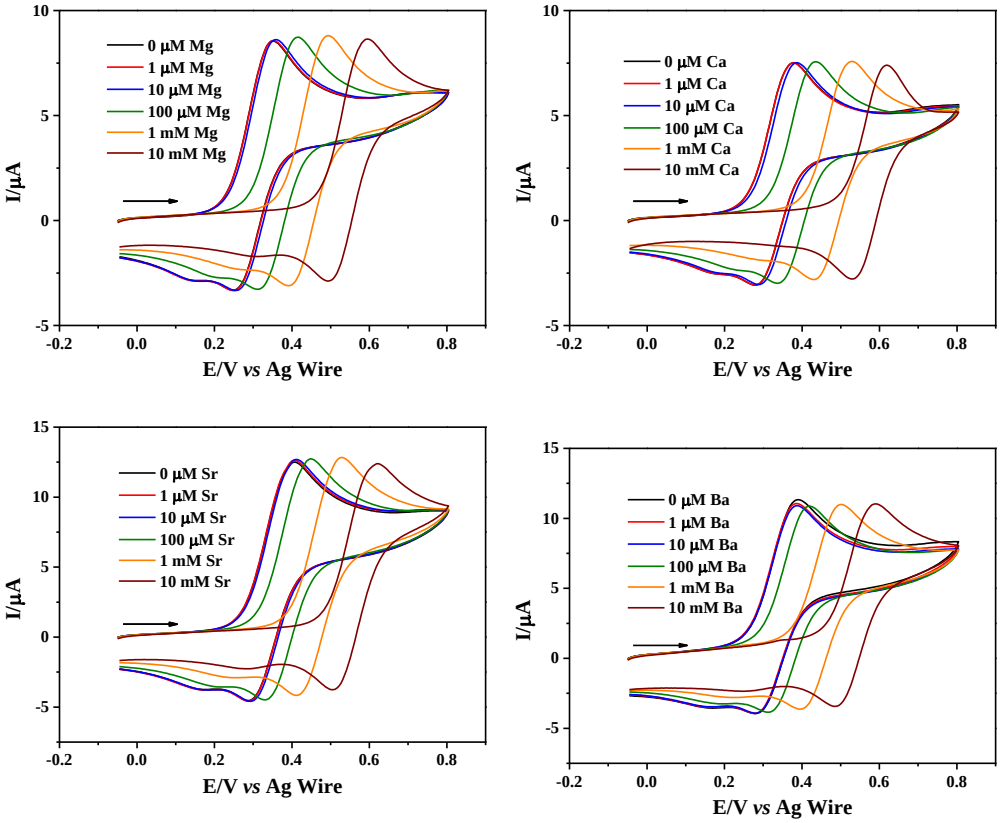

Figure 4.4 - Cyclic voltammograms ($\nu = 0.1$ V s^{-1}) obtained for the sequential addition of $MgCl_2$ (top left), $CaCl_2$ (top right), $SrCl_2$ (bottom left) and $BaCl_2$ (bottom right) to ferrocene (1 mM) with TBAP (0.1 M) in DMSO/H_2O (80:20). Performed at a glassy carbon working electrode (3 mm, BASi), with a graphite counter electrode and silver wire quasi reference electrode at 293.15 ± 1 K.

In all cases the most notable change in the cyclic voltammograms is the large oxidative shift in both the oxidative and reductive peak potentials. Figure 4.5 exhibits that this change occurs after the solubility product of AgCl has been exceeded.[28] It is proposed that this shift is a product of large potential drift and the formation of AgCl on the reference electrode surface.

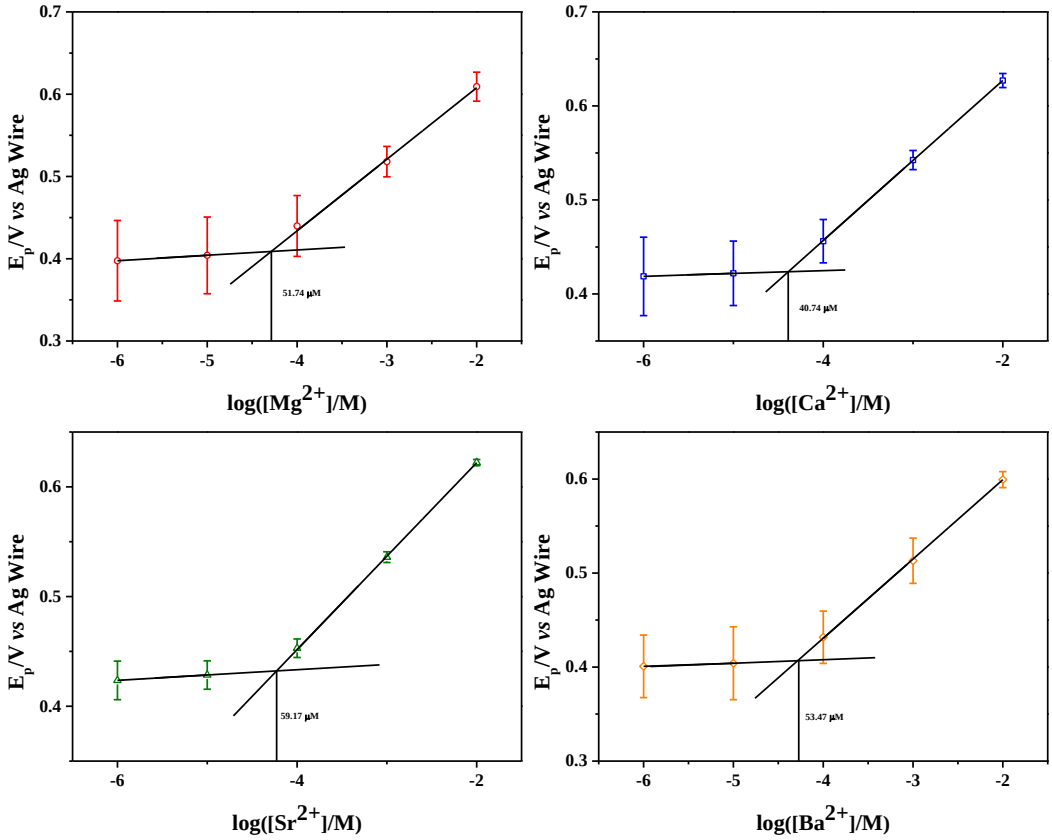

Figure 4.5 - Plots of the cyclic voltammetric ($\nu = 0.1$ V s^{-1}) oxidative peak potentials, E_p, against the log of the concentration of $MgCl_2$ (top left), $CaCl_2$ (top right), $SrCl_2$ (bottom left) and $BaCl_2$ (bottom right) added to ferrocene (1 mM) with TBAP (0.1 M) in DMSO/H_2O (80:20). Performed at a glassy carbon working electrode (3 mm, BASi), with a graphite counter electrode and silver wire quasi reference electrode at 293.15 ± 1 K.

To assess whether the shifts observed were a function of an interaction of the ferrocene or down to the quasi reference electrode, a similar experiment was run with a Ag | AgCl reference electrode in place (BAS). The same solution of ferrocene (1 mM) was prepared with TBAP (0.1 M) in equimolar DMSO / H_2O with additions of $BaCl_2$ (1 - 500 mM). The cyclic voltammograms for this are presented in figure 4.6.

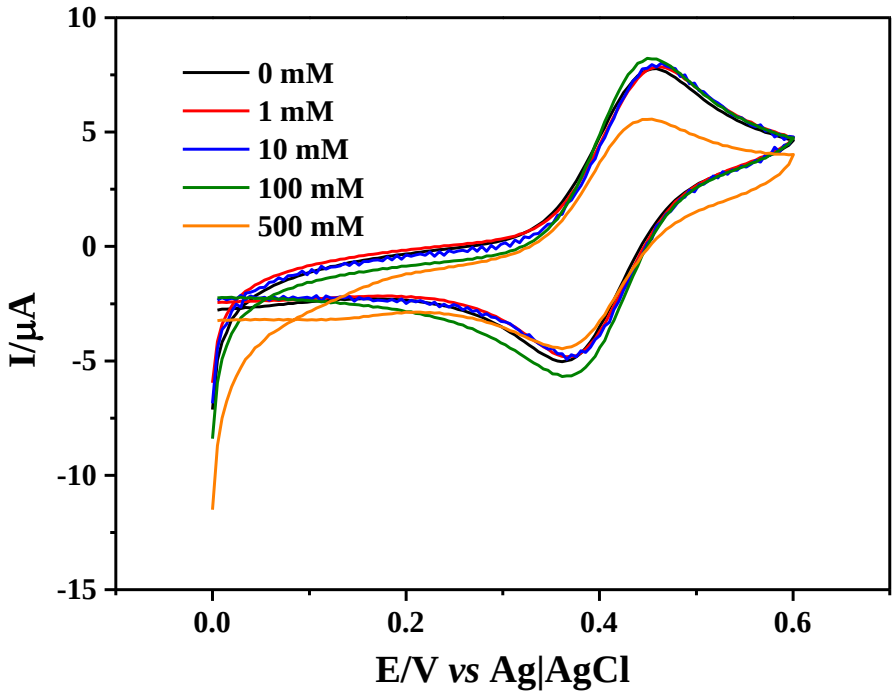

Figure 4.6 - Cyclic voltammograms ($\nu = 0.1$ V s^{-1}) obtained for the sequential addition $BaCl_2$ (1 - 500 mM) to ferrocene (1 mM) with TBAP (0.1 M) in DMSO/H_2O (80:20). Performed at a glassy carbon working electrode (3 mm, BASi), with a graphite counter electrode and Ag | AgCl reference electrode at 293.15 ± 1 K.

It can be seen in figure 4.6 that the peak oxidative and reductive potentials remain constant at E_{mid} = 0.410 ± 0.005 V *versus* an Ag | AgCl reference electrode. This is evidence that the shift in peak potentials observed previously is due to the Ag wire quasi-reference used. In figure 4.6, the peak oxidative current is of interest; as barium is added to the blank solution it remains constant between 1 - 10 mM. Once 100 mM is added to the solution there is a distinct increase in the peak oxidative current of 1 ± 0.05 µA. Following this a large decrease in the peak oxidative current is observed at 500 mM $BaCl_2$ to 5.56 ± 0.05 µA.

To determine whether these changes in peak oxidative current were caused by the barium or the chloride interacting with the ferrocene, the same experiment was

performed except replacing additions of $BaCl_2$ with $Ba(NO_3)_2$. The cyclic voltammograms ($\nu = 0.1$ V s^{-1}) obtained in this scenario are presented in figure 4.7.

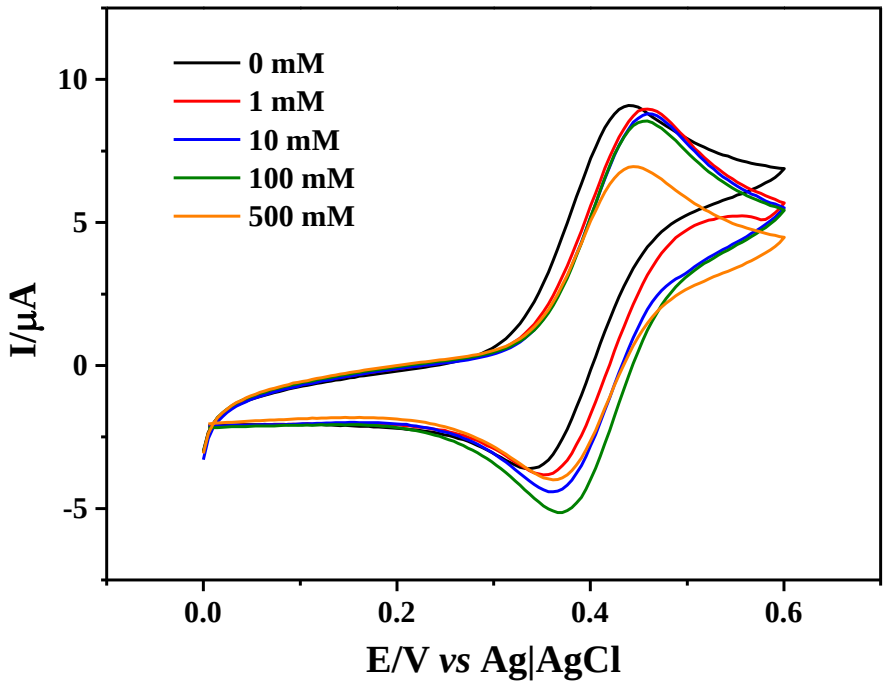

Figure 4.7 - Cyclic voltammograms ($\nu = 0.1$ V s^{-1}) obtained for the sequential addition $Ba(NO_3)_2$ (1 - 500 mM) to ferrocene (1 mM) with TBAP (0.1 M) in DMSO/H_2O (80:20). Performed at a glassy carbon working electrode (3 mm, BASi), with a graphite counter electrode and Ag | AgCl reference electrode at 293.15 ± 1 K.

In figure 4.7, there is an oxidative shift in the peak potentials once barium is added to the system. Following this the peak potentials begin to shift reductively as the concentration of barium nitrate is increased. There is no increase in the measured peak currents. Instead there is a decrease in this parameter for every addition of barium nitrate, from 8.98 ± 0.05 µA at 1 mM barium nitrate to 6.97 ± 0.04 µA at 500 mM barium nitrate.

If the cations were interacting with the solvent molecules through complexation, the consequential enhancement in solvent structure would be noticeable when observing the calculated experimental diffusion coefficients for each concentration. That is to say, if an enhanced solvent structure is being formed in the solution, diffusion of electroactive species from this bulk solution to the electrode surface should be reduced

as the pathway is increasingly hindered. The calculated diffusion coefficients for the ferrocene with each ion present at concentrations of 0.1 and 1 mM, concentrations directly in the linear portion of the oxidative shift, are presented in table 4.1.

Table 4.1 - A table showing the variation in calculated experimental diffusion coefficient for ferrocene (1 mM) with TBAP (0.1 M) in DMSO/H_2O (80:20) depending on which alkaline-earth metal cation is present and the concentration of it.

Metal Ion	Concentration / mM	D_{exp} x 10^{-10} / m^2 s^{-1}
None	0	2.1 ± 0.3
Mg	0.1	2.0 ± 0.2
Mg	1	2.1 ± 0.2
Ca	0.1	1.9 ± 0.2
Ca	1	1.9 ± 0.2
Sr	0.1	2.0 ± 0.2
Sr	1	2.0 ± 0.3
Ba	0.1	2.0 ± 0.2
Ba	1	2.0 ± 0.2

The results of this clearly show no discernible alteration in the diffusion coefficient occurs, which would indicate no change in the solvent structure is occurring. The same experiments were repeated using a glassy carbon microelectrode (11 μm, BASi), as microelectrodes produce enhanced electrode kinetics. The data previously has shown that any shift in potential is due to the instability of the Ag pseudo reference electrode rather than any interactions with the scaling ions. Hence, for experimental ease an Ag wire was again used for the microelectrode studies. Cyclic voltammograms were recorded for the sequential addition of each alkaline-earth metal cation at a scan rate of 0.02 V s^{-1}, figure 4.8; which was found to be slow enough to allow for steady state to be obtained.

Much of the same trends can be seen in the cyclic voltammograms obtained at a microelectrode. There is a clear shift in $E_{1/2}$ once concentrations in excess of 0.1 mM are introduced into the system. In addition to this, a well-defined decrease in the limiting current for 10 mM and 100 mM additions is present. This is important to note when using microelectrodes as the steady state limiting current is directly proportional

to the diffusion coefficient. Consequently, this reduction in experimental limiting current is indicative of the diffusion coefficient decreasing. This supports the hypothesis that the solvent system is becoming more structured, including the possible complexation of cations with the dimethyl sulfoxide; consequently, slowing down the rate at which electroactive species can diffuse from the bulk solution to the electrode surface.

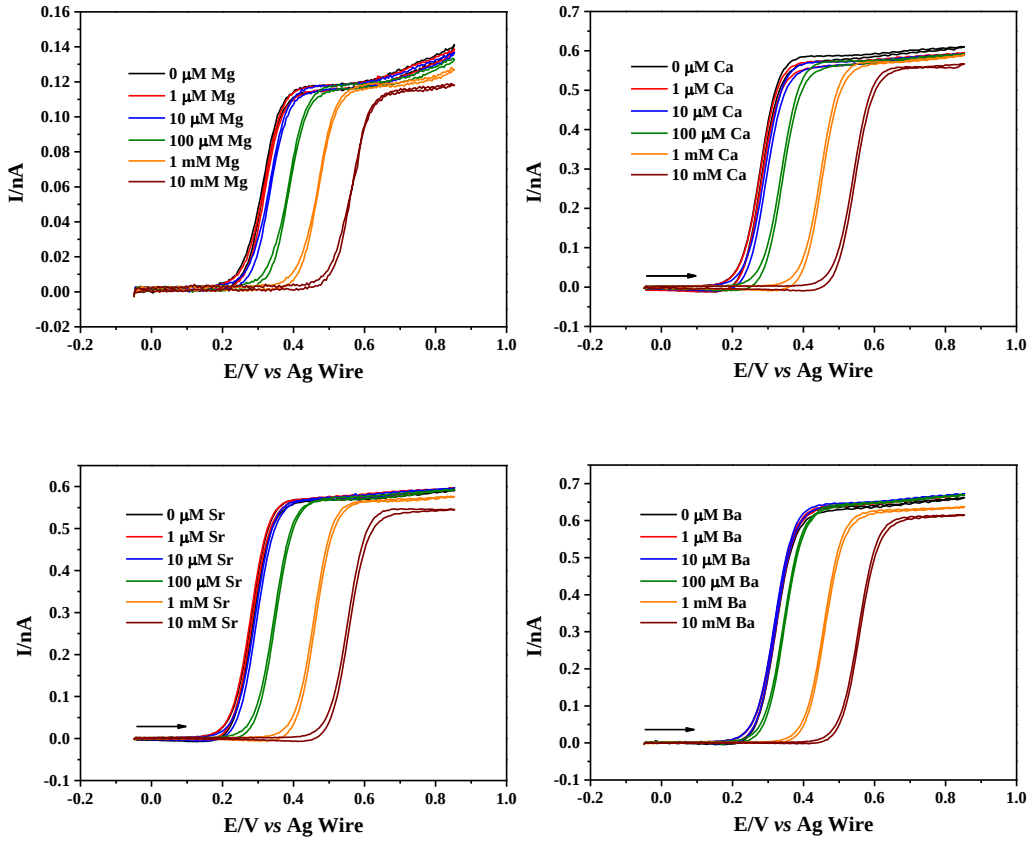

Figure 4.8. Cyclic voltammograms (ν = 0.02 V s^{-1}) obtained for the sequential addition of $MgCl_2$ (top left), $CaCl_2$ (top right), $SrCl_2$ (bottom left) and $BaCl_2$ (bottom right) to ferrocene (1 mM) with TBAP (0.1 M) in DMSO/H_2O (80:20). Performed at a glassy carbon working electrode (11 µm, BASi), with a graphite counter electrode and silver wire quasi reference electrode at 293.15 ± 1 K.

There is clearly a decrease in the measured peak current at a glassy carbon macroelectrode and decrease in the limiting current for a glassy carbon microelectrode upon the addition of high concentrations of alkaline - earth metal chlorides.

The effect of potassium chloride on the cyclic voltammetric response of ferrocene at a macro and microelectrode was tested using the same sequential addition experimental procedure as above. The cyclic voltammetric ($\nu = 0.1$ V s^{-1}) response of ferrocene with the additions of KCl at a glassy carbon macro electrode are presented

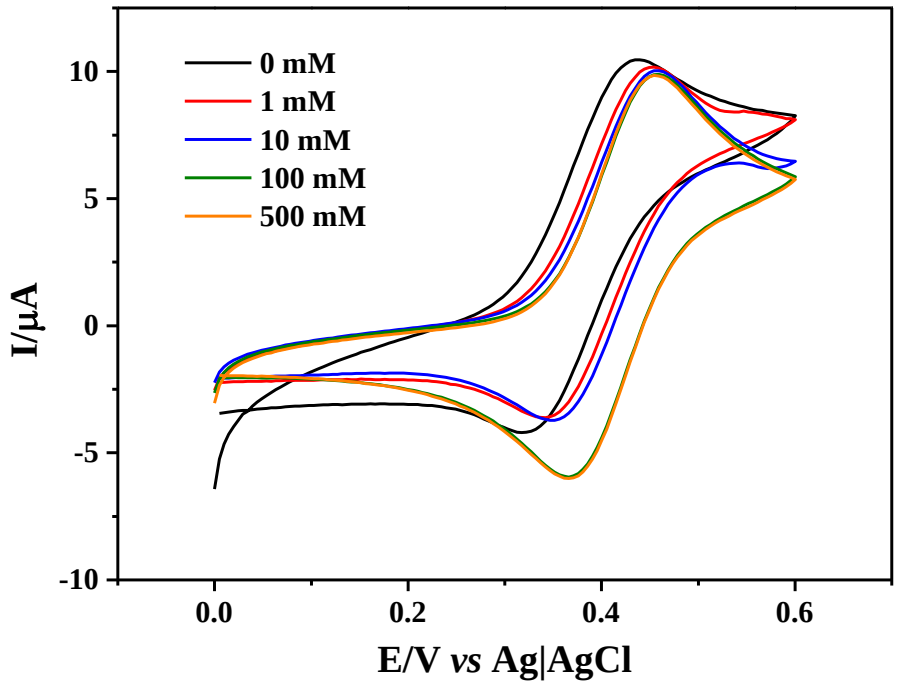

in figure 4.9.

Figure 4.9 - Cyclic voltammograms ($\nu = 0.1$ V s^{-1}) obtained for the sequential addition KCl (1 - 500 mM) to ferrocene (1 mM) with TBAP (0.1 M) in DMSO/H_2O (80:20). Performed at a glassy carbon working electrode (3 mm, BASi), with a graphite counter electrode and Ag | AgCl reference electrode at 293.15 ± 1 K.

The peak potentials in this system shift oxidatively upon the first addition of KCl, but remains constant after that point at + 0.455 V. There is a small decrease (~ 0.75 µA) in the measured peak current but not as large as the one observed for the barium chloride additions.

Figure 4.10 shows the cyclic voltammograms obtained for the addition of KCl to ferrocene at a glassy carbon microelectrode.

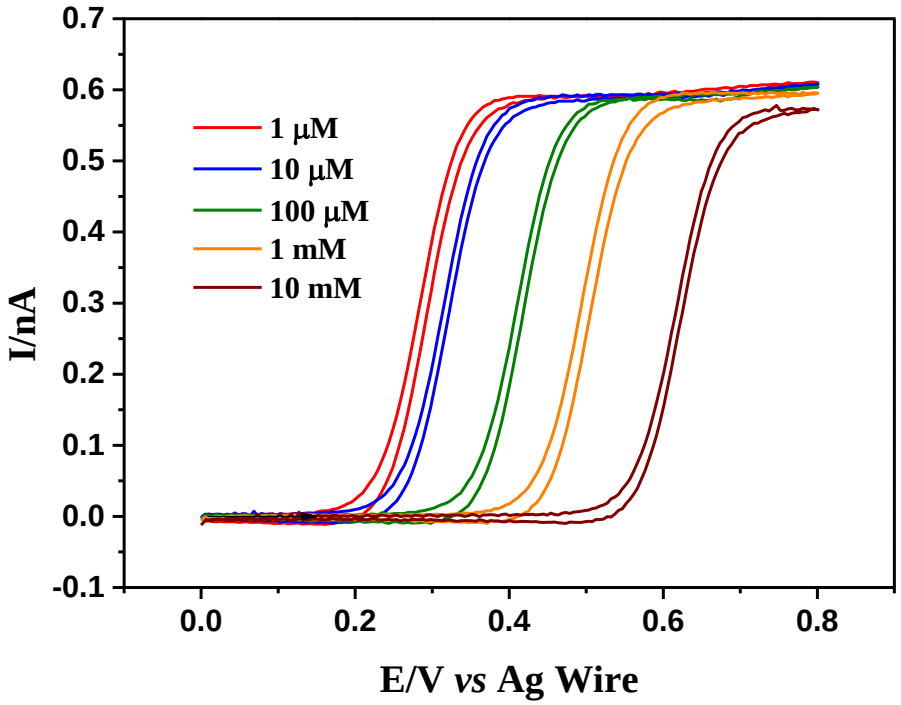

Figure 4.10 - Cyclic voltammograms (ν = 0.02 V s^{-1}) obtained for the sequential addition of KCl (1 µM – 10 mM) to ferrocene (1 mM) with TBAP (0.1 M) in DMSO/H_2O (80:20). Performed at a glassy carbon working electrode (11 µm, BASi), with a graphite counter electrode and silver wire quasi-reference electrode at 293.15 ± 1 K.

In this system it is evident that the decrease in the limiting current is smaller than that observed for the alkaline-earth metal chlorides.

When the chloride compounds are added to the above solutions, it is proposed that, at high concentrations, the solution becomes more viscous, leading to a decrease in diffusion to the electrode surface. This increase in viscosity could be explained by the complexation of the cations to the solvent. The possible change in viscosity was observed using an Ostwald viscometer; whereby, solution with different amounts of cation added to them were tested and compared to a deionised water standard to produce a corrected viscosity reading. The results of these calculated viscosities are presented in figure 4.11.

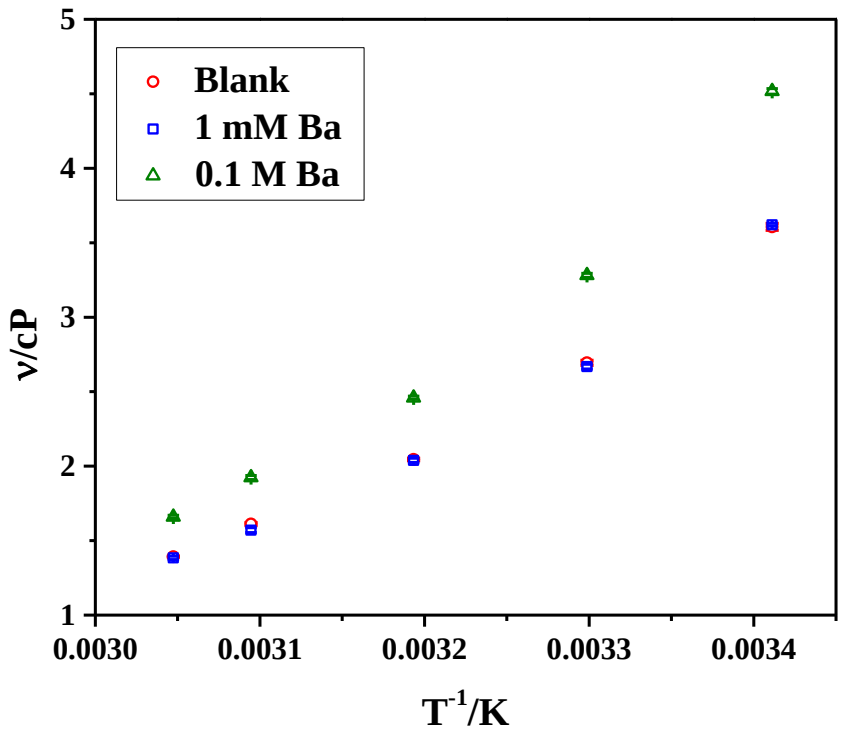

Figure 4.11 - Plot of the calculated viscosity versus 1/T for solutions of ferrocene (1 mM) with TBAP (0.1 M) in DMSO/H_2O (80:20) with additions of $BaCl_2.2H_2O$ (1 mM and 0.1 M).

The measured viscosities gave good agreement with literature values for similar mixed DMSO / H_2O solvent systems.[29–31] It can be seen that the data for the blank solution and the 1 mM solution are virtually identical, with the 0.1 M solution having a much larger viscosity. This shows good agreement with the electrochemical data obtained, whereby, the voltammograms for the concentrations below 0.1 M barium showed a consistent limiting current; with a large decrease observed for the 0.1 M data. This is strong evidence to suggest that the change in voltammograms limiting current was due largely to the increase in viscosity of the solution. This increase in viscosity would directly affect the diffusion coefficient of the solution making it more difficult for the ferrocene to diffuse from the bulk solution to the electrode surface.

Evidence to this point suggests that the interaction between the ferricinium ion and chloride ion could be causing a DISP1 mechanism. A disproportion mechanism is a reversible or irreversible transition in which species with the same oxidation state

combine to yield one of a higher state and one of a lower state.[32,33] It follows that the ferricinium cation will react with the chloride ions present approximately as in equations 4.2-4.5, where ferrocene is represented by Fc, and Cp represent a cyclopentadiene ring and the chloride ions are present in such excess that the reaction is pseudo first order.

$$Fc - e^- \rightleftharpoons Fc^+ \quad 4.2$$

$$FeCp_2^+ + nCl^- \xrightarrow{slow} FeCl_n^{(3-n)+} + 2Cp^- \quad 4.3$$

$$Cp^- + FeCp^+ \rightarrow Cp + FeCp_2 \quad 4.4$$

$$2Cp \xrightarrow{fast} Cp_2 \quad 4.5$$

The observed decrease in limiting current is proposed to be an effect of the increased viscosity of the solution. To adjust for this, a line of best fit was produced for the viscosity results at 293.15 ± 1 K. From this plot the estimated viscosities of all solutions containing various amounts of $BaCl_2$ were calculated, presented in table 4.2.

Table 4.2 – A table with the viscosities of solutions of ferrocene (1 mM) with tetrabutylammonium perchlorate (TBAP, 0.1 M) in equimolar DMSO: H_2O with various amounts of $BaCl_2.2H_2O$ (1 μM – 1 M). Solutions measured using an Ostwald viscometer are presented in black, while estimated values are presented in red.

[$BaCl_2$]/M	Viscosity/cP
0	3.606
1 x 10^{-6}	3.606
1 x 10^{-5}	3.607
1 x 10^{-4}	3.608
1 x 10^{-3}	3.621
1 x 10^{-2}	3.702
1 x 10^{-1}	4.516
5 x 10^{-1}	8.136
7.5 x 10^{-1}	10.40
1	12.66

To correct the measured limiting currents for the viscosity of the solution we introduce two terms, N_{app} and N_{eff}. N_{app} is the measured limiting current of a solution normalised by the limiting current of the blank solution.

$$N_{app} = \frac{i_{lim}}{i_{lim}^{0}} \qquad 4.6$$

N_{eff} is the viscosity of each solution normalised by the viscosity of the blank solution multiplied by N_{app}.

$$N_{eff} = N_{app} \times \frac{\eta}{\eta^{0}} \qquad 4.7$$

If the effect of viscosity is the driving force for the decrease in limiting current, then the calculated N_{eff} value should be greater than unity. This is shown in figure 4.13, where the N_{eff} value is plotted against the concentration of chloride ions present in the solution.

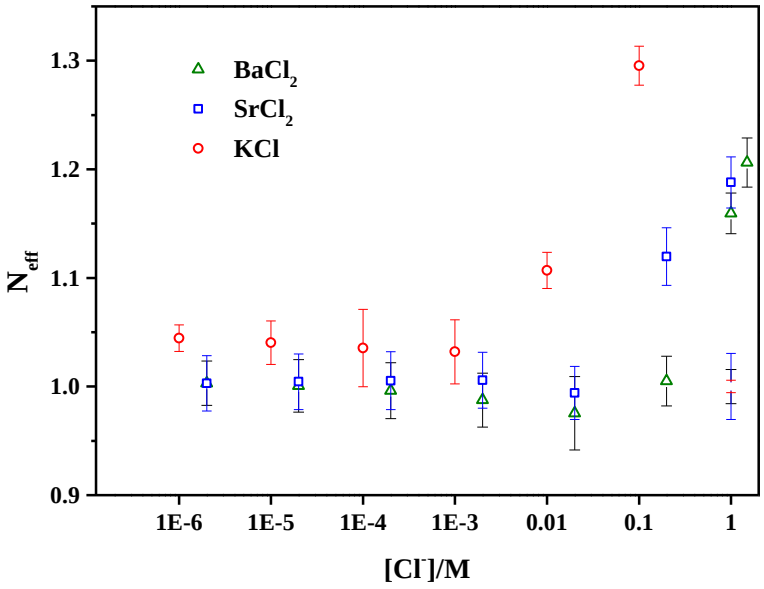

Figure 4.13 - A plot of Neff *versus* the concentration of chloride ions ion solution for the addition of $BaCl_2$, $SrCl_2$ and KCl to a solution of ferrocene (1 mM) with TBAP (0.1 M) in DMSO/H_2O (80:20). Performed at a glassy carbon working electrode (3 mm, BASi), with a graphite counter electrode and Ag | AgCl reference electrode at 293.15 ± 1 K.

It can be seen that the calculated N_{eff} values remain at approximately 1 for low concentrations of chloride ions (< 1 mM). At 10 and 100 mM KCl added there is a sharp rise in the calculated N_{eff}. This is true for the addition of $SrCl_2$ for above 100 mM and $BaCl_2$ above 500 mM. It is proposed that the degree of dissociation between the chloride ion and the counter positive ion has an effect on how early the N_{eff} value rises. In the case of KCl the ions are completely dissociated; therefore, it is expected that the N_{eff} value for this system rises earlier.

The calculated N_{eff} values in this plot allow for the elucidation of a dimensionless rate constant from a simulated curve for a DISP1 mechanism, figure 4.14.

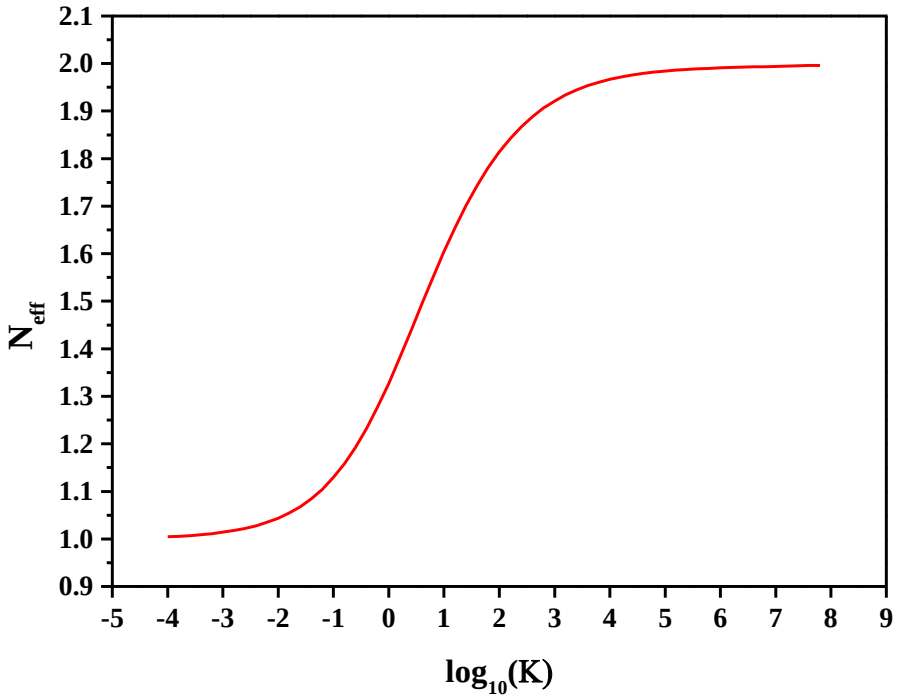

Figure 4.14 - A plot of N_{eff} *versus* the log of the dimensionless rate constant for a DISP1 mechanism. Produced by J Wadhawan.

By inputting the calculated N_{eff} values from figure 4.13 into figure 4.14, the dimensionless rate constants for each system was produced. This dimensionless rate constant, K, can be used to calculate rate constants, k.

$$K = \frac{kr_0^2}{D} \qquad 4.8$$

Therefore, using the diffusion coefficient calculated earlier (2.3 x 10^{-10} m^2 s^{-1}) the rate constants for each system can be calculated. The expected ratio of chloride ions to ferrocene molecules, n, can then be calculated from a gradient of the log of the rate constant *versus* the log of the chloride ions, figure 4.15.

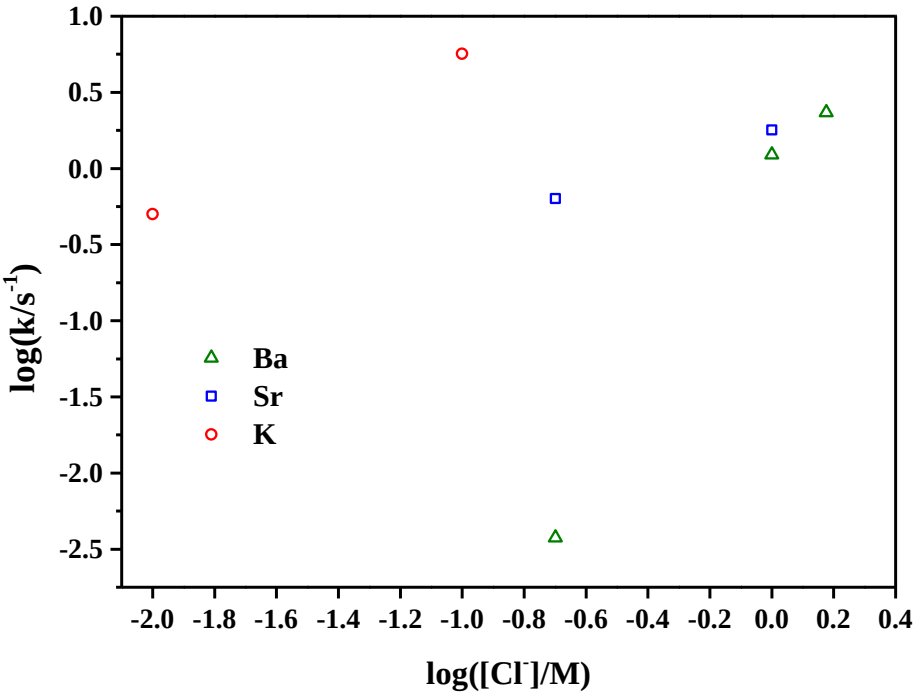

Figure 4.15 - A plot of the log of the rate constant *versus* the log of the concentration of chloride ions.

From the gradients of each system the number of chloride ions, n, that interact with the ferrocene is 3 in the case of barium and 1 in the case of potassium and strontium. This shows that the ferrocene | ferricinium redox couple cannot be treated as a redox couple that is unaffected by its surroundings. When using ferrocene as an internal standard, care must be taken to account for all changes in the system. This includes the effect on the target redox couple and the reference redox couple.

4.3 Conclusions

In this chapter we observed a large shift in the peak potential for the ferrocene | ferricinium redox couple. This was attributed to the Ag wire quasi reference electrode used in the experiment. It is proposed that this shift is down to either potential drift or the formation of silver chloride on the reference electrode surface.

Additions of $BaCl_2$ to the system at a macro electrode showed a small increase in the cyclic voltammetric peak current at 100 mM $BaCl_2$. This was followed by a large decrease in the peak current. The decrease in current was seen at lower concentrations in the limiting currents measured at microelectrodes. This decrease was found to be a product of the increase in viscosity of the solution. As increased concentrations of alkaline-earth metal chlorides are added to the solutions the viscosity of the solution increases. The limiting currents measured can be corrected for this change in viscosity by calculating the N_{eff} value. It was seen that for concentrations of KCl above 10 mM, $SrCl_2$ above 100 mM and $BaCl_2$ above 500 mM there was a large increase in N_{eff} away from unity. These N_{eff} values were used to produce dimensionless rate constants from a simulated fit of a DISP1 mechanism and then a rate constant for the process. Plotting these rate constants against the concentration of chloride in the system gave an indication of the amount of chloride ions interfering with the ferrocene in each case. In the systems where strontium and potassium chloride were added, it was found one chloride ion interferes with the ferrocene. In the case of barium it was found that three chloride ions interfere with the ferrocene.

Overall this shows that the ferrocene | ferricinium redox couple can be used as an internal standard in this solvent mixture with this quasi-reference electrode; however the exact solution conditions must be considered. Any result obtained must be thought of in terms of the system, whereby each components effect on each other must be scrutinised.

4.4 References

1 G. Gritzner and J. Kuta, *Pure Appl. Chem.*, 1982, **54**, 1527–1532.

2 G. Gritzner and J. Kuta, *Pure Appl. Chem.*, 1984, **56**, 461–466.

3 K. Izutsu, in *Handbook of Reference Electrodes*, Springer Berlin Heidelberg, Berlin, Heidelberg, 2013, pp. 145–187.

4 W. A. Pleskov, *Adv. Chem.(USSR)*, 1947, **16**, 254.

5 H. M. Koepp, H. Wendt and H. Stkehlow, *Elektrochem*, 1960, **64**, 483–491.

6 P. D. Beer, P. A. Gale and G. Z. Chen, *Coord. Chem. Rev.*, 1999, **185**, 3–36.

7 P. D. Beer and P. V. Bernhardt, *J. Chem. Soc. Dalt. Trans.*, 2001, **0**, 1428–1431.

8 N. H. Evans, H. Rahman, J. J. Davis and P. D. Beer, *Anal. Bioanal. Chem.*, 2012, **402**, 1739–1748.

9 Y. Fang, Y. Zhou, Q. Rui and C. Yao, *Organometallics*, 2015, **34**, 2962–2970.

10 J.-Z. Ge, Y. Zou, Y.-H. Yan, S. Lin, X.-F. Zhao and Q.-Y. Cao, *J. Photochem. Photobiol. A Chem.*, 2016, **315**, 67–75.

11 M. A. Wani, M. D. Pandey, R. Pandey, S. K. Maurya and D. Goswami, *J. Fluoresc.*, 2017, **27**, 2279–2286.

12 H. Plenio and D. Burth, *Organometallics*, 1996, **15**, 4045–4062.

13 F. Zapata, A. Caballero, A. Espinosa, A. Tárraga and P. Molina, *Org. Lett.*, 2007, **9**, 2385–2388.

14 H. Plenio and C. Aberle, *Organometallics*, 1997, **16**, 5950–5957.

15 J. Maynadié, B. Delavaux-Nicot, S. Fery-Forgues, D. Lavabre and R. Mathieu, *Inorg. Chem.*, 2002, **41**, 5002–5004.

16 M. Li, P. Cai, C. Duan, F. Lu, J. Xie and Q. Meng, *Inorg. Chem.*, 2004, **43**, 5174–5176.

17 M. Alfonso, A. Espinosa Ferao, A. Tárraga and P. Molina, *Inorg. Chem.*, 2015, **54**, 7461–7473.

18 P. A. Gale, M. B. Hursthouse, M. E. Light, J. L. Sessler, C. N. Warriner and R. S. Zimmerman, *Tetrahedron Lett.*, 2001, **42**, 6759–6762.

19 N. H. Evans, C. J. Serpell and P. D. Beer, *Chem. Commun.*, 2011, **47**, 8775.

20 N. H. Evans and P. D. Beer, *Org. Biomol. Chem.*, 2011, **9**, 92–100.

21 N. H. Evans, H. Rahman, A. V. Leontiev, N. D. Greenham, G. A. Orlowski, Q. Zeng, R. M. J. Jacobs, C. J. Serpell, N. L. Kilah, J. J. Davis and P. D. Beer, *Chem. Sci.*, 2012, **3**, 1080.

22 J. Y. C. Lim, M. J. Cunningham, J. J. Davis and P. D. Beer, *Chem. Commun.*, 2015, **51**, 14640–14643.

23 C. M. Cardona, W. Li, A. E. Kaifer, D. Stockdale and G. C. Bazan, *Adv. Mater.*, 2011, **23**, 2367–2371.

24 V. V Pavlishchuk and A. W. Addison, *Inorganica Chim. Acta*, 2000, **298**, 97–102.

25 M. Sato, T. Yamada and A. Nishimura, *Chem. Lett.*, 1980, **9**, 925–926.

26 J. P. Hurvois and C. Moinet, *J. Organomet. Chem.*, 2005, **690**, 1829–1839.

27 N. G. Tsierkezos, *J. Solution Chem.*, 2007, **36**, 289–302.

28 K. Anderson, E. Butler, D. Anderson and E. Woolley, *J. Phys. Chem.*, 1967, **71**, 3566–3569.

29 R. G. LeBel and D. A. I. Goring, *J. Chem. Eng. Data*, 1962, **7**, 100–101.

30 M. D. Archer and R. P. H. Gasser, *Trans. Faraday Soc.*, 1966, **62**, 3451–3458.

31 W. Miao, Z. Ding and A. J. Bard, *J. Phys. Chem. B*, 2002, **106**, 1392–1398.

32 J. B. Clarke, J. W. Hastie, L. H. E. Kihlborg, R. Metselaar and M. M. Thackeray, *Pure Appl. Chem.*, 1994, **66**, 577–594.

33 P. Muller, *Pure Appl. Chem.*, 1994, **66**, 1077–1184.

5 Electrochemical characterisation of quinaldols and investigations into their use for sensing alkaline-earth metal cations

In the previous chapter the reliability of the ferrocene | ferricinium redox couple was investigated for use as an internal standard for potentiometric detection of alkaline-earth metals in non-aqueous environments and was found to be unsuitable in the presence of chloride ions. Given that sea water has *ca.* 35 % salinity, this ultimately precludes the use of ferrocene as an internal standard for potentiometric analysis. Accordingly, an alternative strategy must be sought. In this chapter two derivatives of 8-hydroxyquinoline, chlorquinaldol and broquinaldol, will be investigated in regards to the detection of alkaline-earth metals through an amperometric route. These alterations in voltammetric response are expected to be the product of chelation between the ligands, L, and the metal ions, M, for the case of a one electron electroactive ligand.

$$2L + M^{2+} \rightleftharpoons L_2M^{2+} \quad 5.1$$

$$L - e^- \rightleftharpoons L^{\cdot +} \quad 5.2$$

This can produce three possible scenarios. First, when only the un-coordinated ligand is electrochemically active, the coordination will result in a decrease in the peak current. If both the coordinated and un-coordinated ligand are electrochemically active; changes in both peak potential (due to alterations in the equilibrium) and in peak current (due to variations in the diffusion) will be observed. Last, a scenario can occur where no simple electrode reaction mechanism is present so that complicated voltammetry will occur.

Clearly, it is important to characterise the cyclic voltammetric response of both chlorquinaldol and broquinaldol before progressing to the sensing applications. This begins with chlorquinaldol in acetonitrile and progresses to the same equimolar mixture of dimethyl sulfoxide and water used in the previous chapter.

5.1 Introduction

Chlorquinaldol and broquinaldol, Figure 5.1, are derivatives of the extensively researched 8-hydroxyquinoline.

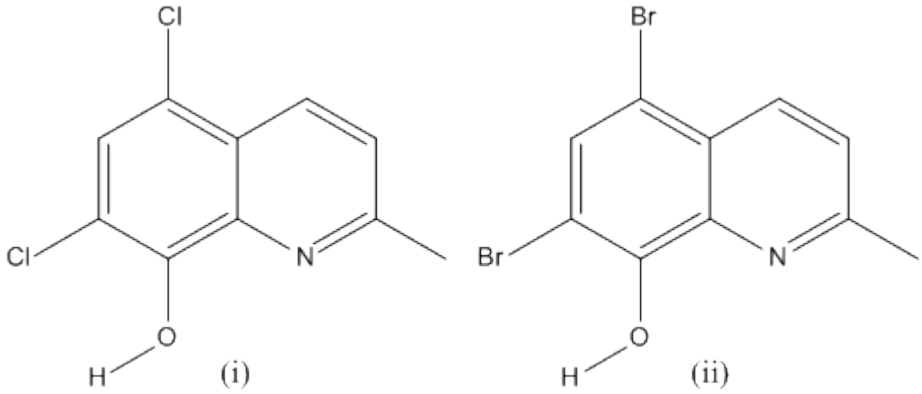

Figure 5.1– The structure of (i) chlorquinaldol and (ii) broquinaldol.

8-hydroxyquinoline has been widely used in analytical processes due to the complexes it forms with Cu^{2+} and Zn^{2+}.[1–3] In conjunction with this, it has been a vital ligand in the extraction and determination of metal ions.[1,4–14] The electrochemical characteristics of this compound have been significantly researched at various working electrodes; including at glassy carbon electrodes[15], carbon paste electrodes[15], dropping mercury electrodes[16] and multiwall carbon nanotube/Nafion.[17]

The electro-oxidation of 8-hydroxyquinoline has been studied computationally, based on AM1 semi-empirical quantum chemical computations of the heats of formation of reaction intermediates, to explain the experimental observations under variations in pH when using a glassy carbon paste electrode.[18] This work proposed various oxidative mechanisms depending on the pH of the solution, presented in figure 5.2, is the dual oxidation process attributing to the mechanism at neutral pH.

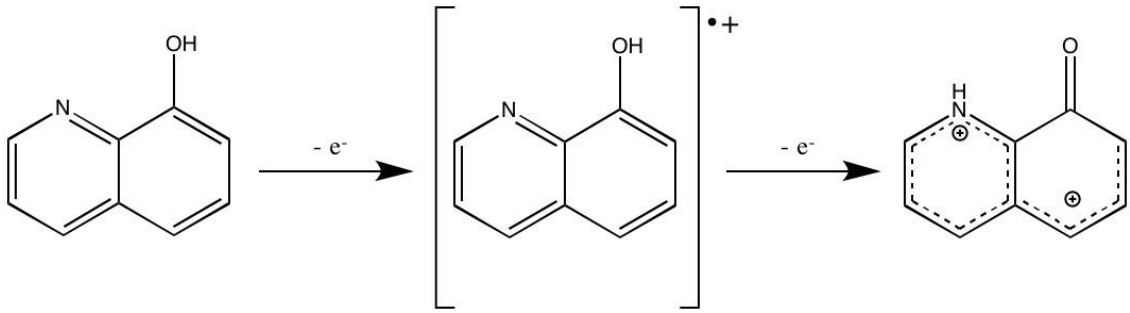

Figure 5.2 – Schematic of the double electron transfer step for the oxidation of 8-hydroxyquinoline at neutral pH (5-9), proposed by Stevic et al.[18]

It is reported that in a solution of approximately neutral pH, 5-9, 8-hydroxyquinoline is found, as presented in figure 5.2, neither protonated or deprotonated. A two-electron oxidation process is observed with cyclic voltammetry, with the first electron transfer step being attributed to the formation of the cation radical intermediate followed by a second oxidation step, including the protonation of the pyridine ring nitrogen and formation of the keto form of the phenol at the 8- position. It is later suggested that the 8-hydroxyquinoline molecules dimerize, in agreement with the Hammond postulate[19], at the 5- position.

Although uncharacterised electrochemically, chlorquinaldol and broquinaldol, shown in figure 4.1, are proposed to chelate with the alkaline-earth metal cations (Mg^{2+}, Ca^{2+}, Sr^{2+} and Ba^{2+}) due to the relative similarities in size and charge between these cations and previously successful systems for other metals, like common derivative clioquinol, and hence characterization is necessary.[20]

Structural differences between these derivatives and the parent compound include the presence of a methyl group substituted at the 2-position along with specified halogens at the 5- and 7-position. The presence of the halogens, specifically in these positions, is predicted to provide a site for possible immobilisation onto an electrode surface as well as steric effects to aid in the discrimination between various alkaline-earth metals in a single solution. The 5-position being occupied by a halogen should also block the suggested dimerization that occurs in the parent compound. Dimerization has however been shown in the solid state form for chlorquinaldol *via* hydrogen bonding between corresponding nitrogen and phenol moieties groups, shown in figure 5.3, yielding an inter-molecular 10-ring system.[21]

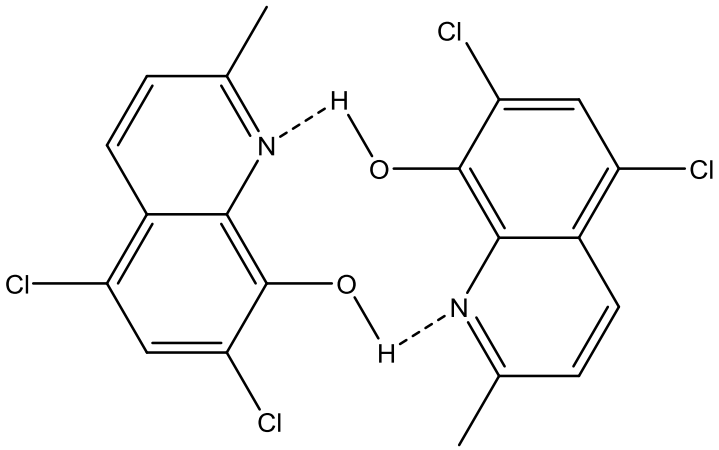

Figure 5.3 – A skeletal representation of the dimer found in the X-ray crystal structure of chlorquinaldol presented by Malecki *et al.*[21]

In this chapter the electrochemical characteristics of the two mentioned systems will be probed with cyclic voltammetry and rotating disc electrode voltammetry. Following this, investigations will be carried out into the ability for these molecules to performed as an electrochemical sensor and if successful the mechanism into how this is achieved.

5.2 Results and Discussion

5.2.1 Electrochemistry of chlorquinaldol in acetonitrile

Voltammograms were obtained for the cyclic voltammetry of chlorquinaldol (10 mM) in acetonitrile with tetrabutylammonium perchlorate (TBAP, 0.1 M) as the supporting electrolyte at scan rates in the range 0.02 – 0.5 V s^{-1}, figure 5.4. Two oxidative waves are observed consecutively over the range 1.05 < E/V *vs.* Ag wire < 1.15 and 1.25 < E/V *vs.* Ag wire < 1.35, with higher scan rates noticeably shifting the peak potential oxidatively, figure 5.5. A single immediate reduction signal was observed for slower scan rates (0.02 and 0.05 V s^{-1}) which disappeared with increasing scan rates.

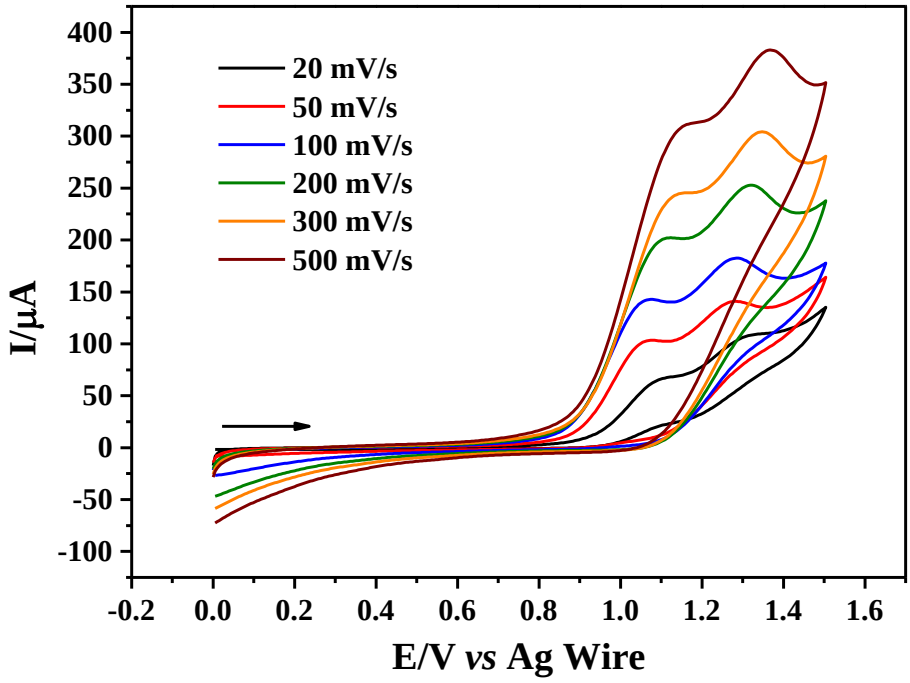

Figure 5.4 - Cyclic voltammograms (ν = 0.02, 0.05, 0.1, 0.2, 0.3 and 0.5 V s^{-1}) for chlorquinaldol (10 mM) with TBAP (0.1 M) in acetonitrile; performed at a glassy carbon electrode (3 mm, BASi) with graphite counter and Ag wire reference at 293.15 ± 1 K.

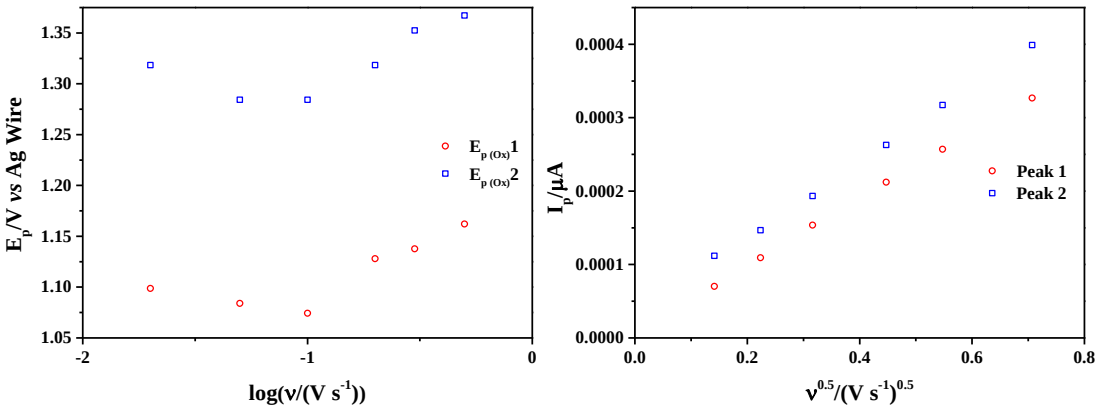

Figure 5.5 – Plots of (left) peak potential *vs.* the log of the scan rate and (right) peak current *vs.* the square of the scan rate for both peaks, 1 and 2, for chlorquinaldol (10 mM) with TBAP (0.1 M) in acetonitrile. Performed at a glassy carbon electrode (3 mm, BAS) with graphite counter and Ag wire reference at 293.15 ± 1 K.

The peak current for both oxidative peaks is observed to increase with respect to the scan rate, illustrated in figure 5.5. The plots of peak current, I, *vs.* the square of the scan rate, ν, are slightly curved. The diffusion coefficients for each oxidised species present in the system can be calculated using the Randles-Ševčík equation and the linear fit through the origin. The diffusion coefficients for the two species were calculated, assuming that the number of electrons transferred, n, in each case is one, to be $D_1 = 4.9 \times 10^{-10}$ m^2 s^{-1} and $D_2 = 7.7 \times 10^{-10}$ m^2 s^{-1} respectively.

A mechanism for the dual peak oxidation process is proposed in figure 5.6. It is very difficult to distinguish between DISP1 and ECE type processes, but it is proposed that an ECE type reaction occurs where the second step is slower than then first and the oxidative potential of the second electron transfer is greater than the first electron transfer. This follows a similar proposal by Stevic *et al*.[18] for the parent 8-hydroxyquinoline molecule.

The initial electron transfer process is attributed to the formation of the appropriate cation radical through the oxidation of the phenol group. Following this, it is proposed that the chemical step includes the loss of a hydrogen ion, allowing the radical to resonate around the fused ring structure. It is stabilized at the 2-position by the presence of the methyl group in addition to the resonance effects presented by the pyridine ring and lone pair from the nitrogen. In accordance with the Hammond postulate[19], identifying regioselectivity as being governed by the stability of the transition states rather than the products, the second electron transfer process is attributed to the formation of the corresponding carbon cation at the 2-position. This is supported by the extra stability a carbocation would receive from tertiary carbons, resonance effects and lone pair availability.

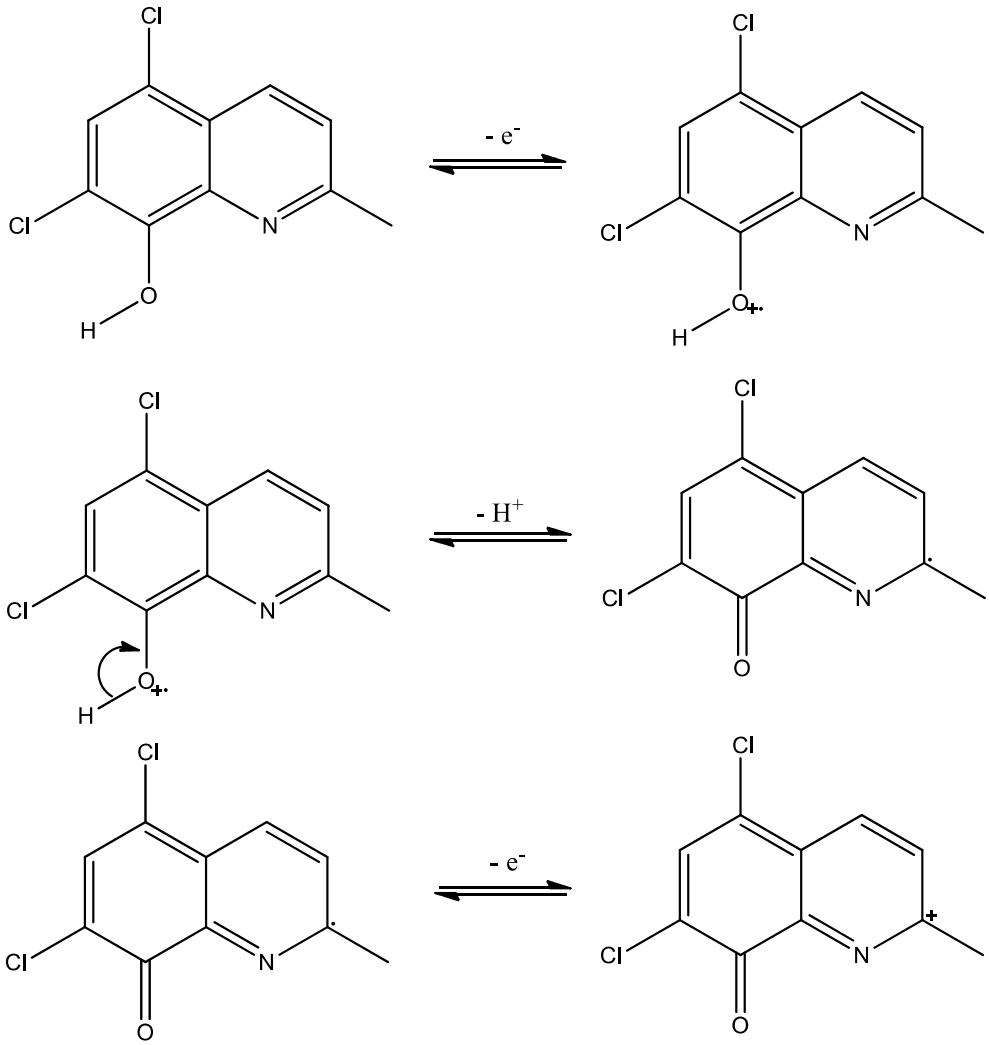

Figure 5.6 – A proposed mechanism for the ECE type oxidation process of chlorquinaldol in acetonitrile at a glassy carbon macro electrode (3 mm, BASi).

Further observations were made into the diffusion processes in the system using rotating disc voltammetry, figure 5.7. The same glassy carbon electrode was used in conjunction with an external motor to rotate the electrode at various frequencies (500 – 3000 rpm).

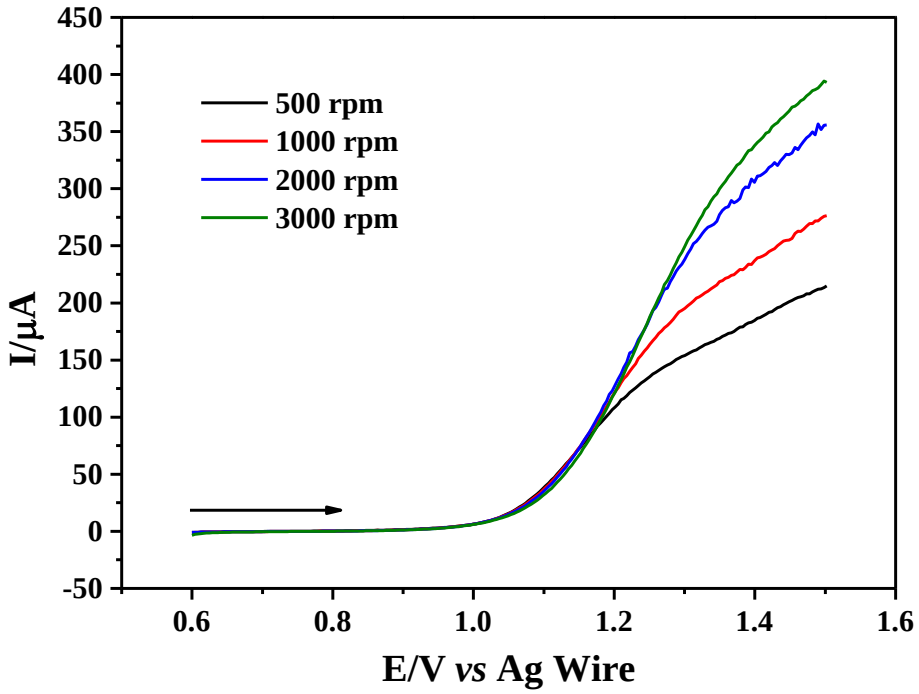

Figure 5.7 – A plot showing the current response of chlorquinaldol (10 mM) with TBAP (0.1 M) in acetonitrile against the applied potential at a various rotation speeds (500, 1000, 2000 and 3000 rpm), at a glassy carbon electrode (3 mm BAS) at 5 mV s^{-1} at 293.15 ± 1 K.

The limiting current at each rotation speed can be obtained by finding the value at which, when an extended linear fit is applied, the final gradient of each scan deviates from the experimentally obtained scan. In conjunction with a Levich plot, figure 5.8, this information is used to elucidate a diffusion coefficient for the system, for n equal to one of 6.0 ± 0.3 × 10^{-10} m^2 s^{-1} and n equal to 2 of 3.0 ± 0.1 × 10^{-10} m^2 s^{-1}, when controlled by mass transfer and n is the number of electrons transferred. The calculated diffusion coefficient from the Randles-Ševčík plot falls in the middle of these two values, indicating the process could be n equalling 1 + x; $0 \leq x \leq 1$.

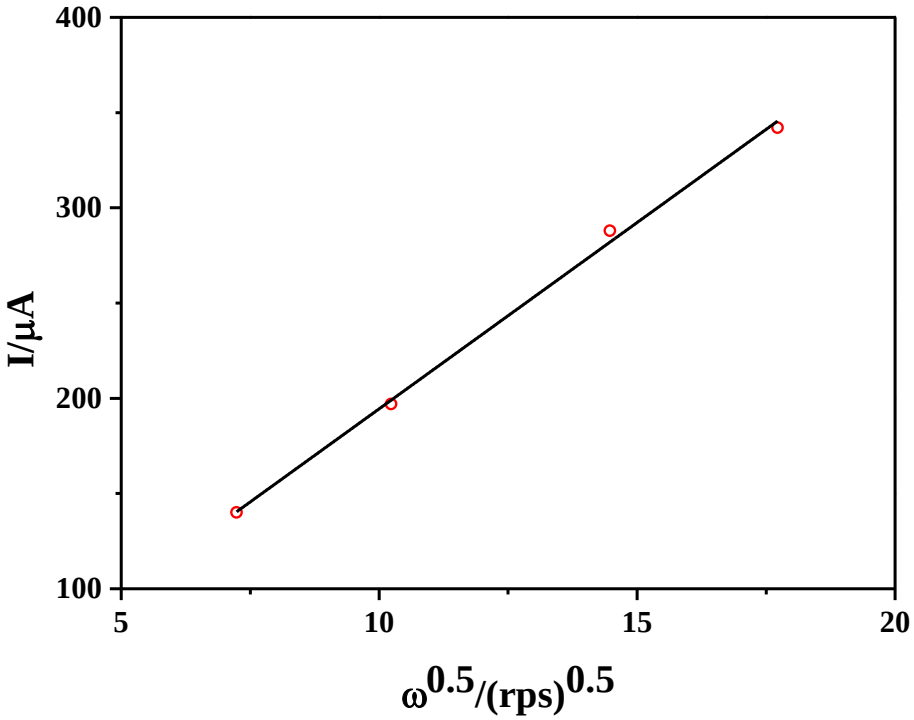

Figure 5.8 – A Levich plot of the limiting current for chlorquinaldol (10 mM) with TBAP (0.1 M) in acetonitrile. Performed at a glassy carbon electrode (3 mm, BAS) rotated at various speeds (500, 1000, 2000 and 3000 rpm) at 293.15 ± 1 K.

This can be further investigated using the Wilke-Chang method for estimating the diffusion coefficient, D, for systems based on the association coefficient, α_{sv}, the molecular weight, M_{sv}, and the viscosity of the solvent, η_{sv}.

$$D = \frac{7.4 \times 10^{-8}\, T \sqrt{\alpha_{sv} M_{sv}}}{\eta_{sv} V_b^{0.6}} \qquad 5.3$$

Where T is the absolute temperature and V is the molar volume. Many solvents do not have well-defined association coefficients; for acetonitrile it is estimated[22] α_{sv} = 1.48. Using this value the calculated D = 4.5 x 10^{-10} m^2 s^{-1} with a 10 % error.[24] This again falls between the calculated values from rotating disc voltammetry indicating that the process is between a one and two electron process.

Solubility of alkaline-earth metal chlorides is much higher in dimethyl sulfoxide than acetonitrile, however the voltammetric response in this solvent alone is poor. The addition of water, as well as increasing solubility further, increased the clarity of the voltammetry. A composition of equimolar DMSO/H_2O was established based on observable precipitation of the electrolyte, tetrabutylammonium perchlorate (TBAP). The system was characterized without the presence of alkaline-earth metal ions to observe any variation in the electrochemistry in the different solvents.

5.2.2 Voltammetry of chlorquinaldol in equimolar DMSO/H_2O

Voltammograms were obtained for the cyclic voltammetry of chlorquinaldol (1 mM) in equimolar DMSO/H_2O with tetrabutylammonium perchlorate (TBAP, 0.1 M) as the supporting electrolyte at scan rates from 0.02 – 0.5 V s^{-1}, figure 5.9.

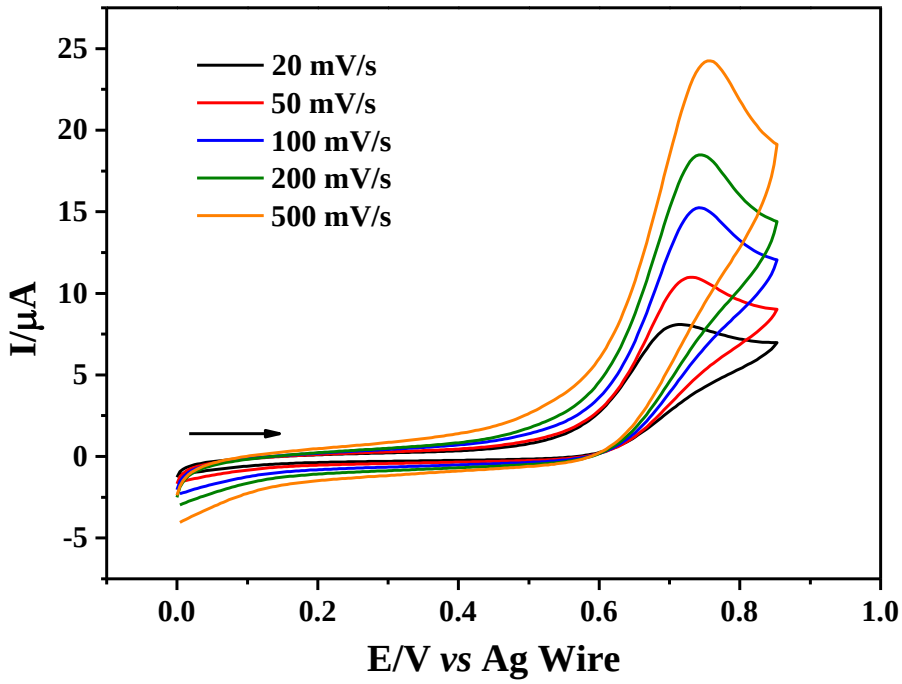

Figure 5.9 - Cyclic voltammograms (ν = 0.02, 0.05, 0.1, 0.2, 0.3 and 0.5 V s^{-1}) for chlorquinaldol (1 mM) with TBAP (0.1 M) in equimolar DMSO/H_2O. Performed at a glassy carbon electrode (3 mm, BAS) with graphite counter and Ag wire reference at 293.15 ± 1 K.

Most notably, in comparison to when acetonitrile was the solvent, a single oxidation peak is observed in DMSO at lower potential values, in the range + 0.71 < E/V *vs* Ag wire < + 0.76. The higher scan rates noticeably shifting the peak potential to more oxidative values, figure 5.10 (left).

As before, the plot of peak oxidative current against the square of the scan rate produces a slightly curved plot, figure 5.10 (right). Using the produced linear fit through the origin the diffusion coefficient was calculated using the Randles-Ševčík equation to be $D = 5 \pm 2 \times 10^{-10}$ m^2 s^{-1}; which is in agreement with the values calculated earlier.

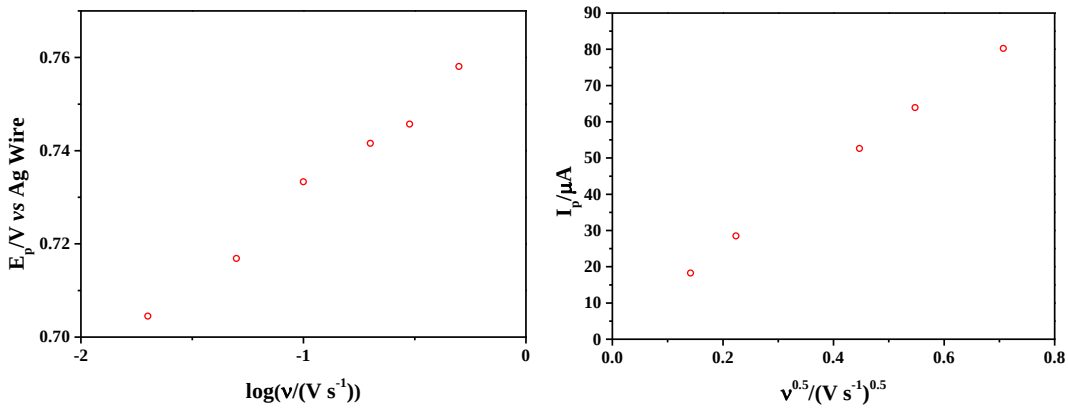

Figure 5.10 - Plots of (left) peak potential versus the log of the scan rate and (right) peak current versus the square of the scan rate, for chlorquinaldol (1 mM) with TBAP (0.1 M) in equimolar DMSO/water. Performed at a glassy carbon electrode (3 mm, BAS) with graphite counter and Ag wire reference at 293.15 ± 1 K.

The single observed oxidation peak is explained in the proposed mechanism, figure 5.11, which is a disproportionation process. The same initial oxidation is suggested, whereby the electron transfer refers to the removal of an electron from the phenol to produce the corresponding cation radical. It is suggested that the second, chemical step, is the rate determining step (DISP1 mechanism); whereby, a hydrogen is expelled from the molecule and the remaining radical is able to resonate around the fused ring system, stabilizing in the 2-position. The difference between the DMSO and acetonitrile based systems is at this point, in acetonitrile there is a second oxidation; whereby, a second electron transfer step produces a carbocation in the 2-position. For DMSO, due to its composition, it is proposed that the radical extracts a hydrogen from

the solvent or the product of the first oxidation to produce the hydrogenated form presented. This stabilizes the product and therefore means the second oxidation step occurs in homogeneous solution rather than at the electrode surface.

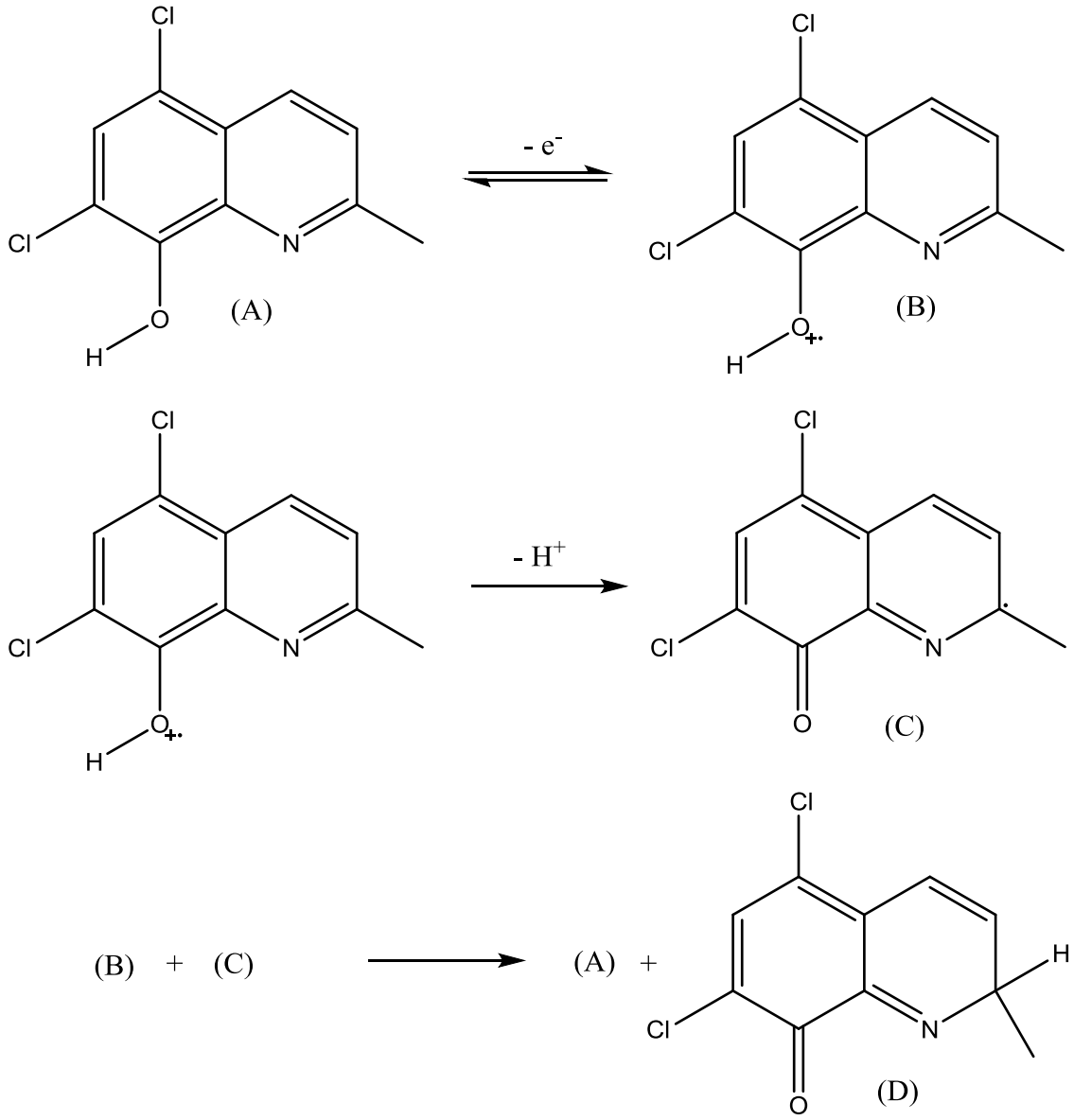

Figure 5.11 – A proposed mechanism for the DISP mechanism proposed for chlorquinaldol in an equimolar mixture of DMSO and water.

The Randles-Ševčík plots observed throughout this chapter are curved in nature. This curved nature is also seen in a plot of the peak current measured at 0.1 V s^{-1} normalised by the square root of the concentration of chlorquinaldol in figure 5.12.

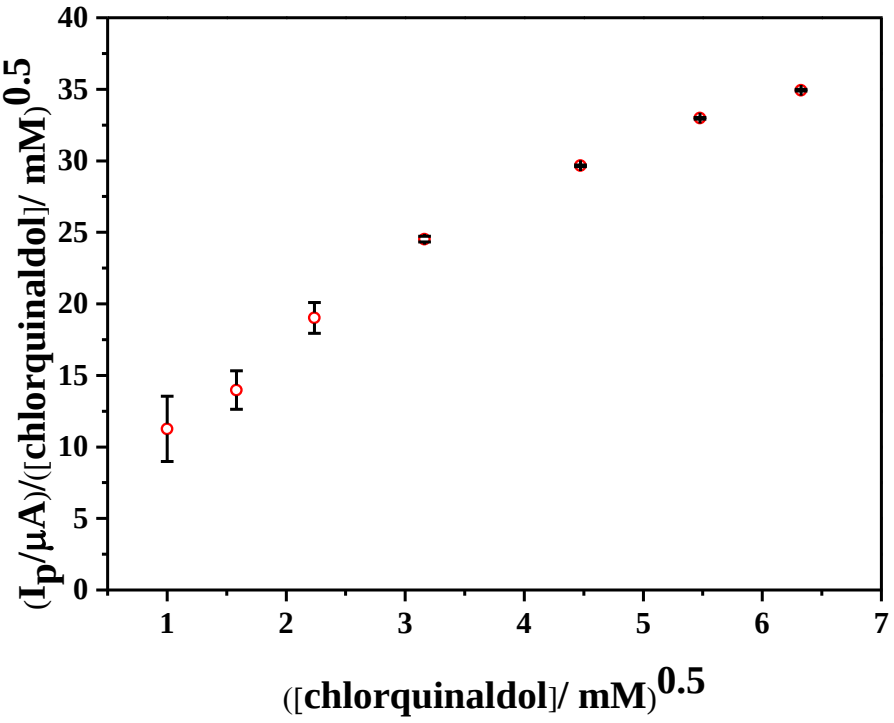

Figure 5.12 – Plot of the peak current, obtained from cyclic voltammetry (ν = 0.1 V s^{-1}), normalised by the square of the concentration versus the square of the concentration for chlorquinaldol (1 – 40 mM) with TBAP (0.1 M) in equimolar DMSO/ water. Performed at a glassy carbon electrode (3 mm, BAS), with a graphite counter and Ag wire reference at 293.15 ± 1 K.

A linear fit is observed between 1 - 5 mM chlorquinaldol. After this point, there is a clear shift in gradient of the linear relationship away from the origin; the plot effectively bends towards a horizontal position. This is evidence to the fact something has altered in the way the chlorquinaldol molecules interact when the concentration is increased. This trend can indicate the possibility of aggregation in the system but also a change in the apparent diffusion coefficients with respect to the concentration of chlorquinaldol.

By treating the curved Randles-Ševčík plots as a one electron process and varying the concentration of chlorquinaldol the change in calculated diffusion coefficient can be observed, figure 5.13.

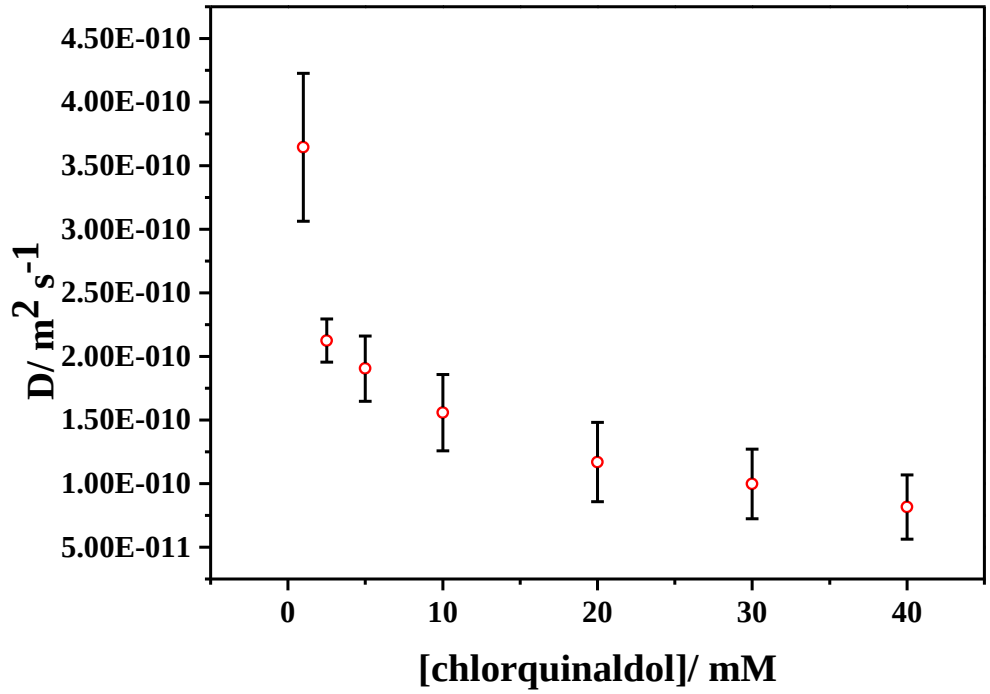

Figure 5.13 – Plot of calculated diffusion coefficient versus the concentration of chlorquinaldol (1 - 40 mM) with TBAP (0.1 M) in equimolar DMSO/water. Performed at a glassy carbon electrode, with graphite counter and Ag wire reference at 293.15 ± 1 K.

This shows that the diffusion coefficient decreases as the concentration of chlorquinaldol increases. Using the diffusion coefficient from the smallest concentration measured, $D_{C\rightarrow 0}$, the N_{eff} value can be calculated.

$$\frac{D}{D_{C\rightarrow 0}} = \frac{1}{N_{eff}^2} \qquad 5.4$$

The results of this show that as the concentration of chlorquinaldol is increased, the diffusion coefficient decreases and the N_{eff} value increases, as shown in table 5.1.

Table 5.1 – A table showing the diffusion coefficients and N_{eff} values for chlorquinaldol in equimolar DMSO/H_2O.

[Chlorquinaldol]/ mM	D x 10^{-10}/ m^2 s^{-1}	N_{eff}
1.0	3.64	1
2.5	2.12	1.31
5.0	1.91	1.38
10.0	1.55	1.53
20.0	1.18	1.76
30.0	1.00	1.91
40.0	0.81	2.11

This can be translated into rate constants in the same way as chapter 4, see plot 4.14-4.15. These are presented in figure 5.14, where it can be seen that as the concentration of chlorquinaldol is increased the rate constant also increases.

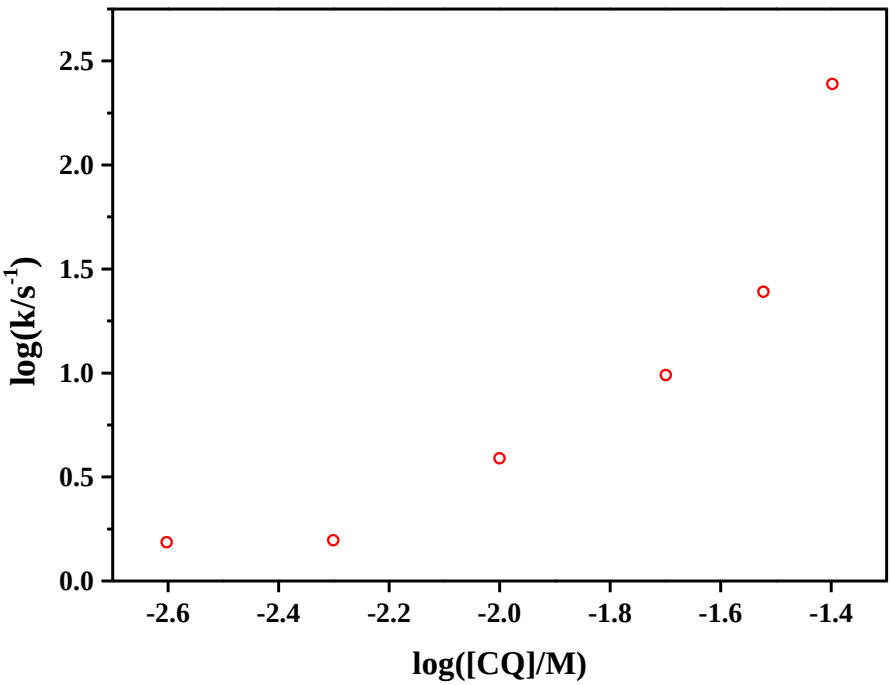

Figure 5.14 - A plot of the log of the rate constant *versus* the log of the concentration of chlorquinaldol (CQ) in equimolar DMSO/H_2O. Numbers generated from a DISP1 model for a macro electrode, created by J Wadhawan.

The gradient in this plot is ~ 2 which indicates the process is second order, not first order. This suggests that the second step is slow and the process is DISP2. It follows that since the proton transfer is usually fast. The deviations are probably due to the breakdown of the assumed DISP1 process.

This shows how chlorquinaldol acts in equimolar DMSO/H_2O, next the same analysis will be applied to broquinaldol, figure 5.1. The two derivatives will then be compared and applied to the detection of alkaline-earth metal ions.

5.2.3 Voltammetry of broquinaldol in equimolar DMSO/H_2O

Broquinaldol is another derivative of the archetypal 8-hydroxyquinilone molecule, it is identical to chlorquinaldol in every way apart from the replacement of the chlorines in position 5- and 7- with bromines. Electrochemical characterization was carried out, figure 5.15, for broquinaldol (5 mM) in equimolar DMSO/H_2O with TBAP (0.1 M) using cyclic voltammetry at scan rates from 0.02 – 0.5 V s^{-1}.

Similarly, to the chlorquinaldol system, a single oxidation peak is observed at + 0.82 < E/V *vs* Ag wire < + 0.94. This is evidence towards to the broquinaldol being more difficult to oxidize than its chlorine counterpart which is not expected. The potential drift in the Ag wire quasi-reference electrode observed throughout chapter 4 and 5 mean this cannot be taken as fact. The most striking variation between the two systems is the very clear definition of the first reverse peak for broquinaldol at + 0.28 < E/V *vs* Ag wire < +0.41. In the same way as chlorquinaldol, broquinaldol produces an oxidative peak potential that trend to higher values as the scan rate is increased, figure 5.16.

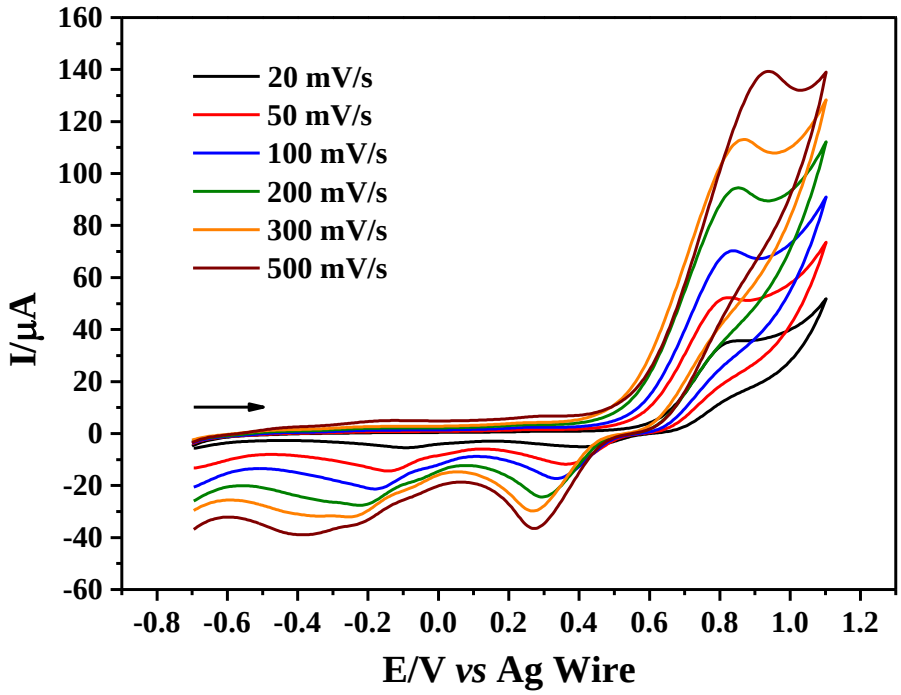

Figure 5.15 – Cyclic voltammograms (ν = 0.02, 0.05, 0.1, 0.2, 0.3 and 0.5 V s^{-1}) for broquinaldol (10 mM) with TBAP (0.1 M) in equimolar DMSO/H_2O. Performed at a glassy carbon electrode (3 mm, BAS) with graphite counter and Ag wire reference at 293.15 ± 1 K.

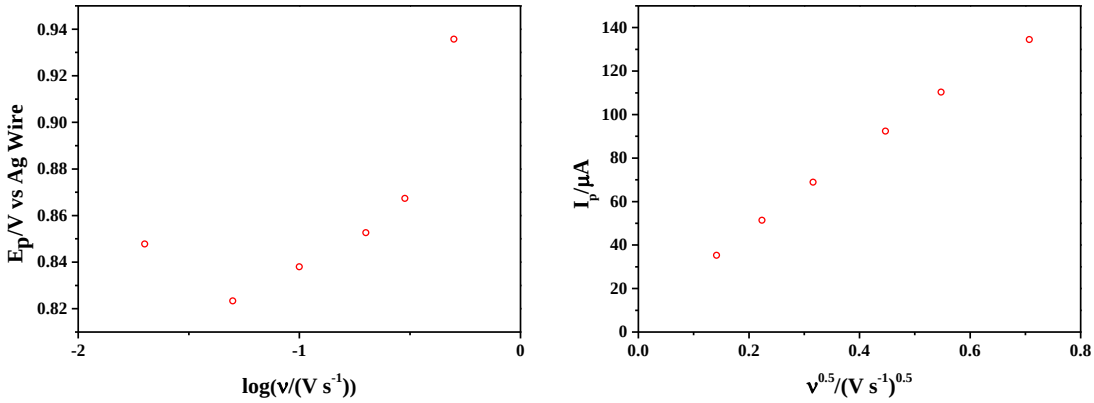

Figure 5.16 - Plots of (left) peak current versus the square of the scan rate and (right) peak potential versus the log of the scan rate, for broquinaldol (10 mM) with TBAP (0.1 M) in DMSO: water (80: 20 %). Performed at a glassy carbon electrode (3 mm, BAS) with graphite counter and Ag wire reference at 293.15 ± 1 K.

This system, as with its derivative, is shown to produce a curved fit when plotting the peak current versus the square root of the scan rate. Utilizing the Randles-Ševčík equation, the diffusion coefficient for broquinaldol in this DMSO based system was calculated to be $D = 1.3 \pm 0.2 \times 10^{-10}$ m^2 s^{-1}. This is smaller than that found for chlorquinaldol.

Due to the distinct similarities between the electrochemical response of broquinaldol and chlorquinaldol, it is proposed that they follow the same mechanism. The first electron transfer step is proposed to be the oxidation of the phenol group to form the cation radical. This is followed by a chemical step whereby a hydrogen is lost from the molecule and the radical can resonate around the fused ring system, being stabilized in the 2-position by the combination of methyl group, pyridine ring resonance and nitrogen lone pair. Finally, the second step of the DISP2 process occurs, where the electron transfer is in homogeneous solution rather than at the electrode surface.

Further observations into the similarity between the chlorquinaldol and broquinaldol system presented evidence into aggregation for the broquinaldol in DMSO through a plot of peak current normalized by the square of the concentration versus the square of the concentration of broquinaldol, figure 5.17.

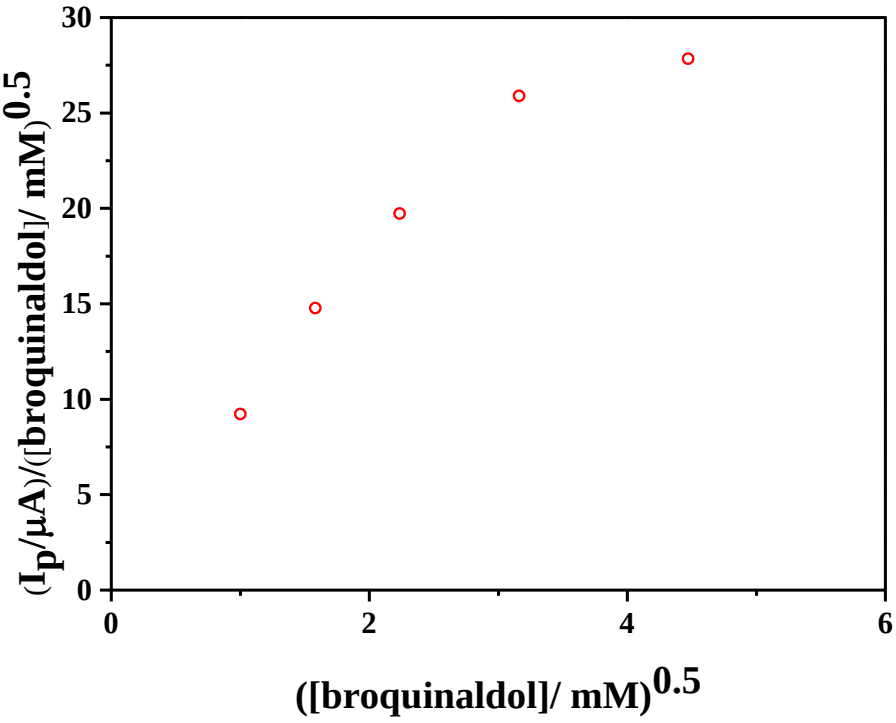

Figure 5.17 - Plot of the peak current, obtained from cyclic voltammetry (ν = 0.1 V s^{-1}), normalised by the square of the concentration versus the square of the concentration for broquinaldol (1 – 30 mM) with TBAP (0.1 M) in equimolar DMSO/water. Performed at a glassy carbon electrode (3 mm, BAS), with a graphite counter and Ag wire at 293.15 ± 1 K.

In the same way as above, figure 5.12, the plot of the normalised peak current, figure 5.17, is curved in nature. This can be indicative of aggregation within a system or a change in the diffusion coefficient. The diffusion coefficients can be calculated from the curved R-S plots, as above, assuming a one electron process.

The change in the diffusion coefficients for these concentrations of broquinaldol are presented in figure 5.18. As seen in the chlorquinaldol system, figure 5.13, the diffusion coefficient for broquinaldol in equimolar DMSO/H_2O decreases as the concentration of broquinaldol is increased.

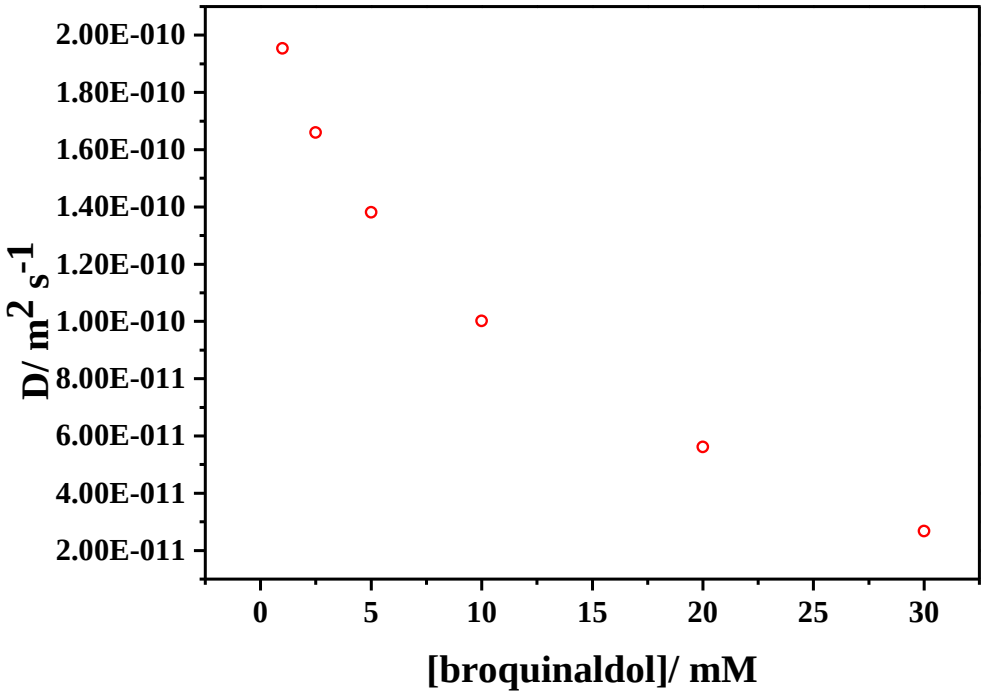

Figure 5.18 - Plot of calculated diffusion coefficient versus the concentration of broquinaldol (1 - 30 mM) with TBAP (0.1 M) in equimolar DMSO/water. Performed at a glassy carbon electrode, with graphite counter and Ag wire reference at 293.15 ± 1 K.

The values of the diffusion coefficients can be used to calculate the N_{eff} values as in equation 5.4. The values for this are presented in table 5.2.

Table 5.2 - A table showing the diffusion coefficients and N_{eff} values for broquinaldol in equimolar DMSO/H_2O.

[Chlorquinaldol]/ mM	D x 10^{-10}/ m^2 s^{-1}	N_{eff}
1.0	1.95	1.00
2.5	1.66	1.08
5.0	1.38	1.19
10.0	1.00	1.40
20.0	0.56	1.86
30.0	0.26	4.79

Again, this shows that the N_{eff} value increases as the concentration of broquinaldol increases. This can be used to work out the rate constant as in chapter 4. Figure 5.19 shows that the rate constant increases as the concentration of broquinaldol concentration increases. As with chlorquinaldol, the gradient of this plot is ~ 2 indicating that broquinaldol also follows a DISP2 process.

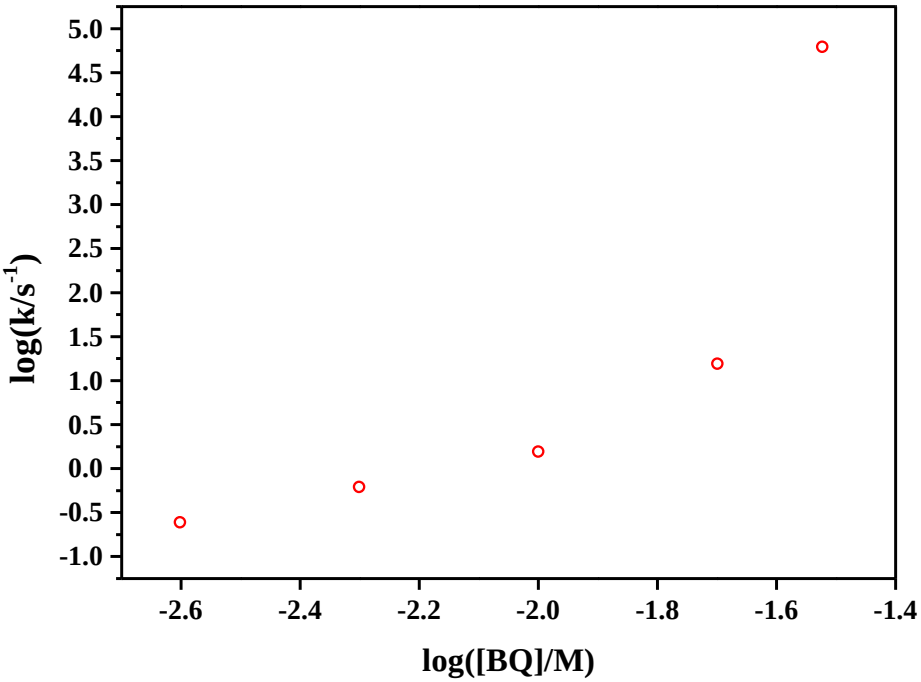

Figure 5.19 - A plot of the log of the rate constant *versus* the log of the concentration of broquinaldol (BQ) in equimolar DMSO/H_2O. Numbers generated from a DISP1 model for a macro electrode, created by J Wadhawan.

This shows how broquinaldol acts in equimolar DMSO/H_2O. The two derivatives will now be compared and applied to the detection of alkaline-earth metal ions in equimolar DMSO/H_2O.

5.2.3 Effect of alkaline – earth metals on the voltammetry of chlorquinaldol and broquinaldol

To observe the sensing capabilities of chlorquinaldol and broquinaldol in relation to the alkaline – earth metals, square wave voltammograms were obtained for sequential additions of $BaCl_2.2H_2O$ (1, 2.5, 5 and 10 mM); presented in figure 5.20.

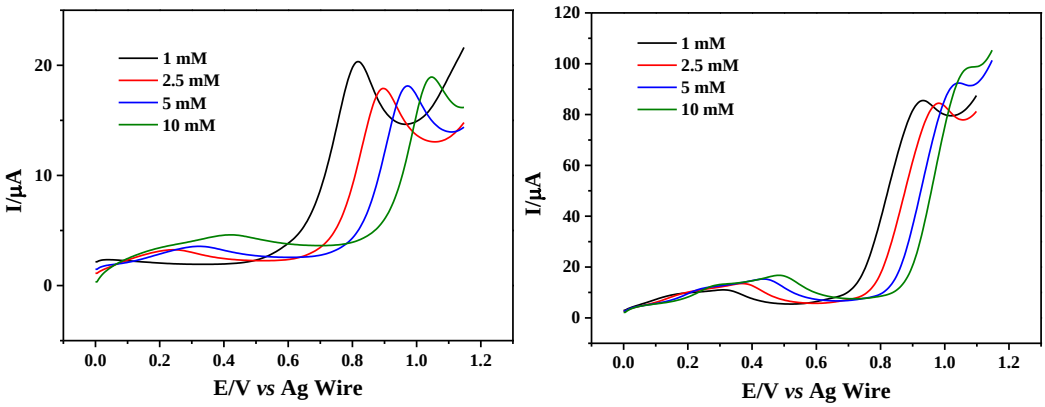

Figure 5.20 – Square wave voltammograms (f = 25 Hz) obtained for the sequential addition of $BaCl_2.2H_2O$ (1, 2.5, 5 and 10 mM) to (left) chlorquinaldol (5 mM) and (right) broquinaldol (5 mM) with TBAP (0.1 M) in equimolar DMSO/water. Performed at a glassy carbon electrode, with graphite counter and Ag wire reference at 293.15 ± 1 K.

Both molecules, chlorquinaldol and broquinaldol, exhibit an oxidative shift *versus* the Ag wire quasi-reference with increasing amounts of $BaCl_2.2H_2O$. The peak shapes produced for chlorquinaldol were much more pronounced. Both systems show an initial decrease in the peak current followed by an increase; this increase was much larger for broquinaldol.

This experiment was expanded to look at a wider range of additions of $BaCl_2.2H_2O$ (1 µM – 0.1 M). In addition to this, the mixing time for sequential additions was probed, allowing for 5, 15 and 30 minutes of mixing before results were obtained. The results for these additions, to chlorquinaldol and broquinaldol, are presented in figure 5.21. This response matches well to the shift in oxidative peak potential observed in the previous chapter for ferrocene. There is very small deviations in measured peak potentials for the same concentrations of barium chloride over time. This is evidence towards potential instability in the reference electrode caused by the addition of chloride ions to the system and not just the quasi-reference alone.

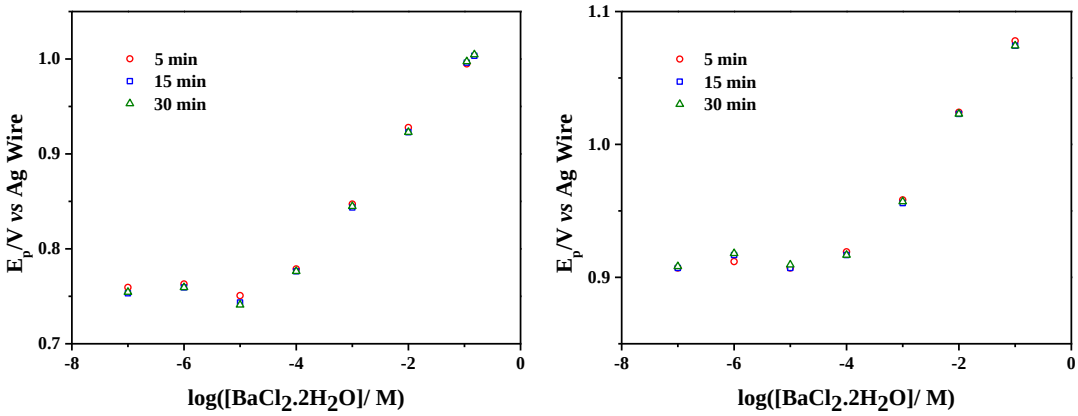

Figure 5.21 – Plots showing the shift in square wave (f = 25 Hz) peak potentials versus the log of the concentration of $BaCl_2.2H_2O$ (1 μM – 0.1 M), at varying mixing times, added to (left) chlorquinaldol (5 mM) and (right) broquinaldol (5 mM) with TBAP (0.1 M) in equimolar DMSO/water. Performed at a glassy carbon electrode, with graphite counter and Ag wire reference at 293.15 ± 1 K.

To account for the viscosity changes over this large concentration range, the viscosities of the solutions are estimated from the previous chapter and presented in table 5.3.

Table 5.3 – A table of the estimated viscosities for chlorquinaldol in equimolar DMSO/H_2O with various concentrations of $BaCl_2.2H_2O$.

[$BaCl_2.H_2O$]/M	**η/cP**
0.0	3.61
1.0×10^{-7}	3.61
1.0×10^{-6}	3.61
1.0×10^{-5}	3.61
1.0×10^{-4}	3.61
1.0×10^{-3}	3.62
1.0×10^{-2}	3.70
1.0×10^{-1}	4.52
1.1×10^{-1}	4.61
1.5×10^{-1}	4.97
2.0×10^{-1}	5.42

Using the estimated viscosities for the solutions containing the various concentrations of $BaCl_2.2H_2O$ the measured peak currents can be corrected. This produces the N_{eff} value for each solution in the same way as the last chapter in equations 4.6 and 4.7.

The N_{eff} values for chlorquinaldol and broquinaldol in the presence of various concentrations of $BaCl_2.2H_2O$ are shown in table 5.4 and figure 5.22.

Table 5.4 – A table showing the calculated N_{eff} values for chlorquinaldol (CQ) and broquinaldol (BQ) in solutions containing various amounts of $BaCl_2.2H_2O$ (0.1 μM – 0.2 M).

[$BaCl_2.H_2O$]/M	**N_{eff} (CQ)**	**N_{eff} (BQ)**
0.0	1.00	1.00
1.0×10^{-7}	0.89	0.96
1.0×10^{-6}	0.88	0.95
1.0×10^{-5}	0.84	0.90
1.0×10^{-4}	0.86	0.91
1.0×10^{-3}	0.89	0.93
1.0×10^{-2}	0.98	0.99
1.0×10^{-1}	1.38	1.21
1.1×10^{-1}	1.46	-
1.5×10^{-1}	1.62	-
2.0×10^{-1}	1.81	-

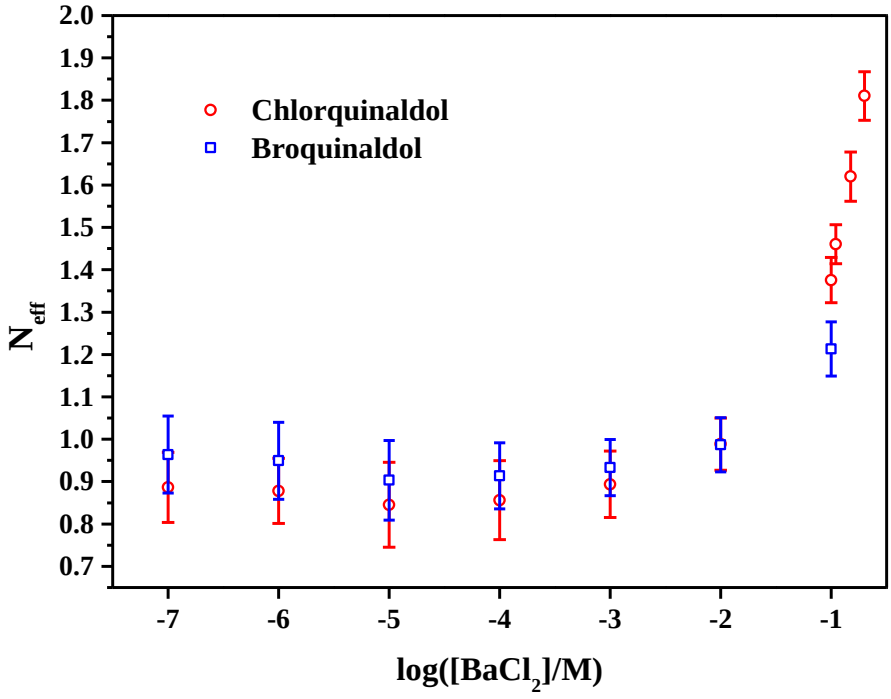

Figure 5.22 – A plot of N_{eff} for chlorquinaldol and broquinaldol *versus* the concentration of $BaCl_2.2H_2O$ in solution.

It can be seen in figure 5.22 that the N_{eff} values for both compounds are similar at low concentrations of $BaCl_2.2H_2O$ (< 10 mM). Above this concentration there is a sharper increase in the N_{eff} value for chlorquinaldol, suggesting that the chelating species (M^{2+}) may promote the kinetics of the dimerisation.

The same experiment was then undertaken on solely chlorquinaldol for the addition of other alkaline-earth metal chlorides, strontium and calcium. The shifts in the measure peak potentials are presented in figure 5.23.

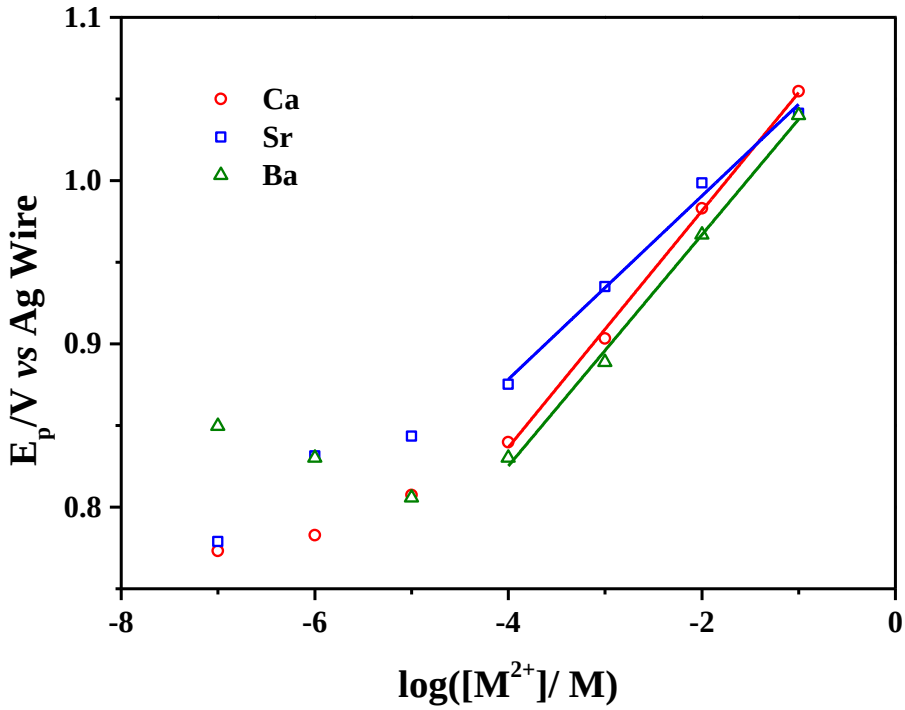

Figure 5.23 – A plot showing all the peak potential shifts for chlorquinaldol (5 mM) with TBAP (0.1 M) in equimolar DMSO/H_2O from the three studied scaling ions (Ca^{2+}, Sr^{2+} and Ba^{2+}, 0.1 μM – 0.1 M) on one plot. Performed at a glassy carbon electrode, with graphite counter and Ag wire reference at 293.15 ± 1 K.

Figure 5.23 shows that a similar trend is observed for all of the alkaline-earth metals. There is quite a bit of variation in the measure peak potentials at concentrations below 0.1 mM which is attributed to potential drift from the quasi-reference electrode. In terms of the measure peak currents, the same procedure as in table 5.4 was followed and is presented in table 5.5 and figure 5.24.

Table 5.4 – A table showing the calculated N_{eff} values for chlorquinaldol in solutions containing various amounts of $BaCl_2.2H_2O$, $CaCl_2$ and $SrCl_2$ (0.1 μM – 0.2 M).

[$BaCl_2.H_2O$]/M	N_{eff} (Ba^{2+})	N_{eff} (Sr^{2+})	N_{eff} (Ca^{2+})
0.0	1.00	1.00	1.00
1.0×10^{-7}	0.89	-	0.87
1.0×10^{-6}	0.88	0.91	0.83
1.0×10^{-5}	0.84	0.84	0.83
1.0×10^{-4}	0.86	0.82	0.83
1.0×10^{-3}	0.89	0.85	0.85
1.0×10^{-2}	0.98	0.94	0.95
1.0×10^{-1}	1.38	1.15	1.11
1.1×10^{-1}	1.46	-	
1.5×10^{-1}	1.62	-	
2.0×10^{-1}	1.81	-	

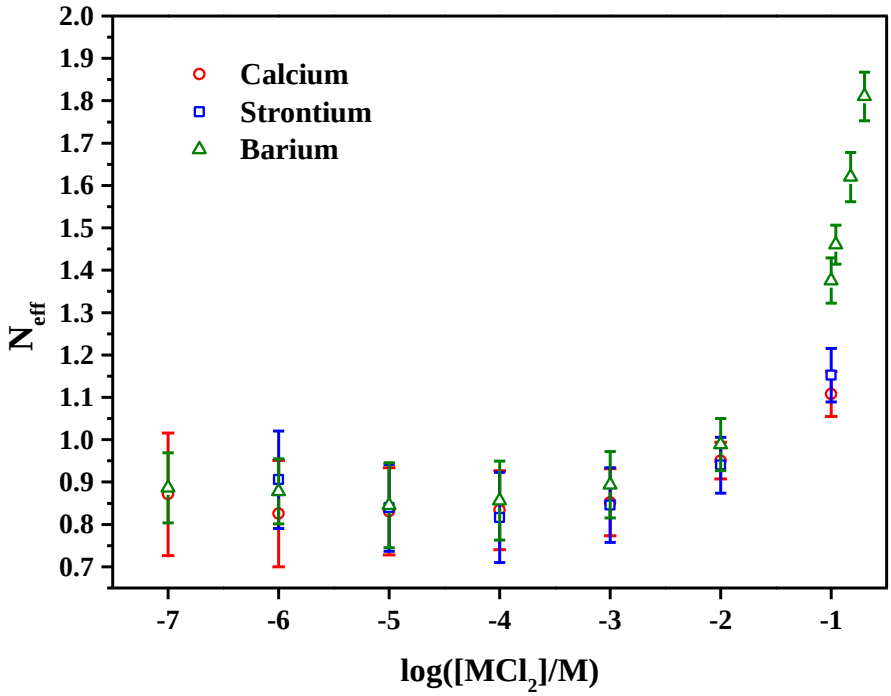

Figure 5.24 – A plot of N_{eff} for chlorquinaldol *versus* the concentration of MCl_2 in solution.

Figure 5.24 shows that for 0.1 M additions of all three alkaline-earth metal chlorides there is an increase in the calculated N_{eff} value. This observed increase is greater in the case of barium indicating the chlorquinaldol is more sensitive to the addition of this alkaline-earth metal. Strontium and calcium produce a very similar response, with strontium giving a slightly stronger shift, N_{eff} = 1.15 rather than 1.11 for calcium.

The investigations presented in this chapter to this point shows that there is a potential shift for chlorquinaldol in an equimolar DMSO/H_2O solution, similar to that seen for ferrocene in the previous chapter. There is also an increase in the N_{eff} values for chlorquinaldol, as seen for ferrocene, but to a much larger extent. Next the two systems, ferrocene and chlorquinaldol, will be added to the same solution to see if any differences are observed when they are present in the same solution.

5.2.4 Ferrocene as an internal standard

The ferrocene | ferricinium redox couple is the archetypal internal standard used in electrochemical systems where the reference is found, or thought to be, unreliable. It was known to be suitable for the use in the system probed in this chapter due to the well-defined redox potentials. The chlorquinaldol oxidation peak was found to be at approximately + 0.75 V, with the oxidation of ferrocene typically around + 0.3 V. This meant there would be no overlap in the measured peak potentials, as shown in figure 5.25.

It is clear both peaks appear in the expected areas on the potential scale, with it being easy to identify each peak by comparing the excellent known reversibility of the ferrocene | ferricinium redox couple to the irreversibility of chlorquinaldol in this solvent composition. It is important to observe whether the addition of ferrocene had any impact on the chlorquinaldol. The measured peak currents, i_p, can be compared using the reported diffusion coefficient of ferrocene of 4.4 x 10^{-10} m^2 s^{-1}.[25]

$$i_p \propto \sqrt{D}.C_0 \qquad 5.5$$

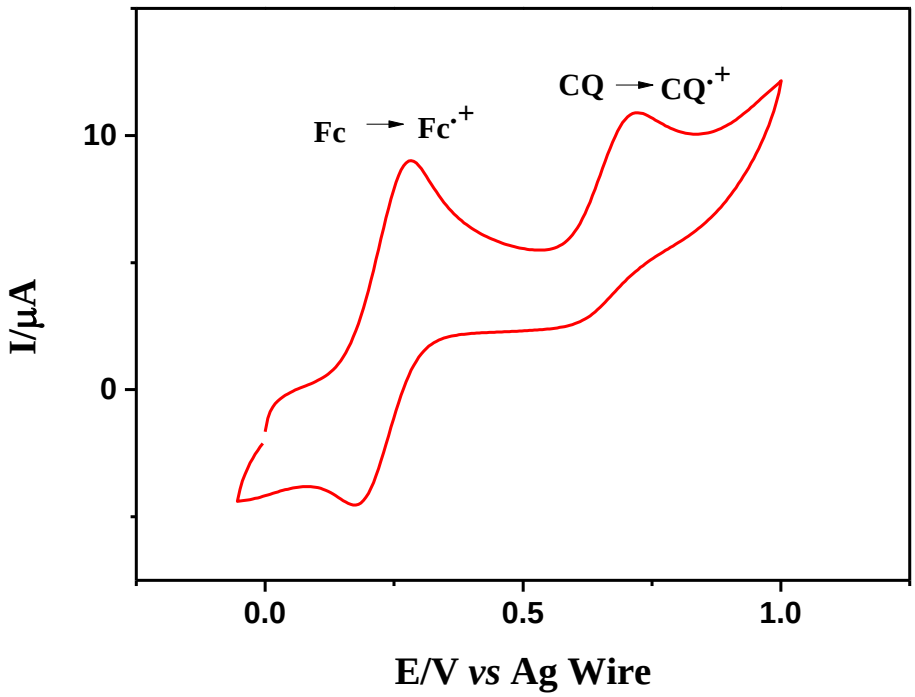

Figure 5.25 - Cyclic voltammogram (ν = 0.1 V s^{-1}) for ferrocene (1 mM) and chlorquinaldol (1 mM) with TBAP (0.1 M) in equimolar DMSO/H_2O. Performed at a glassy carbon electrode (3 mm, BASi) with graphite counter and Ag wire reference at 293.15 ± 1 K.

This produces a diffusion coefficient for chlorquinaldol of approximately 1.8 x 10^{-10} m^2 s^{-1}. This is not within experimental error of the diffusion coefficient calculated earlier of 5 ± 2 x 10^{-10} m^2 s^{-1}. This indicates that the ferrocene internal standard is having some effect on the chlorquinaldol redox couple.

5.3 Conclusions

The electrochemical response of chlorquinaldol was first studied in acetonitrile; it was found to be under diffusion control and exhibit two oxidative peaks, at + 1.05 < E/V *vs* Ag wire < + 1.15 and + 1.25 < E/V *vs* Ag wire < + 1.35 respectively, of a quasi reversible nature. The diffusion coefficient for each peak of chlorquinaldol in this system was found to be $D_1 = 4.9 \times 10^{-10}$ m^2 s^{-1} and $D_2 = 7.7 \times 10^{-10}$ m^2 s^{-1}. This diffusion was investigated further using rotating disc voltammetry with diffusion coefficients

found to be $D = 6.0 \pm 0.3 \times 10^{-10}$ m^2 s^{-1} for an n = 1 framework and $D = 3.0 \pm 0.1 \times 10^{-12}$ m^2 s^{-1} for an n = 2 framework. This showed that the calculated diffusion coefficient for chlorquinaldol fell in the middle of a one and two electron system. This was confirmed through a Wilke-Chang calculation that gave $D = 4.5 \times 10^{-10}$ m^2 s^{-1}. An ECE type mechanism was proposed for this system, figure 5.6, in which the first electron transfer step removes an electron from the phenolate group. Following this a chemical step removed a hydrogen ion from the system and the radical resonates around the fused ring system before being stabilised in the 2-position due to the effects of the methyl group, pyridine ring and lone pair on the nitrogen. The second electron transfer step is then the formation of the corresponding carbocation in this 2-position.

The electrochemical characteristics of chlorquinaldol and broquinaldol were then investigated in a DMSO: H_2O (80: 20 %) solvent composition. The electrochemistry was found to be under diffusion control; however, only one oxidation peak was found at + 0.71 < E/V *vs* Ag wire < + 0.76 and + 0.82 < E/V *vs* Ag wire < + 0.94 for chlorquinaldol and broquinaldol respectively, with a well-defined reverse peak at + 0.28 < E/V *vs* Ag wire < +0.41 for only the broquinaldol. The diffusion coefficients for chlorquinaldol and broquinaldol in this DMSO: H_2O framework were found to be $D = 5 \pm 2 \times 10^{-10}$ m^2 s^{-1} and $D = 1.3 \pm 0.2 \times 10^{-10}$ m^2 s^{-1} respectively. The mechanism proposed to explain the appearance of a single oxidation peak, figure 4.8, was identical to the acetonitrile system up until the end of the chemical step. At this point, it is proposed that a DISP1 mechanism is followed and the chlorquinaldol radical extracts a hydrogen from the chlorquinaldol cation radical to stabilize itself at the 2-position and reproduce chlorquinaldol.

The change in the electrochemical response upon the introduction of alkaline-earth metal cations was probed. It was seen, through square wave voltammetry that an oxidative shift in peak potential occurred upon the sequential addition of $BaCl_2.2H_2O$ that was stable over time for both chlorquinaldol and broquinaldol. Calculating N_{eff} for the change in the peak current showed that at high concentrations of $BaCl_2.2H_2O$ the N_{eff} value increased well above unity once the concentration was raised above 10 mM. This shift was found to be greater for chlorquinaldol than broquinaldol. In

addition to this, the N_{eff} values were calculated for the addition of $CaCl_2$ and $SrCl_2$. Both cases exhibited a similar trend to $BaCl_2.2H_2O$ in which the N_{eff} value increased above unity when the concentration of MCl_2 was above 10 mM. The largest increase in N_{eff} was observed for $BaCl_2.2H_2O$, followed by $SrCl_2$ and then $CaCl_2$.

Due to the use of a quasi reference electrode, preliminary tests using the ferrocene | ferricinium redox couple as an internal standard were performed. These showed that the ferrocene and chlorquinaldol electrochemical profiles did not appear to overlap, were at approximately their expected peak potentials and easily identifiable. Calculating the approximate diffusion coefficient of chlorquinaldol from the measured peak currents and known ferrocene diffusion coefficient showed that the chlorquinaldol diffusion coefficient did not statistically agree with the one calculated earlier. This indicated that the ferrocene could be interfering with the chlorquinaldol in some way.

In this chapter, the voltammetric response of chlorquinaldol and broquinaldol was probed, alongside the effect alkaline – earth metal cations have on this response. An oxidative shift was observed similar to the one in the previous chapter for ferrocene. This is proposed to be due to the quasi-reference electrode. Due to the unreliable nature of the quasi-reference electrode observed in the two chapters so far, sensing chemistry in an aqueous environment will be investigated. This will allow for the use of a commercial Ag | AgCl reference electrode.

5.4 References

1 T. H. E. Reactions and J. P. Phillips, *Chem. Rev.*, 1956, **56**, 271–297.

2 E. R. de Sousa, E. P. Marques, E. N. Fernandes, J. Zhang and A. L. B. Marques, *J. Braz. Chem. Soc.*, 2006, **17**, 177–183.

3 V. Arancibia, M. Zúñiga, M. C. Zúñiga, R. Segura and M. Esteban, *J. Braz. Chem. Soc.*, 2010, **21**, 255–261.

4 Q. Fernando and J. P. Phillips, *J. Am. Chem. Soc.*, 1952, **74**, 3103–3105.

5 R. M. Dagnall and S. K. Hasanuddin, *Talanta*, 1968, **15**, 1025–1029.

6 S. L. Gupta and P. S. Raghavan, *Electrochim. Acta*, 1971, **16**, 1613–1618.

7 P. Bosserman, D. T. Sawyer and A. L. Page, *Anal. Chem.*, 1978, **50**, 1300–1303.

8 Y. Nagaosa and K. Kobayashi, *Talanta*, 1984, **31**, 593–596.

9 C. M. G. Van Den Berg, *J. Electroanal. Chem. Interfacial Electrochem.*, 1986, **215**, 111–121.

10 B. Magyar and P. Richner, *Mikrochim. Acta*, 1987, **92**, 121–131.

11 M. G. van den Berg, *Analyst*, 1989, **114**, 1527.

12 Z. Navrátilová and M. Kopanica, *Anal. Chim. Acta*, 1991, **244**, 193–196.

13 J. Wang, *Talanta*, 1992, **39**, 801–804.

14 M. G. Paneli and A. Voulgaropoulos, *Electroanalysis*, 1993, **5**, 355–373.

15 Z. P. Yang, M. Alafandy, K. Boutakhrit, J.-M. Kauffmann and J. Arcos, *Electroanalysis*, 1996, **8**, 25–29.

16 J. T. Stock, *J. Chem. Soc.*, 1949, 586.

17 S. Guo, X. Wu, J. Zhou, J. Wang, B. Yang and B. Ye, *J. Electroanal. Chem.*, 2011, **655**, 45–49.

18 M. C. Stević, L. M. Ignjatović, G. Ćirić-Marjanović, S. M. Stanišić, D. M. Stanković and J. Zima, *Int. J. Electrochem. Sci.*, 2011, **6**, 2509–2525.

19 S. Hammond, *Trans. Faraday Soc.*, 1953, **77**, 334–338.

20 V. Prachayasittikul, S. Prachayasittikul, S. Ruchirawat and V. Prachayasittikul, *Drug Des. Devel. Ther.*, 2013, **7**, 1157–1178.

21 G. Malecki, J. E. Nycz, E. Ryrych, L. Ponikiewski, M. Nowak, J. Kusz and J. Pikies, *J. Mol. Struct.*, 2010, **969**, 130–138.

22 K. Miyabe and R. Isogai, *J. Chromatogr. A*, 2011, **1218**, 6639–6645.

23 K. Miyabe and R. Isogai, *J. Chromatogr. A*, 2011, **1218**, 6639–6645.

24 R. Sitaraman, S. H. Ibrahim and N. R. Kuloor, *J. Chem. Eng. Data*, 1963, **8**, 198–201.

25 N. G. Tsierkezos, *J. Solution Chem.*, 2007, **36**, 289–302.

6 Characterisation of the ferrocenemethanol and thiol interaction through cyclic voltammetry and its application toward alkaline-earth metal ion detection

In the previous chapter the possibility of using the chelation between chlorquinaldol and alkaline–earth metal ions was investigated. Due to the aqueous nature of the desired application of this work, the following chapter looks to assess the use of ferrocenemethanol (a more water soluble derivative of ferrocene). This will follow an amperometric route, utilising thiol containing compound (tiopronin) as a redox catalyst. In addition to characterising the interaction of tiopronin and ferrocenemethanol; the ability of the system to detect barium ions in aqueous solution will be probed.

6.1 Introduction

The IUPAC recommended redox couple ferrocene | ferricinium redox couple was explored in chapter 4.[1,2] Ferrocenemethanol, figure 6.1, is a common, water soluble, derivative of ferrocene that exhibits a well-defined, chemically reversible, one-electron electrochemical process.[3] Previously, ferrocenemethanol (FcMeOH) has been utilised as a mediator in aqueous environments due to its fast heterogeneous and homogeneous electron transfer kinetics and stability in both the oxidised and reduced forms.[4,5]

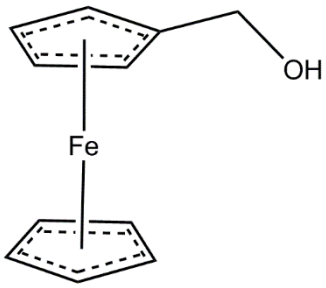

Figure 6.1 – Skeletal structure of ferrocenemethanol.

Tiopronin (α-mercaptopropionylglycine), figure 6.2, is a synthetic compound known to be a potent free radical scavenger.[6] It is commonly utilised in the treatment of cystinuria.[7–10] Patients affected by cystinuria excrete increased concentrations of cysteine in their urine, which increases the risk of kidney stone formation.[11,12] Tiopronin aids in reducing the concentration of cysteine through the free thiol group forming a more soluble disulphide complex.[13]

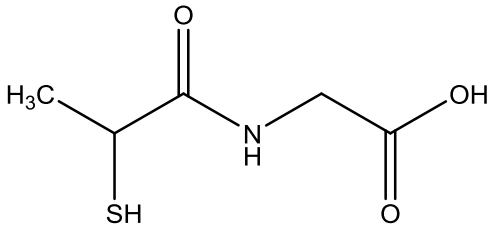

Figure 6.2 – Skeletal structure of tiopronin.

Tiopronin can act as a terdentate ligand above pH 12 through the deprotonation of the amide; below this pH, coordination occurs in a bidentate manner through the deprotonated thiol and carbonyl.[14] The thiol group of tiopronin has a lower pK_a (8.33)[14] than many thiol containing molecules;[15] due to the stabilisation effects afforded by the amide group.[16] Tiopronin has been observed to form complexes with Ni^{2+}, Co^{2+} and Cu^{2+} through the bidentate coordination mentioned above.[14,17,18] It has been shown computationally that, under physiological conditions (pH 7.4), the most stable complexes of tiopronin with Cu^{2+} occur *via* coordination through the deprotonated thiol group in a square planar geometry.[16]

Thiol determination *via* direct oxidation at a solid electrode is plagued by poor voltammetric behaviour, electrode fouling and the requirement for large overpotentials.[19] As such, alternative methods have been investigated using electrochemical indicators,[20] derivatization,[21] enzymes[22] and mediators. Mediators facilitate electron transfer in the system through shuttling electrons between the substrate and electrode. The thiol compound will be oxidised by the mediator; which is then regenerated at the electrode surface, figure 6.3. The oxidation current is therefore directly related to the thiol concentration.[19]

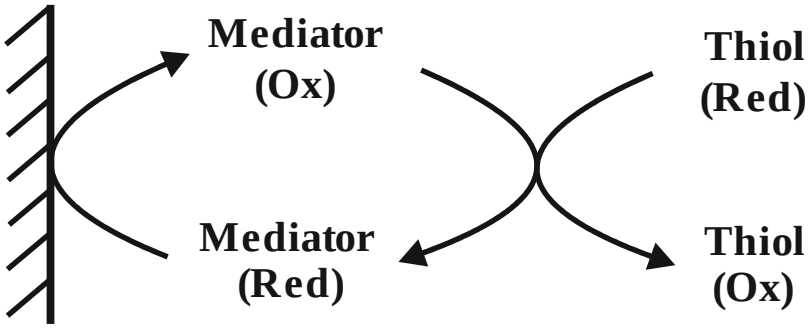

Figure 6.3 - A schematic representing the oxidation of a thiol *via* a mediator. The mediator is then regenerated at the electrode surface.

This chapter investigates the relationship between ferrocenemethanol and tiopronin; and whether this combination can be manipulated for the detection of alkaline-earth metal ions. Ferrocene derivatives have been shown to follow an EC' mechanism in conjunction with the thiol containing L-cysteine.[23] First the interaction between ferrocenemethanol and tiopronin will be probed *via* cyclic voltammetry to establish the occurrence of redox catalysis. Following this, barium nitrate will be added to the solutions and observed through cyclic voltammetry and square wave voltammetry. Barium nitrate is used as a barium source in place of barium chloride due to the effect chloride ions had on the ferrocene redox couple, explored in chapter 4. It is expected that the system containing ferrocenemethanol and tiopronin will follow the same mechanism as ferrocene derivatives and L-cysteine. Prior to results it is important to consider the electron transfer mechanism underpinning this chapter; the EC' mechanism, which is explained in detail in chapter 2.

6.2 Results and Discussion

6.2.1 Electrochemical characterisation

The cyclic voltammetric response, figure 6.4, of unbuffered ferrocenemethanol (0.5 mM) was investigated at various scan rates (0.02 - 0.3 V s^{-1}) in aqueous KCl (0.1 M) at glassy carbon electrode (3 mm, BAS) at 293.15 ± 1 K. The voltammetric response exhibited a single oxidation wave at + 0.22 V and the corresponding single reduction peak at + 0.14 V *versus* a silver | silver chloride reference electrode. This is

attributed to the ferrocenemethanol | ferriciniummethanol redox couple with $E_{mid} = 1/2(E_p^{Ox} + E_p^{Red}) = + 0.18$ V.

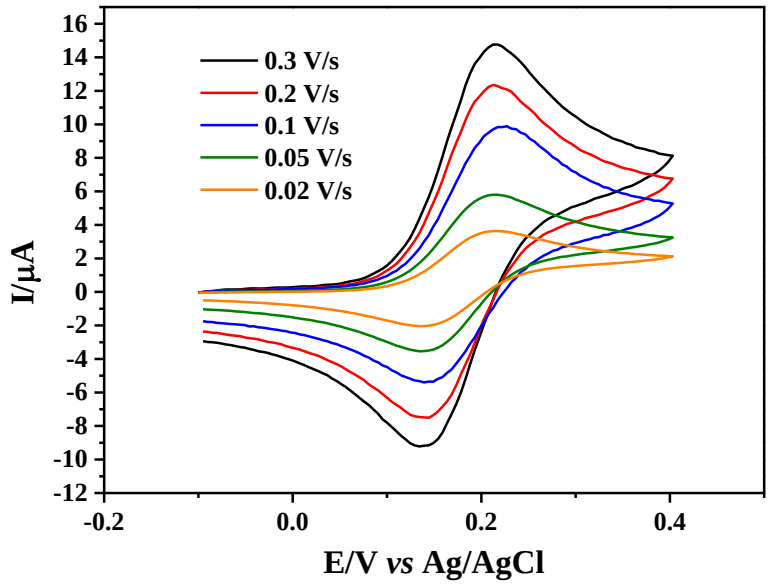

Figure 6.4 - Cyclic voltammograms for unbuffered ferrocenemethanol (0.5 mM) in water with KCl (0.1 M). Performed at a glassy carbon electrode (3 mm, BAS) with a graphite counter and Ag|AgCl (BAS) reference electrode at 293.15 ± 1 K.

The peak potentials for the single electron oxidation and corresponding reduction are plotted against the decadic logarithm of the scan rate (ν), figure 6.5 (left). The minimal deviation in peak potentials (< 4 mV) indicates an electrochemically reversible process; however, the peak-to-peak separation is greater than 59 mV, $\Delta E = 76.6 \pm 3$ mV. This could be explained by a variation in the diffusion coefficients between the oxidised and reduced forms, which has been shown to change by a factor of 3 for the ferrocene | ferricinium redox couple.[24] The peak current was found to be linear with the square root of the scan rate, figure 6.5 (right). This indicates that both the oxidation and reduction processes are of a diffusion-controlled nature. The ratio of anodic peak current to cathodic peak current, $I_p^a/I_p^c = 1.06 \pm 0.07$, being almost unity is more evidence of an almost electrochemically reversible system. The plot of peak current *versus* the square of the scan rate allowed for the elucidation of the diffusion coefficient *via* the Randle-Sevcik equation, $D_{FcMeOH} = 8.21 \pm 1 \times 10^{-6}$ cm^2 s^{-1}; which is in good agreement with literature.[25]

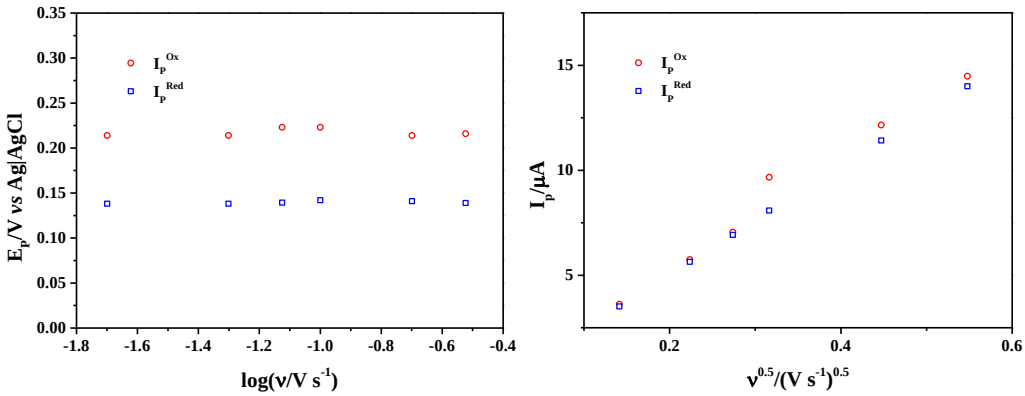

Figure 6.5 - Plot of oxidative and reductive peak potential, E_p, versus the log of the scan rate (left) and peak current, I_p, versus the square root of the scan rate (right) for ferrocenemethanol (0.5 mM) in aqueous KCl (0.1 M). Performed at a glassy carbon working electrode (3 mm, BASi), with a graphite counter electrode and Ag|AgCl reference electrode (BAS) at 293.15 ± 1 K.

The effect that tiopronin (0.5 - 16 mM) has on the ferrocenemethanol | ferriciniummethanol (0.5 mM) redox couple was investigated *via* cyclic voltammetry. The voltammograms obtained for the systems containing 4 mM and 16 mM tiopronin are presented in figures 6.6 and 6.7 respectively. There are trends present in how the voltammograms obtained change in regards to both the peak potentials, E_p, peak currents, I_p, and the waveshapes. These changes in the waveshape indicate a change in electron transfer mechanism of the ferrocenemethanol | ferriciniummethanol redox couple from an E process.

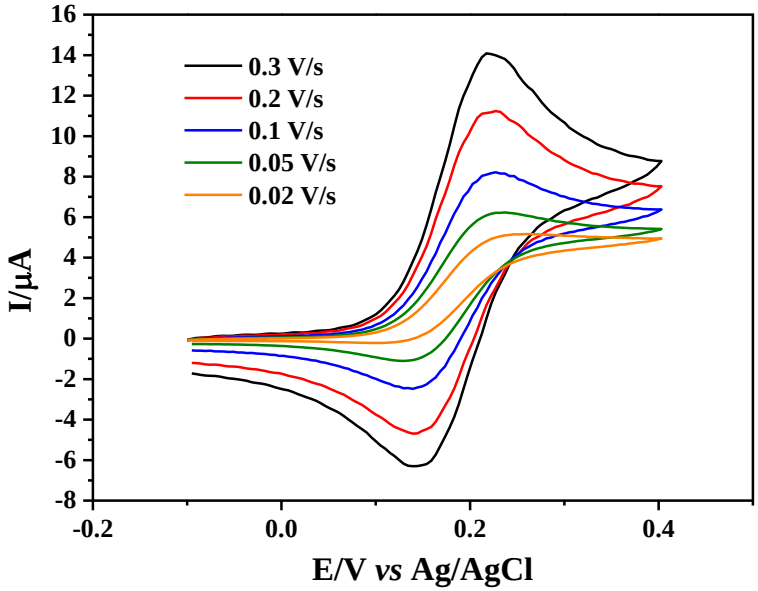

Figure 6.6 - Cyclic voltammograms (ν = 0.02 – 0.3 V s^{-1}) for unbuffered ferrocenemethanol (0.5 mM) in aqueous KCl (0.1 M) with tiopronin (4 mM). Performed at a glassy carbon electrode (3 mm, BAS) with a graphite counter and Ag|AgCl (BAS) reference electrode at 293.15 ± 1 K.

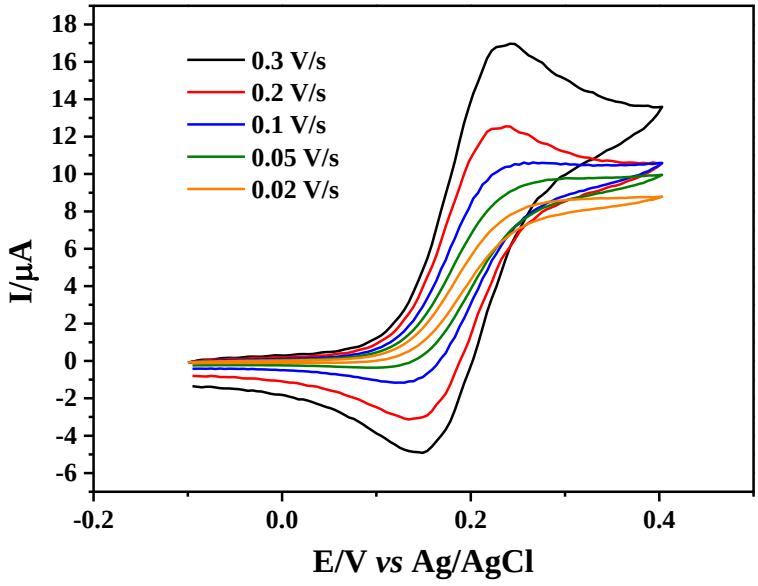

Figure 6.7 - Cyclic voltammograms (ν = 0.02 – 0.3 V s^{-1}) for unbuffered ferrocenemethanol (0.5 mM) in aqueous KCl (0.1 M) with tiopronin (16 mM). Performed at a glassy carbon electrode (3 mm, BAS) with a graphite counter and Ag|AgCl (BAS) reference electrode at 293.15 ± 1 K.

One of the key changes in the cyclic voltammetric response of a system that indicates the presence of the EC' electron transfer mechanism is an increase in the peak oxidative current, I_p^{ox}. This is due to the catalytic effect of the system. The increase of the peak current with the addition of 4 mM and 16 mM tiopronin are represented by the ratio between their peak current, I_p^{Tio}, and the peak current with no tiopronin present, I_p^{Blank}, at different scan rates, figure 6.8. This refers to the turnover number (TON) of the system. The variations in the turnover number for increasing excess factors, γ, of catalyst at different scan rates are shown in table 6.1.

It can be seen from table 6.1 and in figure 6.8 that the turnover number increases with increasing excess factor, with the most pronounced increase occurring at lower scan rates and, therefore, higher kinetic parameters, λ; giving a $k_{EC'} \sim 10^2$-10^3 M^{-1} s^{-1}.

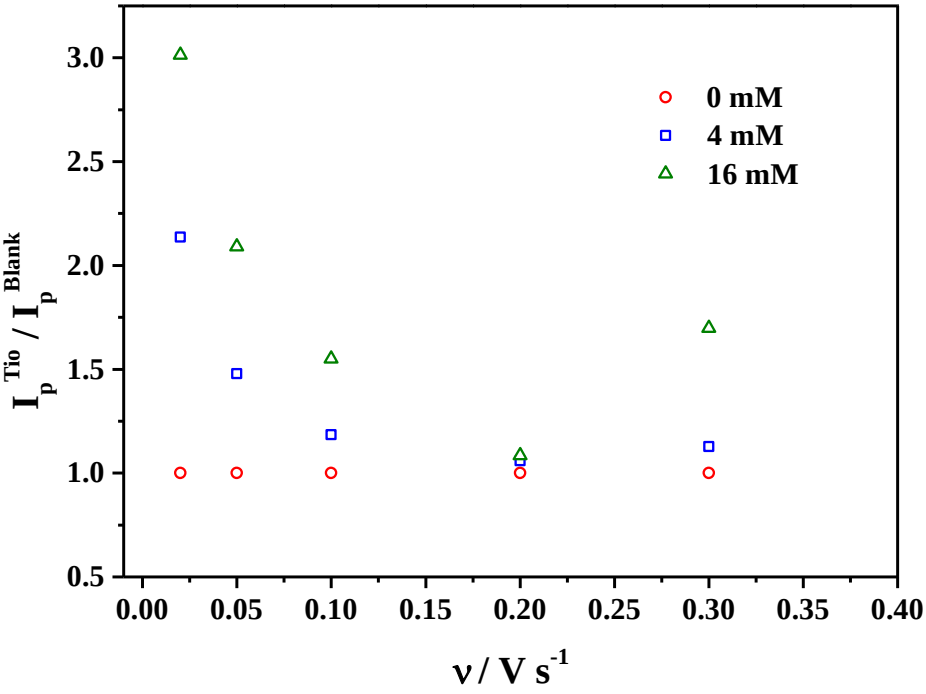

Figure 6.8 - Plot of the ratio of peak current for ferrocenemethanol (0.5 mM) in aqueous KCl (0.1 M) with and without tiopronin (0, 4 and 16 mM) present (I_p^{Tio}/I_p^{Blank}) versus the scan rate. Performed at a glassy carbon working electrode (3 mm, BASi), with a graphite counter electrode and Ag|AgCl reference electrode (BAS) at 293.15 ± 1 K.

Table 6.1 - A table compiling the peak currents, excess factors and turnover number for solutions of ferrocenemethanol (0.5 mM) in the presence of different concentrations of tiopronin (0.5 - 16 mM) at various scan rates (0.02 - 0.3 V s^{-1}).

[FcMeOH]/ mM	[Tiopronin]/ mM	ν/ V s^{-1}	I_p^{Ox}/ μA	γ	I_p^{Ox}/I_p^0
0.5	0	0.02	3.34	0	1.00
0.5	0	0.05	5.36	0	1.00
0.5	0	0.075	6.67	0	1.00
0.5	0	0.1	8.29	0	1.00
0.5	0	0.2	11.4	0	1.00
0.5	0	0.3	14.0	0	1.00
0.5	0.5	0.02	4.06	1	1.22
0.5	0.5	0.05	5.96	1	1.11
0.5	0.5	0.075	6.66	1	1.00
0.5	0.5	0.1	8.10	1	0.97
0.5	0.5	0.2	11.0	1	0.97
0.5	0.5	0.3	13.9	1	0.99
0.5	1	0.02	5.85	2	1.75
0.5	1	0.05	6.92	2	1.29
0.5	1	0.075	7.97	2	1.19
0.5	1	0.1	8.37	2	1.01
0.5	1	0.2	12.4	2	1.08
0.5	1	0.3	14.3	2	1.02
0.5	2	0.02	4.77	4	1.43
0.5	2	0.05	5.95	4	1.11
0.5	2	0.075	7.47	4	1.12
0.5	2	0.1	8.08	4	0.98
0.5	2	0.2	11.4	4	1.00
0.5	2	0.3	14.6	4	1.05
0.5	4	0.02	7.12	8	2.14
0.5	4	0.05	7.93	8	1.48
0.5	4	0.075	8.57	8	1.28
0.5	4	0.1	9.83	8	1.19
0.5	4	0.2	12.1	8	1.06
0.5	4	0.3	15.8	8	1.13
0.5	16	0.02	10.1	32	3.01
0.5	16	0.05	11.2	32	2.09
0.5	16	0.075	12.3	32	1.85
0.5	16	0.1	12.9	32	1.55
0.5	16	0.2	12.4	32	1.08
0.5	16	0.3	23.7	32	1.70

At the highest kinetic parameter (which is the slowest scan rate investigated, 0.02 V s^{-1}), the peak current, when the excess factor is 32, is 3.01 times larger than when no tiopronin is present. This implies that once the ferrocenemethanol is oxidised

to ferriciniummethanol, the tiopronin will reduce it allowing for a larger concentration of ferrocenemethanol at the electrode surface. As the kinetic parameter decreases this ratio tends towards unity; consequently, as the reaction time is reduced, the turnover number is reduced too. This is a common response of an EC' electron transfer and describes characteristics similar to that of the KD zone in figure 2.19.[26] The change in the measured peak potentials for the ferrocenemethanol | ferriciniummethanol (0.5 mM) redox couple in the presence of various amounts of tiopronin (0.5 - 16 mM) are presented in table 6.2.

Table 6.2 - A table compiling the peak potentials and peak-to-peak separation for solutions of ferrocenemethanol (0.5 mM) in the presence of different concentrations of tiopronin (0.5 - 16 mM) at various scan rates (0.02 - 0.3 V s^{-1}).

γ	ν/ V s^{-1}	E_p^{Ox}/ V	E_p^{Red}/ V	ΔE/ mV	E_{mid}/ V
0	0.02	0.213	0.138	75	0.176
0	0.05	0.214	0.137	77	0.176
0	0.1	0.222	0.141	81	0.182
0	0.2	0.213	0.138	75	0.176
0	0.3	0.215	0.138	77	0.177
1	0.02	0.223	0.130	93	0.177
1	0.05	0.221	0.132	89	0.177
1	0.1	0.217	0.133	84	0.175
1	0.2	0.213	0.133	80	0.173
1	0.3	0.215	0.135	80	0.175
2	0.02	0.222	0.142	80	0.182
2	0.05	0.225	0.141	84	0.183
2	0.1	0.220	0.141	79	0.181
2	0.2	0.218	0.143	75	0.181
2	0.3	0.221	0.142	79	0.182
4	0.02	0.227	0.138	89	0.183
4	0.05	0.222	0.142	80	0.182
4	0.1	0.221	0.143	78	0.182
4	0.2	0.219	0.143	76	0.181
4	0.3	0.221	0.145	76	0.183
8	0.02	0.248	0.109	139	0.179
8	0.05	0.233	0.130	103	0.182
8	0.1	0.226	0.138	88	0.182
8	0.2	0.223	0.141	82	0.182
8	0.3	0.221	0.143	78	0.182
32	0.02	0.306	0.075	231	0.191
32	0.05	0.293	0.098	195	0.196
32	0.1	0.266	0.124	142	0.195
32	0.2	0.234	0.137	97	0.186
32	0.3	0.234	0.145	89	0.190

Below 4 mM tiopronin there was no deviation in E_{mid} = + 0.18 V or the peak-to-peak separation, ΔE = 76.6 ± 3 mV. For the addition of 16 mM tiopronin, there is a shift in E_{mid} to a larger oxidative potential, E_{mid} = + 0.19 V. In both the 4 mM and 16 mM addition of tiopronin there is a larger peak-to-peak separation as the scan rate is decreased; with the largest separation observed for the 0.02 V s^{-1} scan rate (13.9 mV for 4 mM tiopronin and 23.1 mV for 16 mM tiopronin), figure 6.9. These shifts are expected for this EC' reaction scheme.

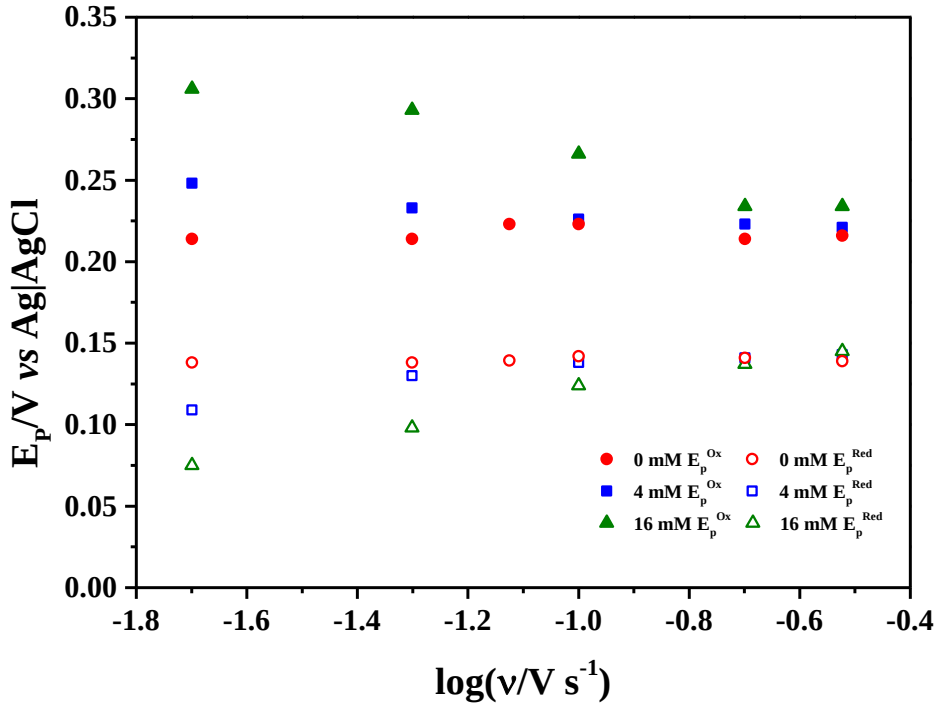

Figure 6.9 - Plot of oxidative and reductive peak potential, E_p, versus the log of the scan rate for ferrocenemethanol (0.5 mM) in aqueous KCl (0.1 M) with varied amounts of tiopronin (0, 4 and 16 mM). Performed at a glassy carbon working electrode (3 mm, BASi), with a graphite counter electrode and Ag|AgCl reference electrode (BAS) at 293.15 ± 1 K.

This change in the peak-to-peak separation is accompanied by an alteration of the wave-shape. It can be seen that the waveshape changes from a classical reversible peak shape, observed in zone D in figure 2.19, towards a more sigmoidal shaped wave, observed in zone KS in figure 2.19, as the concentration of tiopronin is increased and the scan rate is decreased.

The evidence of an increase in E_{mid}, the peak-to-peak separation and the peak oxidative current are all indicative of an EC' type reaction. They are compatible with a scenario where no substrate is consumed and the wave-shape is dependent on the reaction kinetics of the chemical step, where RFc corresponds to ferrocenemethanol and RSH represents tiopronin.

$$RFc - e^- \rightleftharpoons RFc^+ \quad 6.1$$

$$RFc^+ + RSH \xrightarrow{slow} RFC + RSH^{\cdot +} \quad 6.2$$

$$RSH^{\cdot +} \rightarrow RS^{\cdot} + H^+ \quad 6.3$$

$$2RS^{\cdot} \rightarrow RSSR \quad 6.4$$

In this way, as the scan rate is increased, the wave-shape tends toward the KD zone.

The effects that changes in the scan rate and tiopronin concentration have on the cyclic voltammetric response of ferrocenemethanol have been observed. It is important to consider how the pH of the solution will alter the structure and reactivity of the tiopronin. The thiol group of tiopronin has a pKa of 8.33; therefore, at pH 6 the protonated form will dominate and at pH 9 the thiolate (deprotonated form) will dominate.

$$RSH \rightleftharpoons RS^- + H^+ \quad 6.5$$

The thiolate group is more nucleophilic and easier to oxidise than the thiol group and therefore, possesses enhanced electron donating abilities. In the chemical step of the EC' mechanism, the thiolate will now act as the electron donor to reduce the ferriciniummethanol. It is therefore expected that with the increased reactivity of the thiolate, the regeneration of ferrocenemethanol should be enhanced, resulting in an increased peak current.

The cyclic voltammetric response of ferrocenemethanol (0.5 mM) with KCl (0.1 M) in pH 6 ammonium chloride (0.1 M) buffer and pH 9 borate (0.1 M) buffer in the presence of tiopronin (4 mM) at 0.02 V s^{-1} and 0.1 V s^{-1} are presented in figure 6.10 and 6.11 respectively.

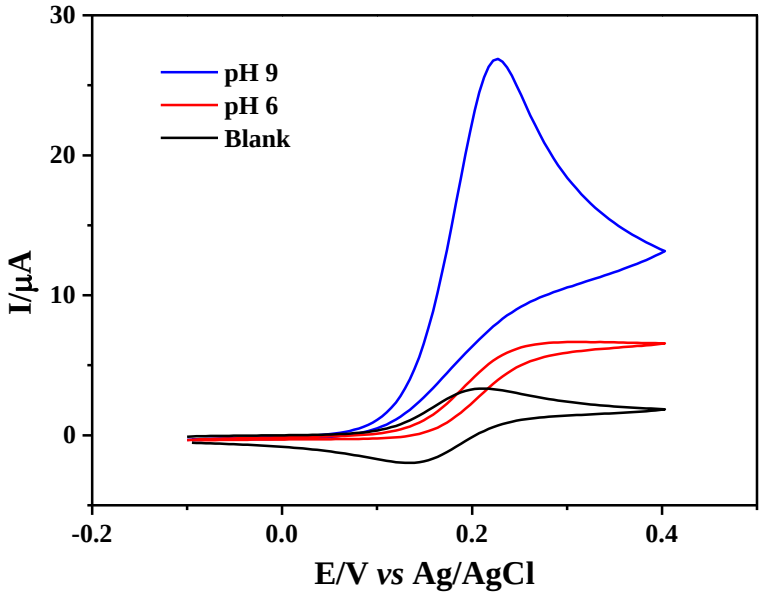

Figure 6.10 - Cyclic voltammograms for ferrocenemethanol (0.5 mM) with KCl (0.1 M) in pH 6 ammonium chloride (0.1 M) buffer and pH 9 borate (0.1 M) buffer in the presence of tiopronin (4 mM) at 0.02 V s^{-1} Performed at a glassy carbon electrode (3 mm, BAS) with a graphite counter and Ag|AgCl (BAS) reference electrode at 293.15 ± 1 K.

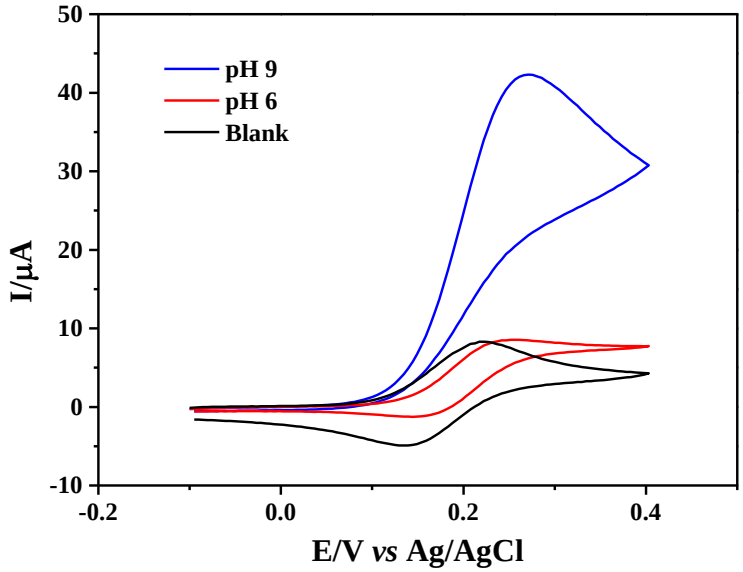

Figure 6.11 - Cyclic voltammograms for ferrocenemethanol (0.5 mM) with KCl (0.1 M) in pH 6 ammonium chloride (0.1 M) buffer and pH 9 borate (0.1 M) buffer in the presence of tiopronin (4 mM) at 0.1 V s^{-1} Performed at a glassy carbon electrode (3 mm, BAS) with a graphite counter and Ag|AgCl (BAS) reference electrode at 293.15 ± 1 K.

It can be seen in both figure 6.10 and 6.11 that the peak current is greatly increased when the solution is at pH 9 with tiopronin compared to pH 6 and just ferrocenemethanol. The turnover numbers for each case shown in figures 6.10 and 6.11 are presented in table 6.3.

Table 6.3 - A table compiling the peak currents, excess factors and turnover number for solutions of ferrocenemethanol (0.5 mM) with tiopronin (4 mM) unbuffered, at pH 6 and pH 9 at two scan rates (0.02 and 0.1 V s^{-1}).

pH	**[FcMeOH]/ mM**	**[Tiopronin]/ mM**	**ν/ V s^{-1}**	**I_p^{Ox}/ μA**	**γ**	**I_p^{Ox}/I_p^0**
N/A	0.5	0	0.02	3.34	8	1.00
6	0.5	4	0.02	6.96	8	2.09
9	0.5	4	0.02	26.5	8	7.95
N/A	0.5	0	0.1	8.29	8	1.00
6	0.5	4	0.1	8.58	8	2.57
9	0.5	4	0.1	43.5	8	5.25

The turnover numbers observed for both the 0.02 and 0.1 V s^{-1} scan rates at pH 9 (7.95 and 5.25 respectively) is much larger than that observed at pH 6 (2.09 and 2.57 respectively). In this way the system at pH 6 has an estimated $k_{EC'} \sim 10^2$ M^{-1} s^{-1} and pH 9 has an estimated $k_{EC'} \sim 10^3$ M^{-1} s^{-1}. This is evidence toward the thiolate being a better catalyst than the thiol in this EC' system.

The oxidative peak potentials for pH 6 shift to higher potentials, + 0.32 V for 0.02 V s^{-1} and + 0.25 V for 0.1 V s^{-1} than ferrocenemethanol on its own which remained constant at + 0.22 V. This trend is consistent with the unbuffered systems explored previously, where the peak potential was increasingly oxidatively shifted as you decreased the scan rate. The opposite trend is observed for the system at pH 9, where the oxidative potential decreases as the scan rate is decreased; from + 0.27 V to + 0.23 V for 0.1 V s^{-1} and 0.02 V s^{-1} respectively.

There is also a change in waveshape when you change from pH 6 to pH 9. The shape of the wave at pH 6 is reminiscent of the ones in the unbuffered system, where as the scan rate is decreased, the waveshape tends toward a sigmoidal shape; this was linked

to the KS zone in the kinetic zone diagram, figure 2.19. At pH 9, there is a peak shape that reaches a maximum before decreasing due to the competition between the consumption of the substrate through the rate determining step and the diffusion of the substrate from the bulk solution to the electrode surface. In addition to this there is no reverse redox process observed due to the catalytic turnover. These traits are characteristic of a system in the K zone of the kinetic zone diagram in figure 2.19.

The cyclic voltammetric response of ferrocenemethanol has been observed in the presence of tiopronin at different pH. It is known that tiopronin can form complexes with some metal ions, including Cu, Ni and Co.[14, 17, 18] It is proposed that if tiopronin forms complexes with the alkaline-earth metal ions that this will impede the ability for it to act as a catalyst in the reduction of ferriciniummethanol. This will be reflected in a decrease in the turnover number as the excess factor is reduced. Figure 6.7 showed that 16 mM of tiopronin was enough to produce sigmoidal shaped voltammograms for scan rates up to 0.1 V s^{-1} which is not desired for the next section. It was decided therefore that 4 mM tiopronin will be used going forward. Initially the cyclic voltammetric response of ferrocenemethanol with tiopronin (4 mM) was observed in the presence of increasing concentrations of Ba^{2+}.

6.2.2 Barium detection

As mentioned above, tiopronin has been seen to coordinate with some metal 2+ cations. If tiopronin binds to alkaline-earth metal cations then it will be taken away from the EC' mechanism seen earlier. This would result in a decrease in the peak current and turnover numbers recorded. The effect of Ba^{2+} on the cyclic voltammetric response of the ferrocenemethanol and tiopronin system was investigated. Cyclic voltammograms of ferrocenemethanol (0.5 mM) in the presence of tiopronin (4 mM) and various amounts of barium nitrate ($Ba(NO_3)_2$, 1 μM - 1 M) at pH 6 after 3 hours incubation are presented in figure 6.12.

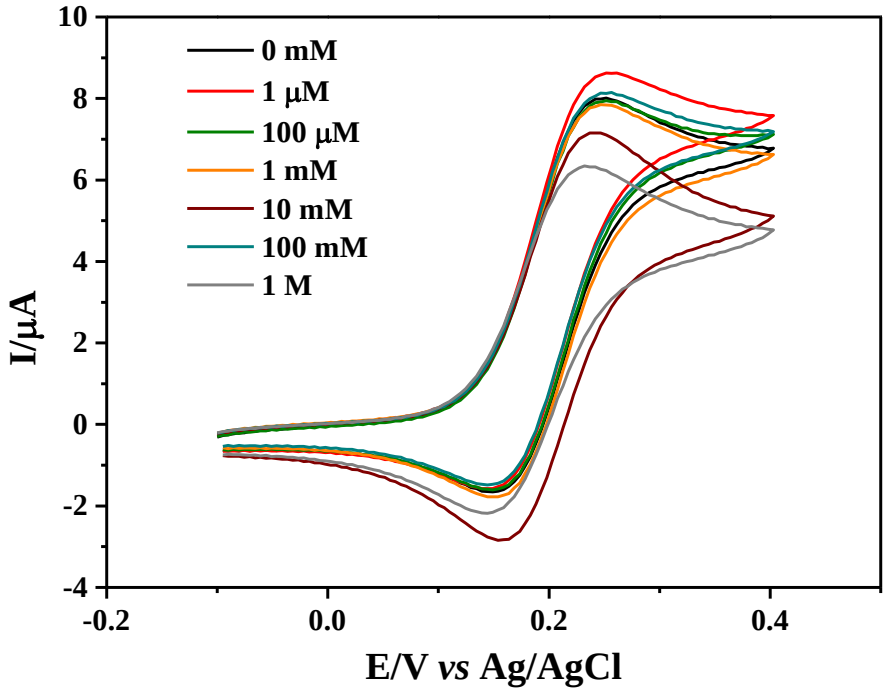

Figure 6.12 - Cyclic voltammograms (ν = 0.1 V s^{-1}) for ferrocenemethanol (0.5 mM) with KCl (0.1 M), tiopronin (4 mM) and various additions of $Ba(NO_3)_2$ (1 µM - 1 M, 3 h incubation) in ammonium chloride buffer (pH = 6, 0.1 M). Performed at a glassy carbon electrode (3 mm, BAS) with a graphite counter and Ag|AgCl (BAS) reference electrode at 293.15 ± 1 K.

There is no discernible trend present in figure 6.12, with the only statistically significant decrease in peak current from the blank system occurring for the 1 M addition of $Ba(NO_3)_2$. This is reflected in the calculated turnover numbers for the results obtained at 0.02 and 0.1 V s^{-1} scan rates are presented in table 6.4.

Table 6.4 - A table compiling the peak currents, excess factors and turnover number for solutions of ferrocenemethanol (0.5 mM) with tiopronin (4 mM) at pH 6 with various additions of $Ba(NO_3)_2$ (1 μM – 1 M).

pH	[FcMeOH]/ mM	[Tiopronin]/ mM	[$Ba(NO_3)_2$]/ M	ν/ V s^{-1}	I_p^{Ox}/ μA	I_p^{Ox}/I_p^0
N/A	0.5	0	0	0.02	3.34	1.00
N/A	0.5	0	0	0.1	8.29	1.00
6	0.5	4	0	0.02	6.96	2.09
6	0.5	4	1×10^{-6}	0.02	5.28	1.58
6	0.5	4	1×10^{-5}	0.02	11.6	3.48
6	0.5	4	1×10^{-4}	0.02	7.01	2.10
6	0.5	4	1×10^{-3}	0.02	5.52	1.65
6	0.5	4	1×10^{-2}	0.02	4.60	1.38
6	0.5	4	1×10^{-1}	0.02	6.18	1.85
6	0.5	4	1	0.02	3.86	1.16
6	0.5	4	0	0.1	8.58	2.57
6	0.5	4	1×10^{-6}	0.1	8.09	2.43
6	0.5	4	1×10^{-5}	0.1	12.5	3.76
6	0.5	4	1×10^{-4}	0.1	8.89	2.66
6	0.5	4	1×10^{-3}	0.1	7.75	2.32
6	0.5	4	1×10^{-2}	0.1	7.18	2.15
6	0.5	4	1×10^{-1}	0.1	8.05	2.41
6	0.5	4	1	0.1	6.35	1.90

It can be seen from table 6.4 that for both scan rates tested there is a large turnover number in the absence of barium nitrate, 2.09 for 0.02 V s^{-1} and 2.57 for 0.1 V s^{-1}. This value remains constant within statistical error for all the additions of barium except two. For the addition of 10 μM, the turnover number increases to 3.48 for 0.02 V s^{-1} and 3.76 for 0.1 V s^{-1}, this is proposed to be due to experimental error in the solution preparation. When 1 M barium nitrate is added to the solutions, the turnover number statistically significantly decreases to 1.16 for 0.02 V s^{-1} and 1.90 for 0.1 V s^{-1}. This is proposed to be caused by the barium inhibiting the ability for tiopronin to partake

in the reaction. These decreases in turnover number are reflected in the decrease in measure peak currents in figure 6.13.

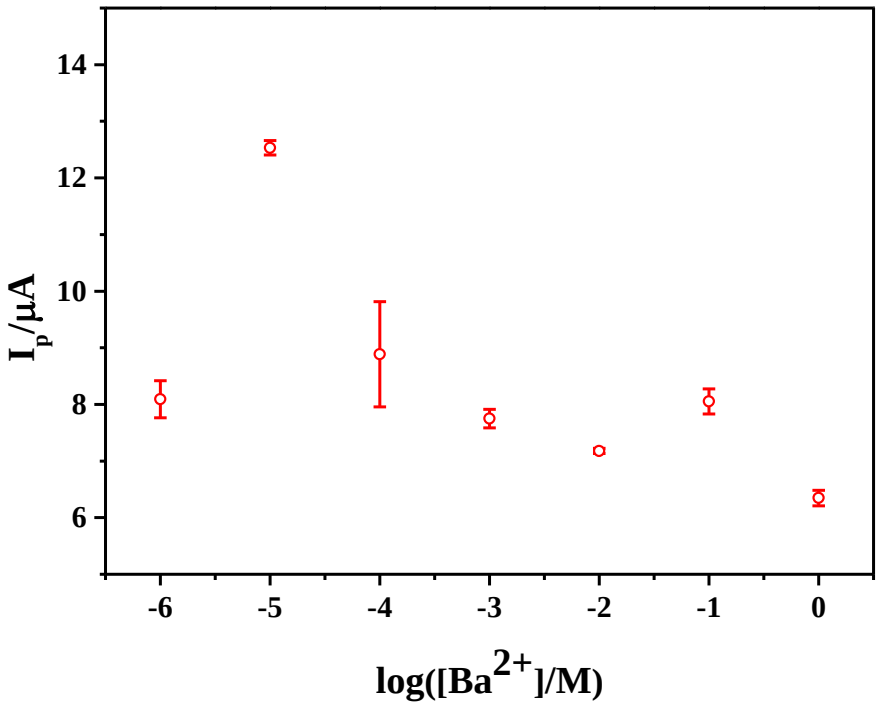

Figure 6.13 - Plot of peak current of cyclic voltammograms ($\nu = 0.1$ V s^{-1}) versus the log of the concentration of $Ba(NO_3)_2$ (1 µM - 1 M) added to ferrocene methanol (0.5 mM) in water with KCl (0.1 M) and tiopronin (4 mM) at pH 6. Performed at a glassy carbon electrode (3 mm, BAS) with a graphite counter and Ag|AgCl (BAS) reference electrode at 293.15 ± 1 K.

The peak oxidative potentials, E_p^{Ox}, observed, figure 6.14, show an ~13 mV shift to lower potentials from the blank system at + 0.250 V to the solution containing 1 M Ba^{2+} at + 0.237 V. This shift is not a linear one, with the solution with 0.1 M Ba^{+2} exhibiting an increase in the peak oxidative potential to + 0.252 V from + 0.243 V at 10 mM. The 1 M Ba^{2+} solution also exhibits the only statistically significant decrease in E_{mid} to E_{mid} = 0.19 V from + 0.20 V.

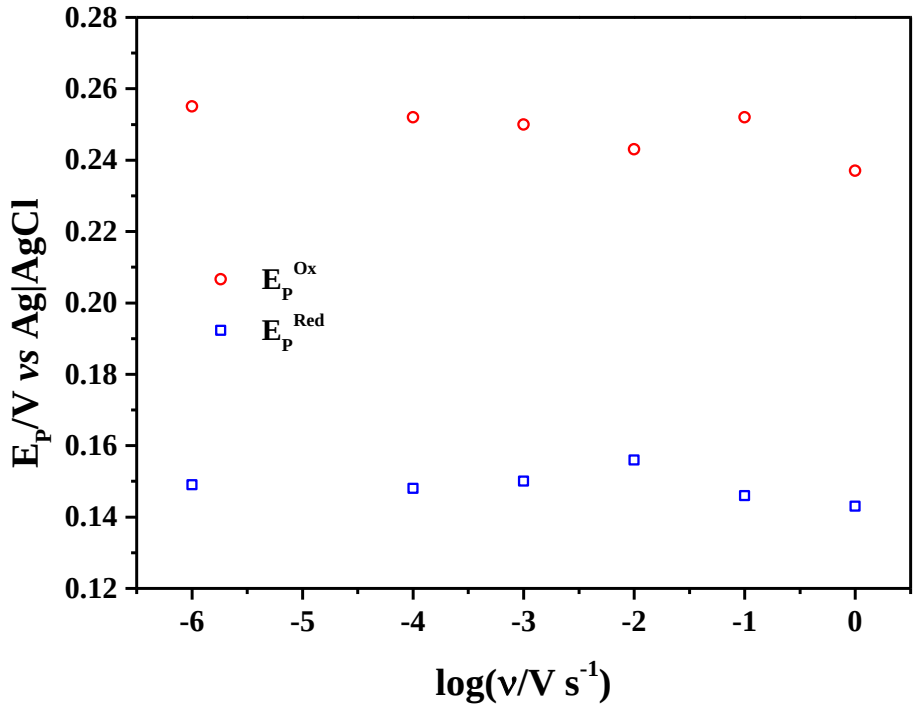

Figure 6.14 - Plot of peak potential of cyclic voltammograms (ν = 0.1 V s^{-1}) versus the log of the concentration of $Ba(NO_3)_2$ (1 µM - 1 M) added to ferrocene methanol (0.5 mM) in water with KCl (0.1 M) and tiopronin (4 mM) at pH 6. Performed at a glassy carbon electrode (3 mm, BAS) with a graphite counter and Ag|AgCl (BAS) reference electrode at 293.15 ± 1 K.

As observed in figures 6.10 and 6.11 the voltammetric wave shape changes depending on the pH of the solution. This is observed again when comparing the addition of $Ba(NO_3)_2$ (0 – 1 M) to a solution of ferrocenemethanol (0.5 mM) and tiopronin (4 mM) at pH 6, figure 6.14, and pH 9, figure 6.15. The wave-shape at pH 6 has both an oxidative reductive peak with a peak-to-peak separation of ~ 0.1 V. In contrast, at pH 9 there is no reductive peak at all due to the catalytic turnover described in the K zone of the kinetic zone diagram in figure 2.19.

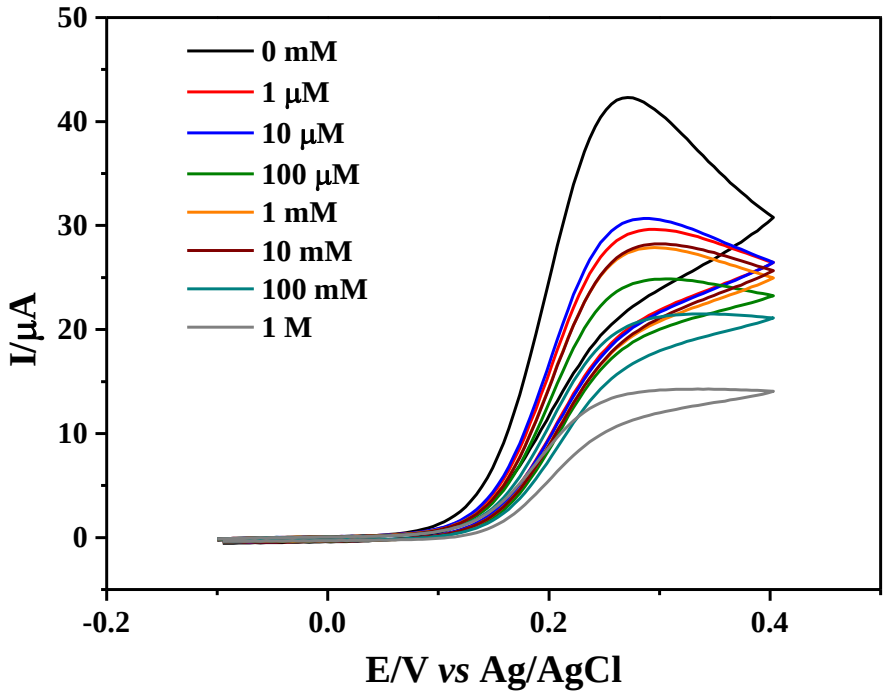

Figure 6.15 - Cyclic voltammograms (ν = 0.1 V s^{-1}) for ferrocenemethanol (0.5 mM) with KCl (0.1 M), tiopronin (4 mM) and various additions of $Ba(NO_3)_2$ (1 µM - 1 M, 6 h incubation) in borate buffer (pH = 9, 0.1 M). Performed at a glassy carbon electrode (3 mm, BAS) with a graphite counter and Ag|AgCl (BAS) reference electrode at 293.15 ± 1 K.

In this framework, there is a large decrease in the peak current observed in the presence of Ba^{2+} from 42.3 ± 0.5 µA in the blank to 30.1 ± 0.3 µA in the presence of 1 µM $Ba(NO_3)_2$. After this addition there is no statistically significant changes in the peak current or turnover numbers until 10 mM barium nitrate is added to the system. This trend is observed at both scan rates (0.02 V s^{-1} and 0.1 V s^{-1}) and is summarised below in table 6.4

Table 6.4 - A table compiling the peak currents, excess factors and turnover number for solutions of ferrocenemethanol (0.5 mM) with tiopronin (4 mM) at pH 9 with various additions of $Ba(NO_3)_2$ (1 μM – 1 M).

pH	[FcMeOH]/ mM	[Tiopronin]/ mM	[$Ba(NO_3)_2$]/ M	ν/ V s^{-1}	I_p^{Ox}/ μA	I_p^{Ox}/I_p^0
N/A	0.5	0	0	0.02	3.34	1.00
N/A	0.5	0	0	0.1	8.29	1.00
9	0.5	4	0	0.02	26.5	7.95
9	0.5	4	1×10^{-6}	0.02	21.9	6.55
9	0.5	4	1×10^{-5}	0.02	21.2	6.34
9	0.5	4	1×10^{-4}	0.02	19.9	5.97
9	0.5	4	1×10^{-3}	0.02	19.8	5.95
9	0.5	4	1×10^{-2}	0.02	20.7	6.19
9	0.5	4	1×10^{-1}	0.02	16.9	5.07
9	0.5	4	1	0.02	11.5	3.45
9	0.5	4	0	0.1	43.5	5.25
9	0.5	4	1×10^{-6}	0.1	30.1	3.63
9	0.5	4	1×10^{-5}	0.1	30.8	3.71
9	0.5	4	1×10^{-4}	0.1	26.9	3.25
9	0.5	4	1×10^{-3}	0.1	27.2	3.28
9	0.5	4	1×10^{-2}	0.1	28.1	3.39
9	0.5	4	1×10^{-1}	0.1	21.2	2.56
9	0.5	4	1	0.1	14.2	1.72

The decrease in peak current from 0.01 – 1 M, figure 6.16, was found to be reproducible over a time period of 24 h with a linear fit of 7 ± 0.3 μA decade $^{-1}$. After incubation for 96 h, the measured peak current decreased to the approximate current measured with no tiopronin present, represented by the black diamonds on figure 6.16. This indicates that the EC' mechanism that enhanced the peak current is no longer taking place. This is proposed to be due to the tiopronin no longer being free to act as a catalyst due to either being coordinated to Ba^{2+} or having formed disulphide bonds with other tiopronin molecules present in solution.

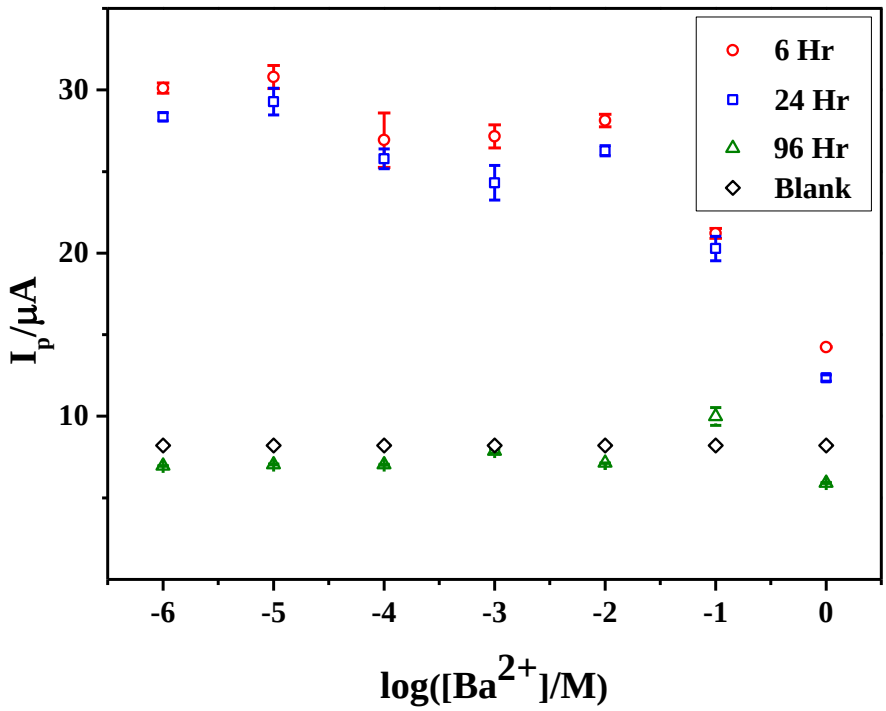

Figure 6.16 - Plot of peak current of cyclic voltammograms ($\nu = 0.1$ V s^{-1}) versus the log of the concentration of $Ba(NO_3)_2$ (1 µM - 1 M) added to ferrocene methanol (0.5 mM) with KCl (0.1 M) and tiopronin (4 mM) in borate buffer (pH 9, 0.1 M) after various incubation times (6 - 96 hrs). Performed at a glassy carbon electrode (3 mm, BAS) with a graphite counter and Ag|AgCl (BAS) reference electrode at 293.15 ± 1 K.

The measure peak oxidative potential, E_p^{Ox}, at pH 9 exhibited a similar trend to the peak current. Upon the addition of 1 µM of Ba^{2+} the peak potential shifted oxidatively to + 0.291 V from + 0.272 V when no barium was present. Figure 6.17 shows the change in the observed peak potential with the addition of various amounts of $Ba(NO_3)_2$ (1 µM – 1 M) after 6 h incubation time at pH 9. There is an overall oxidative shift in the peak potentials from + 0.291 V at 1 µM Ba^{2+} to + 0.323 V at 1 M Ba^{2+}. The shift observed is not uniform with a large increase observed upon the addition of 0.1 M Ba^{2+} to + 0.327 V from + 0.298 V for 10 mM. The absence of any well-defined linear trend in the observed oxidative shifts show that that this method is unsuitable for the detection of Ba^{2+} through monitoring changes in potential.

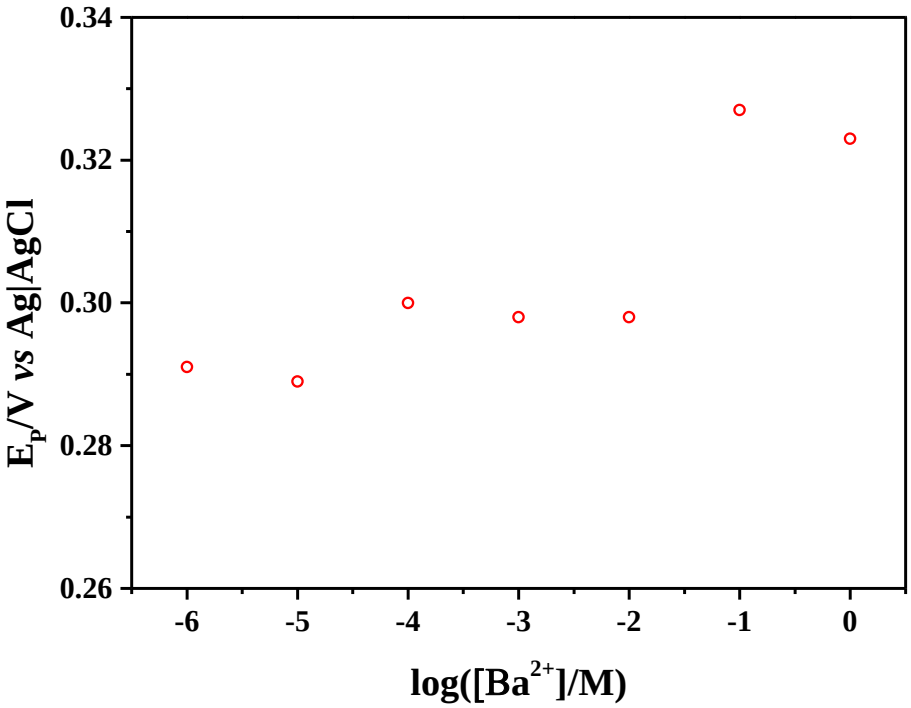

Figure 6.17 - Plot of peak potential of cyclic voltammograms (ν = 0.1 V s^{-1}) versus the log of the concentration of $Ba(NO_3)_2$ (1 µM - 1 M) added to ferrocene methanol (0.5 mM) with KCl (0.1 M) and tiopronin (4 mM) in borate buffer (pH 9, 0.1 M) after 6 h incubation time. Performed at a glassy carbon electrode (3 mm, BAS) with a graphite counter and Ag|AgCl (BAS) reference electrode at 293.15 ± 1 K.

There was an observed linear decrease of 7.0 ± 0.5 µA $decade^{-1}$ in the peak oxidative current. This produced a LOD (limit of detection) of 11 ± 2 mM, by finding the point at which the two linear lines of best fit intercept. Barium sulfate has a solubility product of 1.08 x 10^{-10} which indicates the LOD of the system is far too high for the detection of alkaline-earth metal ions in formation water, see table 1.5.[27] Therefore, altering the concentration of tiopronin present in the solution was investigated to see if this altered the LOD. Figure 6.18 shows the cyclic voltammetric peak current of ferrocenemethanol (0.5 mM) with four different concentrations of tiopronin (0, 1, 4 and 16 mM) and various additions of $Ba(NO_3)_2$ (1 µM – 1 M) with KCl (0.1 M) in borate buffer (pH 9, 0.1 M).

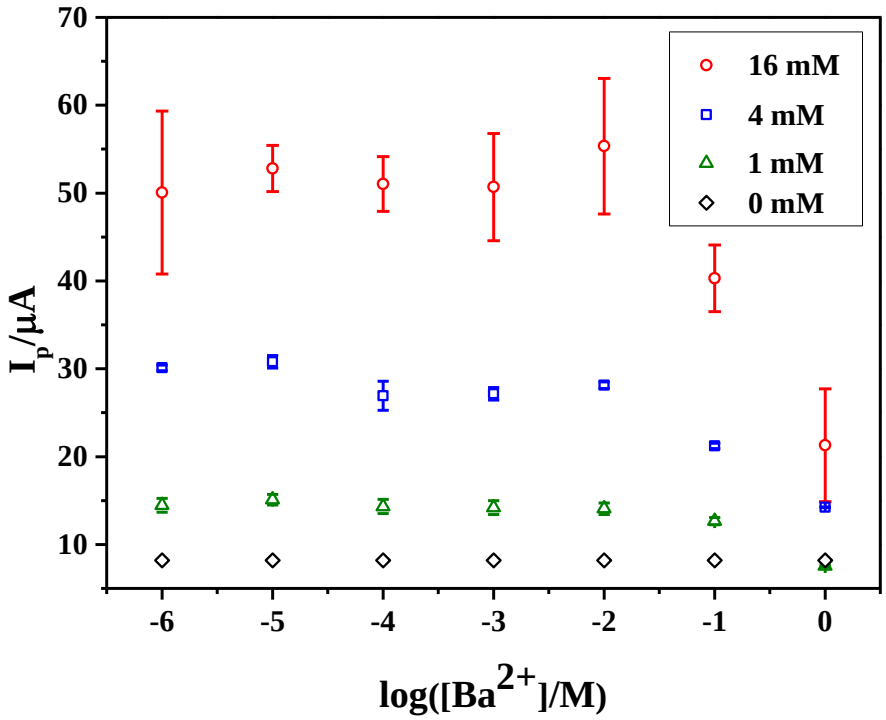

Figure 6.18 - Plot of peak current of cyclic voltammograms ($\nu = 0.1$ V s^{-1}) versus the log of the concentration of $Ba(NO_3)_2$ (1 µM - 1 M) added to ferrocene methanol (0.5 mM) with KCl (0.1 M) and tiopronin (0, 1, 4 and 16 mM) in borate buffer (pH 9, 0.1 M) after 6 h incubation time. Performed at a glassy carbon electrode (3 mm, BAS) with a graphite counter and Ag|AgCl (BAS) reference electrode at 293.15 ± 1 K.

All three systems containing tiopronin produced increased peak currents from the system in the absence of tiopronin. For 1 µM Ba^{2+} additions the measured peak currents were 50 ± 9 µA, 30 ± 0.3 µA and 14 ± 0.8 µA for 16, 4 and 1 mM tiopronin respectively. As the concentration of tiopronin was increased the gradient of the linear best fit also increased from 4 ± 0.7 µA $decade^{-1}$ for 1 mM to 7 ± 0.5 µA $decade^{-1}$ for 4 mM and 17 ± 2 µA $decade^{-1}$ for 16 mM. Neither increasing nor decreasing the concentration of tiopronin had the desired effect on the detection limits of the system. The 16 mM system gave a LOD of 18 ± 2 mM and 1 mM tiopronin produced a LOD of 23 ± 4 mM. Due to the inability to detect Ba^{2+} accurately around the solubility product of barium sulfate, this system was deemed unsuitable for the application to downhole sensing. Further testing would be needed to establish its affinity for the other alkaline-earth metal ions.

6.3 Conclusions

The effect that tiopronin (0.5 – 16 mM) has on the cyclic voltammetry of the ferrocenemethanol | ferriciniummethanol redox couple has been investigated. It has been observed to increase the peak oxidative current, shift the peak potential and alter the wave-shape. It was deduced that the electron transfer mechanism changes from an E type process to an EC' process in the presence of tiopronin. Altering the pH to above the pKa of tiopronin, to produce the more reactive and nucleophilic deprotonated thiol increased the catalytic current produced.

The application of this system to the detection of barium was investigated. No statistically significant trends were observed upon the addition of barium to the system at pH 6. The addition of barium (> 10 mM) gave a large decrease in the oxidative peak current and turnover number at pH 9. Above this concentration a linear trend was observed at 7 ± 0.5 μA decade^{-1} with a limit of detection of 11 ± 2 mM for a system containing 4 mM tiopronin. This was found to be reproducible over a 24 h timeframe. Above this time frame the current response and turnover number was found to have fallen back to the approximate magnitude or a system in the absence of tiopronin. It is proposed that after this time either all of the tiopronin is coordinated to barium or has formed disulphide bonds with other tiopronin molecules; therefore, unable to act as a catalyst in the EC' type mechanism. It was found that the gradient of the linear trend increased with increasing amounts of tiopronin; however, the LOD was still not in the desired range for alkaline-earth metal ion detection in formation water, table 1.5. Reducing the tiopronin concentration reduced the gradient of the linear trend, but again the LOD was not reduced from the 4 mM case.

The system produced LODs that were much higher (10 – 30 mM) than the concentration of Ba^{2+} prior to barium sulfate scale formation (10 μM). This method was therefore deemed unsuitable for the desired application of this work. Future work on this system would include the investigation of the effect of the other alkaline-earth metal ions, Mg^{2+}, Ca^{2+} and Sr^{2+} on the system and the suitability of the system for their detection. For example, calcium ion concentration in produced water can reach higher

than 100,000 mg L^{-1} and therefore this method could be suitable assuming the same interactions were in place.[28]

This chapter focussed on sensing chemistry for alkaline-earth metal cations in aqueous environments. The relationship between tiopronin/barium coordination and the tiopronin/ferrocenemethanol EC' mechanism was utilised to detect the presence of barium cations through a change in the peak current and calculated turnover numbers. In the following chapter sodium rhodizonate will be used in an aqueous environment to detect alkaline-earth metal cations through a shift in the peak potentials and change in the peak current.

6.4 References

1 G. Gritzner and J. Kuta, *Pure Appl. Chem.*, 1982, **54**, 1527–1532.

2 G. Gritzner and J. Kuta, *Pure Appl. Chem.*, 1984, **56**, 461–466.

3 W. Miao, Z. Ding and A. J. Bard, *J. Phys. Chem. B.*, 2002, **106**, 1392–1398.

4 B. Lertanantawong, A. P. O'Mullane, J. Zhang, W. Surareungchai, M. Somasundrum and A. M. Bond, *Anal. Chem*, 2008, **80**, 6515–6525.

5 M. H. Pournaghi-Azar and R. Ojani, *Talanta*, 1995, **42**, 1839–1848.

6 G. Atmaca, *Yonsei Med. J.*, 2004, **45**, 776.

7 B. Hercelin, P. Leroy, A. Nicolas, C. Gavriloff, D. Chassard, J. J. Thébault, M. T. Reveillaud, M. F. Salles and P. Netter, *Eur. J. Clin. Pharmacol.*, 1992, **43**, 93–5.

8 M. S. Carlsson, T. Denneberg, B. M. Emanuelsson, B. Kågedal and S. Lindgren, *Eur. J. Clin. Pharmacol.*, 1993, **45**, 79–84.

9 X. Giannakopoulos, V. Kalfakakou, P. Tsoumanis, S. Karkabounas, D. Giannakis, P. Chambilomatis, A. Evangelou and G. Kallistratos, *J. Urol. (Paris).*, 1994, **100**, 129–34.

10 A. Lindell, T. Denneberg and J. O. Jeppsson, *Nephron*, 1995, **71**, 328–42.

11 L. E. Rosenberg, S. Downing, J. L. Durant and S. Segal, *J. Clin. Invest.*, 1966, **45**, 365–71.

12 M. S. Pearle, D. S. Goldfarb, D. G. Assimos, G. Curhan, C. J. Denu-Ciocca, B. R. Matlaga, M. Monga, K. L. Penniston, G. M. Preminger, T. M. T. Turk, J. R. White and American Urological Assocation, *J. Urol.*, 2014, **192**, 316–324.

13 C. Y. Pak, C. Fuller, K. Sakhaee, J. E. Zerwekh and B. V Adams, *J. Urol.*, 1986, **136**, 1003–8.

14 B. Harman and I. Sóvágó, *Inorganica Chim. Acta*, 1983, **80**, 75–83.

15 ev Shaked, R. P. Szajewski and G. M. Whitesides, *Biochemistry*, 1980, **19**, 4156–4166.

16 R. Castañeda-Arriaga, A. Vivier-Bunge and J. Raul Alvarez-Idaboy, *Comput. Theor. Chem.*, 2016, **1077**, 48–57.

17 I. Sovago and R. B. Martin, *J. Inorg. Nucl. Chem.*, 1981, **43**, 425–429.

18 Z. Chen, Z. Wang, J. Chen and W. Gao, *Talanta*, 2012, **99**, 774–779.

19 P. C. White, N. S. Lawrence, J. Davis and R. G. Compton, *Electroanalysis*, 2002, **14**, 89–98.

20 N. S. Lawrence, J. Davis and R. G. Compton, *Talanta*, 2001, **53**, 1089–1094.

21 P. C. White, N. S. Lawrence, J. Davis and R. G. Compton, *Anal. Chim. Acta*, 2001, **447**, 1–10.

22 L. Mao and K. Yamamoto, *Electroanalysis*, 2000, **12**, 577–582.

23 P. Song, A. C. Fisher, J. D. Wadhawan, J. J. Cooper, H. J. Ward and N. S. Lawrence, *RSC Adv.*, 2016, **6**, 70237–70242.

24 R. D. Martin and P. R. Unwin, *Anal. Chem.*, 1998, **70**, 276–284.

25 W. Miao, Z. Ding and A. J. Bard, *J. Phys. Chem. B*, 2002, **106**, 1392–1398.

26 E. S. Rountree, B. D. McCarthy, T. T. Eisenhart and J. L. Dempsey, *Inorg. Chem.*, 2014, **53**, 9983–10002.

27 D. R. Lide, *Handbook of Chemistry and Physics*, CRC Press, 84th edn., 2004.

28 J. M. Neff, *Bioaccumulation in Marine Organisms*, Elsevier Ltd., Oxford, 2002.

7 Sodium rhodizonate as a voltammetric sensing platform for the detection of alkaline – earth metal cations in water

Chapters 5 and 6 explored using changes in either the measured potential or current of an electrochemically active molecule. The following chapter seeks to utilise an entirely novel approach to ion sensing; using changes in both the potential and current to successfully determine the concentration of alkaline-earth metal cations in aqueous solution.

7.1 Introduction

The ligand chosen for investigation is the rhodizonate dianion, which was discovered as rhodizonic acid by Johann Heller in 1837[1] and is found commercially in the form of disodium rhodizonate. Rhodizonic acid has a pK_1 of 4.378 ± 0.009 and pK_2 of 4.652 ± 0.014 at 298.15 K and forms the rhodizonate dianion which is a symmetric, aromatic compound that is unhydrated, unlike the monoanion.[2] The dianion has been shown to form coloured precipitates with some univalent (Ag^+ and Hg^+) and divalent (Cu^{2+}, Pb^{2+}, Zn^{2+}, Ca^{2+}, Sr^{2+} and Ba^{2+}) metal ions.[3–5] Disodium rhodizonate, figure 7.1, consists of alternating layers of hexagonally packed Na^+ cations and rhodizonate dianions.[6]

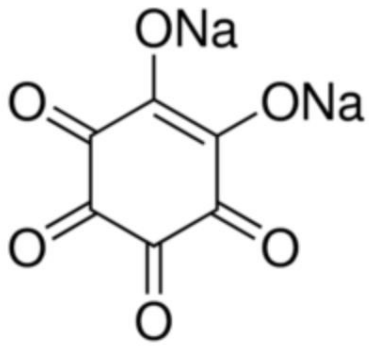

Figure 7.1 - The skeletal structure of disodium rhodizonate.

Sodium rhodizonate is soluble in aqueous conditions, forming a orange/yellow coloured solution, figure 7.2, depending on the concentration. This solution

decolourises over time due to the decomposition of the rhodizonic acid over ~36 h for a 0.01 M solution.[7] Solutions of sodium rhodizonate have been shown to be stable over a few days in the absence of oxygen at pH 8.3; where in the absence of oxygen it will eventually decompose to the tetrahydroxybenzoquinone (THBQ) anion and in the presence of oxygen it will decompose to croconic acid.[8,9]

Figure 7.2 - A picture showing the orange coloured solution formed when disodium rhodizonate (4 mM) is dissolved in aqueous KCl (0.1 M) with boric acid (0.1 M).

Rhodizonate has been used regularly in histochemical studies, in regards to the determination of chemicals such as lead in gunshot residues, to varying degrees of success.[10] In addition to this there has been some effort into utilising the rhodizonate anion for the detection of lead in water samples.[11] Recent work has looked to utilise the lithium and sodium salts of rhodizonate for use in lithium and sodium ion batteries.[12,13]

The rhodizonate dianion has been shown to form a 1:1 complex with Ba^{2+} cations by I.R and Raman spectroscopy.[14] The complexation of rhodizonate and barium was first used as a test for sulfate in titrations.[15] With the system later being used for the detection of barium through spot tests by Feigl.[16] This test has been manipulated to selectively detect barium over strontium and calcium with the addition of dilute HCl to spots.[17]

Disodium rhodizonate has been shown to complex with the alkaline-earth metal ions of interest to this work and is electrochemically active.[13] In the following chapter the electrochemistry of disodium rhodizonate will be explored using cyclic voltammetry (CV) and square wave voltammetry (SWV). The application of this compound toward

the selective determination of alkaline-earth metals in aqueous environments will then be characterised. It is proposed that due to the lower solubility of barium rhodizonate (K_{sp} = 2.14 x 10^{-9} at 293 K)[18] will result in precipitation and hence a reduction in the measured current alongside a possible shift in peak potential due to complexation.

$$Ba^{2+}_{(aq)} + RZ^{2-}_{(aq)} \rightleftharpoons BaRZ_{(aq)} \quad 7.1$$

$$BaRZ_{(aq)} \rightleftharpoons BaRZ_{(s)} \quad 7.2$$

7.2 Results and discussion

7.2.1 Cyclic voltammetric response of disodium rhodizonate

The cyclic voltammetric response, figure 7.3, of disodium rhodizonate (NaRZ, 4 mM) was investigated at various scan rates (0.02 - 500 V s^{-1}) in aqueous KCl (0.1 M) with boric acid (0.1 M) at pH 8.5. The measurements were performed at a Au macro electrode (3 mm, BAS) at 293.15 ± 1 K. The solution degassed with nitrogen (BOC Gases, UK) for 30 min prior to any electrochemical measurements being taken; this was done for all experiments throughout this chapter. Even with vigorous degassing, the cyclic voltammetric response showed a substantial peak, attributed to oxygen, at ~ - 0.6 V *versus* a Ag|AgCl reference electrode. At > - 1.0 V a single irreversible reductive peak was observed, proposed to be corresponding to the reduction of the rhodizonate dianion present at pH 8.5.[2]

The peak potentials, E_p, for the single electron reductions are plotted against the decadic logarithm of the scan rate (v), figure 7.4 (left). There is a clear shift in reductive peak potential of 75 ± 3 mV $decade^{-1}$ to more negative potentials as the scan rate is increased. This behaviour supports the irreversible nature of the electrode reaction. The plot of peak current versus the square root of the scan rate, figure 7.4 (right), is curved in nature.

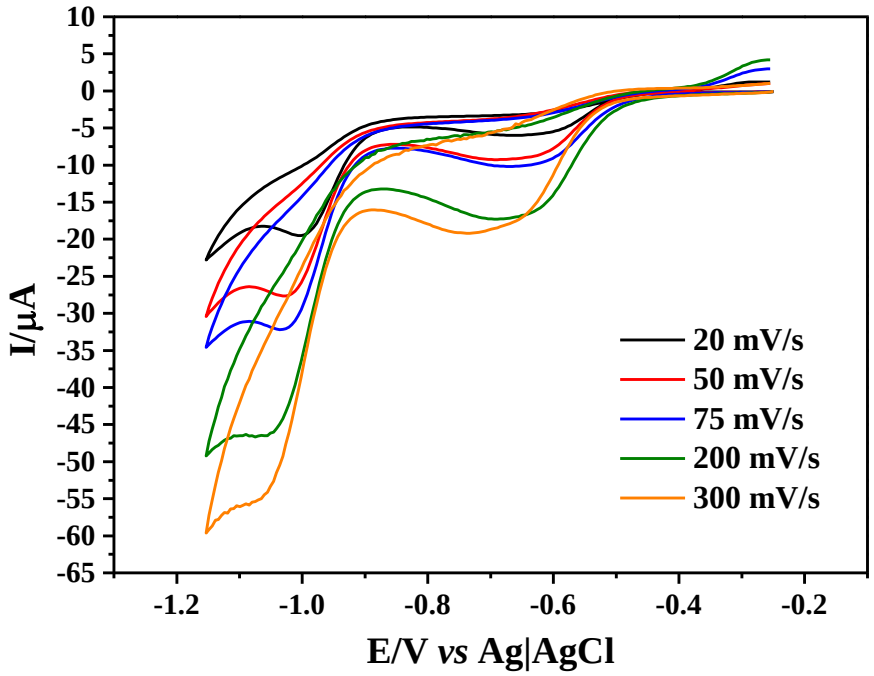

Figure 7.3 - Cyclic voltammograms (ν = 0.02 - 0.3 V s^{-1}) for disodium rhodizonate (4 mM) in aqueous KCl (0.1 M) with boric acid (0.1 M) at pH 8.5. Performed at an Au electrode (3 mm, BAS) with a graphite counter and Ag|AgCl (BAS) reference electrode at 293.15 ± 1 K.

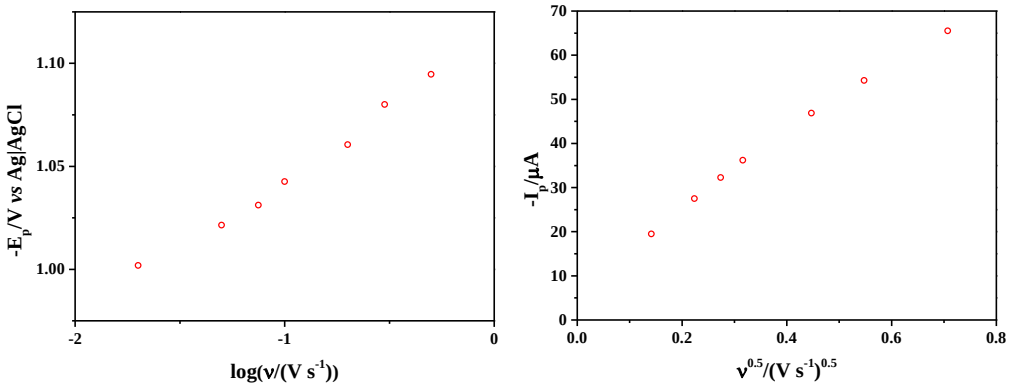

Figure 7.4 - Plot of reductive peak potential, E_p, versus the log of the scan rate (left) and peak current, I_p, versus the square root of the scan rate (right) for sodium rhodizonate (4 mM) in aqueous KCl (0.1 M) with boric acid (0.1 M) at pH 8.5. Performed at a Au working electrode (3 mm, BASi), with a graphite counter electrode and Ag|AgCl reference electrode (BAS) at 293.15 ± 1 K.

7.2.2 The influence of barium on the cyclic voltammetry of disodium rhodizonate

The influence of barium di - cations on the cyclic voltammetric response, figure 7.5, of NaRZ (4 mM) was studied in aqueous KCl (0.1 M) and boric acid (0.1 M). Sequential amounts of barium nitrate ($Ba(NO_3)_2$, 0.1 - 6 mM) was added to the solutions and cyclic voltammetry performed. Figure 7.5 shows a selection of the voltammograms obtained with barium (0.5 – 4 mM) added. There is clear variation in both the peak reductive potential and measured peak current; with the peak shifting oxidatively and the current decreasing, as expected from equation 7.1 and 7.2.

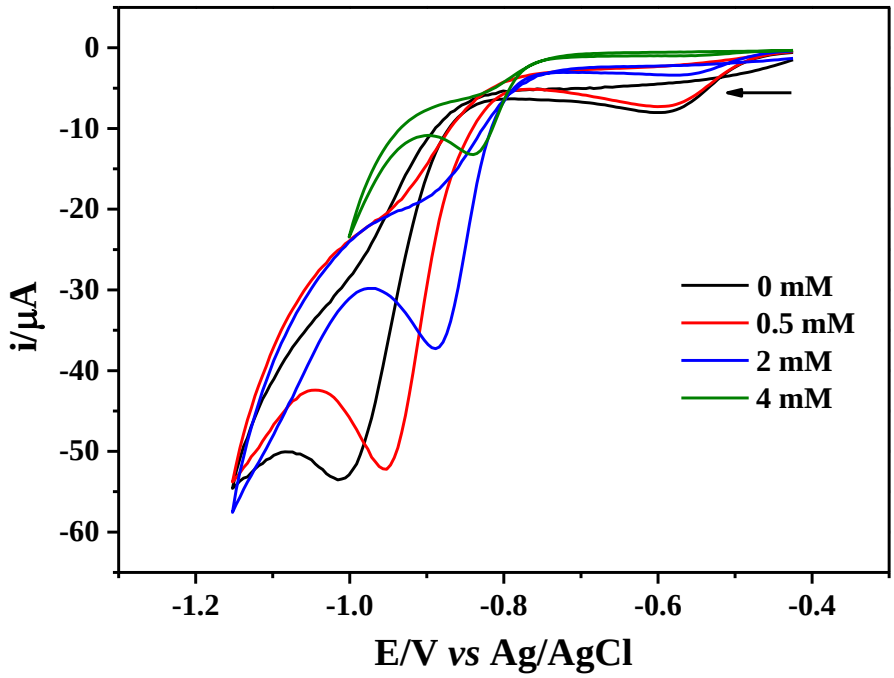

Figure 7.5 – Cyclic voltammograms ($\nu = 0.1$ V s^{-1}) for disodium rhodizonate (4 mM) with sequential amounts of barium nitrate ($Ba(NO_3)_2$, 0.5 - 4 mM) in aqueous KCl (0.1 M) with boric acid (0.1 M) at pH 8.5. Performed at an Au electrode (3 mm, BAS) with a graphite counter and Ag|AgCl (BAS) reference electrode at 293.15 ± 1 K.

A single reductive peak was observed in the absence of barium at - 1.012 V and - 46 ± 1 μA, when baseline corrected for the presence of residual oxygen species present in solution. The potential shifted oxidatively and the current decreased, where at 4 mM Ba^{2+} the peak potential was - 0.838 V and the corrected peak current

- 12 ± 1 µA. The voltammetric response, figure 7.6, to additions of the Ba^{2+} cation gave rise to an oxidative shift in peak potential (Ep) with a linear Nernstian relationship of 29.1 ± 0.1 mV $decade^{-1}$ above 0.5 mM Ba^{2+}. The limit of detection (LOD) was calculated using the intersection of the two linear fits present in a full range of additions (10 µM - 6 mM) as 570 ± 70 µM.

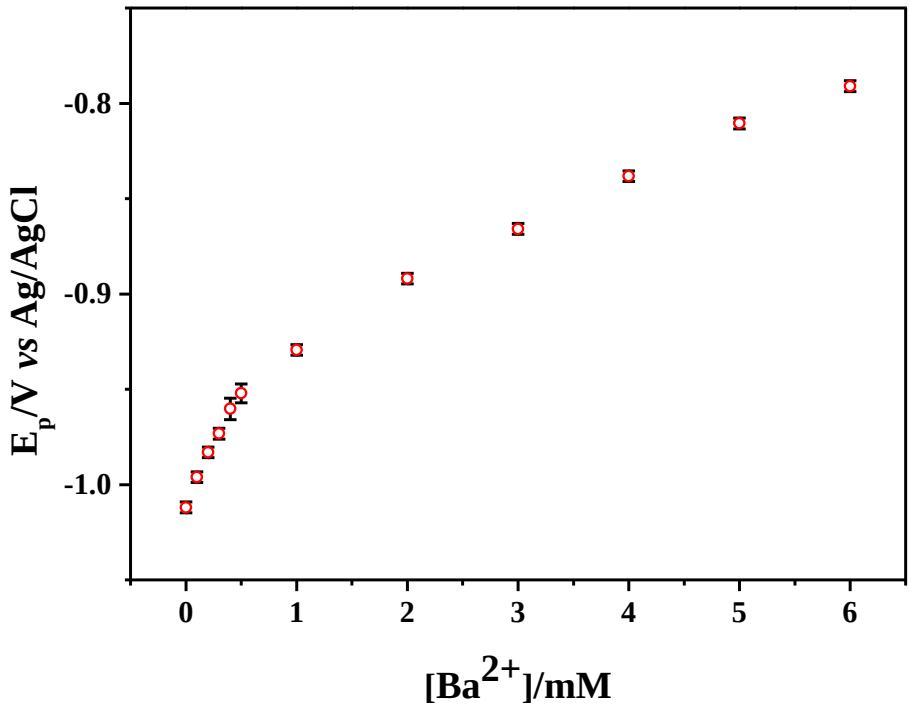

Figure 7.6 - Plot of reductive cyclic voltammetric (ν = 0.1 V s^{-1}) peak potential, E_p, versus the concentration of $Ba(NO_3)_2$ (0.1 - 6 mM) added for sodium rhodizonate (4 mM) in aqueous KCl (0.1 M) with boric acid (0.1 M) at pH 8.5. Performed at an Au working electrode (3 mm, BASi), with a graphite counter electrode and Ag|AgCl reference electrode (BAS) at 293.15 ± 1 K.

Amperometrically, there is initially a small increase in peak current of ~ 2 µA between the absence of Ba^{2+} and 0.1 mM. Following this, there was an observed linear decrease in the baseline corrected peak current (Ip) of 9.88 ± 0.25 mA $decade^{-1}$ between 0.5 mM and 5 mM, with a calculated LOD of 430 ± 30 µM.

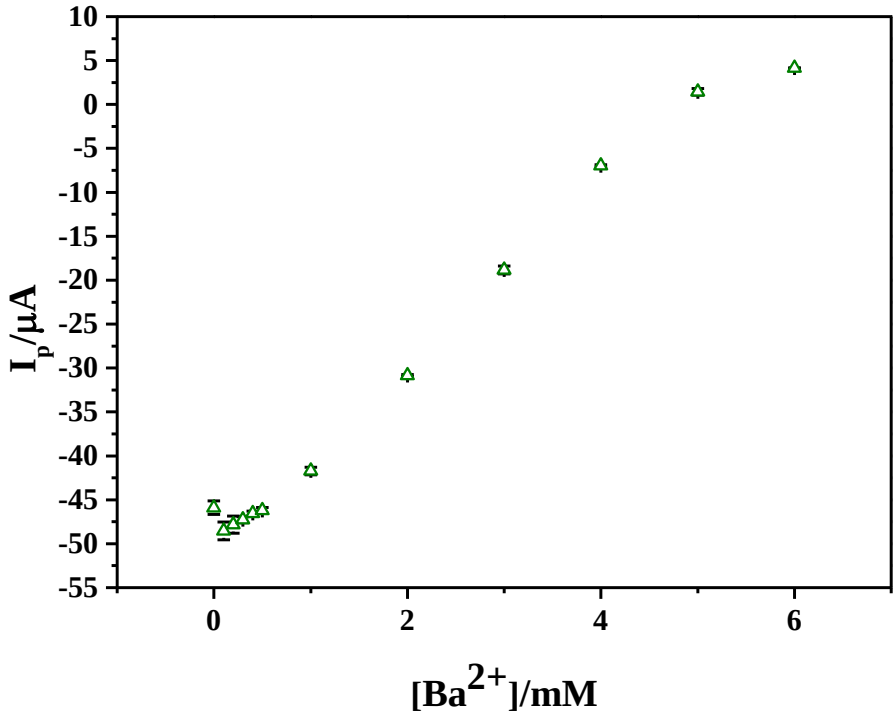

Figure 7.7 - Plot of reductive cyclic voltammetric (ν = 0.1 V s^{-1}) peak potential, E_p, versus the concentration of $Ba(NO_3)_2$ (0.1 - 6 mM) added for sodium rhodizonate (4 mM) in aqueous KCl (0.1 M) with boric acid (0.1 M) at pH 8.5. Performed at an Au working electrode (3 mm, BASi), with a graphite counter electrode and Ag|AgCl reference electrode (BAS) at 293.15 ± 1 K.

The changes in voltammetry are attributed to the formation of barium rhodizonate; of which a precipitate was clearly visible, figure 7.8, at the concentrations described above, once the solubility product of K_{sp} = 2.14 x 10^{-9} at 293 K is exceeded.[18]

$$Ba^{2+}_{(aq)} + RZ^{2-}_{(aq)} \rightleftharpoons BaRZ_{(aq)} \quad 7.3$$

$$BaRZ_{(aq)} \rightleftharpoons BaRZ_{(s)} \quad 7.4$$

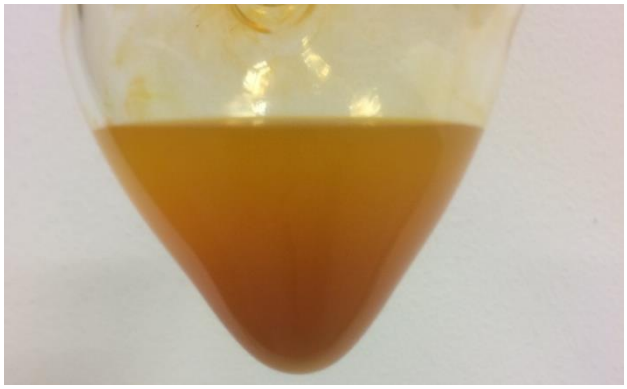

Figure 7.8 - A picture showing the orange coloured solution with dark precipitate formed when disodium rhodizonate (4 mM) is dissolved in aqueous KCl (0.1 M) with boric acid (0.1 M) with $Ba(NO_3)_2$ (4 mM) added to it.

The stability of these trends over different incubation times was investigated using square - wave voltammetry. Separate solutions of sodium rhodizonate (4 mM) were prepared with different concentrations of $Ba(NO_3)_2$ (0.1 - 4 mM). Each of these solutions was tested after being incubated for different lengths of time (1, 5 and 7 h). The change in the peak potential, E_p, for each concentration at different incubation times is presented in figure 7.9.

It can be seen that the peak potentials stay statistically consistent over 7 hours of incubation time. Any significant deviation is observed below the concentration at which the Nernstian range begins, with a slope of 29.1 ± 0.1 mV $decade^{-1}$ above 0.5 mM Ba^{2+}. The change in the peak current for the same solutions is presented in figure 7.10.

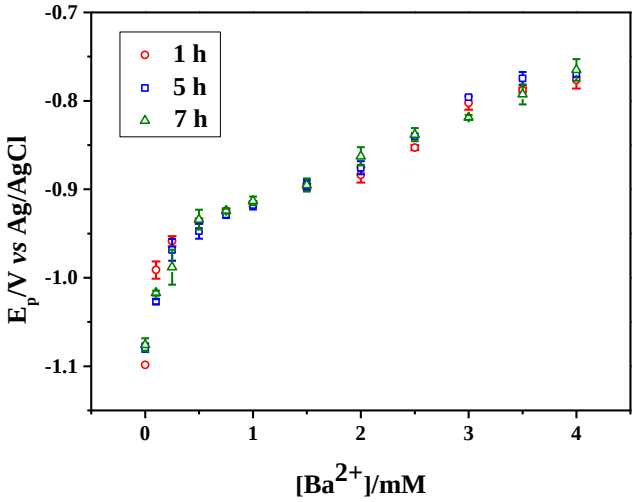

Figure 7.9 - Plot of reductive square-wave (f = 25 Hz, A = 0.1 V, Step = 0.05 V) peak potential, E_p, after various incubation times (1 - 7 h) versus the concentration of $Ba(NO_3)_2$ (0.1 - 6 mM) added for sodium rhodizonate (4 mM) in aqueous KCl (0.1 M) with boric acid (0.1 M) at pH 8.5. Performed at an Au working electrode (3 mm, BASi), with a graphite counter electrode and Ag|AgCl reference electrode (BAS) at 293.15 ± 1 K.

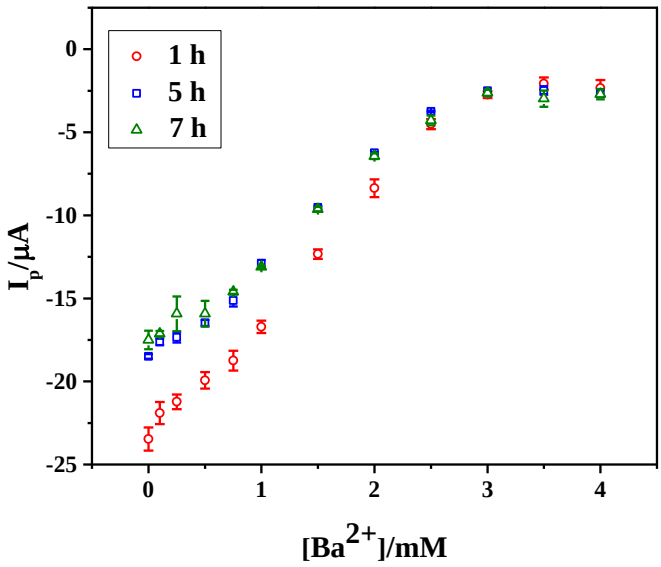

Figure 7.10 - Plot of reductive square-wave (f = 25 Hz, A = 0.1 V, Step = 0.05 V) peak current, I_p, versus the concentration of $Ba(NO_3)_2$ (0.1 - 6 mM) added for sodium rhodizonate (4 mM) in aqueous KCl (0.1 M) with boric acid (0.1 M) at pH 8.5. Performed at an Au working electrode (3 mm, BASi), with a graphite counter electrode and Ag|AgCl reference electrode (BAS) at 293.15 ± 1 K.

Unlike the peak potentials, the peak currents exhibit large deviations in values between the different incubation times. There is a large decrease in the measured peak current between the 1 h and 5 h incubation times.

In the absence of barium ions, after 1 hour, the peak current is measured at -23.5 ± 0.7 μA; whereas after 5 hours this decreases to -18.5 ± 0.2 μA. After another two hours this current decreases further to -17.5 ± 0.5 μA. As the concentration of barium ions is increased, the separation between the measured currents after 1 and 5 h is reduced. At 2 mM barium ions the current measured at 1 h is 2.1 ± 0.5 μA larger than at 5 h compared to a difference of 5.0 ± 0.9 μA in the absence of barium ions. This raises questions about the suitability of the current measurements for use in accurate determination of the amount of barium present, especially at concentrations ≤ 2 mM. Although the values show a large deviation, a similar trend is exhibited across all three incubation times, with a linear response being shown between 0.5 mM and 2.5 mM.

The concentration of barium rhodizonate required to exceed the solubility product was calculated to be 41.8 μM from the K_{sp} value reported by Pan *et al.*[18] at 293 K and the average activity coefficients for KCl at 0.1 M. To explore this square wave voltammetry was utilised to reach lower detection limits and minimize the contributions of non-faradaic processes. The square wave voltammograms for the addition of $Ba(NO_3)_2$ (10 - 80 μM) are presented in figure 7.11.

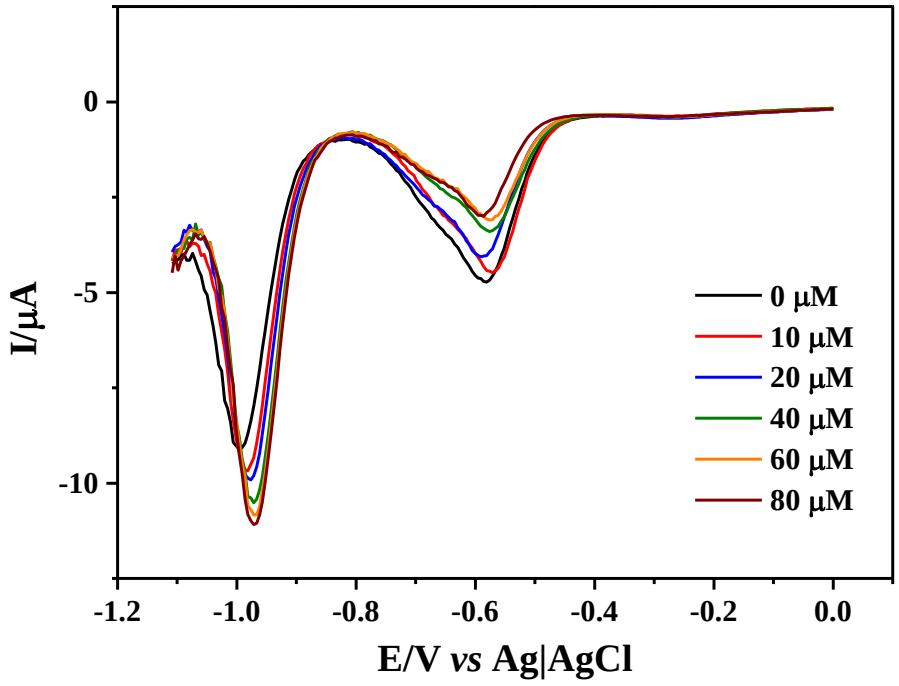

Figure 7.11 - Square - wave voltammograms (f = 25 Hz, A = 0.1 V, Step = 0.05 V) for disodium rhodizonate (4 mM) with sequential amounts of barium nitrate ($Ba(NO_3)_2$, 10 - 80 µM) in aqueous KCl (0.1 M) with boric acid (0.1 M) at pH 8.5. Performed at a Au electrode (3 mm, BAS) with a graphite counter and Ag|AgCl (BAS) reference electrode at 293.15 ± 1 K.

Similar to the cyclic voltammograms obtained previously, see figure 7.3 and 7.5, there is a large peak found at ~ -0.6 V, which is attributed to the residual presence of oxygen in the system after the 30 min degas. This peak does not have a significant trend in terms of its peak potential; however, the peak current measured decreases with increasing concentration of barium. The single reductive peak found at ~ - 1.0 V attributed to the reduction of the rhodizonate shows variations in both the measured peak potentials and currents as the concentration of barium is increased. There is an increase in the measured peak current from -9.1 ± 0.2 µA in the absence of barium to -11.1 ± 0.2 µA in the presence of 80 µM Ba^{2+}.

There was an observed large oxidative shift in the measured reductive potentials upon the addition of Ba^{2+} (10 - 50 µM), figure 7.12. There was a measured peak potential

of -1.014 V in the absence of Ba^{2+} and -0.998 V with 50 µM Ba^{2+}. Plotting two linear trends on figure 7.12, one from 0-40 µM and a second from 50-70 µM, and finding the point at which they cross gave a concentration of 42 ± 1 µM which is excellent agreement with the work from Pan *et al.*.[18]

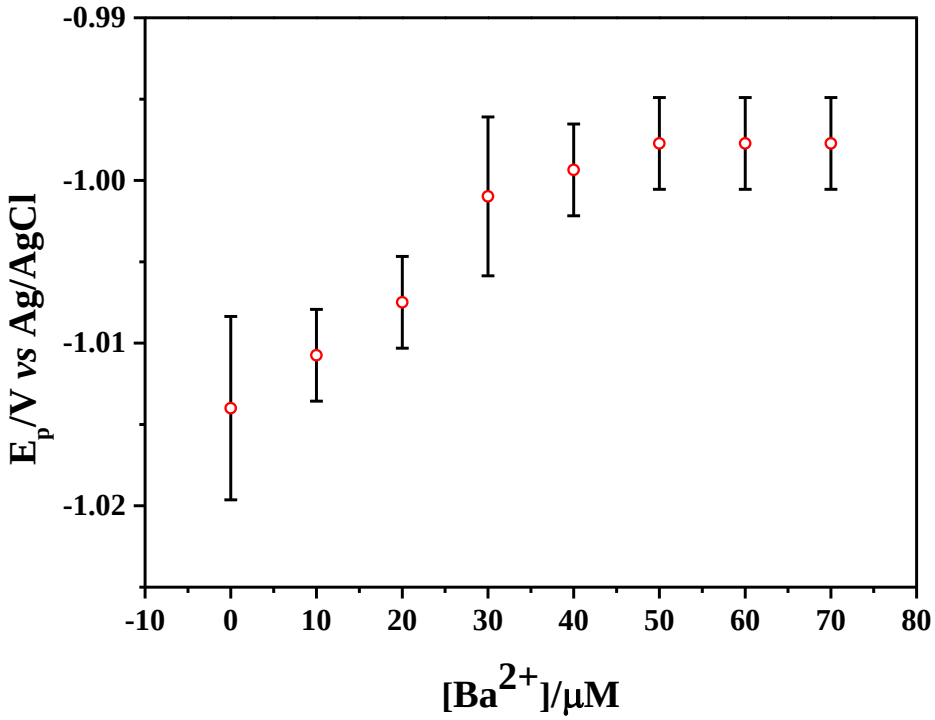

Figure 7.12 – Plot of square wave I forward (f = 25 Hz, A = 0.1 V, Step = 0.05 V) Ep *versus* the concentration of Ba^{2+} added to sodium rhodizonate (4 mM) with KCl (0.1 M) and boric acid (0.1 M) in water.

The oxidative shift in reductive Ep was proposed as the 1:1 complexation between the barium dication and rhodizonate dianion to form the aqueous barium rhodizonate before the solubility product is reached.

$$Ba^{2+}_{(aq)} + RZ^{2-}_{(aq)} \rightleftharpoons BaRZ_{(aq)} \qquad 7.5$$

Square-wave voltammetry was then performed for the addition of barium, strontium and calcium (0.1 - 4 mM) to observe any differences in the effect on the peak potentials and currents, presented in figure 7.13, 7.14 and 7.15.

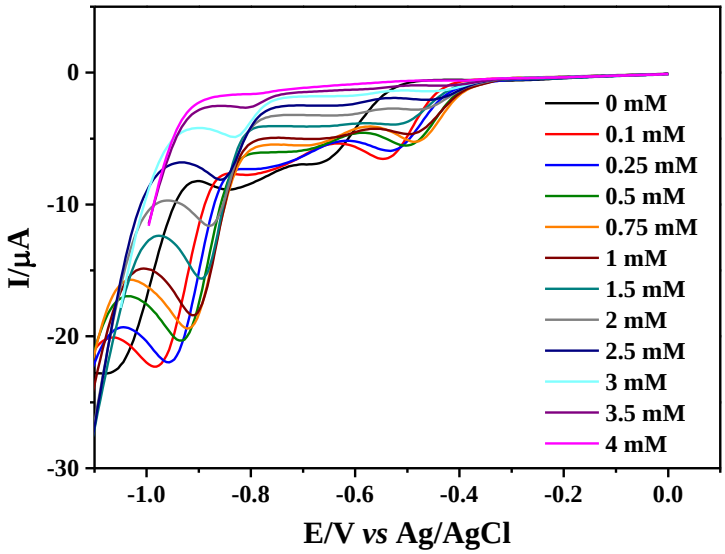

Figure 7.13 - Square - wave voltammograms (f = 25 Hz, A = 0.1 V, Step = 0.05 V) for disodium rhodizonate (4 mM) with sequential amounts of calcium nitrate (0.1 - 4 mM) in aqueous KCl (0.1 M) with boric acid (0.1 M) at pH 8.5. Performed at an Au electrode (3 mm, BAS) with a graphite counter and Ag|AgCl (BAS) reference electrode at 293.15 ± 1 K.

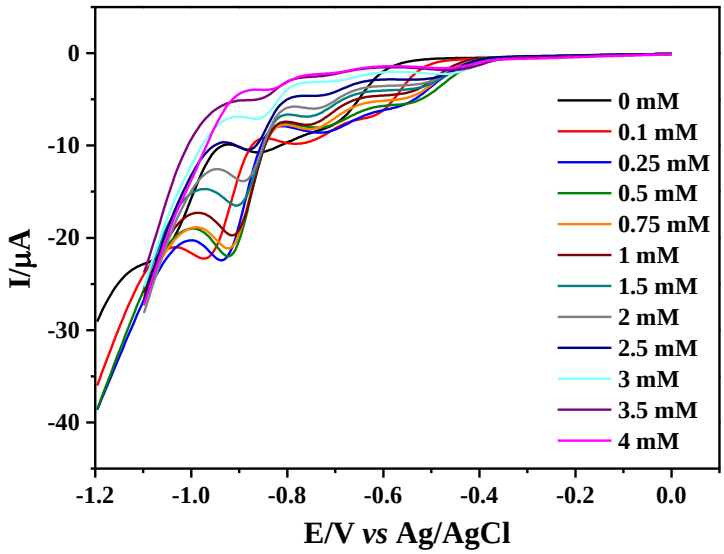

Figure 7.14 - Square - wave voltammograms (f = 25 Hz, A = 0.1 V, Step = 0.05 V) for disodium rhodizonate (4 mM) with sequential amounts of strontium nitrate (0.1 - 4 mM) in aqueous KCl (0.1 M) with boric acid (0.1 M) at pH 8.5. Performed at an Au electrode (3 mm, BAS) with a graphite counter and Ag|AgCl (BAS) reference electrode at 293.15 ± 1 K.

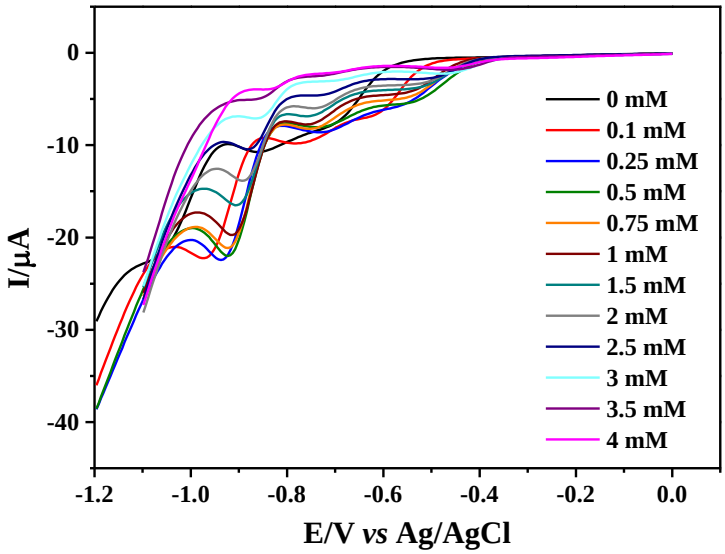

Figure 7.15 - Square - wave voltammograms (f = 25 Hz, A = 0.1 V, Step = 0.05 V) for disodium rhodizonate (4 mM) with sequential amounts of barium nitrate (0.1 - 4 mM) in aqueous KCl (0.1 M) with boric acid (0.1 M) at pH 8.5. Performed at an Au electrode (3 mm, BAS) with a graphite counter and Ag|AgCl (BAS) reference electrode at 293.15 ± 1 K.

All three of the systems in figure 7.13-7.15 exhibited similar trends with initially stable peak currents and large oxidative shifts in the measured reductive potentials, typically ~ 10 mV for the addition of 0.25 mM. After this concentration a linear trend was observed both for the decrease in the peak current and shift in peak potential.

It was observed that the platform was sensitive to calcium and strontium in addition to the barium di – cation. The sensitivity of the system towards alkaline – earth metals was found to be Ba^{2+} > Sr^{2+} > Ca^{2+}, as shown in figure 7.16. The oxidative shift in reductive Ep was found to decrease from 41.6 ± 1.8 mV $decade^{-1}$ for Ba^{2+} to 22.3 ± 2.2 mV $decade^{-1}$ for Sr^{2+} and 19.9 mV/decade for Ca^{2+}. A similar trend was found with regards to the amperometric measurements, figure 7.17, with a decrease from 63.7 ± 0.1 μA $decade^{-1}$ for Ba^{2+} to 59.4 ± 0.1 μA $decade^{-1}$ for Sr^{2+} and 53.3 ± 0.06 μA $decade^{-1}$ for Ca^{2+}.

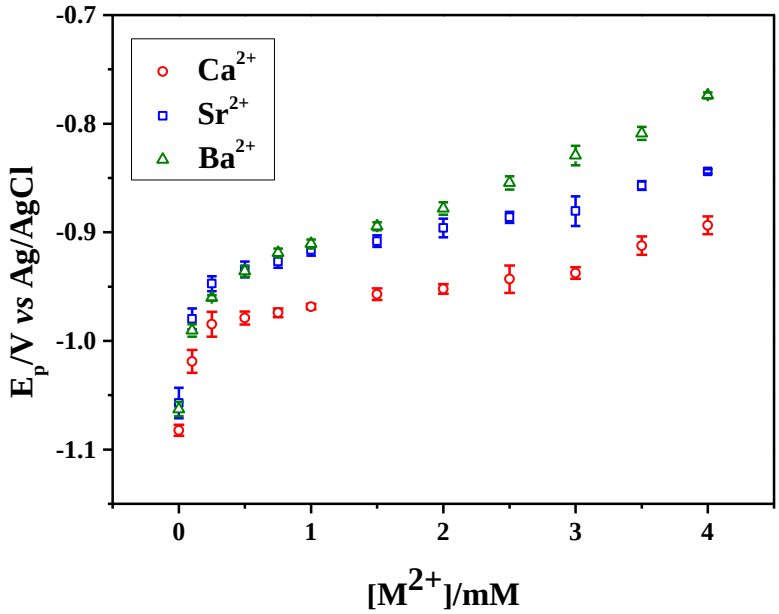

Figure 7.16 – Plots of E_p *versus* M^{2+} concentration for the additions of alkaline-earth di – cations to sodium rhodizonate (4 mM) with KCl (0.1 M) and boric acid (0.1 M) in water.

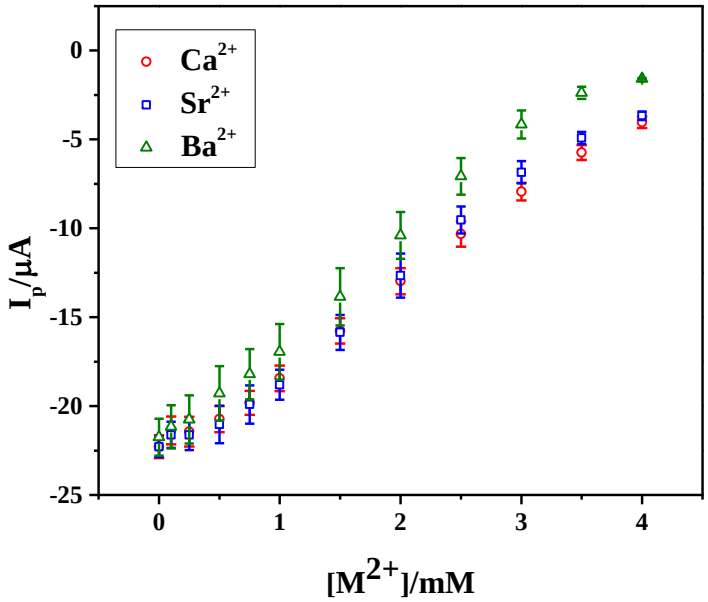

Figure 7.17 – Plots of I_p *versus* M^{2+} concentration for the additions of alkaline-earth di – cations to sodium rhodizonate (4 mM) with KCl (0.1 M) and boric acid (0.1 M) in water.

The measurements up to this point have been performed in a solution free from interference and have exhibited strong trends toward being able to detect the presence of alkaline - earth metal cations in aqueous conditions. The system has shown that it is capable of detecting strontium and calcium at appropriate levels for detection in sea water (~ 0.1 and ~10 mM respectively) and the possibility of detecting typical concentrations of barium (~ 0.1 µM).[19,20] To further test this in laboratory conditions solutions were made to pH 8.5 which is close to that found at the high end of sea water pH, 8.4.[21] In addition to this the solutions were made to 35 salinity by the addition of NaCl and the same experimental procedure followed to that in figures 7.13-7.15.

7.2.3 Application to sea water

Sea water conditions at 35 salinity were produced using NaCl (0.6 M). Other than the increase in salinity of the solutions, the experiments were performed with an identical procedure to those in figure 7.13-7.15. The square - wave voltammograms obtained for the addition of Ba^{2+}, Sr^{2+} and Ca^{2+} to NaRZ (4 mM) are presented in figure 7.18-7.20.

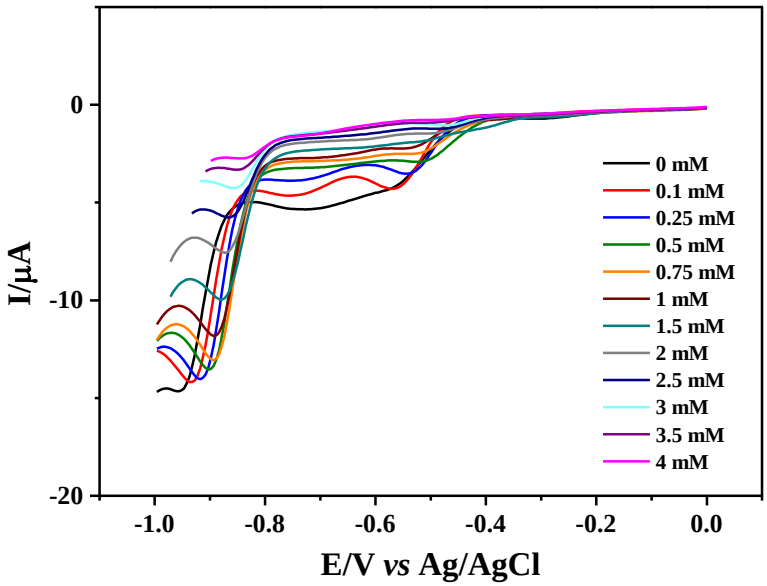

Figure 7.18 - Square - wave voltammograms (f = 25 Hz, A = 0.1 V, Step = 0.05 V) for disodium rhodizonate (4 mM) with sequential amounts of calcium nitrate (0.1 - 4 mM) in aqueous NaCl (0.6 M) with boric acid (0.1 M) at pH 8.5. Performed at an Au electrode (3 mm, BAS) with a graphite counter and Ag|AgCl (BAS) reference electrode at 293.15 ± 1 K.

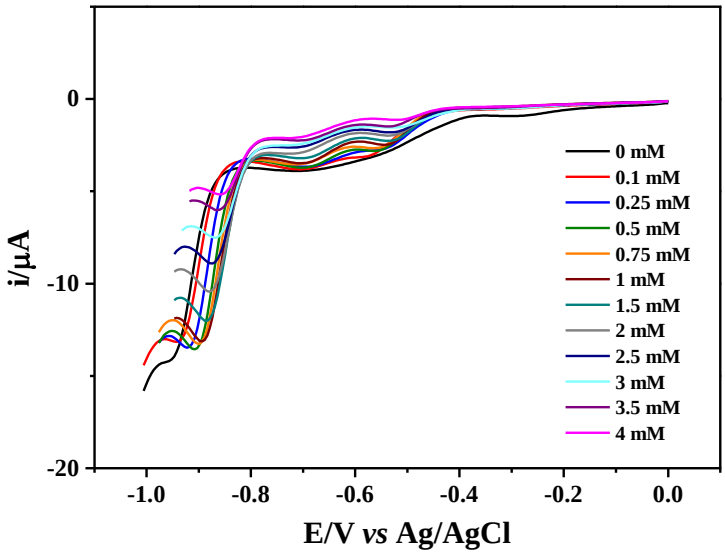

Figure 7.19 - Square - wave voltammograms (f = 25 Hz, A = 0.1 V, Step = 0.05 V) for disodium rhodizonate (4 mM) with sequential amounts of strontium nitrate (0.1 - 4 mM) in aqueous NaCl (0.6 M) with boric acid (0.1 M) at pH 8.5. Performed at an Au electrode (3 mm, BAS) with a graphite counter and Ag|AgCl (BAS) reference electrode at 293.15 ± 1 K.

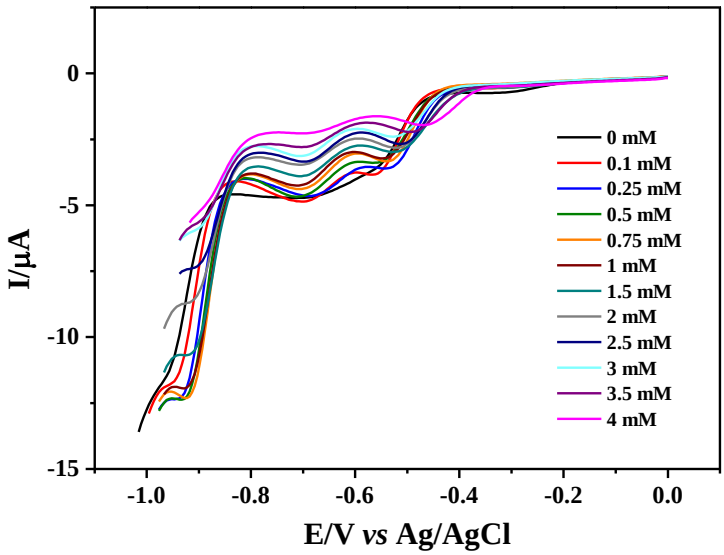

Figure 7.20 - Square - wave voltammograms (f = 25 Hz, A = 0.1 V, Step = 0.05 V) for disodium rhodizonate (4 mM) with sequential amounts of barium nitrate (0.1 - 4 mM) in aqueous NaCl (0.6 M) with boric acid (0.1 M) at pH 8.5. Performed at an Au electrode (3 mm, BAS) with a graphite counter and Ag|AgCl (BAS) reference electrode at 293.15 ± 1 K.

The voltammograms obtained in the 35 salinity experiments exhibit similar properties to those obtained in aqueous KCl. Initially there is no deviation in the measured peak current and a large oxidative shift in the reductive peak potential. The wave shapes obtained, especially in the case of Ca^{2+}, were not as well-defined as in previous experiments.

Noticeably, there is a decrease in the reductive peak potential and measured peak current in the absence of Ba^{2+} from the system with KCl. The initial peak potential decreases by ~ 50 mV and the peak current decreases by almost a factor of 2; giving -0.960 ± 0.005 V and -13.0 ± 0.4 µA respectively, figure 7.21 and 7.22. Even so, similar trends were observed in 35 salinity conditions as before. Barium remained the ion that had the most significant impact on the measured potentials and currents. The shifts for both of these parameters were reduced from before; but still larger than the other ions at 15.8 ± 0.6 mV decade^{-1} and 37 ± 2 µA decade^{-1}.

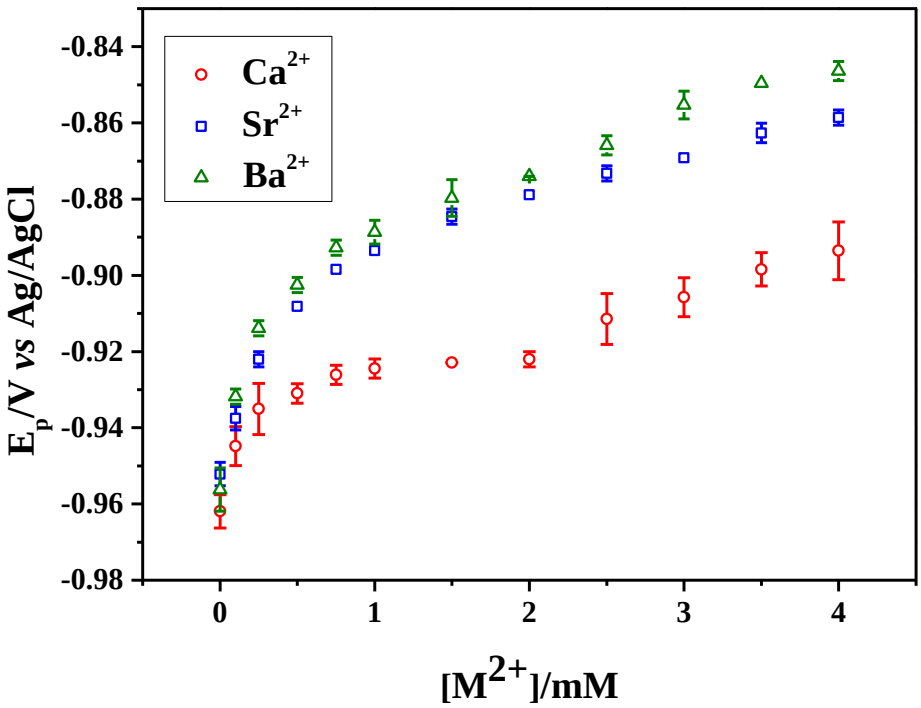

Figure 7.21 - Plots of E_p *versus* M^{2+} concentration for the additions of alkaline-earth di – cations to sodium rhodizonate (4 mM) with NaCl (0.6 M) and boric acid (0.1 M) in water.

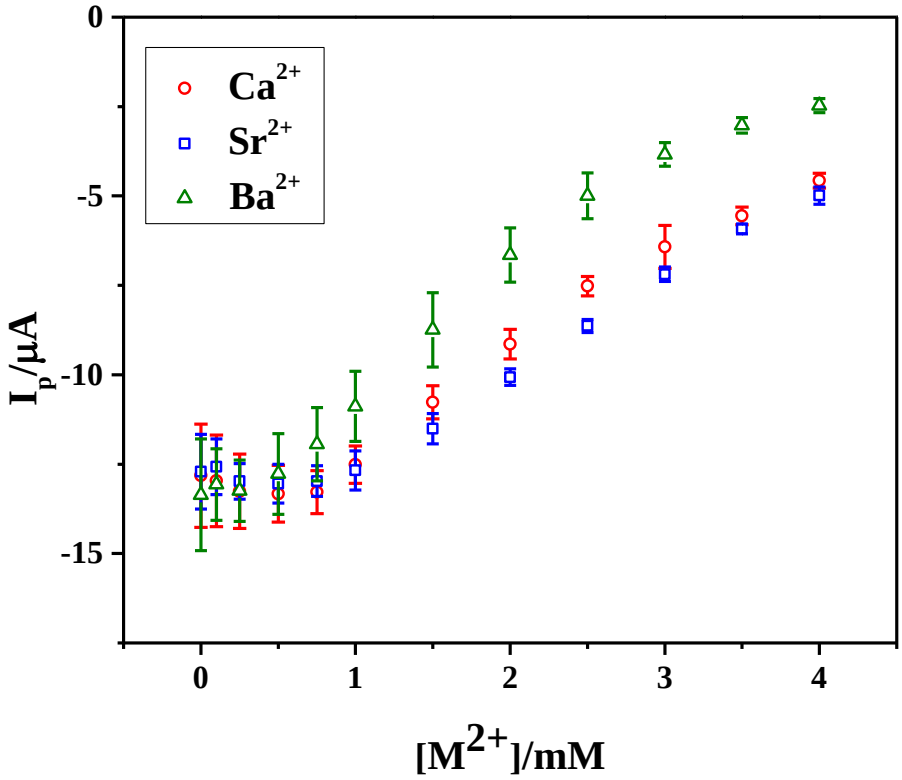

Figure 7.22 - Plots of I_p *versus* M^{2+} concentration for the additions of alkaline-earth di – cations to sodium rhodizonate (4 mM) with NaCl (0.6 M) and boric acid (0.1 M) in water.

It was found that strontium gave a similar oxidative shift to that observed for barium, whereas calcium was greatly reduced. Therefore, as barium appeared to bind preferentially to the rhodizonate, solutions containing a predetermined concentration of strontium (0.5 - 4 mM) were produced and tested under the same conditions as before. The change in the measured reductive peak potentials and measured peak currents with different amounts of barium and strontium present are shown in figure 7.23 and 7.24 respectively.

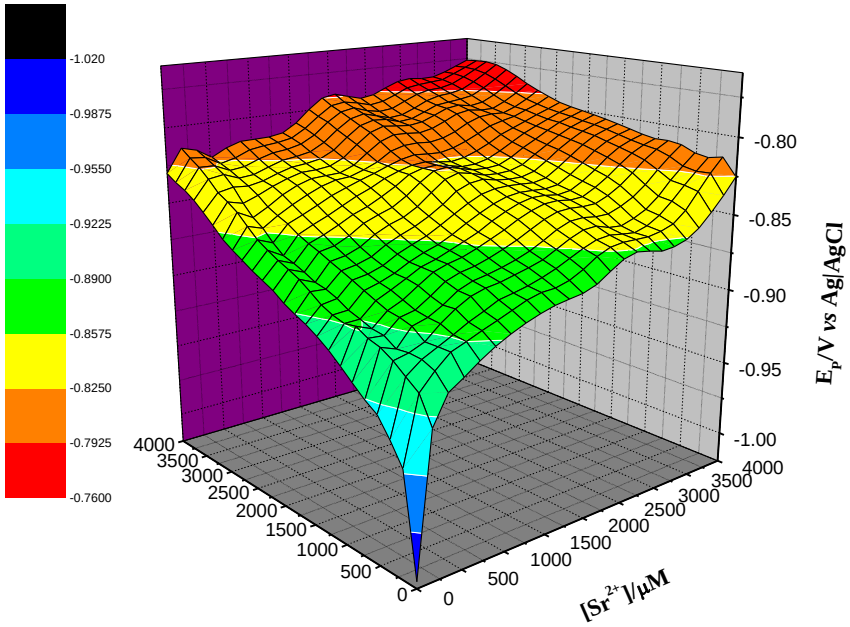

Figure 7.23 – 3D interference plot the change in peak potential for the addition of Ba^{2+} to sodium rhodizonate (4 mM) with Sr^{2+} present.

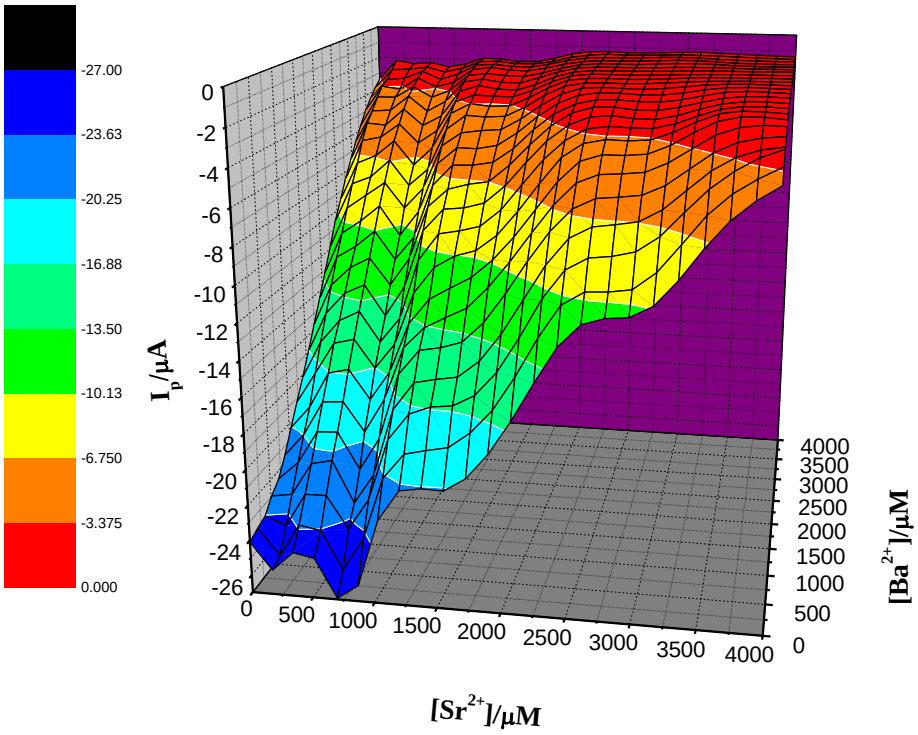

Figure 7.24 – 3D interference plot the change in peak current for the addition of Ba^{2+} to sodium rhodizonate (4 mM) with Sr^{2+} present.

It was observed that at high concentrations of strontium, the change in current with respect to barium concentration was greatly diminished. With respects to the change in the peak potential, even at high concentrations of strontium, an oxidative shift in the peak potential was still observed.

We have observed that this system still gives a measurable oxidative shift in the reductive peak potential in conditions of 35 salinity and in the presence of equal concentrations of strontium as an interfering ion. Sea water and formation water have extremely varied compositions, along with the concentrations of analyte ions being significantly different; for example, barium can be found in concentrations up to ~ 15 mM.[19] Therefore, to translate this method into a detection method suitable for down - hole applications, the system must be tested in appropriate conditions within the laboratory; namely at pH 7 and increased temperatures or pressures.

7.2.4 Application to formation water

In formation water, the concentration of barium can reach levels of up to ~ 15 mM. Therefore, due to the 1:1 ratio of Ba^{2+}: RZ^{2-}, the concentration of NaRZ used in solutions was increased to 16 mM and the pH reduced to pH 7. In addition to this, the concentration of boric acid was increased to maintain the same boric acid: NaRz ratio. The experiments were performed in an identical way to previously, with sequential additions of the alkaline - earth metal ions being added to the de - gassed system. The square - wave voltammograms obtained for the addition of barium, strontium and calcium nitrate are presented in figure 7.25-7.27.

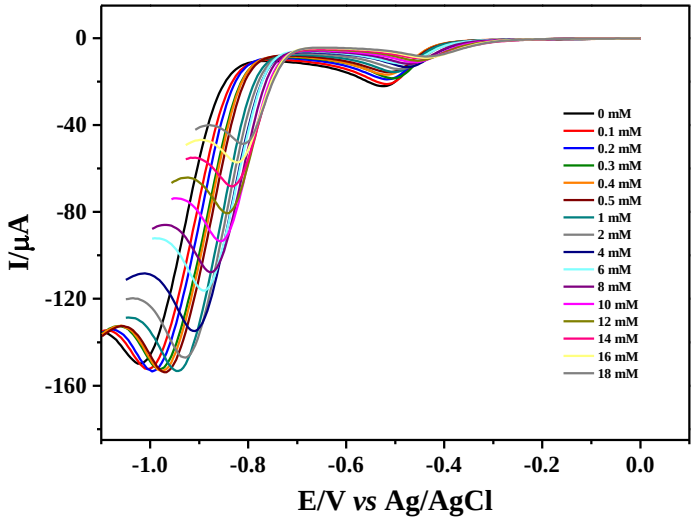

Figure 7.25 – Square-wave voltammograms (f = 25 Hz, A = 0.1 V, Step = 0.05 V) for disodium rhodizonate (16 mM) with sequential amounts of calcium nitrate (0.1 - 18 mM) in aqueous KCl (0.1 M) with boric acid (0.4 M) at pH 7. Performed at a Au electrode (3 mm, BAS) with a graphite counter and Ag|AgCl (BAS) reference electrode at 293.15 ± 1 K.

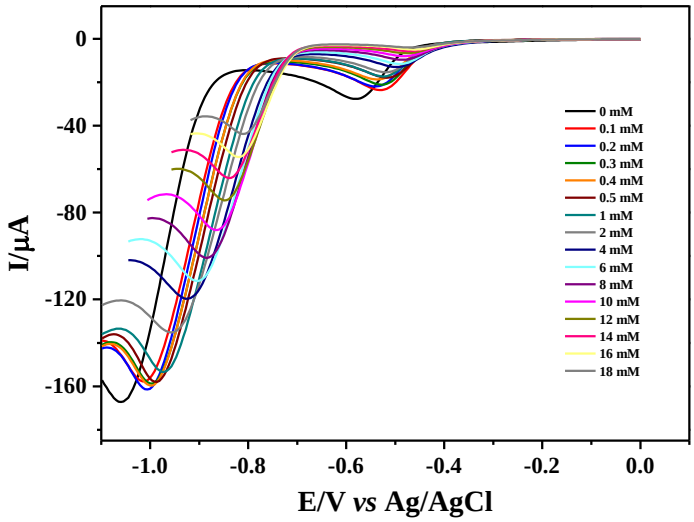

Figure 7.26 – Square-wave voltammograms (f = 25 Hz, A = 0.1 V, Step = 0.05 V) for disodium rhodizonate (16 mM) with sequential amounts of strontium nitrate (0.1 - 18 mM) in aqueous KCl (0.1 M) with boric acid (0.4 M) at pH 7. Performed at a Au electrode (3 mm, BAS) with a graphite counter and Ag|AgCl (BAS) reference electrode at 293.15 ± 1 K.

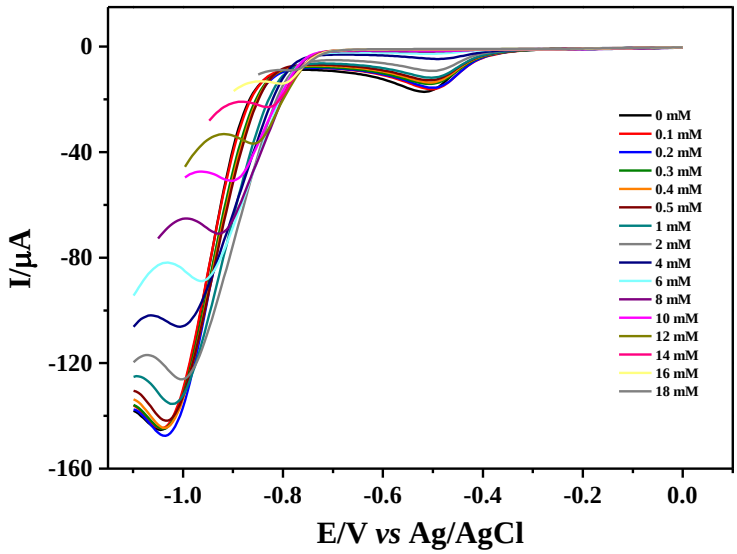

Figure 7.27 – Square-wave voltammograms (f = 25 Hz, A = 0.1 V, Step = 0.05 V) for disodium rhodizonate (16 mM) with sequential amounts of barium nitrate (0.1 - 18 mM) in aqueous KCl (0.1 M) with boric acid (0.4 M) at pH 7. Performed at a Au electrode (3 mm, BAS) with a graphite counter and Ag|AgCl (BAS) reference electrode at 293.15 ± 1 K.

Greater oxidative shifts in reductive Ep and decreases in Ip were both exhibited for the complexation with Ba^{2+}, figure 7.28 and 7.29, at 14.8 ± 0.4 mV $decade^{-1}$ and 85.2 ± 2.7 μA $decade^{-1}$. The response of the system to the addition of Ca^{2+} and Sr^{2+} was very similar with Ep shifts of 7.7 ± 0.4 mV $decade^{-1}$ and 9.5 ± 0.4 mV $decade^{-1}$ respectively, and Ip decreases of 63.8 ± 1.1 μA $decade^{-1}$ and 64.2 ± 3.4 μA $decade^{-1}$ respectively. Magnesium produced by far the lowest response in the system for both Ep shift, 3.9 ± 0.1 mV $decade^{-1}$, and Ip decrease, 41.1 ± 1.8 μA $decade^{-1}$.

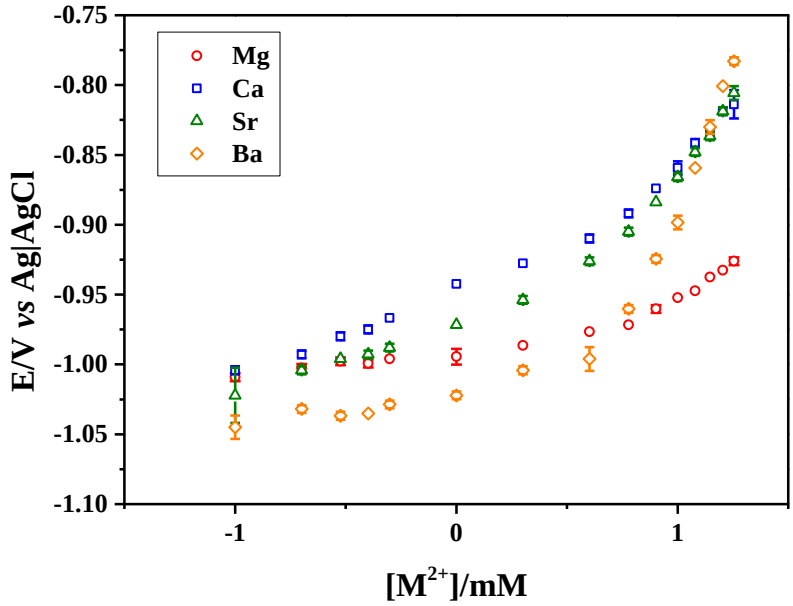

Figure 7.28 - Plots of square wave I forward E_p *versus* the log of the concentration of M^{2+} (M = Mg, Ca, Sr and Ba) to sodium rhodizonate (16 mM).

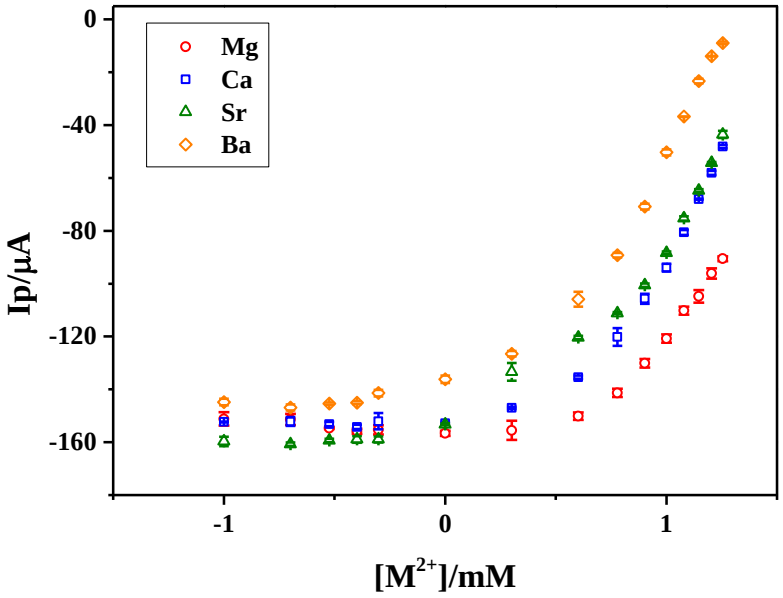

Figure 7.29 - Plots of square wave I forward I_p *versus* the log of the concentration of M^{2+} (M = Mg, Ca, Sr and Ba) to sodium rhodizonate (16 mM).

Previous experiments showed that detection was reliable up to 1:1 metal: ligand ratio; therefore, sodium rhodizonate (16 mM) was prepared. Upper and lower limits of Sr^{2+} (2 and 8 mM) and Ca^{2+} (20 and 200 mM) concentrations for formation water were added to the NaRZ solution prior to the sequential additions of Ba^{2+} and measurement with square wave voltammetry, figure 7.30.

The results observed show that Ca^{2+} significantly hinders the ability of the system to detect Ba^{2+} due to its naturally high concentration in the medium. At the highest concentration of Ca^{2+} the Ip decrease was almost completely negated at 3.9 ± 1.2 μA decade^{-1} and only a very small Ep oxidative shift is present at 1.5 ± 0.3 mV decade^{-1}. As calcium is so abundant in the environment down-hole, even the lowest average concentration showed significant reductions in Ep and Ip shifts of 4.9 ± 0.3 mV decade^{-1} and 28.4 ± 4.1 μA decade^{-1} respectively. Sr^{2+} showed significantly less hindrance to the detection of Ba^{2+} with the biggest deviation seen in the Ep oxidative shifts; they decreased to 11.5 ± 0.4 mV decade^{-1} and 8.1 ± 0.4 mV decade^{-1} for 2 mM and 8 mM interferences respectively. There were also decreases, albeit smaller, in Ip for Sr^{2+} interferences to 77.6 ± 1.8 μA decade^{-1} and 60.9 ± 3.7 μA decade^{-1} for 2 mM and 8 mM respectively.

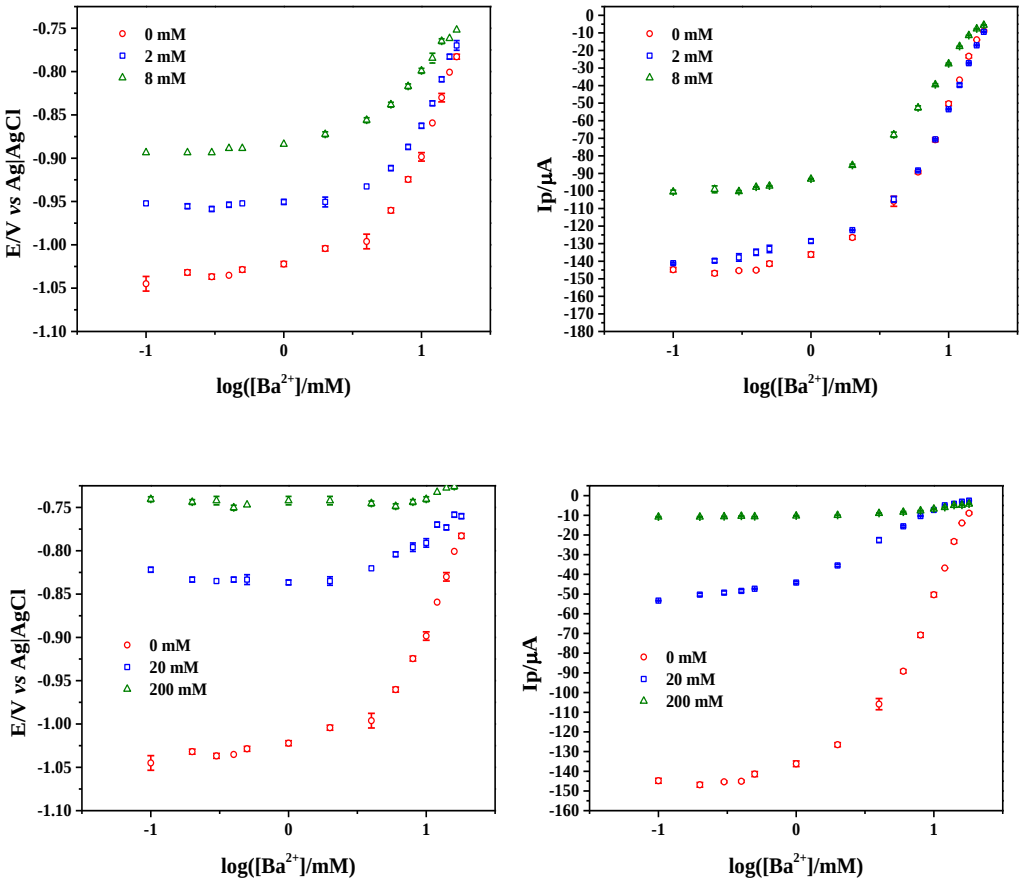

Figure 7.30 - Plots of square wave I forward Ep (left) and Ip (right) *versus* the concentration of Ba^{2+} added to solutions with pre - added strontium (top) and calcium (bottom).

Figure 7.31 shows a 3-D plot of the peak potential response of rhodizonate for the addition of barium (0.1 - 18 mM) to solutions containing a known amount strontium (0, 1, 3, 5 and 8 mM). After obtaining the detection curves corresponding to these additions, a 3-D surface plot was obtained using a polynomial 2-D model in Origin. The formula of this surface allowed a model to be created for the estimation of expected peak potentials for solutions of known concentration; and vice versa, the estimation of concentrations of analyte from a known peak potential.

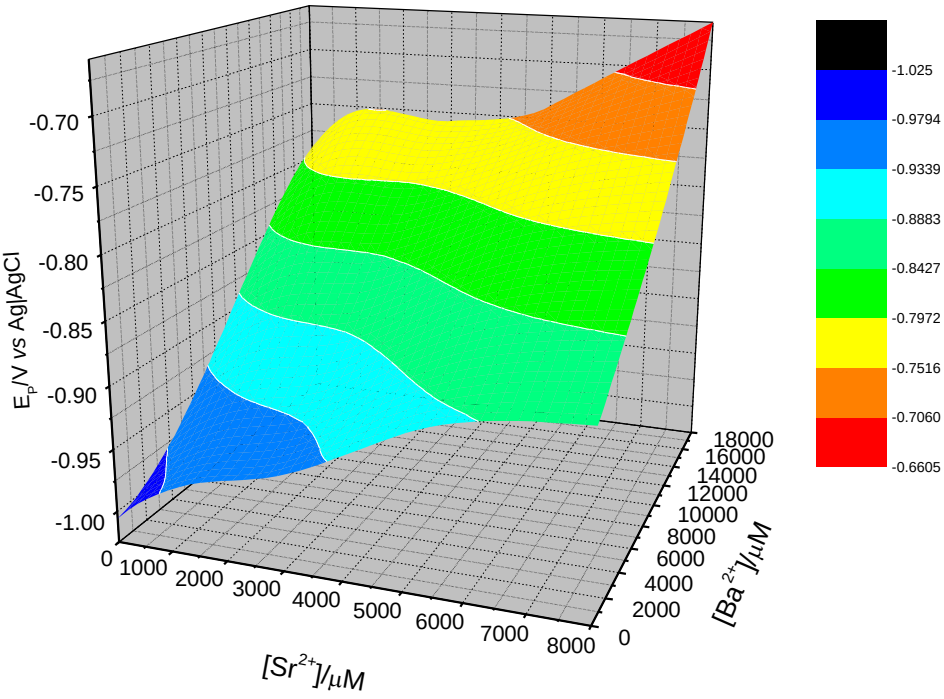

Figure 7.31 - 3-D surface plot obtained for the reduction potential of rhodizonate (16 mM) with additions of barium (0.1 - 16 mM) and interference from strontium (1 - 8 mM).

Solutions of disodium rhodizonate were prepared in the same way as above with a known concentration of strontium nitrate added. This solution was degassed and then an known concentration of barium nitrate, but one that was not used previously, was added. Using the known concentrations of the two ions a predicted peak potential was obtained from the model. Square-wave voltammetry was then performed on the solution and the experimental peak potential recorded. These results are compared to the predicted peak potentials in table 7.1. It is seen that the polynomial 2-D model predicts the peak potential well, with all results within a 5 mV range of expected.

Table 7.1 - A table representing the model predicted peak potential and experimentally obtained peak potential for barium added to sodium rhodizonate (16 mM) with a known strontium interference (2 mM).

[strontium]/ mM	**[barium]/ mM**	**Model Ep/ V**	**Experimental Ep/ V**	**Difference in model and experimental/ mV**
2	4.72	-0.918	-0.923	5.0
2	5.88	-0.904	-0.909	5.0
2	9.30	-0.862	-0.861	0.1
2	11.5	-0.833	-0.837	4.0
2	13.7	-0.806	-0.804	2.0
2	16.9	-0.773	-0.774	1.0

The model exhibited excellent agreement with the experimental values obtained, showing that the system is suitable for the determination of barium concentration in aqueous samples at pH 7 in the presence of strontium.

Pressure and temperature down-hole will be markedly different to that of a laboratory environment. To probe this, the system was tested at a raised temperature (50 °C), with the square wave reductive I_F again being measured. The response in terms of the measured current and potential in the conditions described were recorded, figure 7.32. The results showed a clear destruction in the ability for the system to detect barium cations. Initially, at low concentrations, the same trend was apparent; with the peak potential and current remaining constant. Where, in the room temperature experiments, a linear decrease in both potential and current was observed; at 50 °C, there was no linear trend. In addition to this, once 12 mM of barium had been injected into the system, there was a complete destruction of the peak; whereas before a peak was observed up to 24 mM Ba^{2+}.

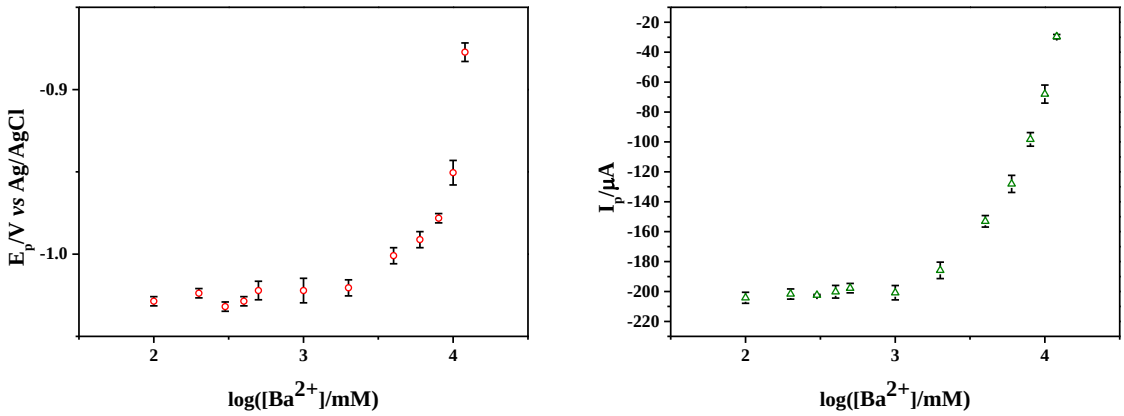

Figure 7.32 - Plots of square wave I forward Ep (left) and Ip (right) *versus* the log of the concentration of Ba^{2+} (0.1 - 12 mM) to sodium rhodizonate (16 mM) at 50 °C.

This indicates that the system itself is inappropriate for use in an environment as harsh as down-hole in an oilfield.

7.3 Conclusions and future work

In this chapter, the rhodizonate dianion was investigated in terms of its suitability for the detection of alkaline - earth metal ions in aqueous environments. The cyclic voltammetric response of disodium rhodizonate yielded a large oxygen peak at ~ - 0.6 V after 30 min degassing. In addition to this a single electron, irreversible reduction was observed at ~ - 1.05 V. The addition of barium nitrate to the system produced an oxidative, linear Nernstian shift of 29.1 ± 0.1 mV $decade^{-1}$ that was stable over a 7 h timeframe. The oxidative shift was accompanied by a decrease in the measured peak current. The trend of this decrease was reproducible; however, the measured values were not consistent over the same 7 h timeframe. The system gave good agreement with the K_{sp} of barium rhodizonate presented by Pan *et al.*[18] with the shift in reductive peak potentials from square wave voltammetry producing a shift until 42 ± 1 µM.

The changes in the peak potential and peak current were observed for strontium and calcium as well; with the most sensitive response being for barium and least sensitive for calcium. The system was tested in artificial sea water conditions at 35 salinity,

where the same trends in shifts were observed but with reduced magnitudes. The response of the system to barium remained the most sensitive by it was reduced from 41.6 ± 1.8 mV decade^{-1} to 15.8 ± 0.6 mV decade^{-1}. In these tests, the response toward strontium was similar to that of barium; whereas the response to calcium was significantly smaller. The interference of strontium was tested by adding a known amount of strontium to the solutions of disodium rhodizonate prior to the addition of barium. The shift in peak potential remained for the addition of barium; however, the decrease in peak current was greatly diminished.

The system was applied to the application of detection in formation water by increasing the concentration of disodium rhodizonate to 16 mM and reducing the pH to 7. The same trends were observed in peak potential and peak current, but with a reduced magnitude to the original pH 8.5 plots. The shift in peak potentials for barium was found to be the most sensitive at 14.8 ± 0.4 mV decade^{-1}. The interference on this response for calcium and strontium was tested. Calcium, as it is typically present in such large concentrations (> 200 mM) in formation water samples, greatly interfered with the response. Strontium however, did not interfere as much and a model was produced to predict the concentration of barium present in solution in the presence of strontium. This model produced accurate results with all readings being within 5 mV of the absolute concentration. The system did not produce accurate results at raised temperature (323 K) which means the method is unsuitable for down-hole application.

This system showed some promise toward the detection of alkaline-earth metal ions at surface conditions in water samples. More work would need to be done on interferences suffered in the different water conditions at room temperature.

7.4 References

1 J. F. Heller, *Ann. der Pharm.*, 1837, **24**, 1–17.

2 R. I. Gelb, L. M. Schwartz and D. A. Laufer, *J. Phys. Chem.*, 1978, **82**, 1985–1988.

3 F. Feigl, *Ind. Eng. Chem.*, 1942, **14**, 840–842.

4 H. V. Weiss and W. H. Shipman, *Anal. Chem.*, 1957, **29**, 1764–1766.

5 H. V. Weiss and M. G. Lai, *Anal. Chem.*, 1960, **32**, 475–478.

6 R. E. Dinnebier, H. Nuss and M. Jansen, *Acta Crystallogr. E*, 2005, **61**, 2148–2150.

7 R. A. Chalmers and G. M. Telling, *Microchim. Acta*, 1967, **55**, 1126–1135.

8 G. Iraci and M. H. Back, *Can. J. Chem.*, 1988, **66**, 1293–1294.

9 B. Zhao and M. H. Back, *Can. J. Chem.*, 1991, **69**, 528–532.

10 S. Andreola, G. Gentile, A. Battistini, C. Cattaneo and R. Zoja, *J. Forensic Sci.*, 2011, **56**, 771–774.

11 E. Jungreis and M. Nechama, *Microchem. J.*, 1986, **34**, 219–221.

12 H. Chen, M. Armand, M. Courty, M. Jiang, C. P. Grey, F. Dolhem, J.-M. Tarascon and P. Poizot, *J. Am. Chem. Soc.*, 2009, **131**, 8984–8988.

13 C. Wang, Y. Fang, Y. Xu, L. Liang, M. Zhou, H. Zhao and Y. Lei, *Adv. Funct. Mater.*, 2016, **26**, 1777–1786.

14 R. T. Bailey, *J. Chem. Soc. B Phys. Org.*, 1971, **0**, 627.

15 G. Gutzeit, *Helv. Chim. Acta*, 1929, **12**, 713–740.

16 F. Feigl and V. Anger, *Spot tests in inorganic analysis*, Elsevier Pub. Co, 1972.

17 R. Chandra, *J. Chem. Educ.*, 1962, **39**, 397.

18 K. Pan, T.-S. Chou and T.-S. Huang, *J. Chinese Chem. Soc.*, 1966, **13**, 99–110.

19 A. G. Collins, *geochemistry of oilfield waters*, Elsevier Pub. Co, New York, 1975.

20 J. M. Neff, *Bioaccumulation in Marine Organisms*, Elsevier Ltd., Oxford, 2002.

21 G. M. Marion, F. J. Millero, M. F. Camões, P. Spitzer, R. Feistel and C.-T. A. Chen, *Mar. Chem.*, 2011, **126**, 89–96.

8 Summary of the thesis

This thesis aimed to develop appropriate sensing chemistry for the electrochemical detection of alkaline-earth metal ions in formation water. Accordingly, the first chapter outlined the relevance of this work and gave an overview of the methods currently used for the determination of alkaline-earth metals in aqueous conditions, such as atomic spectroscopy, fluorescence spectroscopy and ion-selective electrodes. The common underlying theme through the different sensing methods was the use of complexation between ligands and the metal ions. The sensing chemistry routes focussed on throughout this thesis also looked to utilise this interaction. The second chapter detailed the electrochemical concepts that underpin the subsequent results and the third chapter outlined the experimental techniques used throughout this work.

Chapter 4 investigated the reliability of the ferrocene | ferricinium redox couple and finds that chloride ions present in the system interferes with it. It is seen that the calculated N_{eff} values for ferrocene increases above unity in the presence of chloride ions above 10 mM in the case of potassium chloride, 100 mM in the case of strontium chloride and 500 mM in the case of barium chloride. Rate constants for these scenarios were produced from a simulated DISP1 mechanism, which allowed for the elucidation of how many chloride ions were interfering with the ferrocene in each scenario. In this way it was found that one chloride was interfering in the case of potassium and strontium chloride, whereas three chlorides were interfering in the case of barium chloride. This chapter shows that the ferrocene | ferricinium redox couple can be used as an internal standard in non-aqueous environments alongside a quasi-reference electrode; however, the exact solution composition and conditions must be considered. Therefore, any result obtained must be thought of in terms of the system, where each component must be scrutinised.

Chapter 5 focussed on the interaction of chlorquinaldol and broquinaldol with alkaline-earth metals as a route for detection. Firstly, the voltammetric response of chlorquinaldol in acetonitrile was characterised using cyclic voltammetry followed by the two quinaldols being characterised in equimolar DMSO/H_2O with a DISP2

reaction process proposed. This was due to the decrease in apparent diffusion coefficients with increasing concentrations on quinaldol. Both ligands produced an increase in the N_{eff} values in the presence of barium ions above 10 mM with chlorquinaldol producing a larger shift than broquinaldol. It is also demonstrated that chlorquinaldol is more sensitive to barium ions over strontium ions and calcium ions.

The use of compounds soluble in aqueous conditions allowed for the use of a reliable commercial Ag | AgCl reference electrode. Ferrocenemethanol is a water-soluble derivative of ferrocene that interacts with thiols. Chapter 6 explored the EC' electrode mechanism that is present for ferrocenemethanol and tiopronin. It showed how the turnover number can be manipulated by changing the solution pH in order to increase the reactivity of the tiopronin; with pH 6 giving a turnover number of 2.09 and pH 9 giving 7.95 (ν = 0.02 V s^{-1}). The introduction of barium ions to the system (above 10 mM) was shown to reduce the turnover number at pH 6 and pH 9. A greater decrease was observed for pH 9 where the reduction in peak current gave a linear trend of 7 ± 0.5 μA $decade^{-1}$ with a LOD of 11 ± 2 mM.

The first two sensing methodologies explored utilised amperometric changes to determine the presence of alkaline-earth metal cations. Chapter 7 utilised an entirely novel approach to ion sensing by using changes in both the peak potential and current to successfully determine the concentration of alkaline-earth metal ions. It looked at the voltammetric response of disodium rhodizonate which is a water soluble compound that can bind with barium to produce a solid precipitate. This complexation is shown to produce a linear Nernstian oxidative shift of 29.1 ± 0.1 mV $decade^{-1}$ in the reductive peak potentials and a decrease in the peak current. The results showed good agreement with the K_{sp} value reported in literature of 42 ± 1 μM. The system exhibited the ability to detect alkaline-earth metal cations in this way at pH 8.5 (sea water), pH 7 (formation water) and at 35 % salinity (sea water). It was shown that the disodium rhodizonate was more sensitive to the addition of barium ions over strontium ions and calcium ions. A 3-D model was produced that allowed for the prediction of barium ion concentration in samples containing strontium ions as an interfering substance. This model produced good results with every test sample producing a peak potential within 5 mV of the true value.

9 Future work

This thesis investigated three different methods of sensing chemistry for the determination of alkaline-earth metal ions. The first two, chlorquinaldol and tiopronin, both produced results that showed the determination of barium ions was possible. However, neither of them could achieve this at a low enough concentration to be used for the desired application. The system that used disodium rhodizonate produced good results at appropriate concentration levels to be used. It was found that this system was only suitable to ambient temperature sensing. More interference studies would need to be done using this system to determine whether it is suitable for use in a sensing system. In addition to this work would need to be done to work out how to apply this sensing chemistry to a full sensing platform for use in water samples. Problems could be encountered due to the precipitation present upon complexation.